

BAE SYSTEMS

Electronics & Integrated Solutions

P.O. Box 868, Nashua, NH 03061

Device Demonstration

Contract Value: \$8,760,163

Contract N00019-01-C-0088

Final Status Report

December 6, 2001 to December 31, 2006

Prepared for

**Department of the Navy
Naval Air Systems Command
Naval Aviation Systems Team
Patuxent River MD 20670**

**Glenn Marshall
Technical Point of Contact
RF Sensors Division, A1R455
Bldg 2187, Suite 2190
48110 Shaw Rd, Unit 5
Patuxent River, MD 20670-1906**

December 31, 2006

Distribution Approved for Public Release; Distribution is Unlimited

Table of Contents

	Page
I. Introduction	3
II. Hardware Development	4
III. Application to GaAs MMIC Device Fabrication	9
IV. Application to CRAM	17
A. Introduction	
B. X-ray Tool Operation and Maintenance	
C. CRAM Process Development Results	
V. Summary and Conclusions	46
VI. Appendices	47
A. SRL DPF Final Report	
B. JMAR/SAL Final Report	
C. Shipley Final Report	
D. CNTech Final Report	
E. Xmetrics Final Report	
F. SRL Final Report	
G. <i>Rev. Sci. Instrum.</i> Paper	

I. Introduction

The goal of the Defense Advanced Research Projects Agency (DARPA) Advanced Lithography research program was to revolutionize semiconductor lithography through accelerated research of highly innovative approaches that would enable pattern transfer to wafers of features 100 nm and below. To this end, DARPA, via a Broad Agency Announcement, BAA 00-04, solicited proposals for R&D to understand and overcome specific technological obstacles to the realization of lithography for critical dimensions of 100 nm and smaller and the supporting technologies relevant to more than one lithography technology option. In response, Sanders, A Lockheed Martin Company, proposed “Device Demonstrations Using Point Source X-ray Lithography Technology” to enhance and utilize a previously developed X-ray lithography system to address next-generation sub-100 nm lithography demonstrations using point source X-ray Lithography. This program started in December 2001 and was eventually taken over by BAE Systems, Inc. after their acquisition of Sanders. Summarized in this Final Report are the highlights and current status of this effort.

To achieve the principal goal of the program, the use of X-ray based lithographic processes and techniques to realize sub-100 nm feature sizes for semiconductor wafer fabrication, multiple thrusts were taken. The principal ones have been:

- Increase in output power of the X-ray point source
- Improvement of stepper performance
- Development of faster resists
- Development of an X-ray collimator to increase X-ray intensity at the wafer surface
- Development of improved, high resolution masks
- Demonstration by the system to fabricate high performance MIMIC devices
- Development of processes to utilize point source X-ray lithography for CRAM

Although this Final Report will address all these and other relevant topics, emphasis is given to the more recent activities and achievements since they most accurately reflect the current status and future prospects for this important and exciting technology of point-source based X-ray lithography.

II. Hardware Development

An artist's conception of the originally proposed X-ray exposure system is shown in Figure 1. The basic concept of this approach is to generate soft X-rays (approximately 1 keV in energy) from a low pressure (~1-2 Torr) neon (Ne) plasma in a DPF (dense plasma focus) source, to transport the X-rays through a low attenuation beamline, and to finally have them illuminate a semiconductor wafer mounted on a high-precision stepper through a suitable mask. By using short wavelength (approximately 1 nm) X-rays rather than visible or even ultraviolet light with wavelengths >100 nm, ultra-high definition of lithographic patterns should be possible. In principle, feature dimensions of 50 nm or even smaller should be possible to achieve.

Photographs of the actual X-ray system installed at the Microelectronics Center (MEC) of BAE Systems, Inc. in Nashua, NH appear in Figures 2 to 5. Figure 2 shows an overall view of the exposure tool, Figures 3 and 4 are views of the pulsed DPF source, and Figure 5 shows the actual stepper.

Figure 1. Artist's conception of a DPF-based X-ray exposure system used for semiconductor lithography.

Figure 2. Overall view of X-ray lithography system in its current configuration showing the stepper control panel (left), electronics cabinet (center), and stepper chamber (right).

Figure 3. Back-end view of DPF source with access doors open.

Figure 4. Front-end view of DPF source before mating with the stepper chamber.

Shown in Figure 6 is the DPF computer main graphical user interface (GUI) screen after completion of a typical run. Table 1 summarizes the principal tool parameters that are used during a typical exposure run.

During the hardware development phase of this program, a number of issues were addressed in several key subcontracts. The results of these efforts are discussed in detail in Appendices A through F. Appendix A presents the results of the DPF development task. Presented in Appendix B are results pertaining to stepper improvements. In Appendix C are the results of efforts to develop improved resist materials that were used to subsequently fabricate T-gate GaAs MIMIC FETs. Appendix D presents the results of additional work in support of the resist development task. Appendix E discusses efforts to develop X-ray collimators to increase the intensity of the X-ray beam at the wafer plane. Appendix F presents the results of an effort to increase the average X-ray output of the anodes used in the DPF source.

Finally, in Appendix G is a publication which appeared in the *Review of Scientific Instruments* that discusses many details of the DPF X-ray source.

Figure 5. Interior view of the stepper chamber showing the XRS 2000 wafer stepper.

Figure 6. Graphical User Interface (GUI) for the main screen of the DPF controller computer. Shown here is the result of a successful exposure run at 110 mJ/cm^2 at 16 Joules/shot and a run time of 14.3 minutes.

Table 1. Typical run parameters and conditions for the X-ray lithography tool installed at BAE Systems.

Parameter	Typical Value	Remarks
Source		
Ne pressure	1.6 Torr	
Charging voltage	7.8 kV	
Pulse frequency	27 Hz	
Run time	~11-15 minutes	Assumes dose of 100 mJ/cm^2 and mean anode output of $\geq 5 \text{ J/shot}$
Stepper		
Wafer size	3 or 6-inch diameter	
Mask-to-wafer gap	15 μm	
Field size	~25 x 25 mm	

III. Application to GaAs MMIC Device Fabrication

The fabrication process for T-gate formation in GaAs MMIC devices is essentially as follows:

- GaAs device layers are grown via epitaxy
- Metallization of several levels is via evaporation and liftoff
- MMIC T Gate Lithography Process
 - T cross-section reduces gate resistance, improves performance
 - Defined with bilayer resist process
 - T-Gate requires T-head CD shrink to < 400 nm from 800 nm
 - Novolak photoresists must be formulated in solvents which do not attack gate level pattern
- Following gate definition, recess in GaAs is formed using wet etch; Gate metal is evaporated then lifted off

Figure 7 shows the schematic of a T-gate cross section. The basic concept is to simultaneously provide a very small (short) gate length at the bottom of the T to minimize capacitance and transit time and to provide a larger size at the top to reduce series resistance and provide a larger geometry for interconnect attachment.

Figure 7. T-Gate resist profile.

The system overlay performance is demonstrated in Figure 8. Here the gate stem was defined using X-ray; the gate head was defined with an Ultratech 1500 I-line stepper.

Figure 8. SEM image of a single field from Wafer 000619 showing the actual overlay.

An actual resist image formed with Shipley XP-9947W resist appears in Figure 9. This result was achieved using an X-ray dose of 130 mJ/cm^2 and a $15 \mu\text{m}$ wafer-to-mask gap. These images were formed from a 130 nm feature on a mask supplied by NGL-MCOC (Photronics/IBM).

Figure 9. SEM image of a 90 nm resist pattern formed in Shipley XP-9947W resist using an X-ray exposure of 130 mJ/cm^2 .

Even smaller gate lengths were later achieved. Figure 10 shows a gate length slightly over 70 nm achieved using a dual-layer resist structure and the following process conditions:

Figure 10. SEM image of a 70 nm gate formed by X-ray exposure using Shipley XP-1449L resist. The cursors correspond to a spacing of slightly over 70 nm.

DC test results for X-ray defined FETs are shown in Figures 11 to 13. The drain characteristics for a typical lot are shown in Figure 11. Figure 12 shows the transconductance for this same lot and Figure 11 shows the breakdown voltage.

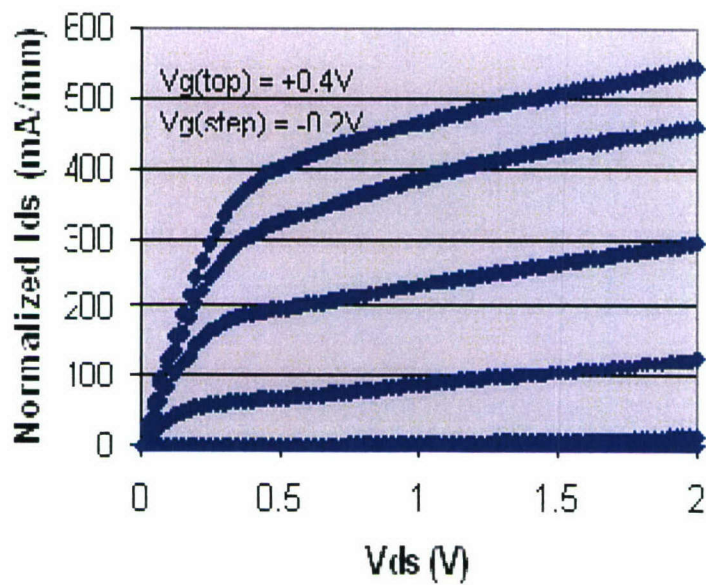


Figure 11. DC drain characteristics for an X-ray defined T-gate FET.

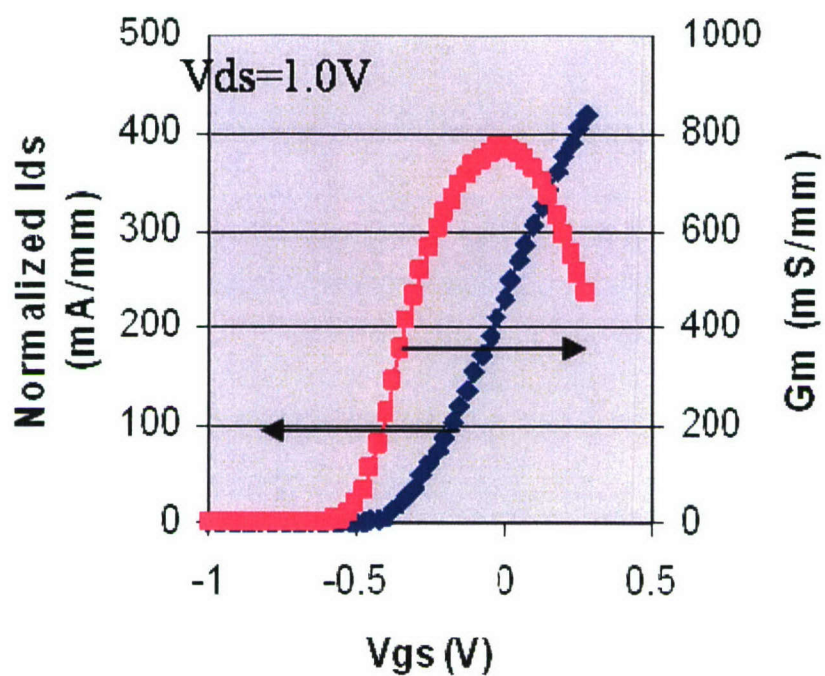


Figure 12. Transconductance characteristic for an X-ray defined T-gate GaAs FET.

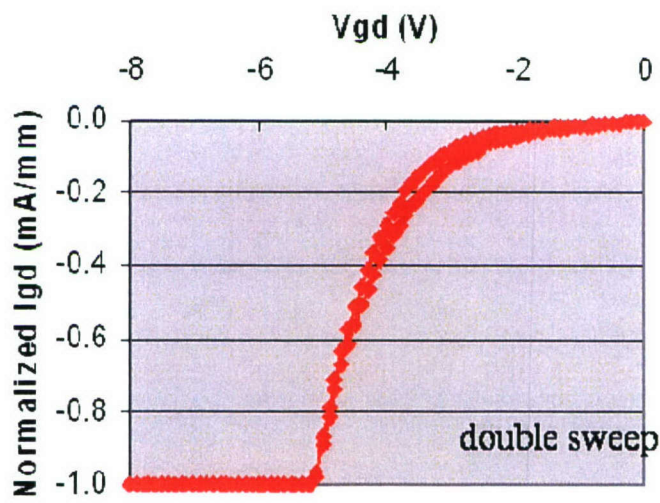


Figure 13. Breakdown voltage characteristic for an X-ray defined T-gate GaAs FET.

One of the high use MMIC applications targeted as a demonstration vehicle for X-ray lithography technology was a low noise amplifier (LNA) MMIC with application to missile seekers. The design is a 150 nm gate length PHEMT device operating in Ka band (see Figure 14a). The LNA was being manufactured using e-beam lithography for gate definition and was selected for use as a demonstration vehicle for the X-ray T-gate process. When fabricated using e-beam lithography, the MMIC exhibited 10 dB of gain from 33 to 37 GHz.

Results from the MMIC fabricated using X-ray lithography appear in Figure 14b. The reduced gain was traced to the difference in input impedance (S_{11}) between the e-beam and X-ray gate FETs used in the MMIC (see Figures 15a and 15b). The MMIC design could be adjusted for this difference to recover the gain. The probable cause for the change is a capacitance difference due to the shorter stem height of the X-ray defined T gate as compared to the typical e-beam defined gate (see Figures 16a and 16b).

Figure 14a. Ka-band MMIC LNA.

Figure 14b. Gain vs. frequency of Ka-band MMIC with gates fabricated by X-ray lithography.

Figure 15a. Input match vs. frequency for e-beam defined gate FET.

Figure 15b. Input match vs. frequency for X-ray defined gate FET.

Figure 16a. X-ray defined T-gate.

Figure 16b. E-beam defined T-gate.

IV. Application to CRAM

A. Introduction

Chalcogenide Random Access Memory (CRAM) devices are of specific importance to the space program for use in satellites and for other military applications requiring radiation-hard memory. The memory state is set by applying controlled heat to the chalcogenide crystal portion of the device effecting change in the electrical properties of the material. Due to the heating requirement in setting the state, stray radiation does not affect the device as in traditional binary RAM, thus giving the device radiation-hard properties. Uniformity of the heater elements at a small size below 100 nm is critical to the process of recording memory bits with precision and efficiency. X-ray lithography is an excellent tool to address the demanding lithography requirement for this critical application.

Key aspects of CRAM are summarized below:

- Chalcogenides: alloys with at least one Group VI element
 - C-RAM uses a $\text{Ge}_2\text{Sb}_2\text{Te}_5$ alloy
 - Can exist in either of two stable states
 - Used in CD-RW and DVD-RW applications
- Three modes of operation –
 - Set (Write a “1”)
 - Apply current to raise memory element temperature to promote crystallization
 - Crystalline state = low resistance = high current
 - Reset (Write a “0”)
 - Apply current to melt memory element
 - Cool quickly to “freeze-in” amorphous state
 - Amorphous state = high resistance = low current
 - Read
 - Low voltage is applied, current determined by resistance of memory element

A drawing showing the basic construction of a CRAM element appears in Figure 17.

Figure 17. Diagram (not to scale) illustrating the basic structure of a CRAM element.

The key parameters of importance for CRAM relating to the lithography step are as follows:

- Small feature size (≤ 70 nm)
- High total count ($> 64 \times 10^6$)
- High aspect ratio ($> 5:1$)
- Large area ($> 1 \text{ cm}^2$)

To this end, significant effort was devoted to developing and demonstrating the ability of X-ray lithography to meet the necessary requirements. The two most significant parts of this effort were (1) maintenance of the X-ray tool to perform the required runs, and (2) actual performance of exposure runs and wafer processing. These two areas are covered in considerable detail below.

B. X-Ray Tool Operation and Maintenance

The X-ray exposure tool is comprised of two basic components – the DPF (Dense Plasma Focus) pulsed X-ray source and the wafer stepper. Maintenance and operation of each are relatively independent of one another, but both must operate properly and consistently to achieve the required program objectives.

1. DPF Source

The X-ray DPF source essentially consists of an evacuated and partially backfilled (with Ne gas) chamber containing of an anode and cathode, a pulsed power supply to provide the input electrical energy, and a computer-controlled user interface to run and monitor the system. Due to the demanding requirements put on this system, considerable effort has been required to both maintain and repair (when necessary) key components. The components requiring most

attention have been the anode and anode base. The anode, which is a consumable component that wears out with use, is made of either all molybdenum (Mo) or a combination of Mo and tungsten (W) to improve component life. A photograph of a typical anode appears in Figure 18. The anode consists of five basic components: base, [water] flow separator, skirt, tip, and baffle. The tip which is closest to the plasma pinch that generates the X-ray pulse wears with use; anodes have been constructed using both Mo and W for this critical part. The remaining parts are all made from Mo and the entire unit is assembled by high temperature brazing using a gold-nickel alloy.

Figure 18. *Photograph of a typical DPF anode that has been cross-sectioned by EDM (electric discharge machining) for diagnostic purposes. The base (which is inserted into a corresponding “anode base” within the source chamber) is to the left; the tip which controls the plasma pinch and X-ray pulse is to the right. The sectioned region in the center shows some of the water-cooling channels that are necessary to achieve high pulse rate and high output power.*

To assure totally leak-free (both water and vacuum) operation, all anode components must be defect and crack-free and the critical brazing step must be done properly to assure absence of any voids. The latter step, in particular, has been problematic throughout much of the program and has consequently required particular attention. Brazing of the anode components is typically done in a vacuum furnace at about 1800°F (~1000°C) using an 82/18 Au/Ni alloy (in either powder or wire form). To achieve success, it is imperative that all components be absolutely clean prior to assembly and that all regions to be brazed are totally filled (but not overfilled) with brazing alloy, either wire or powder depending on the particular joint. In addition, all

components must be crack-free prior to assembly to prevent unwanted water or vacuum leakage paths. Figure 19 shows what can happen if these conditions are not met.



Figure 19. Photograph of a region of the tip-to-skirt interface on the exterior surface of an anode showing a crack in the Mo skirt that has propagated from the brazed interface. Such a crack can provide an unwanted path for cooling water leakage from the anode interior into the DPF chamber.

Another DPF source component that has been particularly problematic has been the anode base which is the part to which the anode mates via a copper sealing gasket. A schematic showing the critical interface region between anode and anode base appears in Figure 20. For a variety of possible reasons, the knife edge connections to the soft copper gasket can fail during use – the most damaging manifestation of such an event is the occurrence of EDM-like etching of one or both of the knife edges. If it occurs to the anode, generally the anode has been lost. If it occurs to the anode base, the base must be removed and the knife edge remachined. Because of the dimensional changes that this creates, a thicker Cu gasket must subsequently be used. Furthermore, after repeated incidents the anode base knife edge can no longer be remachined because it has reached its limit. In the past this has required replacing the entire anode base assembly at considerable cost and time. However, a method to repair the base was developed. In essence, a portion of the stainless steel knife edge insert was removed by machining, a new insert was fabricated, pressed into place, and attached by electron-beam welding, and a new knife edge was formed.

Figure 20. Schematic (not to scale) of the anode/anode-base region of the X-ray source. The copper (Cu) gasket provides both a vacuum/water seal to the chamber and electrical connection between the anode base and anode via the two knife-edges shown.

2. Wafer Stepper

The wafer stepper employed in the X-ray exposure tool is a modified XRS 2000 Mod 5 stepper made by JMAR Systems in South Burlington, VT. To maintain precise and stable positioning of the mask stage relative to the wafer stage, a laser interferometer system is employed. A schematic showing some of the principal components of the interferometer is shown in Figure 21. A particularly troublesome issue that arose with this system was the so-called “loss of laser lock” – i.e., a condition in which closed-loop control of the interferometer would suddenly cease after final positioning of the wafer relative to the mask and during operation of the pulsed X-ray source. The ramification of this condition would range from slight movement and/or drift of one stage relative to the other to a sudden large jump in their relative positioning. Obviously, either was an intolerable event and demanded an immediate solution.

Figure 21. Schematic diagram of the optical portion of the laser interferometer used in the JMAR XRS 2000 Mod 5 stepper.

Since loss of laser lock would only occur while the pulsed DPF source was running, it was suspected that EMI (electromagnetic interference) was a likely cause. Repeated efforts were made to isolate the specific source by performing noise measurements, shielding, regrounding, etc., but to no avail. Finally, through the assistance of an EMI consultant (Silent Solutions, LLC, Amherst, NH) we determined the cause to be related to insufficient optical signal to the Y2 (Theta) fiberoptic receiver. This had been compensated for by increasing the gain setting of the receiver, but at the cost of decreasing the signal-to-noise ratio for that channel. An immediate

program to regularly monitor all three optical channels was instituted. Results as of the end of November 2006 are shown in Figure 22.

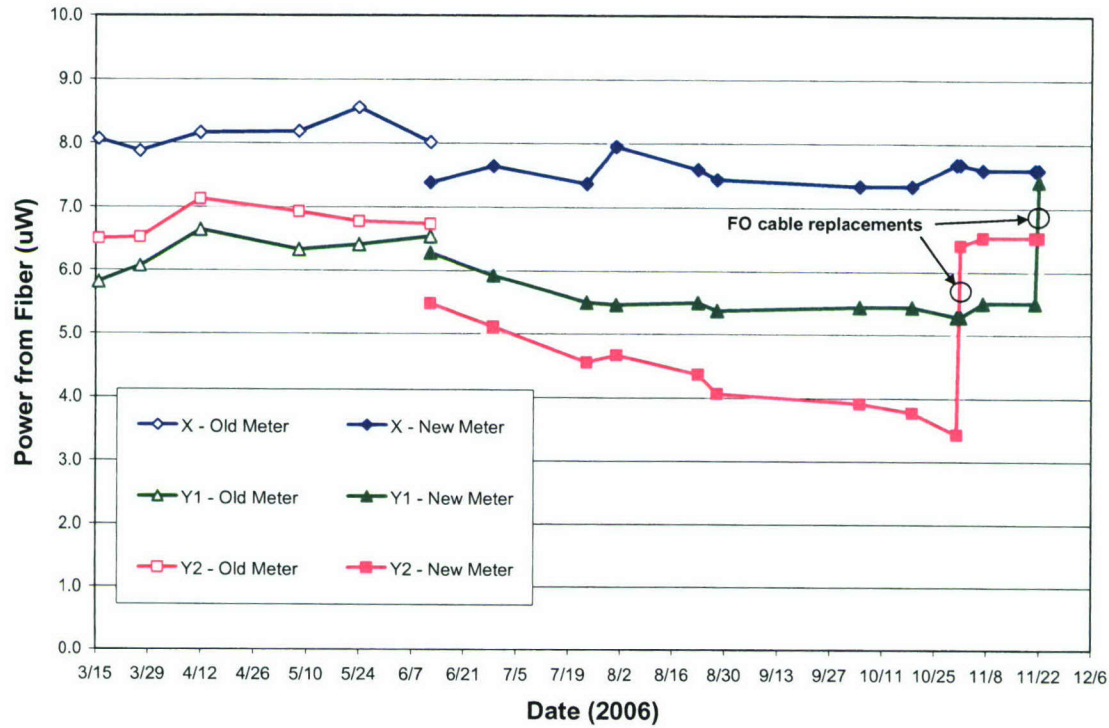


Figure 22. Time chart showing the three laser interferometer intensities at the inputs of the fiberoptic receivers. Also indicated are changes in metering and replacements of two of the optical cables connecting the two-axis differential interferometer to their receivers.

Noted also in Figure 22 are the replacements of the two fiberoptic cables connecting the Y1 and Y2 receivers to the two-axis interferometer. This replacement was required because of the falloff in intensity for these two channels as can be seen in this figure. The repeated periodic measurements of signal intensity had created apparent damage to either these fibers or their connectors thus increasing signal attenuation by the cables. The ramification of this falloff was slight drift between the stages during exposure which resulted in a distortion of the normal circular shape of holes exposed in photoresist (see Figure 23).

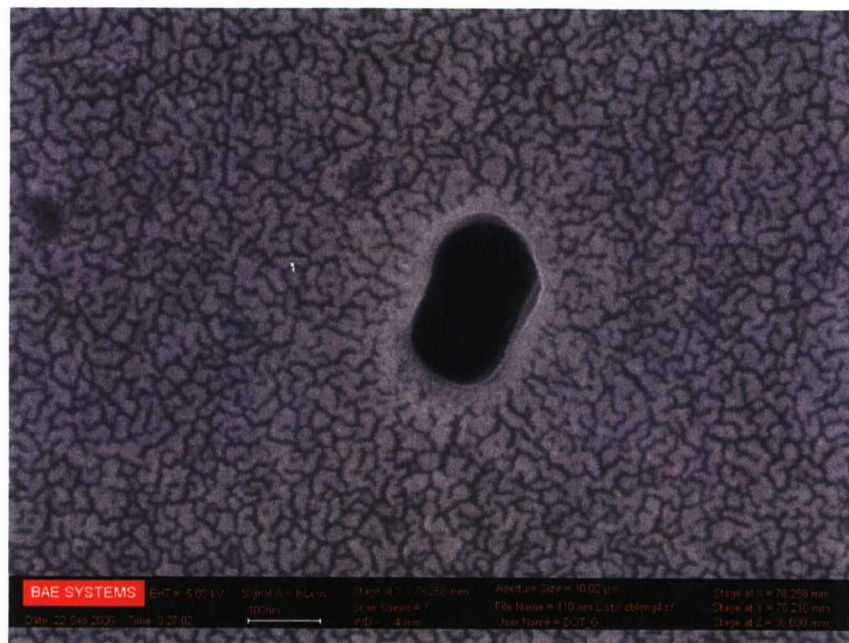


Figure 23. Scanning electron microscope (SEM) image of a nominally round hole in X-ray exposed and developed photoresist. The non-circular shape created by slight movement of the mask stage relative to the wafer stage was the result of reduced intensity in the Y2 channel of the laser interferometer caused by excessive attenuation by its fiberoptic cable. The nominal diameter of this feature is 100 nm.

C. CRAM Process Development Results

A summary of the CRAM exposure runs using Shipley XP-1449L resist, the same resist used for FET T-gate formation, is shown in Table 2. These runs were performed on 3-inch GaAs wafers using the following parameters:

- 140°C, 90 sec dehydration bake
- 3K RPM spin for 60 sec
- 140°C, 120 sec pre-exposure bake
- Expose using CRAM CTP-1 mask with 15µm gap
- 140°C, 90 sec post-exposure bake

Due to the repeating occurrences of loss of laser lock, all of the runs shown in this table were performed at anode voltages below the 7.8 kV allowed maximum. In addition, full exposure of this resist required X-ray doses as high as 140 mJ/cm². For these reasons, individual exposure runs could take as long as 55 minutes.

Table 2. Summary of CRAM mask X-ray exposure runs performed using XP-1449L resist.

Date ('05)	Target Dose (mJ/cm ²)	Actual Dose (mJ/cm ²)	Field #	J/shot	Shots	Laser Lock OK?	Volts (kV)	Remarks	Why run aborted
2/24	140	60	1	10.2	19827	NO	7.2	"1449L-1500" @ 1K RPM	laser
4/18	135	135	1	5.3	86160	ok	7.2	"1449L-3000" @5K RPM	
	125	125	2	-	40390	ok	7.3, 7.5		
4/21	115	115	1	5.9	66193	NO	7.4	New bottle 1449L @ 5K RPM	laser
	115	115	2	5.8	66337	ok	7.4		
4/27	115	-	1	-	-	NO	7.4	Laser lock lost in 3 min	laser
	115	103	2	5.4	62728	NO	7.2, 7.3	Excessive dropouts & laser lock loss	laser
6/2	95	95	1	6.8	-	ok	7.4	1st run with new P.I.	
	90	42	2	7.1	-	NO	7.4		laser
6/10	90	90	1	7.4	-	ok	7.4		
	85	20	2	7.4	-	ok	7.4	Source died	water?
6/14	80	7	1	8.4	-	NO	7.4		laser
	80	13	2	7.5	-	NO	7.3		laser
	80	40	4	7.0	18215	NO	7.2		laser
9/28	80	80	1	10.7	25252	ok	7.4	Install Anode #22	
	100	100	2	9.3	36096	ok	7.4		
	120	120	3	9.1	44642	ok	7.4		
	140	140	4	8.5	55792	ok	7.4		

Investigation into alternative resists revealed a candidate with higher sensitivity than the XP-1449L. OEBR-CAP112 PM made by TOK (Tokyo Ohka Kogyo America, Inc.) is, like the Shipley resist discussed previously, a chemically-amplified resist and was developed originally for e-beam use. Shown in Figure 24 is the manufacturer's spin curve which gives the resist thickness as a function of spin speed for a range of viscosities from 2.15 to 5.0 cP.

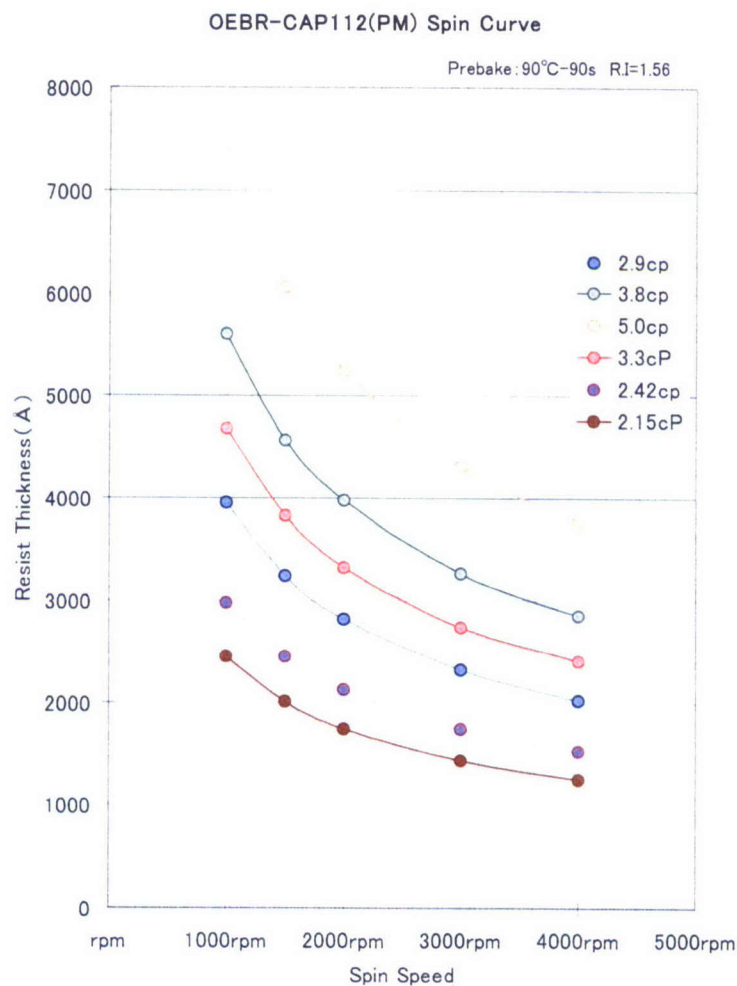


Figure 24. Curves showing resist thickness vs. spin speed for TOK OEBR-CAP112 PM resist for viscosities of 2.15, 2.42, 2.9, 3.3, 3.8, and 5.0 cP. Prebake conditions of 90°C for 90 sec are assumed. (Figure supplied by manufacturer.)

A summary of the CRAM exposure experiments conducted using CAP112 resist appears in Table 3. For all these runs (unless indicated otherwise) the following process parameters were employed:

- 110°C, 90 sec dehydration bake
- 5K RPM spin, 60 sec (2.1 cP viscosity CAP112)
- 90°C, 90 sec pre-exposure bake
- Expose using CRAM CTP-1 mask with 15 μ m gap
- 110°C, 90 sec post-exposure bake
- 60 sec develop in CD-26
- For runs past 12/2005, use 3.3 cP CAP112, 1K RPM spin, NO dehydration bake, but pre-treat with HMDS.

Table 3. Summary of CRAM mask X-ray exposure runs performed using CAP112 photoresist.

Date ('05)	Target Dose (mJ/cm ²)	Actual Dose (mJ/cm ²)	Field #	J/shot	Shots	Laser Lock OK?	Volts (kV)	Remarks	Why run aborted
6/16	100	99	1	9.0	37411	~ok	7.4	3" GaAs wafer. Old resist; 140/140/140 bake T; 45 sec develop; Anode # 18	laser
	90	31	2	9.8	10620	NO	7.4		
~6/20	20	20	1	10.1	6658	ok	7.4	Old resist; 105/85/105 bake T; 45 s develop time	
	10	10	2	9.5	3533	ok	7.4		
7/21	20	20	1	13.7	4904	ok	7.8	Old resist; 105/85/105 bake T; 45 s develop time	water
	80	10.2	2	13.1	2633	ok	“		
7/22	40	40	1	12.5	10819	ok	“	Old resist; 105/85/105 bake T; Start 60 sec develop time	water
	60	27.5	2	9.6	9692	ok	“		
7/26	60	40	1	--	10813	NO	“	Switch to new resist; 105/85/105 bake T; install new (?) W(?) anode (Anode # 31)	laser
	60	60	2	--	18026	ok	“	See “cracked” film	
	80	80	4	--	28068	ok	“		
8/10	90	90	1	12.9	23449	ok	“	Start 110/90/110 bake T; anode replaced again (Anode # 12, old Mo); He line not purged?	
	80	~79	2	12.1	21925	ok	“	Water leak at very end of run	water
8/19	75	75	1	13.8	18365	ok	“		
	80	19	2	13.6	4719	ok	“	Knife-edge arcing developed	arching
8/25	90	90	1	13.1	23166	NO	“	Anode base and anode replaced (Anode #11 - used); wafer broke; features seen (non-uniform)	laser
	85	85	2	15.2/12	22854	NO	7.8/7.6	Features & holes seen	laser
	90	30	4	9.4	10887	NO	7.6	No features visible	laser
9/1	70	70	1	14.9	15852	ok	7.6	180C dehydration bake; very non-uniform exposures (dimpled anode; distorted aperture)	
	85	85	2	13.6	21154	ok	7.6		
	65	65	4	12.8	17170	ok	7.6		
9/8	60	42	1	13.0	11735	NO	7.6	Invert anode (Anode #11); 180C bake	laser
	60	60	2	9.5	21336	ok	7.4		
	70	63	3	8.9	23776	ok	7.4	First time ever Field 3 exposure	water
9/15	60	21	1	12.8	5552	NO	7.4	Use Anode #22 + new Be window; 180C bake	laser
	60	57	2	10.4	18424	NO	7.2		laser
	60	60	3	7.8	25968	ok	7.0	Charging P.S. problems on P.S. #B	
	70	22	4	6.9	10659	NO	7.0		laser

Table 3 (continued). Summary of CRAM mask X-ray exposure runs performed using CAP112 photoresist.

9/22	65	65	1	9.0	24370	ok	7.2	"Wiggled" boards; 180C bake; use P.S. #A	
	70	70	2	8.6	27332	ok	7.2		
	75	75	3	8.2	30981	ok	7.2		
	80	80	4	7.8	34548	ok	7.2		
9/29	70	70	1	10.9	21737	ok	7.5	Last (?) run to use 3" GaAs wafer (?). Pre-treat with HMDS; no dehydration bake	
	80	80	2	9.1	29831	ok	7.5		
10/5	75	75	1	9.1	27943	ok	7.5	6" Si "stack" wafer, 3K rpm spin, no HMDS (Wafer No. "2040512-13")	
	75	75	2	9.0	28070	ok	7.6		
	75	75	3	9.7	26094	ok	7.7		
	75	75	4	10.2	24703	ok	7.8		
	75	75	5	10.3	24516	ok	7.8		
	75	75	6	10.2	24780	ok	7.8		
10/17	100	100	1	11.3	29907	ok	7.8	6" Si "stack" wafer, 5K rpm spin, HMDS (Wafer No. "CRAM MB3-05") (Note: resist was applied 4 days earlier)	
	90	90	2	10.2	29693	ok	7.8		
	80	<10	3	--	<5000	ok	7.8		water?
11/1/05	100	~0	1	<1	~60	OK	7.8	Anode & anode base knife edges damaged.	Arcing
1/12/06	90	~40	1	6.7	20350	OK?	7.8	Anode #11(remachined). Anode base replaced. Wafer 2040512-18. New 5-field Job File. Anode died 1/2 way through; underexposed.	D/O's
1/16	90	90	1	15.5	19535	???	7.8	Anode #13. Wafer 2040512-19. He problem? Very underexposed. May have lost laser lock.	
1/18	100	100	1	15.9	21143	NO	7.8	Wafer 2040512-19 (strip & recoat). Lost laser lock ~3/4 way through. He OK.	
1/19	110	47	4	15.9	10000	NO	7.8	Wafer 2040512-18 (strip & recoat). O ₂ in He not < 0.01; raise dose to compensate. Spots near wafer center → start with Field #4. Wiggled 3 boards before run. Lost X laser lock all 3 times. Try reducing V – did not help.	Laser
	110	23	5	13.0	6061	NO	7.6		Laser
	110	15	1	10.7	4732	NO	7.4		Laser
	110	0	2	--	--	--	--	Stepper hung up w/mask & wafer mounted.	
1/26	100	16	1	15.7	3427	NO	7.8	Wafer 2040512-20 (new). Remove RMX & use contact cleaner on boards & sockets prior to run. Lose X laser lock at ~3400 shots.	Laser
	100	52	2	8.5	20499	NO	7.0	Reduce V to stop laser loss - did not help.	Laser
	100	100	3	13.3	25301	N/A	7.8	Intentionally run laser in open-loop. Some non-uniformity in exposure. Double exposure in x-direction of ~1.0 μm. "XY Stage" readout → x constant but y drifted 0.1 μm in 18 min exposure.	
2/8	100	46	1	13.7	11280	NO	7.8	Wafer 2040512-16 (new). Replace backplane board in RMX computer. Did not help. (Took long time for water ρ to get high enough to run)	Laser

Table 3 (continued). Summary of CRAM mask X-ray exposure runs performed using CAP112 photoresist.

2/9	110	27	2	13.5	6669	NO	7.8	Wafer 2040512-16 (from yesterday). Increase dose because of 1-day old resist. Wiggle connectors of all cables connecting to axis-control boards. Did not help.	Laser
3/2	100	~30	1	~13	~9000	N/A	7.8	Wafer 2040512-22 (new). Run open-loop. 1 st run automatic shut down due to source software error message.	Software
	100	100	2	11.3	28913		7.8		OK
5/4	90	90	1	12.1	25100	OK!!!	7.8	Anode #21 (#13 died from knife-edge arcing). Wafer 2040512-16 (reprocessed). Re-align laser optics per Silent Solutions study. Swap anode base to unit "A". Could not achieve 15 μ m gap (ran at 25 μ m).	
5/9	100	~10	1	< 8	5585	OK	7.8	Wafer 2040512-17 (reprocessed). Gap OK. After 4000 shots anode developed water leak.	Anode
5/24	100	100	5	11.9	28119	OK	7.8	Anode #17. Wafer 2040512-12 (reprocessed). All OK. Had trouble getting 15 μ m gap. Water pump(s) seem noisy.	
5/25	100	90	1	12.1	25137	OK	7.8	Wafer 2040512-18 (reprocessed). Use expired CAP112. Blew Be window; mask OK.	Be window
7/27	100	59	1	11.0	17510	OK	7.8	Wafer 2040512-19 (reprocessed). Use new 1 qt CAP112. New Be window + other rebuilds. Lost sapphire insulator; fixed & restarted. Other unexplained shutdowns (PLC-initiated?).	See Remarks
8/22	100	100	1	11.5	29316	OK	7.8	Wafer 2040512-17 (reprocessed). 100% successful run. Cathode flow sensor interlock overridden. DI filter pump replaced. Got "ovalized" features.	
8/24	110	110	1	9.7	38732	No*	7.8	Wafer 2040512-19 (reprocessed). Sapphire water leaked at 73% point. Repaired leak & finished run. * 3+ hour delay caused loss of laser lock. Wafer NG – double exposure. Strip wafer.	
8/29	110	110	1	16.0	23205	OK	7.8	Wafer 2040512-21 (new ?). Successful run. Exposed for 110 mJ in 16 minutes. Many "specks". Got "ovalized" features.	
8/31	110	110	1	15.2	24404	OK	7.8	Wafer 2040512-19 (reprocessed). Appears less exposed than #21. Got "ovalized" features.	
11/8	100	100	1	10.2	33103	OK	7.8	Wafer 2040512-23 (new). Mask CTP-2 (1 st use). New FO cable. No ovalizing.	
11/16	100	100	4	18.2	18467	OK	7.8	Anode #51 (Brand new). Wafer 2040512-24 (new). Mask CTP-2. Had gapping difficulty. No ovalizing.	

Following exposure and development as outlined above, one of two different paths would typically be taken. The first would be to perform a SEM analysis of the photo pattern on the wafer; the second would be to transfer the photo pattern to the actual wafer by dry etching and to then analyze under the SEM. Generally, both steps would not be taken on the same wafer because a SEM analysis requires a thin (typically 70 to 100 Å) layer of sputtered gold to minimize charging effects and give the best images. Of course, this gold would have to be removed prior to dry etch transfer and this procedure simply inserts another step into the process that could adversely affect the end result.

The basic goals of the photo pattern development task were to achieve consistent and uniform holes over an entire 6-inch diameter wafer, to have the hole diameters be a minimum of 100 nm or less (70 nm would be a very nice achievement), and to have a photo pattern that would allow transfer of these holes to the underlying wafer by subsequent dry etching. To this end, a multitude of different subtasks was required and, to a large extent, formed the basis for the experiments outlined in Table 3 above. For example, a series of experiments using a different resist (Shipley XP-1449L – see Table 2) prior to the experiments outlined in Table 3 demonstrated the need for a faster resist which the TOK CAP112 was able to achieve. Initially, a lower viscosity formulation (2.1 cP) of CAP112 was used, but it was unable to give enough post-development thickness to withstand the rigors of the dry-etch step. Consequently, a higher viscosity (3.3 cP) was employed which resulted in a pre-exposure thickness of approximately 4700 Å.

Various achievements attained during this process development are shown in Figures 25 to 36 and demonstrate the progress made toward reaching our goal. Figure 25 shows a resist hole under the CD-SEM using a thin layer (~1500Å) of XP-1449L resist that was exposed with the DPF source operating at reduced output in order to avoid the laser-lock problem mentioned earlier. Figure 26 is a photograph of a 3-inch GaAs wafer that shows three distinct exposed fields using a worn anode that produced a spatially non-uniform X-ray beam. Shown in Figure 27 is the SEM image of a hole in a thin layer (~1500Å) of CAP112 resist. A histogram showing the results of CD-SEM measurements of a number of similarly exposed and developed holes appears in Figure 28. The results of replacing the worn anode with a newer one appears in Figure 29. Figure 30 shows the “cracking” phenomenon we observed on wafers that were not HMDS-treated prior to resist application; this problem was solved by applying a thin layer of HMDS (hexamethyldisilazane) as shown in Figure 31.

Our first demonstration of a six-field exposure on a 6-inch Si wafer appears in Figure 32. The darkfield optical image of multiple 110-nm diameter holes in a wafer is shown in Figure 33. Figure 34 shows a high-magnification SEM image of a 100 nm hole while operating the stepper in open-loop mode (as another temporary means to reduce the problems associated with loss of laser lock). Finally, Figure 35 shows the result of fixing the laser-lock problem and using a new mask having higher density of holes. Figure 36 is a higher magnification SEM image of nominal 100 nm holes using this new mask.

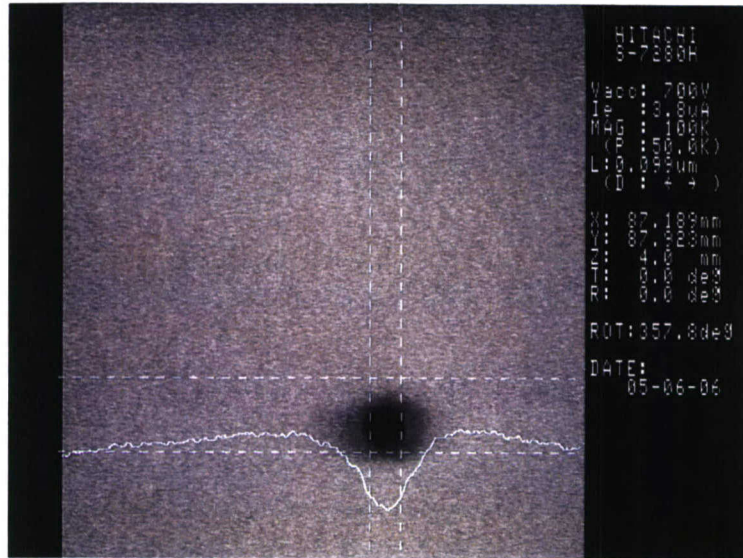


Figure 25. CD-SEM micrograph of an X-ray lithographically defined hole in XP-1449L resist (thickness $\approx 1500 \text{ \AA}$) on a 3-inch diameter GaAs wafer. Mask hole size was 100 nm, proximity gap was 15 μm , and x-ray fluence was 95 mJ/cm^2 (corresponding to a 30 minute exposure at 7.2 kV and 27 Hz with average total pulse energy of 6.8 J). Interferometer laser lock was not lost during this exposure. The spacing between the two vertical dashed calibration lines is 99 nm indicating a patterned feature size very close to the mask size.

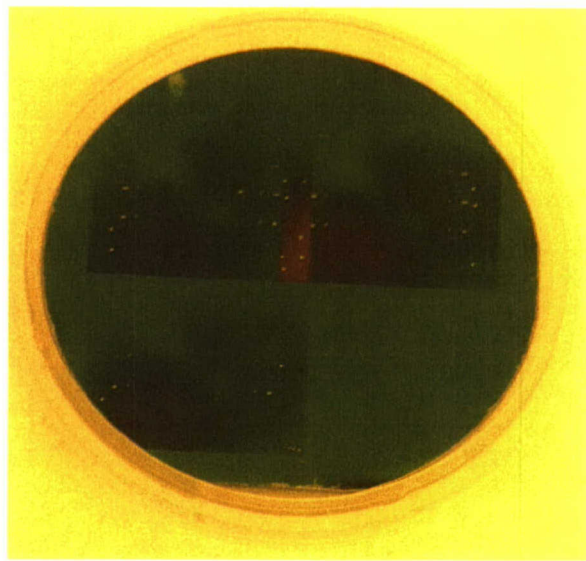


Figure 26. Photograph of an exposed and developed 3-inch GaAs wafer showing three distinct fields. The exposures were made using a well-used, Mo-tipped anode. The non-uniformity which is repeated in each field was due to a combination of an asymmetric or off-center X-ray plasma resulting from uneven anode tip wear and a distorted baffle aperture.

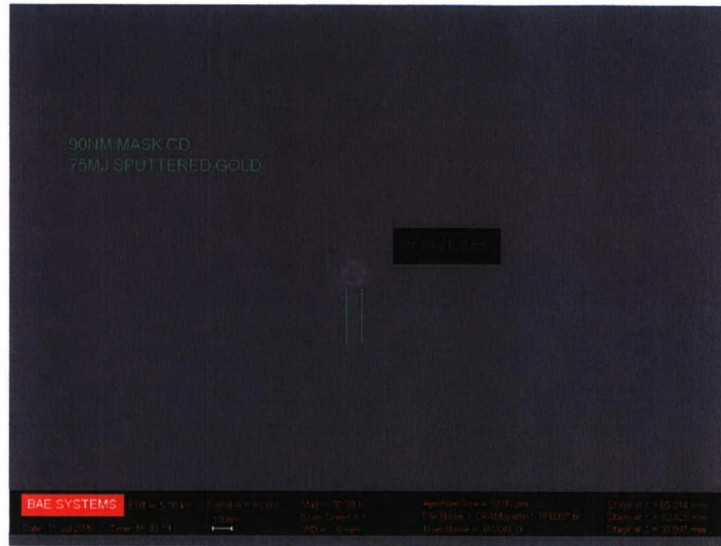


Figure 27. SEM image of a circular hole in a thin layer of developed CAP 112 photoresist exposed with an x-ray dose of 75 mJ/cm^2 using a mask with 90 nm holes. A thin layer of sputtered Au (estimated to be less than 5 nm) was applied prior to measurement. As indicated, the measured diameter of this particular feature is approximately 82 nm.

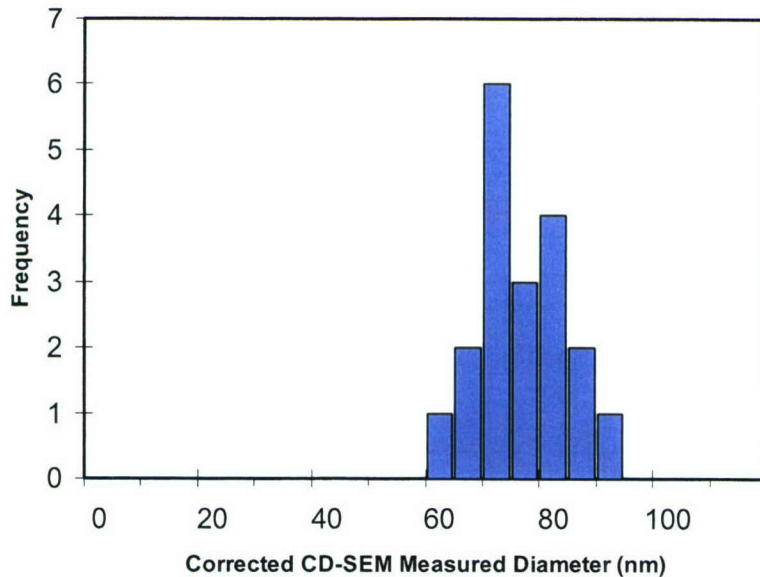


Figure 28. Histogram showing the measured diameters (using a Hitachi S-7280H CD-SEM) of a total of 19 developed holes in CAP 112 resist following exposure at an X-ray dose of 80 mJ/cm^2 through a mask with feature diameter of 90 nm. The mean diameter of these holes is approximately 72 nm.

Figure 29. Photograph of an exposed and developed 3-inch GaAs wafer showing four distinct fields. The improved uniformity of these exposures compared to those shown in Figure 26 is the result of replacing the worn anode having a distorted tip with a newer one having a symmetric tip.

Figure 30. Darkfield photomicrograph of an exposed and developed feature on a 3-inch GaAs wafer using CAP 112 photoresist (overall feature size is approximately 70 μm by 70 μm). X-ray dose was approximately 80 mJ/cm^2 . A “cracking” effect in the resist is very apparent.

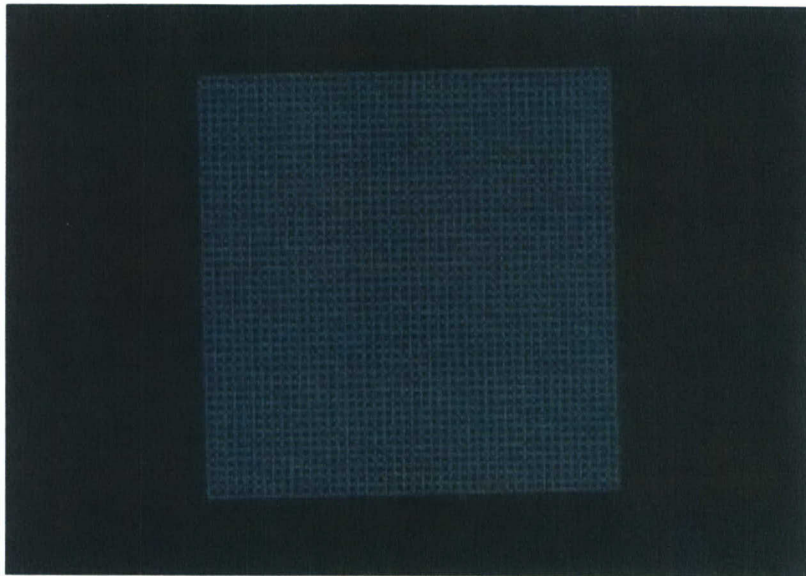


Figure 31. Darkfield photomicrograph of an exposed and developed feature on a 6-inch Si wafer coated with a thin layer ($\sim 500 \text{ \AA}$) of TEOS [Tetraethyl Orthosilicate] oxide. The wafer was pretreated with HMDS, CAP 112 photoresist (viscosity of 2.1 cP) was spun at 5000 RPM, resist thickness was measured to be approximately 1200 \AA , X-ray dose was approximately 100 mJ/cm^2 , and overall feature size is $\sim 80 \text{ \mu m}$ by 80 \mu m . The absence of any “cracking” like that previously in Figure 30 is readily apparent.

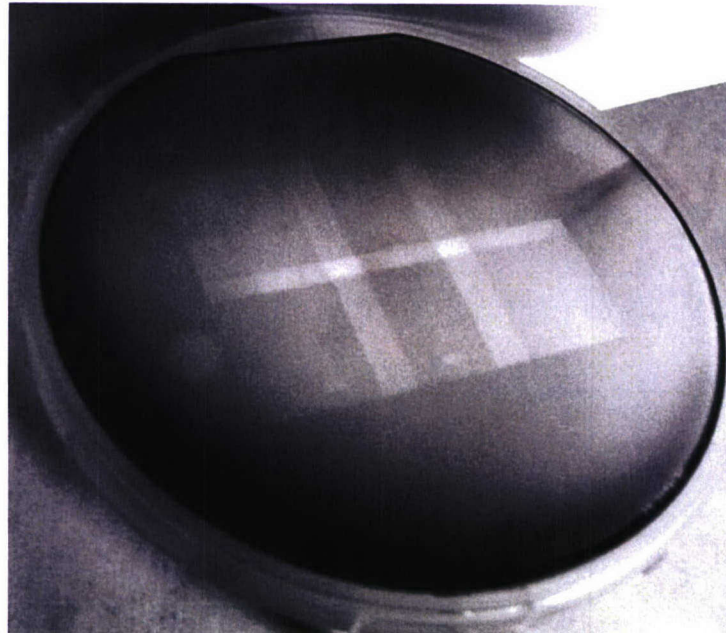


Figure 32. Digitally enhanced photograph of a 6-inch Si “MB-Stack” wafer having six (6) exposed fields using X-ray mask CRAM CTP-1. The wafer was coated with CAP 112 resist and each field was exposed at $\sim 75 \text{ mJ/cm}^2$.

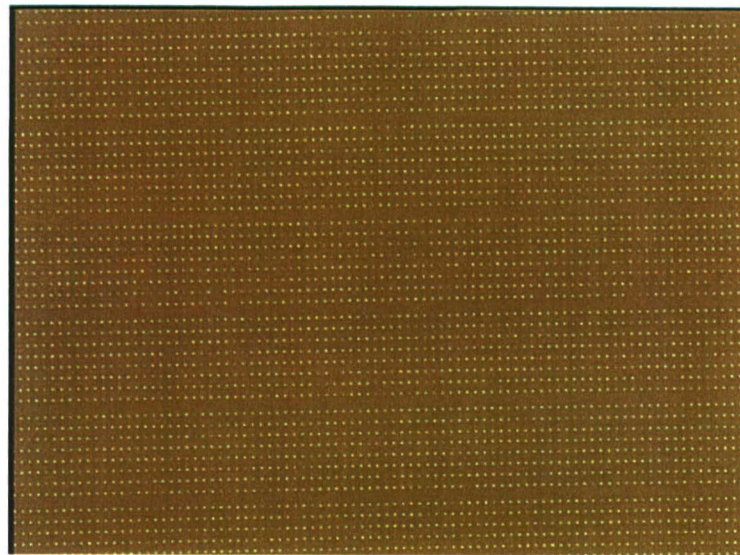


Figure 33. Darkfield image using optical microscopy of a region of a 6-inch oxide-coated Si wafer exposed by X-ray with the stepper operated in open-loop mode. Exposure time was approximately 18 minutes. The nominal 110 nm diameter dots spaced approximately 3 μm apart are clearly observed.

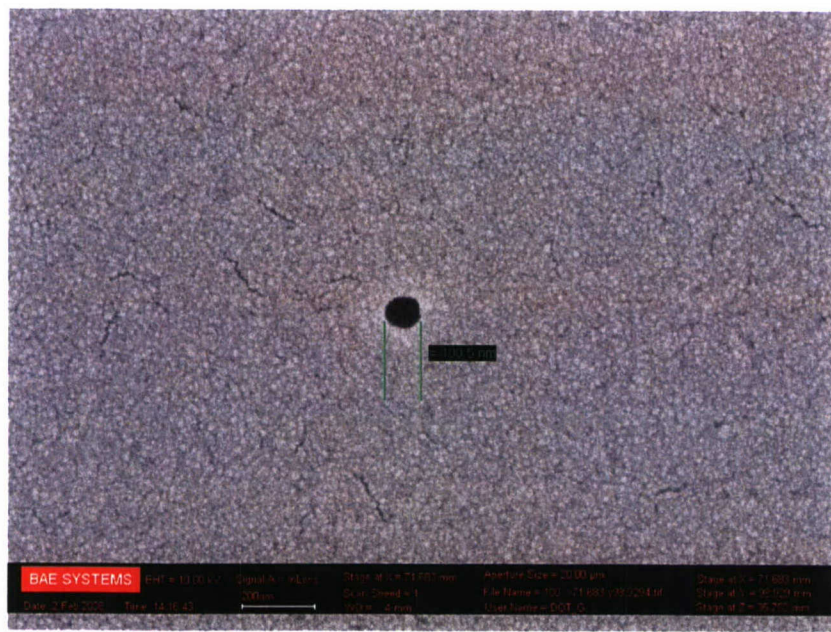


Figure 34. SEM image of a region similar to that shown above of the same open-loop exposed, oxide-coated, 6-inch Si wafer. A well-defined 100 nm hole in the resist is clearly observed.

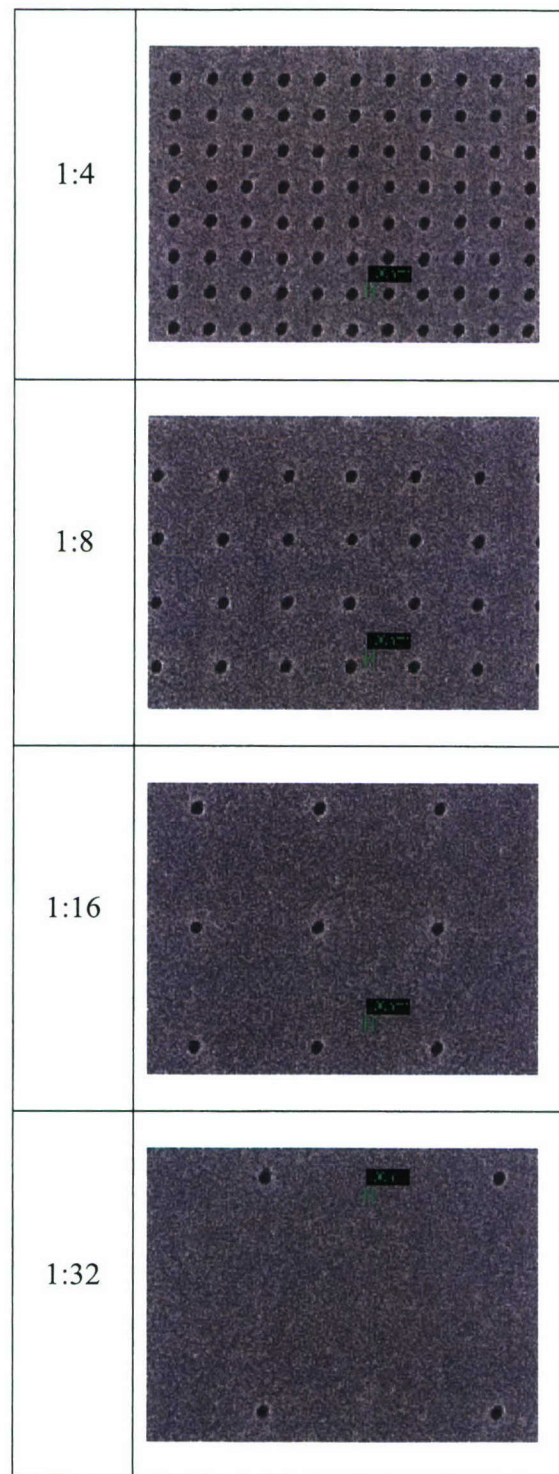


Figure 35. SEM images of nominal 100 nm diameter holes using mask CTP-2 in CAP112 resist on wafer 2040512-23 at four different packing densities and all at the same magnification (10K x)

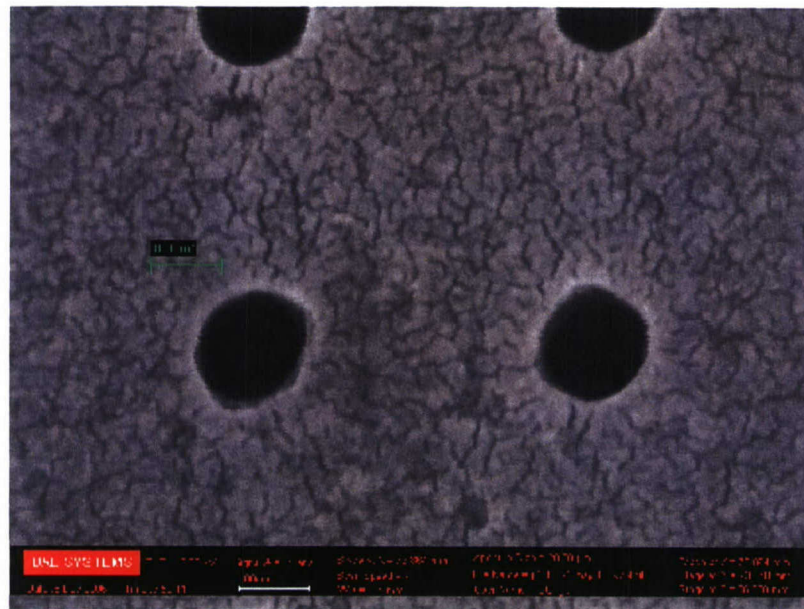


Figure 36. SEM image of exposed and developed holes in CAP112 resist in the 100 nm, 1:4 density region using Mask CTP-2 (i.e., a magnification of the top image in Figure 35). Applied resist thickness was approximately 4700 Å and exposure dose was 110 mJ/cm².

Simply achieving small hole definition in photoresist is not sufficient; it is necessary to transfer these holes to the underlying wafer in order to permit further processing. To this end, an effort parallel with that just described was undertaken. Specifically, the wafers used were 6-inch diameter Si having a 500 Å thick layer of SiO₂ that had been pre-deposited using a TEOS (Tetraethyl Orthosilicate) process. Our goal was to transfer the photo patterns to this layer using a dry-etch step.

A summary of the dry-etch developmental runs appears in Table 4. The particular dry-etch process that was eventually developed is basically as follows:

- The etch tool is an Omega 201 ICP (Inductively Coupled Plasma) single wafer tool with electrostatic chuck hold-down
- Etch gases are SF₆ and Ar
- Pressure = 5 mTorr
- Chuck temperature = 20°C
- Etch time = 90 sec (30 sec on, 60 sec off, repeat 3 times to minimize wafer heating)

Shown in Figures 37 to 45 are examples of results achieved during this phase of the effort. Figures 37 and 38 are SEM micrographs of an early etch attempt where the holes did not reach all the way through the SiO₂.

Table 4. Summary of selected dry-etch runs on 6-inch TEOS oxide and related Si wafers.

Wafer No. (2040512-xx)	Exp. Date	Dose	Etching Experiment	Etching Results	Remarks
	Fields	(mJ/ cm ²)	Details		
xx = 00 new	No resist	--	Calibration Run (12/6/05); 60 sec, Omega 2, 250W ICP, 15W RIE, 5 mTorr, 20°C, 15 ccm SF ₆ , 40 ccm Ar ("SINX1")	~600 Å removed	TEOS oxide taped and etched; no resist applied; no pattern present
CRAM MB3- 05 new	10/17/05 3 fields ~1200 Å	100 90 <10	Etch (12/19/05) 45 sec; same conditions as calibration run	PR disappeared everywhere	2.1 cP, 5K RPM, HMDS (4 day delay before exp.) Laser lock OK
xx = 13 new	10/5/05 6 fields 1400 Å	75	Etch (12/20/05) 45 sec; same conditions as calibration run	Try 6-field sample (PR slightly thicker)	2.1 cP, 3K RPM, <u>no</u> HMDS Laser lock OK
6" Si wafer (notched)	4700 Å CAP112	--	Etch (1/17/06) 60 sec; Resist erosion test	~1500-2000 Å resist removal	3.3 cP, 1K RPM, HMDS
xx = 20 new	1/26/06 3 fields 4700 Å	100 52 16	Etch (2/23/06) 60 sec; same conditions as calibration run	Thicker PR; did not etch to bottom of 500 Å oxide?	3.3 cP, 1K RPM, HMDS Open-loop exposure
xx = 22 new	3/2/06 2 fields 4700 Å	100 30	Etch (3/14/06) 90 sec; same conditions as calibration run; used 6" Si carrier & 130°C wax mount step	Features are enlarged; due to Δt or ΔT ? (three attempts to etch: 3/3, 3/6, & 3/14)	3.3 cP, 1K RPM, HMDS Open-loop exposure
xx = 16 reprocessed	5/4/06 4700 Å	90	Etch 90 sec (6/8/06); same etch conditions as above; electrostatic chuck functioned properly	Distorted shapes; sizes as small as ~100 nm; overheated due to long t?	3.3 cp, 1K RPM, HMDS, 25 μm gap; Laser lock OK
xx = 12 reprocessed	5/24/06 Field #5 4700 Å	100	Scheduled for modified 90 sec etch (30 s on, 60 s off, repeat 3 times)		3.3 cp, 1K RPM, HMDS; Laser lock OK
xx = 18 reprocessed	5/25/06 4700 Å	90	Available for etch		3.3 cp, 1K RPM, HMDS (use expired resist); Laser lock OK; Be window blew out
xx = 17 reprocessed	8/22/06 4700 Å	100	Available for etch (to Au coat, SEM, strip Au, then etch). Au coat & SEM.	Ovalized PR features.	3.3 cp, 1K RPM, HMDS (use <u>new</u> CAP112) Laser lock OK
xx = 21	8/29/06 4700 Å	110	Au coated, SEM'ed, Au stripped, Etch (10/23/06) 90 sec (30 sec on, 60 sec off, repeat 3 times); strip with ST-106 (1 st time)	Ovalized PR features.	3.3 cp, 1K RPM, HMDS Laser lock OK; has numerous "specks"; holes are elongated
xx = 19	8/31/06 4700 Å	110	Au coat & SEM.	Ovalized PR features.	3.3 cp, 1K RPM, HMDS Laser lock OK; same dose as #21 but appears less exposed



Figure 37. SEM image of 120 nm diameter CRAM holes in the top TEOS-oxide layer of a 6-inch Si wafer. This figure shows a relatively large field-of-view (~12 x 18 μm) containing 20 CRAM holes spaced approximately 4 μm apart. All photoresist has been removed and the wafer has been Au coated to facilitate SEM imaging. This wafer was originally exposed by X-ray (~100 mJ/cm^2 dose and 18 min exposure time) with the stepper operated in open-loop mode. The CAP112 resist thickness was 4700 \AA ; dry etching was performed for 60 sec with an ICP tool using an SF₆/Ar ambient. This was our first ever successful pattern transfer of X-ray produced ~100 nm holes to a TEOS oxide coated 6-inch Si wafer.

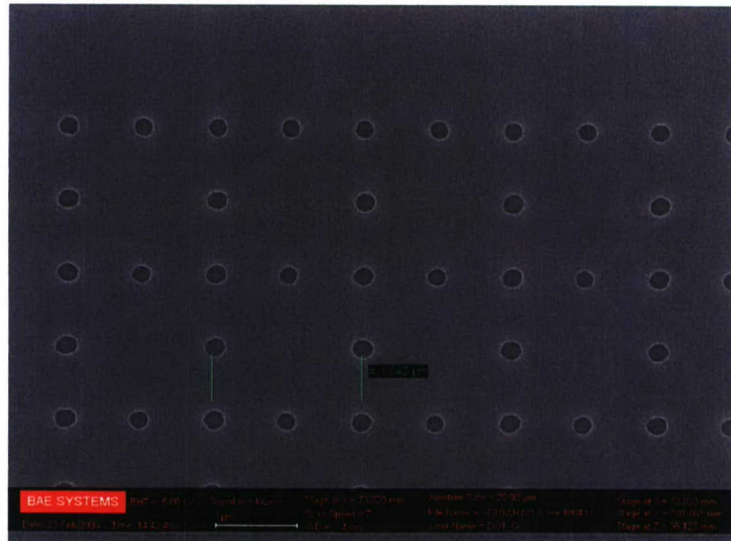


Figure 38. SEM micrograph of the actual etched SiO₂ surface of a 6-inch TEOS oxide Si wafer. The pattern was defined by open-loop X-ray lithography using CAP112 resist, the holes were etched by ICP dry-etching for 60 sec, the resist was chemically stripped, and a 100 \AA gold layer was deposited to assist with SEM examination.

Shown in Figure 39 is a magnified SEM image of the same holes as shown in Figure 38. The similarity of the surface textures outside of the hole and within the hole suggests that incomplete etching of the features was likely made.

Figure 40 shows the etch result for another 6-inch Si wafer. In this case, significant enlargement of the feature size from a nominal 120 nm to a measured 145 nm resulted. However, this wafer had been etched differently. For some still unknown reason, the electrostatic chuck was unable to hold the wafer, so it was mounted to a secondary wafer using a 130°C wax mounting step. Either the high temperature of this step or a higher temperature reached by the wafer during the 90 sec etch step is believed to be responsible for the widening of this feature. Subsequent runs were done by changing the single 90 sec etch to three 30 sec etches separated by 60 sec waiting periods.

Figures 41 and 42 show SEM images of nominal 120 and 110 nm features etched into the TEOS oxide layers using the 3 x 30 sec etch process. Much better agreement between original mask size and final etched hole size is seen.

Shown in Figures 43 and 44 are the smallest etched hole sizes we have been able to achieve to date. Figure 43 shows a head-on view of a measured 85 nm diameter hole, and Figure 44 shows a tilted view of a similar hole where the inside edge of the 50 nm (500 Å) thick TEOS oxide can be seen.

Finally, appearing in Figure 45 are the results of a preliminary statistical study of hole size uniformity for some larger (~130 nm) etched holes. A standard deviation (σ) of 2.7 nm was the result for the given process conditions.



Figure 39. A more detailed view of the same region as Figure 38. To be noted is the similarity in surface texture of both the region outside of the round hole and that within the hole; this fact strongly suggests incomplete etching to the bottom of the 500 Å thick TEOS SiO_2 layer.

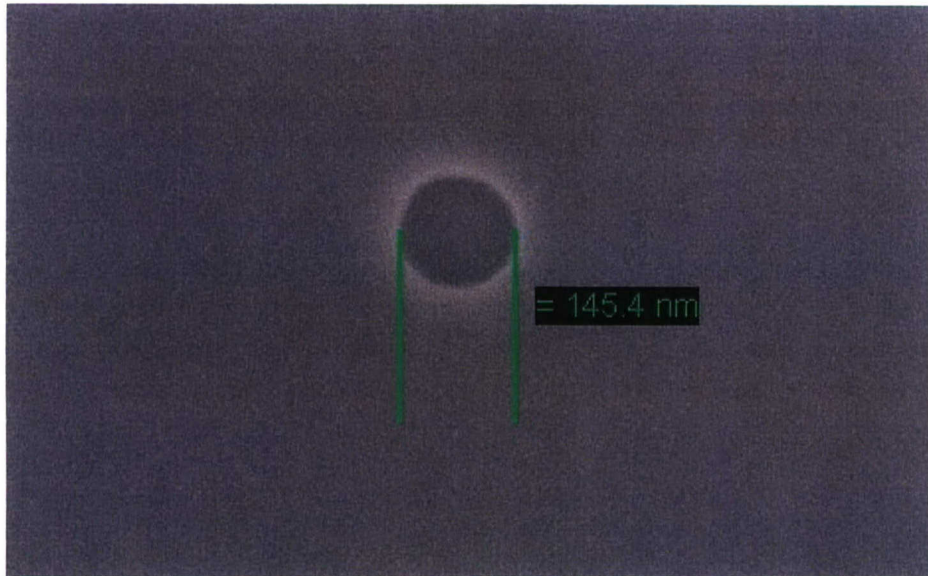


Figure 40. SEM image of an etched hole in a 500 Å thick TEOS oxide layer atop a 6-inch Si wafer. The feature was originally patterned using an open-loop X-ray process with a mask feature size of 120 nm. Etch time in the ICP tool was 90 sec. The primary wafer was mounted on a secondary Si wafer using a wax mounting process that utilized a 130°C step.

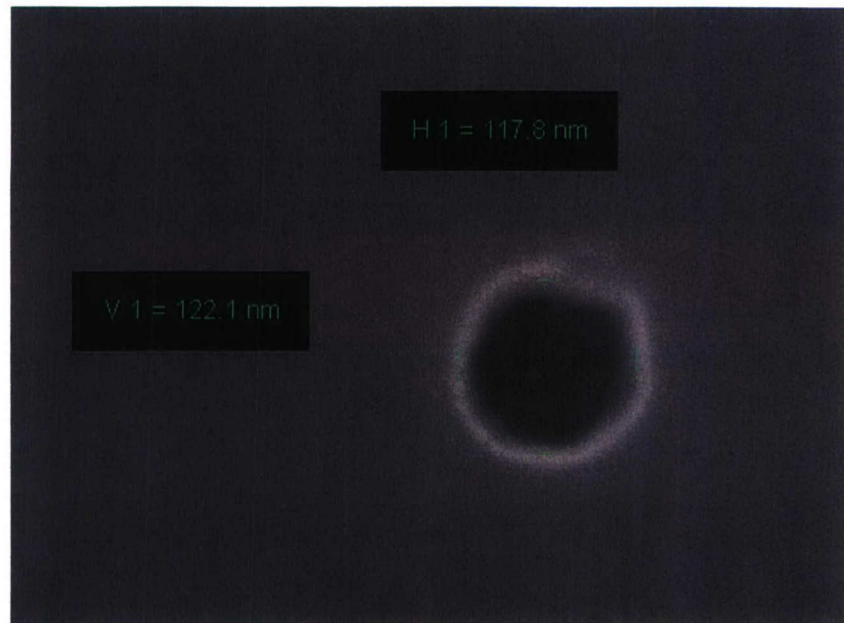


Figure 41. SEM image of a 120 nm feature dry-etched into wafer #16 (see Table 1 and text [CRAM, June 06] for details)

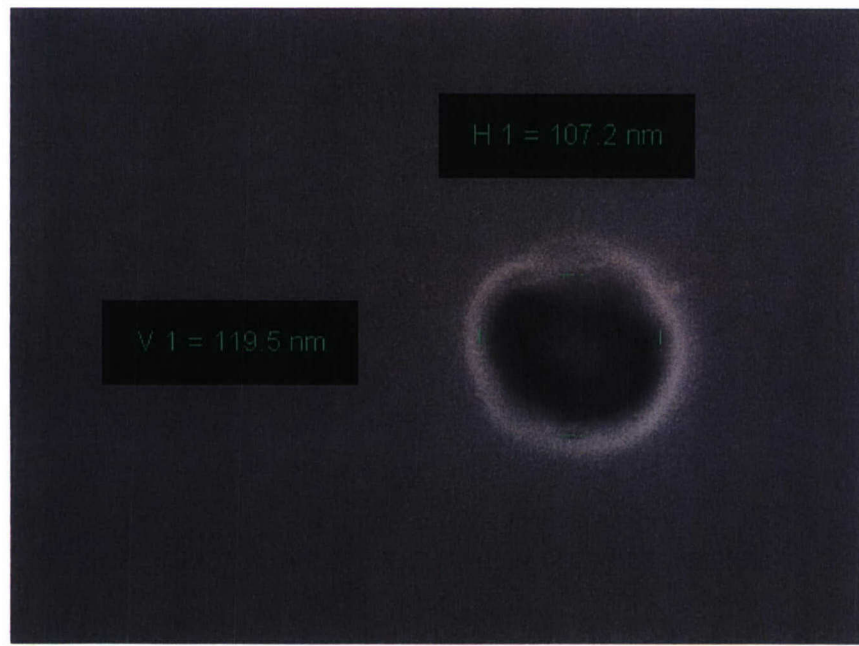


Figure 42. SEM image of a 110 nm feature dry-etched into wafer #16 (see Table 1 and text [CRAM, June 06] for details)

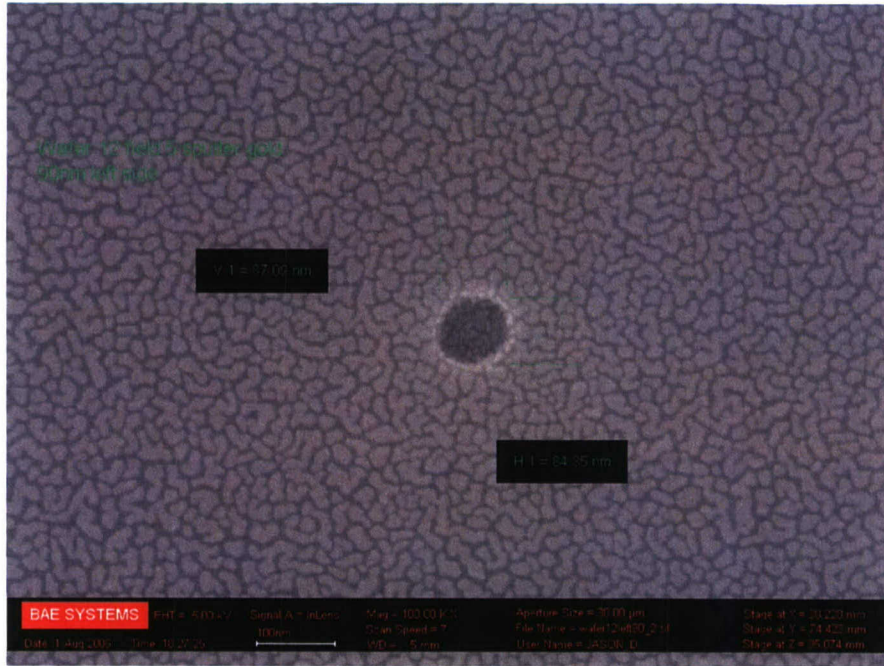


Figure 43. SEM micrograph of a feature in the 90 nm (nominal) portion of TEOS-oxide coated Si wafer #12 after X-ray exposure (100 mJ/cm^2), development, dry etching, resist stripping, and Au sputtering. This feature measures approximately 85 nm in diameter.



Figure 44. SEM micrograph of a similar feature in the same wafer as Figure 1, but with the wafer tilted 25° from normal. The 50 nm (500 Å) thickness of the TEOS oxide can be seen.

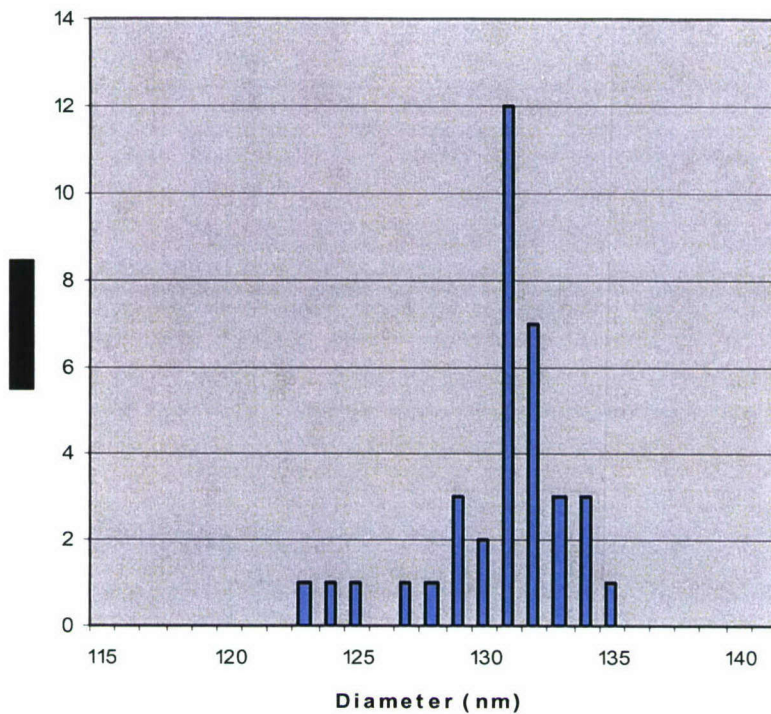


Figure 45. Histogram of SEM-measured diameters of etched holes in Wafer # 2040512-12, Field #5. The diameter of the mask holes used to expose this particular region was 110 nm and a total of 36 measurements were made (a 6 by 6 block of holes). The mean diameter of the measured holes is 130.4 nm and the standard deviation is 2.7 nm. This wafer was exposed at 100 mJ/cm² using CAP112 resist with an applied thickness of 4700 Å, the wafer was developed for 60 sec, and the total etch time was 90 sec. Wafer-to-mask gap was 15 µm.

V. Summary and Conclusions

The original goal of this multi-year program was to develop and demonstrate an X-ray lithography tool capable of achieving features and linewidths smaller than that possible with optical or UV lithography and with higher throughput and speed than that possible with E-beam lithography. To this end, the program was a success. In particular, successful demonstration was achieved for two important applications – high frequency GaAs FETs for MIMIC application and radiation-hard CRAM memory element definition.

The other important outcome of this effort was the identification of key areas that will require additional effort to make X-ray lithography a viable production process. Fortunately, all these areas are ones that only require additional engineering development, not the development of basic technologies. Specifically, they include upgrades to the DPF source to improve its reliability and uptime, and upgrades to the stepper to primarily make the software more user-friendly and less prone to system hang-up. Once these problem areas are tackled and solved, DPF-based X-ray lithography should provide a practical alternative to achieve small feature sizes in semiconductor device production at a practical cost.

VI. Appendices

Appendix A. SRL DPF Final Report

Appendix B. JMAR/SAL Final Report

Appendix C. Shipley Final Report

Appendix D. CNTech Final Report

Appendix E. Xmetrics Final Report

Appendix F. SRL New Anode Final Report

Appendix G. *Rev. Sci. Instrum.* Paper

Appendix A

SRL-F-2003

**Point Source X-Ray Lithographic System
For Sub-0.12 μ m Design Rules**

Prepared by

Dr. R. Petr, Dr. Alexander Bykanov & Mr. J. Freshman

**Science Research Laboratory, Inc.
15 Ward Street
Somerville MA 02143**

(617) 547-1122

FINAL TECHNICAL REPORT

Period for March 2, 2001 to October 31, 2003

Subcontract No. RN3482

Prepared for

**Mr. Alois Geizler
BAE SYSTEMS
65 Spit Brook Road
Nashua NH 03061**

October 31, 2003

"The views and conclusions contained in this document are those of the authors and should not be interpreted as representing the official policies, either express or implied, of the Sanders A Lockheed Martin Company."

TABLE OF CONTENTS

1.0: INTRODUCTION AND SUMMARY	4
1.1: THE DENSE PLASMA FOCUS PROCESS	4
1.2: SYSTEM LAYOUT.....	7
2.0: SYSTEM DESIGN	10
2.1: CLEAN ROOM COMPATIBILITY	10
2.2: FRAME	ERROR! BOOKMARK NOT DEFINED.
3.0: ALL SOLID STATE DRIVER MODIFICATIONS	11
3.1: SOLID-STATE DRIVE MODULE	11
3.2: SOLID-STATE MODULE MEASUREMENTS	ERROR! BOOKMARK NOT DEFINED.
3.3: TRIGGER BOARD IMPROVEMENTS	ERROR! BOOKMARK NOT DEFINED.
3.4: MODULE CURRENT CONNECTIONS	ERROR! BOOKMARK NOT DEFINED.
3.5: CAPACITOR CHARGING MODULE	12
3.6: HEAD	16
4.0: ANODE.....	16
4.1: REFURBISHMENT.....	ERROR! BOOKMARK NOT DEFINED.
4.2: CURRENT CONNECTION.....	17
5.0: CATHODE	18
5.1: CATHODE REFURBISHMENT	18
6.0: ELECTRODE LIFETIME	19
6.1: RISE TIME IMPROVEMENT	19
7.0: X-RAY WINDOW PROTECTION.....	19
7.1: BLAST WAVE ATTENUATION.....	20
7.2: MAGNETIC E BEAM DEFLECTION.....	21
7.3: HIGH VOLTAGE ISOLATION.....	22
7.4: WINDOW MOUNT.....	24
8.0: VACUUM SYSTEM.....	33
8.1: THERMOPHORETIC PARTICLE PRECIPITATOR	34
9.0: COOLING SYSTEM	35
9.1: DI COOLING SUBSYSTEM	35
9.2: STD COOLING SYBSYSTEM	36
9.3: CHILLER SUBSYSTEM.....	36
9.4: MISCELLANEOUS COOLANT SYSTEM FEATURES.....	37
9.5: DEGASSING SYSTEM.....	41
10.0: CONTROLS.....	41
10.1: TRIGGER CONTROLS	43
10.2: DOSE MONITORING.....	44
10.3: STATE MACHINE ARCHITECTURE.....	44
11.0: OPERATION	51
11.1: CONTROL THROUGH STEPPER SOFTWARE.....	52
12.0: SAFETY & FIRE SUPPRESSION SYSTEMS	52
13.0: MAINTENANCE.....	53
14.0: ROUTINE SERVICE	53
15.0: TROUBLE SHOOTING.....	55
16.0: SYSTEM TESTS	56
17.0: PERFORMANCE.....	57

1.0: Introduction and Summary

The goal of this contract has been to develop and place into operation a dense plasma focus (DPF) point source for x-ray lithography that is suitable for entry level micro chip production.

Prior to this contract, SRL, with DARPA funding, developed a point source that was based on a spark gap switched driver. This source succeeded in producing over 10 joules of x-rays per pulse at repetition rates over 20 Hz. However there were serious drawbacks to the use of this machine for practical microchip production. The cost and frequency of replacement of the spark gap switch electrodes was prohibitive. The same was true for the dense plasma focus discharge electrodes. Nonetheless this early work laid the foundations for a number of the features that are included in the present machine. These features include water cooled electrodes capable of high repetition rate, the ability to easily service the DPF electrodes, the EMI shielding that allows for operation in an environment that is highly intolerant of EMI, and a sophisticated computerized control system with built in diagnostics that is necessary for integration with the stepper and for self diagnostics.

Most of the erosion of the DPF electrodes could be attributed to the fact that the spark gap switched driver allowed the discharge current to reverse direction after the x-rays were produced. This knowledge led to DARPA funding for the development of an all-solid-state module with energy snubbing that would form the basis for a multi module driver for a new DPF x-ray source. The energy snubbing feature prevented the unwanted current reversal.

The present contract, funded by DARPA through BAE SYSTEMS, was divided into two phases. Phase I developed a “laboratory prototype”, DPF x-ray source, powered by twelve all-solid-state driver modules. The most important result was that, as predicted, the new driver increased the DPF electrode lifetimes by more than a factor of ten. Moreover, as intended, this machine served as a “proving ground” for the various enabling technologies that were incorporated in the machine that SRL delivered to BAE.

SRL developed and placed in operation at BAE a “deliverable” DPF x-ray source with an all-solid-state driver. The configuration of the BAE installation site required this machine to be more compact than the Prototype SRL machine, with eight instead of twelve driver modules. The modules were redesigned so that eight modules could do the job of twelve. The BAE machine was built to be clean room compatible. The machine is equipped with a more comprehensive and reliable set of controls, and all non-diagnostic operations can be performed at the command of the stepper computer system. The device produces up to 12 joules per pulse averaged, and an output power of 700 W into 4π steradians.

1.1: The Dense Plasma Focus Process

The x-ray source contains “driver modules” and a “head”. The driver modules accept current from a high voltage power supply, stores the energy in capacitors, and then, on command, simultaneously discharge the stored charge through the head. Within each module, high current thyristors in series with saturable magnetic reactors switch energy into the discharge head. The current path from the modules to the head is via a shielded parallel plate transmission line, the “triplate”.

The head of the machine consists of a cylindrical vacuum chamber, and two generally cylindrical electrodes mounted within the chamber. The axes of the chamber and the electrodes are coincident with the x-ray axis. The anode is a water cooled cylindrical shell. One end of the anode "plugs into" the anode base. The anode base is attached to the center "hot" plate of the triplate transmission line. The cathode is a water cooled cylinder (more specifically, it is built from an array of tubes in a cylindrical arrangement) which surrounds the anode. The cathode is attached to the ground plate of the triplate transmission line that is on the inside of the machine. An annular water cooled insulator separates the anode from the cathode in the region of the anode base. The chamber is filled with neon gas at a pressure of about 1 torr.

X-rays are produced by dense plasma focus pinch discharge that begins with a surface breakdown across the insulator between the anode and the cathode upon application of a fast rising voltage pulse between these two electrodes. Azimuthal magnetic fields generated by the axial flow of current on the anode outer surface interact with the radial component of the discharge current to drive the discharge down the length of the anode. This process is illustrated in Fig. 1. The anode length is chosen so that the current is a maximum when the discharge reaches the end of the anode.

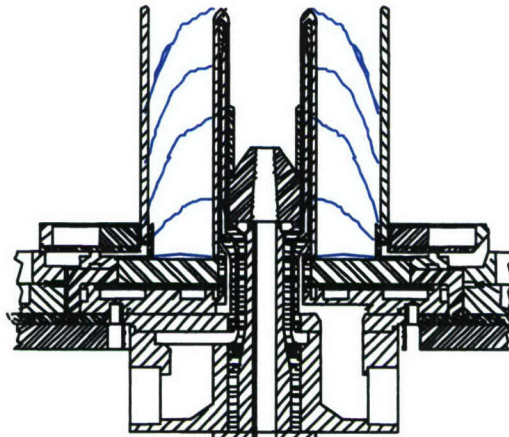


Fig. 1 Axial rundown of plasma following ignition on insulator

When the discharge passes the end of the anode, an axial component of current is suddenly created around the annular tip of the anode. The interaction of this axial current with the azimuthal magnetic field drives the discharge inward in the radial direction. As the radius of the discharge becomes smaller, the azimuthal field becomes stronger. Gas within the converging discharge is captured and compressed into a hot "pinch". The compression process takes about 100 ns. The temperature of the gas reaches on the order of 150 eV, sufficient for the emission of soft x-rays. A schematic representation of the above processes is presented in Fig. 2. Fig. 3 presents an interferogram of the pinch taken at the time of maximum compression.

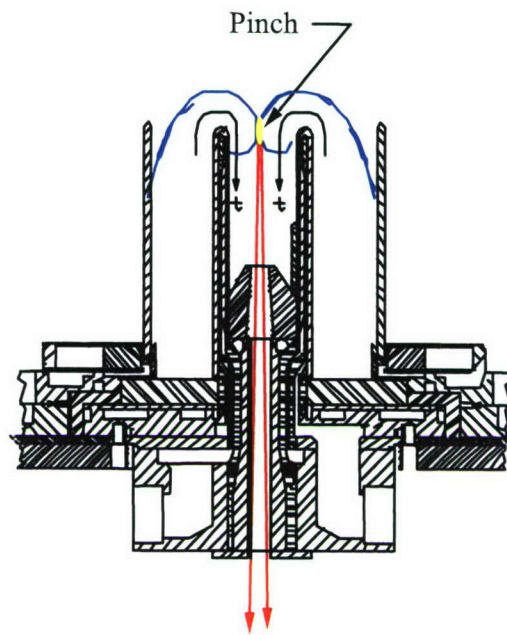


Fig. 2 Pinch and extracted X-ray beam

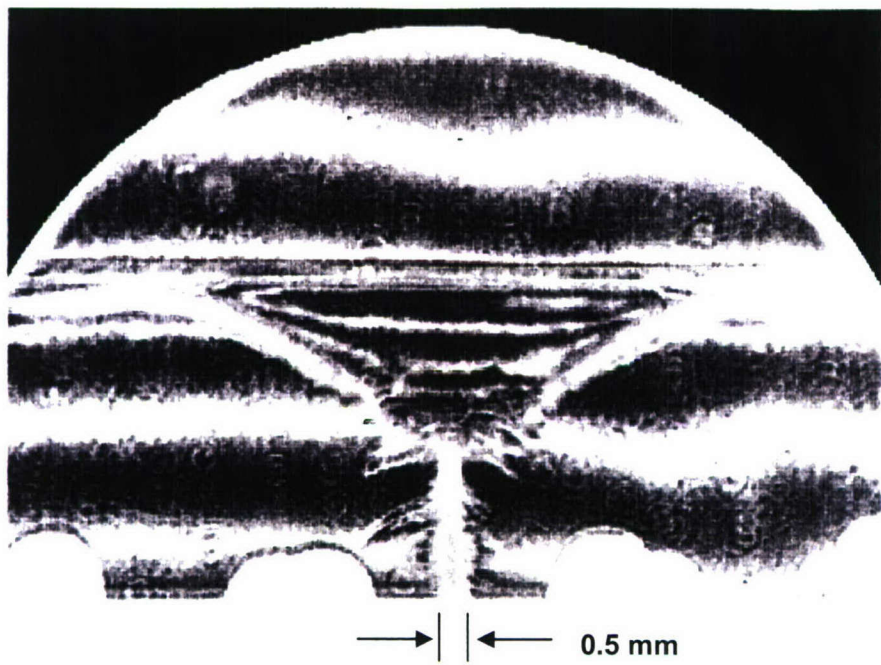


Fig. 3 Interferrogram showing plasma at moment of pinch

1.2: System Layout

The “x-ray source” is a 10 ft wide by 5 ft deep by 6 ft 8 in high structure located within the clean room. A beam of X-rays emanates from the “front end” of the source. The line along the centroid of the X-ray beam defines the “axis” of the source. Fig. 4 presents a view of the front end of the source. The dominant feature visible in this picture is the outer ground plane of the triplate transmission line that conveys the pulse current from the modules to the head. The front end of the source was designed to allow the source and stepper to be placed in close proximity to each other. Specifically the distance from the ultimate source of the x-rays, the plasma pinch, to the wafer mounted in the stepper is 70 cm.

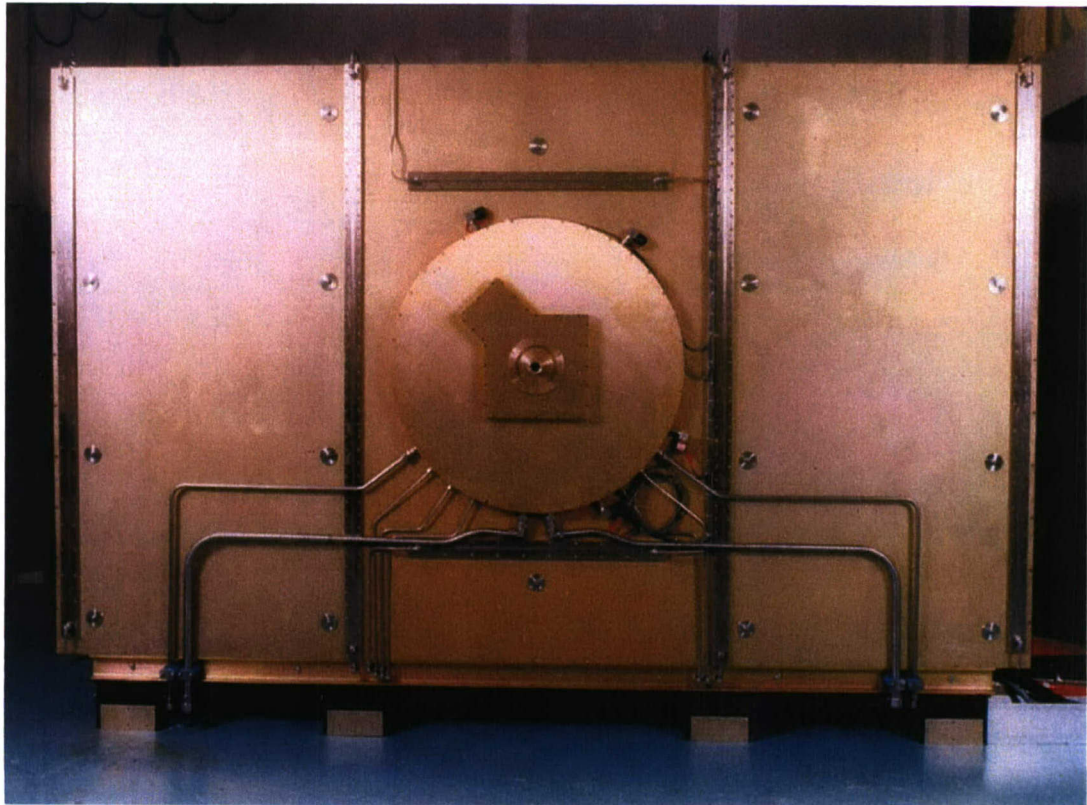


Fig. 4 Front of X-ray source showing triplate, X-ray output (aperture in center), and various water cooling lines

The general dimensions of the source are presented (in inches) in Fig. 5.

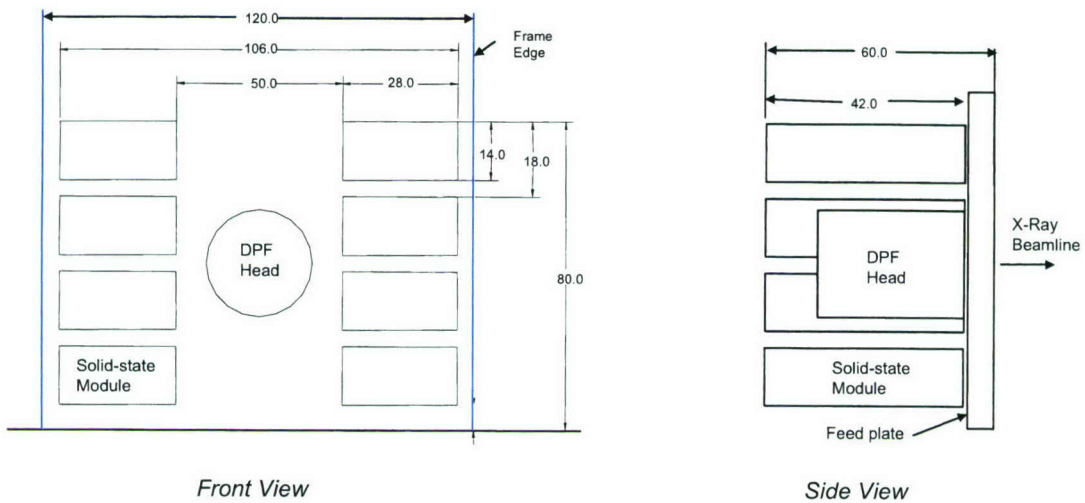


Fig. 5 Dimensions of X-ray source

The “back end” of the source is equipped with four doors. The doors on the left and right hand sides of the back of the source cover the “module bays”. Each of these module bays are divided into four sub-bays. A driver module slides on rails into each bay. A large custom coaxial sliding fitting, connects each module to the triplate. Quick disconnect power, cooling, and control lines connect to the back of each module. The backs of the modules and these lines are visible in Fig. 6.



Fig. 6 Back end of X-ray source showing driver modules with quick disconnect cooling lines, high voltage charging lines, and control lines. The track on which the vacuum cart is retracted to allow for head service is also visible.

The central two doors on the back of the source provide access to the source's "central bay," as is shown in Fig. 7. The central portion of the bay is occupied by the "vacuum cart." The vacuum cart rides on four wheels that are guided by two tracks that extend beyond the back of the source, thereby allowing retraction of the vacuum chamber for servicing of the head.

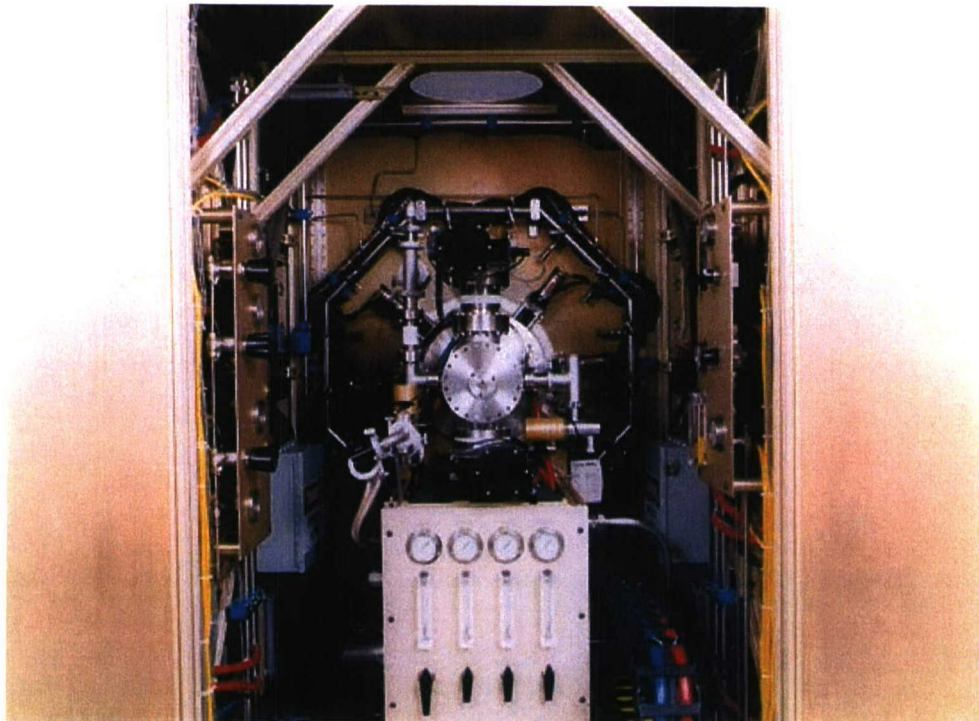


Fig. 7 View in to the central bay of the X-ray source showing vacuum chamber over the head

With the exception of a video monitor and a keyboard, all other auxiliary equipment resides in the chase. These components are shown in Fig. 8. In this photo the DC power supplies, the cooling cart, the controls bay, and the gas storage are located in a mock up of the chase. This mock up was constructed to guarantee a proper fabrication of the interconnects between the various components.

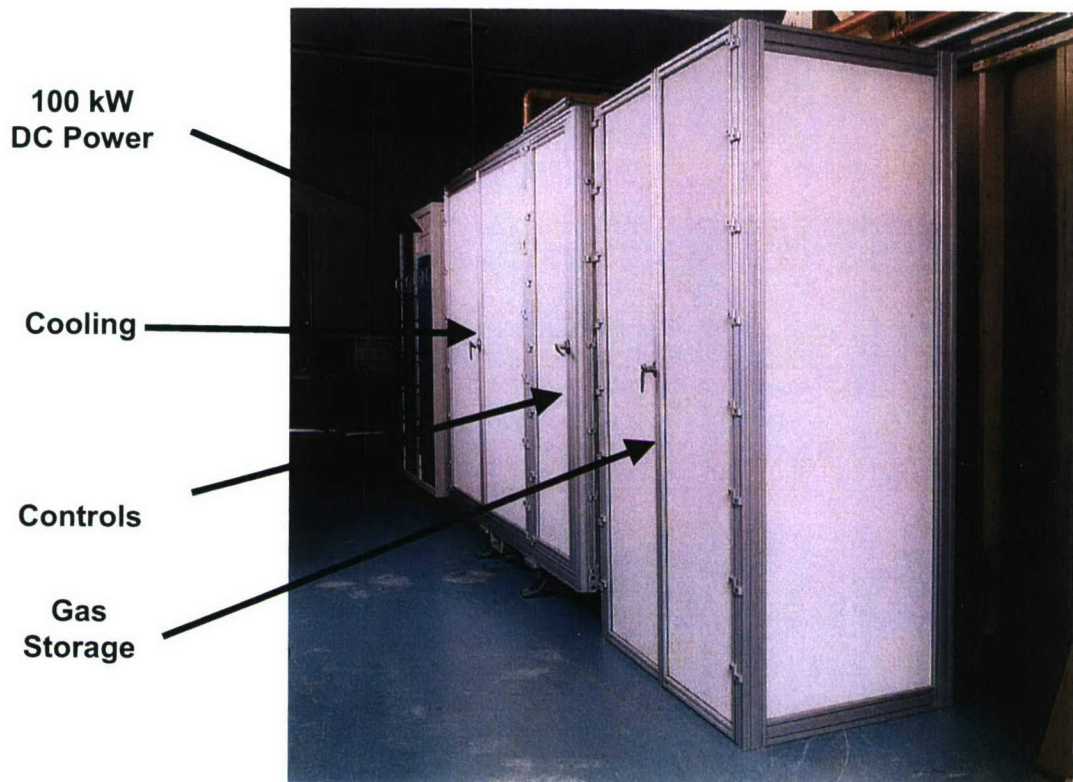


Fig. 8 Auxiliary components for power, cooling, control, and gas storage are located in the chase. (Photo shows a mock up of the chase arrangement as used at SRL)

2.0: System Design

2.1: Clean Room Compatibility

Before beginning the detailed design of the deliverable machine, a review of clean room practices and requirements were conducted. The primary design changes inspired by this study concerned safety, EMI emissions, and cleanliness. Extensive safety and fire protection measures were implemented.

In order to maintain cleanliness, the following measures were taken. Within the clean room proper, all of the external surfaces of the machine were fashioned from unpainted aluminum treated with the alodine process. The surfaces are electrically conductive, thereby discouraging the attachment of dust particles.

Doors in the back of the X-ray source provide access to the interior in order to allow routine service of the head or replacement of a defective charging module. Provisions have been made to insure that dust from the interior of the machine does not contaminate the clean room. Duct work connects the interior of the X-ray source to an exhaust system provided by BAE. Whenever an access door is opened, a motorized damper in the duct work opens. The exhaust capability was specified so as to provide a minimum flow from the clean room through the

opened doors of at least 50 ft/min. Whenever the vacuum chamber is pulled back on rails from the DPF head to allow for service, a separate exhaust system connected to the vacuum chamber by a flexible hose is activated. This insures that nano particles produced by the discharge will not contaminate either the interior of the source or the clean room.

3.0: All Solid State Driver Modifications

This section describes engineering upgrades to the Phase III solid-state driver that was developed to drive the dense plasma focus x-ray source. Table 1 compares the design goals of the Phase II and Phase III solid-state drivers. The upgraded Phase III power supply construct utilizes 8 parallel drive modules that together produce the fast-rising 8 kV, 260 kA electrical pulses needed to power the x-ray source. Each module contains 6.0 μ F of storage capacitance, so that the total system discharge capacitance is 48 μ F. The capacitor charging supply is rated at 100 kJ/sec, or 100 kW average power. The DPF system can operate up to a pulse recurrent frequency of 60 Hz at 8 kV charge voltage.

Table 1. Phase II DPF Solid-State Power Supply Design Specifications.

<i>Nominal Parameters</i>	<i>2001 Phase III Pulser 8 Module Configuration</i>	<i>1998 Phase II Pulser 8 Module Configuration</i>
Charge Voltage	8 kV	8 kV
Output Current	270 kA into live load	240 kA into live load
Current Pulse Duration (half sine)	2.5 μ sec	2.5 μ sec
Current Risetime (10%-90%)	< 700 nsec	< 700 nsec
Storage Capacitance	48 μ F	36 μ F
Load Energy (per pulse @ 8kV)	>1550 J	1150 J
Number of Parallel Modules	8	8
Charging Power Supply	100 kJ/sec @ 8kV	100 kJ/sec @ 8 kV
Pulse Recurrent Frequency	60 Hz @ 8kV	87 Hz @ 8 kV
System Inductance	< 12 nH	< 12 nH
Feed plate Inductance	< 2 nH	< 2 nH
Pulser Inductance	< 10 nH	< 10 nH
Energy Transfer Efficiency	>85%	>85%
Pulser System Volume	120 in wide by 84 in wide by 50 in deep	120 in wide by 120 in high by 50 in deep

3.1: Solid-State Drive Module

The circuit topology for the upgraded solid-state drive modules is based on fast-switching thyristor technology developed by ABB Semiconductors, Lenzberg, Switzerland. These high current thyristor switches are capable of switching tens of kiloamperes on the microsecond time scale required by the DPF x-ray source. A top-level schematic of a solid-state module is shown

in Fig. 9. Solid-state module schematic diagram. 8 parallel modules make up the full power DPF driver.. It consists of a $6 \mu\text{F}$ storage capacitor switched by 3 series thyristors. The module output is connected to the x-ray source through a ferrite isolator assembly. Snubber diode circuits are also connected across the storage capacitor in order to clamp reverse voltage across the capacitor. This is a key design feature that ensures no reverse current flows through the x-ray head during a discharge, which is necessary to improve electrode lifetime.

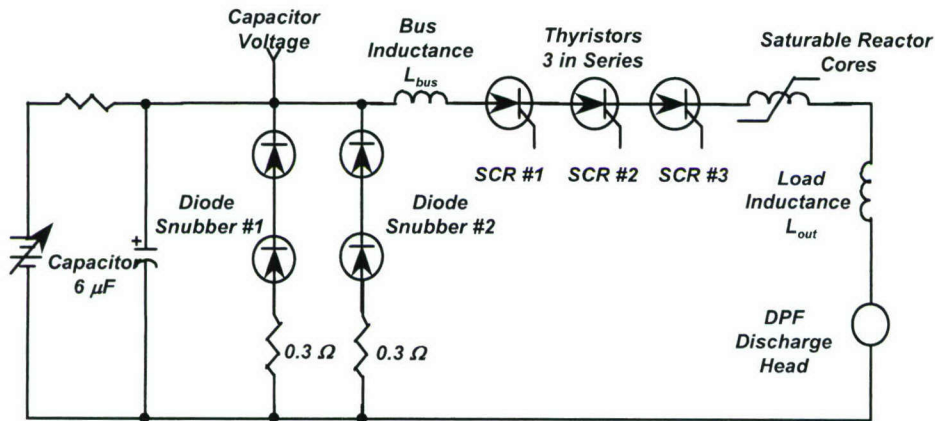


Fig. 9. Solid-state module schematic diagram. 8 parallel modules make up the full power DPF driver.

3.2: Capacitor Charging Module

The DPF capacitor charging module has been designed to provide the DPF x-ray source with a peak charging power of 100 kJ/sec at 8 kV charge voltage. Under maximum voltage conditions this can result in an electrical input power of 100 kW. The capacitor charging module is designed to be a stand-alone unit. The charging module housed in a standard double-bay 19 inch rack assembly, and is air-cooled. The output voltage from the charge module is programmable from 0 to 8 kV. Table 2 summarizes the top-level physical parameters of the charging module.

Table 2. Summary of DPF Capacitor Charging Module

<i>Parameter</i>	<i>Rating</i>
Housing	Double bay 19 inch rack assembly Dimensions: 48" wide by 36" deep by 80" high
Weight	Approximately 1000 lbs
Cooling	Air cooled
Switching Power Supplies	10 Maxwell Laboratories (CCDS 8kV @10 KJ/sec) power supplies
Output Voltage	0 to 8 kV (programmable)
Uninterruptable Power Supplies	2 supplies rated at 1400W each
Maximum Output Power to DPF Solid-State Drive Modules	100 kJ/sec @ 8kV
Input Voltage	480 VAC 3 phase 60 Hz
Maximum Input Power	120 kW
Maximum Power Tested to Date	80 kW
Measured Component Temperature Rise at Maximum Test Power	30 deg C

Fig. 10 shows a top-level schematic diagram of the capacitor charging module. It utilizes 10 switching power supplies (Maxwell Laboratories CCDS-8kV@10kJ) that are connected in parallel to charge the solid-state drive modules that power the DPF discharge. The Maxwell charging supplies operate with 480 VAC 3 phase input voltage, and the outputs of the power supplies are protected with resistor and diode snubbers. The module doors are interlocked, and automatically shut off AC power when opened. The module also contains an internal high voltage switch and dump resistor that connects the high voltage output to ground in the off-state. Two un-interruptible power supplies (UPS's) are located in the charge module that provide AC bias power to the charging module control logic, as well as to the solid-state drive modules in the x-ray source. A charge controller logic assembly conditions signals to provide the required pulse charge output to operate the DPF source. Charging commands and acknowledgements are received and transmitted to the trigger/fault module across a DB37 communication cable.

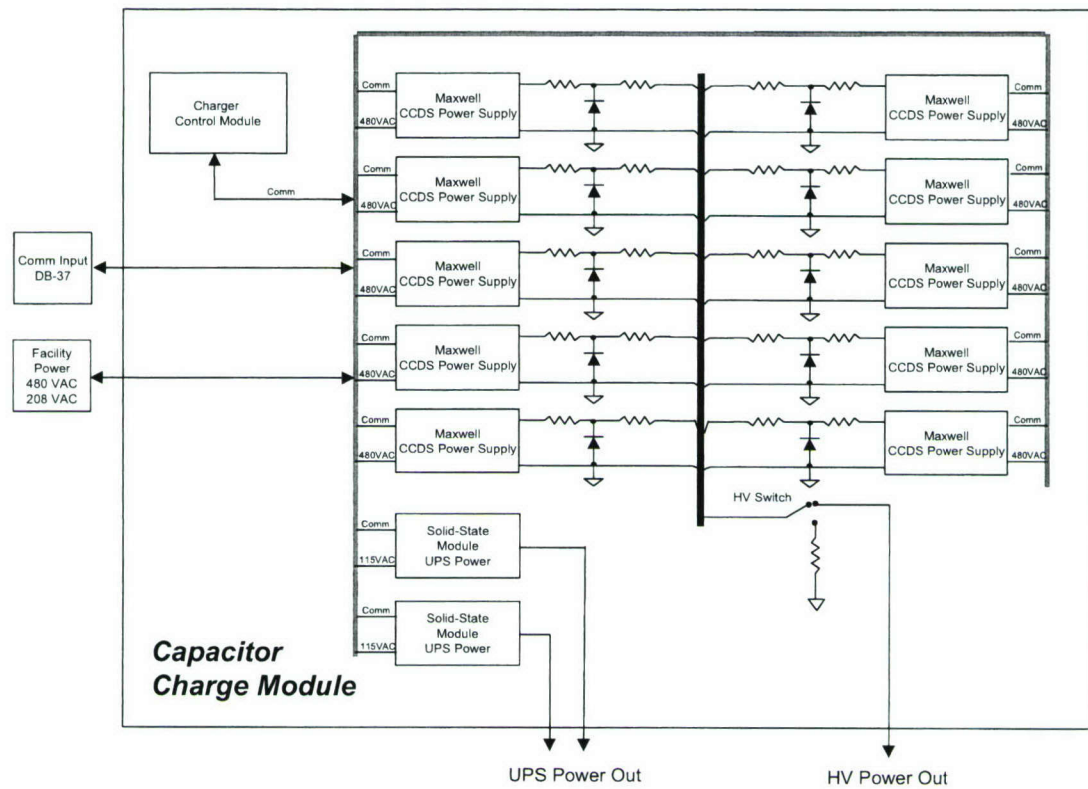


Fig. 10. Schematic of the DPF capacitor-charging module.

Fig. 11 shows a top-level of the charge control module. The module consists of several sub-circuits that condition and control data signals to and from the Maxwell power supplies. These circuits, for example, turn the Maxwell supplies on and off, condition the pulse charge power format for the supplies, as well as monitor the output high voltage and fault status of the Maxwell supplies.

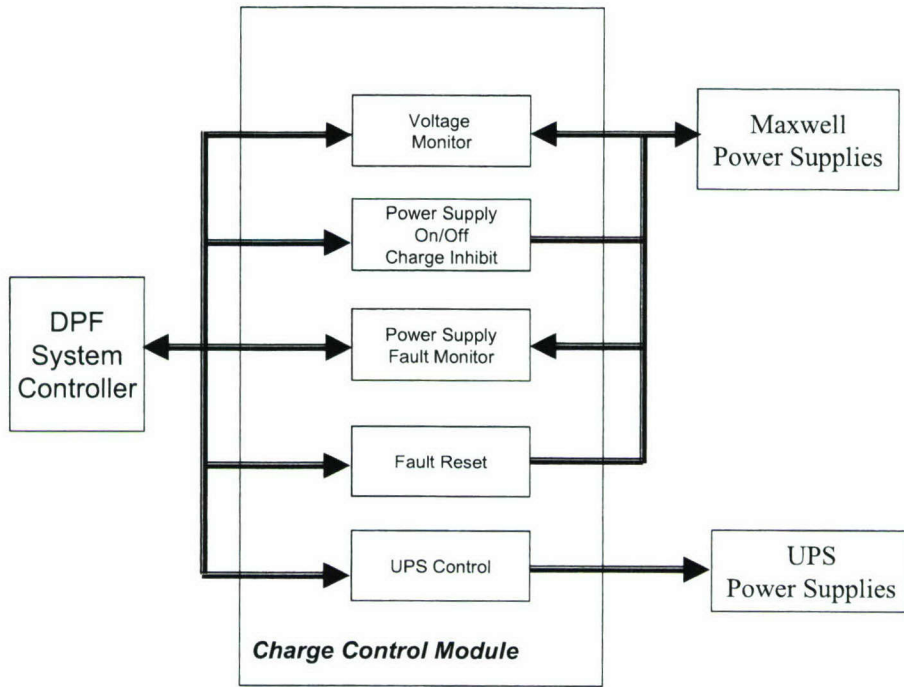


Fig. 11. Top-level block diagram of the control electronics for the capacitor charge module.

The capacitor charging module is designed to provide a pulse-charge power format to the solid-state x-ray drive modules. This has several system advantages which include (1) reducing the dwell time that components must support high voltage, which improves component lifetime and (2) keeping high voltage off the solid-state module thyristors until they have recovered their high voltage hold-off capability after a discharge. This is especially important for this DPF application where thyristors operate at high peak current levels.

The charging current is conveyed from the charging module to the x-ray source by means of sixteen equal length RG8 coaxial cables, with two cables connecting to each driver module within the x-ray source. Custom made high voltage terminations are used on each end of the cables. This system has been effective in keeping ground bounce to low levels and in shielding against EMI. All connections from the charging module and the control module are effected through opto isolators. This precaution avoids noise pickup and/or generation due to ground loops.

3.6: Head

The head of the machine consists of a cylindrical vacuum chamber, and two generally cylindrical electrodes mounted within the chamber. The axes of the chamber and the electrodes are coincident with the x-ray axis. The anode is basically a water cooled cylindrical shell. One end of the anode "plugs into" the anode base. The anode base is attached to the center "hot" plate of the triplate transmission line. The cathode is a water cooled cylinder (more specifically, it is built from an array of tubes in a cylindrical arrangement) which surrounds the anode. The cathode is attached to the ground plate of the triplate transmission line that is on the inside of the machine. An annular water cooled insulator plate separates the anode from the cathode in the region of the anode base. The chamber is filled with neon gas at a pressure of about 1 torr.

4.0: Anode

Phase III efforts regarding the anode focused on demonstrating an increase of the anode life to 5,000,000 shots.. This was accomplished by replacing the molybdenum tip with a tungsten tip and improving the reliability of the anode current connection.

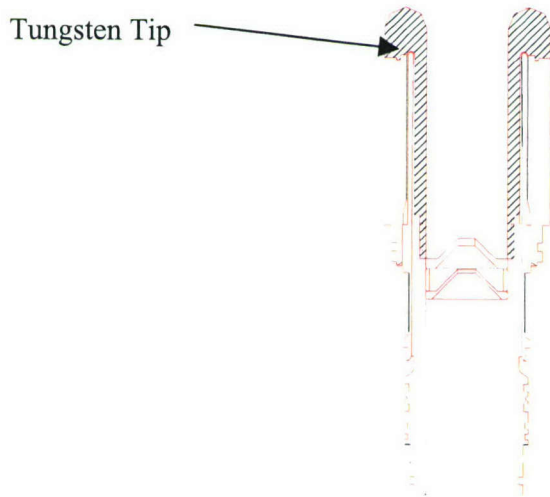


Fig. 12. Tungsten tip anode shown brazed to molybdenum

Good thermal contact between the tungsten tip and the original part is critical. In order to insure this contact braze preps have been machined into the molybdenum.. . This construction allows the placement of a braze material which will cover the entire surface of the interface.

4.2: Current Connection

The knife edge connections between the anode and the anode base were designed to last indefinitely at an peak linear current density greater than 80 kA per inch and an RMS averaged linear current density greater than 800 A per inch. The connection is effected by pulling on the “tail” of the anode with a pneumatic piston so that a metal washer is compressed between mating “Conflat” knife edges on the anode and the anode base.

Failures were experienced at the knife edge current connection between the anode and the anode base. The damage destroyed the knife edges on the anode and the anode base, and generated arcs internal to the anode base that caused further damage. The failure was due to the fact that the knife edge penetrations into the copper washer were not sufficient. The brazed joints in the anodes were not strong enough to take the forces necessary to achieve the design knife edge penetration. The anode and the anode base are shown in Fig. 13. This illustration shows the copper gasket current connection, the lockdown piston with bayonet fitting, and the critical anode joints .

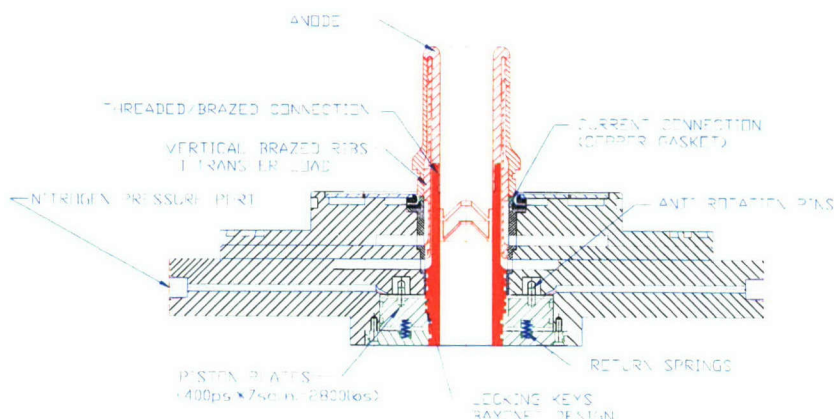


Fig. 13. Anode and anode base, showing copper gasket current connection, lockdown piston with bayonet fitting, and strengthened anode joints.

Washers were constructed from softer materials in order to achieve greater current contact area. These washers performed well for a time, but creep in the material would eventually allow the good current connection to be broken, and the damage to the system would follow. In order to have the a warning at the onset of any damage, a probe was installed that could sense a potential difference between the portion of the anode that is within the anode base and the anode base. This probe was fiber optic isolated from ground, because the anode pulses to

high potential. Sensitivity was approximately a volt. Unfortunately the damage was being done at a lower potential.

The problem was solved by redesigning the anodes so that no braze joints were subject to shear forces when the anode “tail” is pulled by the pneumatic piston. Design penetrations into the copper gasket were achieved, and there was negligible creep of the gasket with time. Since instituting this change, there have been no failures of this critical connection.

5.0: Cathode

The cathode consists of an array of hollow molybdenum tubes that encircle the anode. Molybdenum was chosen for the cathode tube material because it has a low sputtering coefficient, and it's high temperature properties.. The tubes are longer than the anode in order to provide a controlled electrostatic field environment during the plasma ignition phase. The tubes are inserted in a massive copper base. The tubes are water cooled. Water enters the base radially via a circular array of holes equally spaced around the edge of the base. A similar circular array of exit holes alternates with the entry holes. The flow turns 90 degrees, parallel to the axis and flows to a header at the end of the rods where the flow is turned and directed back towards the base through an adjacent rod. The cathode base is connected to feed and exit plenums via high pressure flexible hoses equipped with quick disconnected fittings so as to allow rapid replacement of the cathode. A set of pneumatic clamps press the cathode base against the transmission line insulation, where a pair of O-rings effect a vacuum seal. A differential pumping channel is provided between this O-ring pair . This feature allows good vacuum to be reached and it greatly simplifies leak detection. An array of thick radially orientated copper fins are brazed to the water cooled cathode base. These fins serve to cool the recirculating neon gas between pulses.

Three modifications were made to the cathodes from those first employed on the prototype machine. Firstly, the heat transfer capability of the molybdenum rods was significantly enhanced by placing inserts in the rods. These inserts were designed to increases the flow velocity in the areas of the rod than were contacted by the plasma. Secondly, a method for refurbishing the cathodes was developed and tested. Thirdly reliability problems with the current connection between the cathode and the triplate current feed were eliminated. A view of the cathode is provided in Fig. 14.

5.1: Cathode Refurbishment

Eighty per cent of the cost for the cathodes is in the copper base. Only the tubes and the ring at the base to which the rods are attached are subject to wear. The cathode was redesigned so that the “cathode cage”, consisting of the tubes, the ring at the base of the tubes, and the header (which can be reused) are removed as a unit and replaced with a new one. (See figure 20) The cathode cage is bonded to the base with soft solder. The joints are water tight, and easily handle the 230 kA peak currents. The melting temperature of the soft solder is low, so neither the brazed joints in the cathode cage or in the copper base are affected by the bonding process.

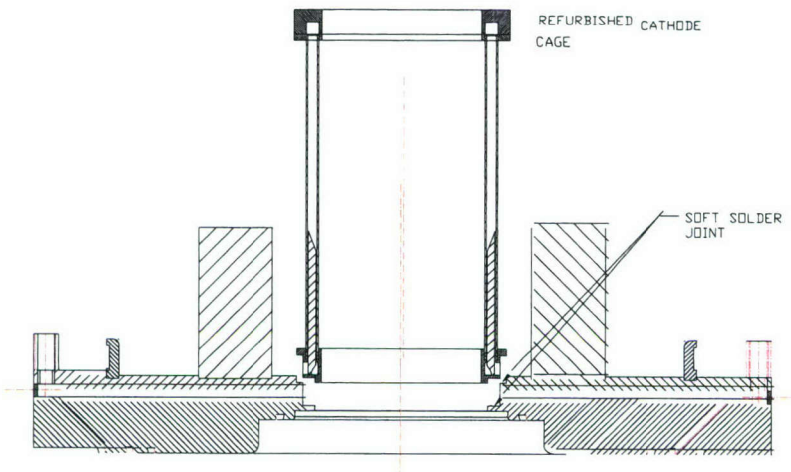


Fig. 14. Refurbishable cahthode assembly showing solder joint where new cage is attached

5.2: Current Connection

The cathode base makes current connection to the ground plate of the Triplate transmission line by means of "Multilam" finger stock on its edge. Major improvements in the reliability of the electrode high current connections were made. Although the cathode current connection had performed for seven months without any problems, there was a sudden onset of deterioration due to arcing between the Multilam and the aluminum feed plate. Examination showed that, following a number of installations, the cathode had shifted off center with respect to the feedplate. Consequently, the current connections were not equally good around the circumference. The rebuilt system interposes an easily replaceable copper ring between the feed plate and the Multilam. The ring is fashioned so as to insure proper centering of the cathode.

7.2: Magnetic E Beam Deflection

The x-ray window was redesigned to accommodate the larger solid angle required by the collimator. This section will review the analysis that is basis of the design. The x-ray output window must be protected from the high energy e-beam that is generated at the time of pinch. Permanent magnets mounted in the anode base serves to deflect the e-beam into a dump located upstream from the window. After extended runs, the magnetic material became hot and the magnetic field was destroyed. A system was designed to allow water cooling of the magnets.

There was an unanticipated beneficial fall out from the e-beam modeling. Previously, there was no known way that the full solid angle of the Xmetrics collimator could be employed, because the e-beam deflection magnets would block part of the solid angle. The study showed that a suitable deflection magnet system could be buried in the anode mounting base such that the full solid angle of the Xmetrics collimator, and more, could be accommodated.

7.3: Magnet Design for an Anode with Increased Collecting Angle.

New anode design is required to support the x-ray collimator installation on the BAE point source. The collimator requires a 3x increase in x-ray collection solid angle. The beryllium output window is subjected to shock waves, sputtering particles and other energetic agents generated by the electron beam and the plasma. A new design of the anode complex is needed that will ensure a reduction in these adverse effects, and will enable a reliable operation of the point source. This chapter is devoted to the design of the magnet in the anode complex, which will deflect the electron beam, thus providing better protection for the beryllium window.

7.3.1: Electron beam parameters and deflection approach

The voltage across the plasma reaches a value of up to several times the capacitor charge voltage during the collapse phase of the plasma, due to the large rate of change of the plasma inductance (the IdL/dt term). Simulation [1] for a charge voltage of $V=17$ kV, $C=90\mu F$, $L=16$ nH $R=3.3$ mOhm, and a peak current of 540 kA predicts a peak voltage of 40 kV. The full-width half-maximum duration time of the generated pinch in this simulation is 120 ns. At high energies (80 kJ) the predicted V_p rises up to 80-100 kV. This voltage accelerates electrons toward the anode base of the X-ray point source, resulting in an electron beam with an energy of several tens of kV up to 100 kV and a time durations of about 100 ns, which impinges on the output window.

Permanent magnets should be installed to deflect the electron beam. The magnetic field strength required for the beam deflection depends on the electron energy and the length of the interaction region along the beam propagation direction (axis of the anode in our case). In first approximation the deflection angle of the beam is determined by the Larmore radius R_L :

$$R_L = \frac{V}{B} \frac{m}{Z} \quad (1)$$

Where $V = \sqrt{2E/m}$ -- is the electron velocity, B -- is the field strength, m -- is the particle (electron) mass and Z -- is the particle (electron) charge. If the length of the interaction region with the magnetic field along the axis exceeds the Larmore radius, the beam will be reflected back.

7.3.2: TriComp computer code

Using simplified estimations of Larmore radius for the calculation of the deflection angle cannot provide sufficiently accurate results in the real case, because the magnetic field is essentially non-uniform and one has to take into account the actual spatial distribution of the magnetic field for the real anode geometry. Also, for the electron energies involved, one cannot disregard relativistic corrections.

We used the TriComp 4.0 computer code for the detailed simulation of the magnetic field profiles and for the calculation of the electron trajectories in the field, taking into account the relativistic corrections. This code has several packages for solving various electrostatic and magneto-static problems with finite elements analysis method. For the calculation of the magnetic field profile created by the permanent magnets we used the PerMag package of the code. The package has the following features:

- The geometry can be loaded from an AutoCAD file.
- The parameters of the permanent magnets (B_r and B_e in particular) are required.
- Nonlinear elements can be simulated using tabulation of their properties.
- The magnetic permeability of the other fields in the geometry is required.
- Fields have 2-D geometry, although orbits are calculated in 3-D space.
- Relativistic equations are used.

Dirichlet boundary condition was used in the current problem i.e. the vector potential was taken as constant ($A=0$) on the external boundary line of the geometry. Electron trajectories were calculated with the TRAK 5.0 package from TriComp. TRAK and PerMag are integrated software packages used for analyzing particle beams and calculating generalized single particle trajectories in electric and magnetic fields. These calculations are valid for relatively low current beams, when the fields created by the beam are much weaker than the applied fields.

7.3.3: Permanent magnet materials analysis

We considered several materials which could be used for the permanent magnets in the anode design. The materials are characterized by a coercitive force H_c , a remanence B_r and by the magnetic energy product BH_{max} (see **Figure ZZZ.1**)

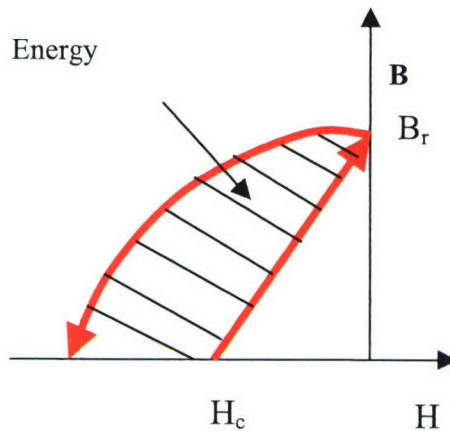


Figure ZZZ.1. B-H curve for a permanent magnet

The parameters of commercially available magnets are presented in **Table ZZZ.1**.

Table ZZZ.1. Parameters of commercial permanent magnet materials

Material	H_c , kOe	B_r , Tesla	Energy, MG*Oe	Tmax, °C
SmCo	9.2	1.05	26	300
NdFe	12.3	1.28	40	150
AlNiC	0.64	1.25	5.5	540
Ceramic	3.2	0.39	3.5	300

The SmCo magnet was selected as optimal for the current design. This material creates almost the same strong magnetic field as NdFe, but it can operate at much higher temperature (300°C versus 150°C), which is critical for the considered application.

7.3.4: The Non-collimator anode design

The design of the non-collimator anode with installed SmCo magnets is shown in **Figure ZZZ.2**.

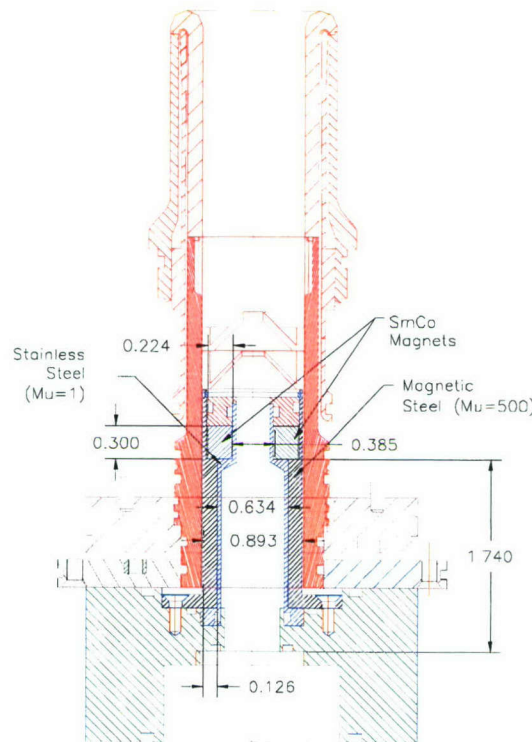


Figure ZZZ.2. The Non-collimator anode design

The anode has a plane collecting angle of 3.8° . The SmCo magnets have the following dimensions:

Length along the anode axis	0.3 inches
Width:	0.2 inches
Thickness (in the radius direction):	0.22 inches
Distance between the magnets:	0.4 inches

The anode design with the magnets assembly was simplified for the analysis with the TRICOMP software. The results of the simulation of the magnetic field profile for two directions (along the anode axis and along the line normal to the magnets) are presented in **Figure ZZZ.3**.

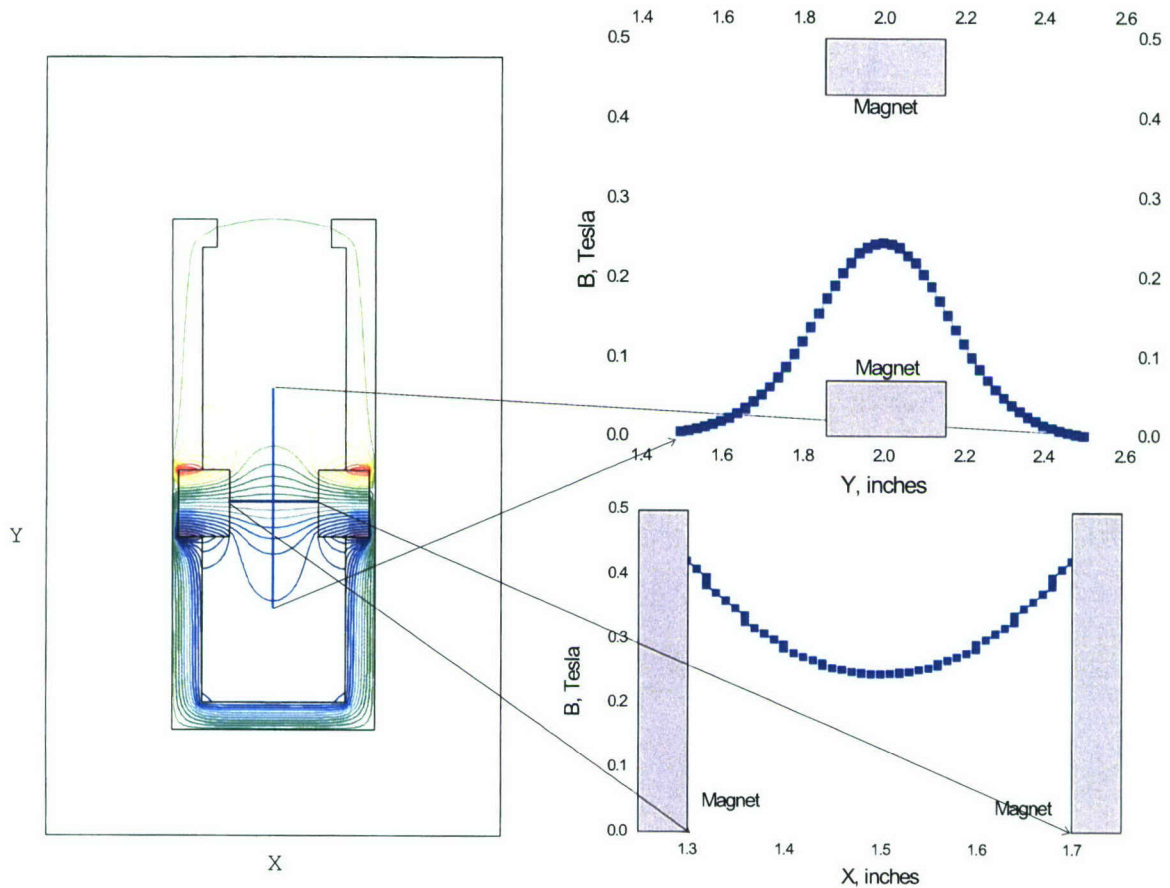


Figure ZZZ.3. Magnetic field profile for the non-collimator anode

7.3.5: Simulation of the field required for electron beam reflection

Reflection of the electron beam by the magnetic field of the permanent magnets was simulated by the TRAK package. Figure ZZZ.4 shows reflection of electrons with energies from 10 to 40 keV by the field of permanent magnets having a maximum strength in the center 0.25T (2500G).

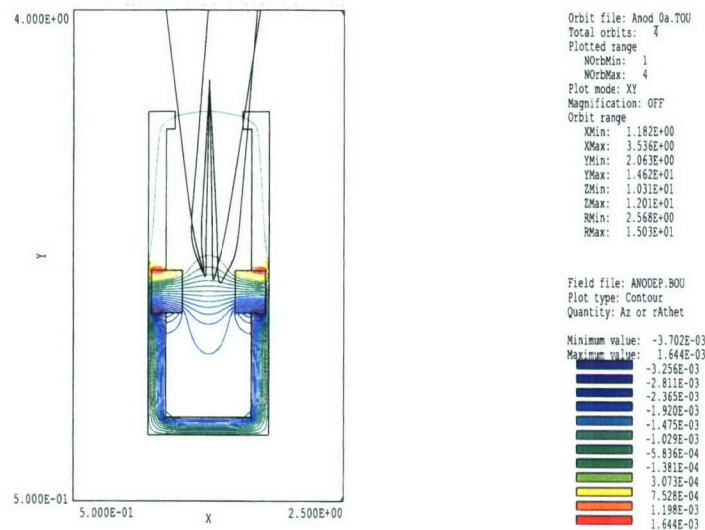


Figure ZZZ.4. Reflection of low-energy electrons (from 10 to 40 keV) by permanent magnetic field

Figure ZZZ.5 shows the interaction of high-energy electrons (100, 200, 300 and 400 keV) with the permanent magnetic field.

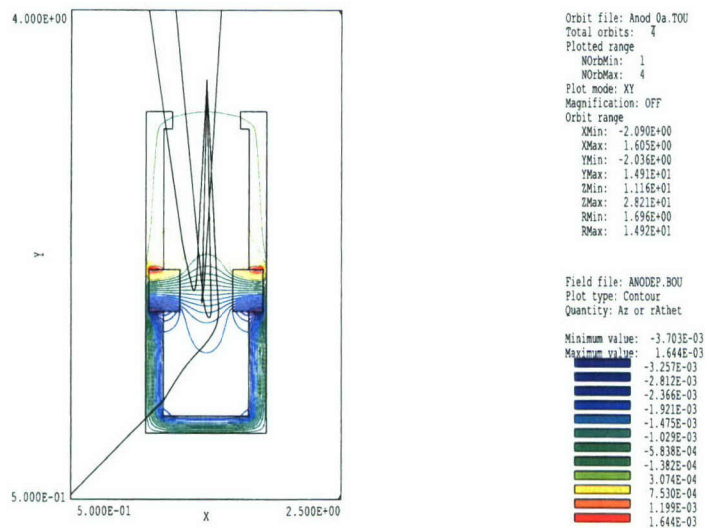


Figure ZZZ.5. Interaction of high-energy electrons (100, 200, 300 and 400 keV) with the permanent magnetic field

One can see that only electrons having an energy greater than 300 keV can penetrate the field.

By using the TRAK package we scaled the magnetic field to define the minimal field strength required for the reflection of electrons having a given energy. **Figure ZZZ.6** shows the penetration of 30 keV electrons through the field having a strength of 0.055 (550 G) in the center.

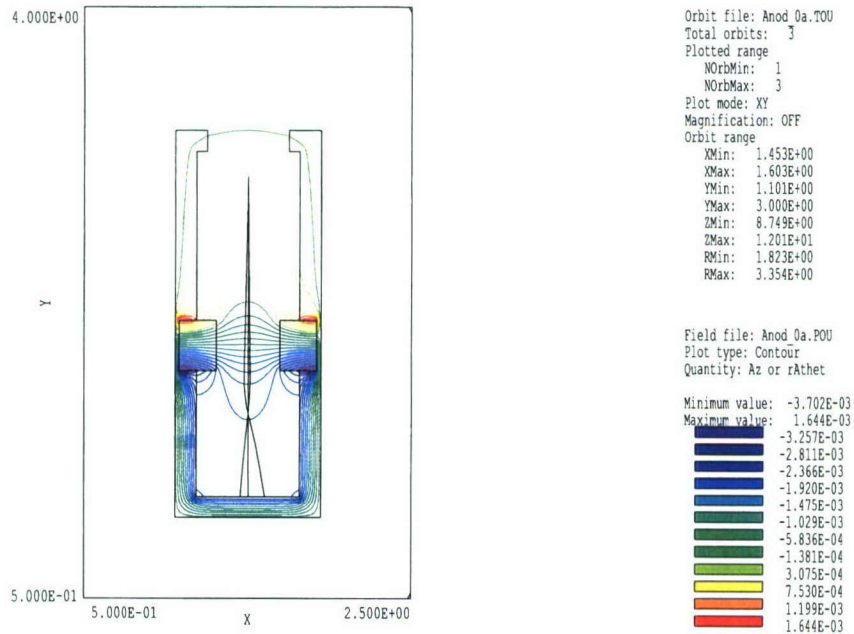


Figure ZZZ.6. Penetration of 30 keV electrons through the field with a strength of 550 G in center.

The simulation was performed for two different length of magnets along the anode axis and for the electron energy range from 10 to 100 keV. The results of the simulation are summarized in **Figure ZZZ.7**.

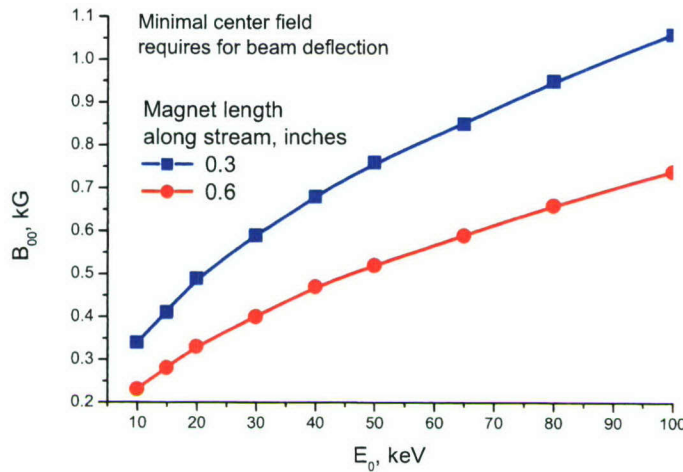


Figure ZZZ.7. Permanent magnet field strength (in center) required for the reflection of electrons with a given energy

For a given geometry (magnet length along the axis) the required field is proportional to the square root of the electron energy. This is an expected result as can be easily seen from **equation ZZZ.1**.

Assuming that the electrons could have energies of up to 100 keV, the permanent magnet system in the anode designed for the collimator should have a strength of 1000 G if the magnet length is 0.3 inches and 700 G if the magnet length is 0.6 inches. These numbers are in a good agreement with those of the non-collimator anode design. The measured value of the magnetic field in center is 1200 G which is adequate for beam deflection for a magnet length of 0.3 inches.

7.3.6: Two magnets design for the anode with increased collecting angle

In the anode design with increased collecting angle the magnet opening aperture is 0.625 inches. Several magnet system designs were analyzed. The simplest one is a two magnets design similar to the non-collimator anode. Several parameters were varied to optimize the field. The maximum magnetic field in center is 700 G and the field profile is substantially non-uniform, as shown in **Figure ZZZ.8**.

The field profiles are shown for two axis: X and Y, as explained in **Figure ZZZ.9**. The magnet holder is made of magnetic steel with high magnetic permittivity. Magnets are installed into the steel ring to some depth. Figure ZZZ.8 shows the field profile for various depths. The strongest magnetic field corresponds to the minimal depth

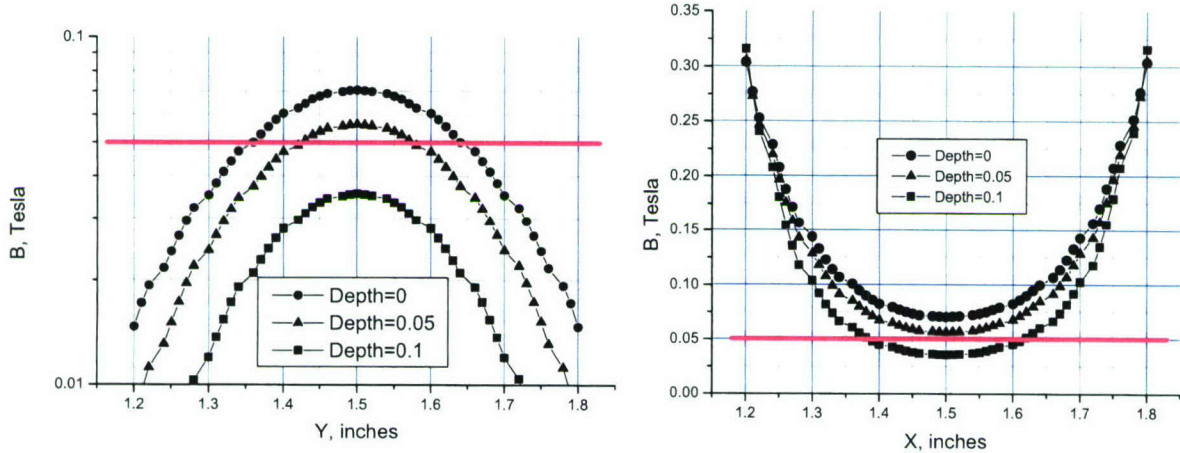


Figure ZZZ.8. Magnetic field profiles along the X and Y axis for an anode with increased collecting angle.

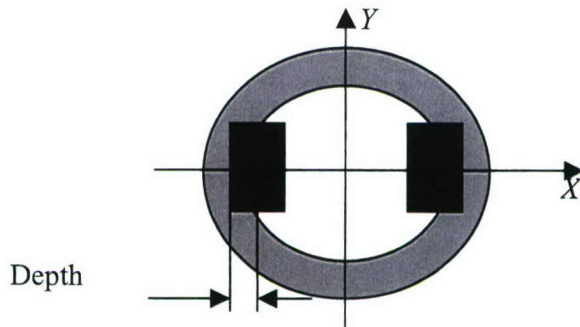


Figure ZZZ.9. Plane geometry of the magnet system

Several other parameters were varied to see their influence on the magnetic field. In particular, the variation of the magnetic field profile with the variation of the magnetic permittivity of the magnet holder is shown in **Figure ZZZ.10**.

One can see that the magnetic field increases with an increase in the permittivity of the magnet holder, but saturates when permittivity exceeds 200.

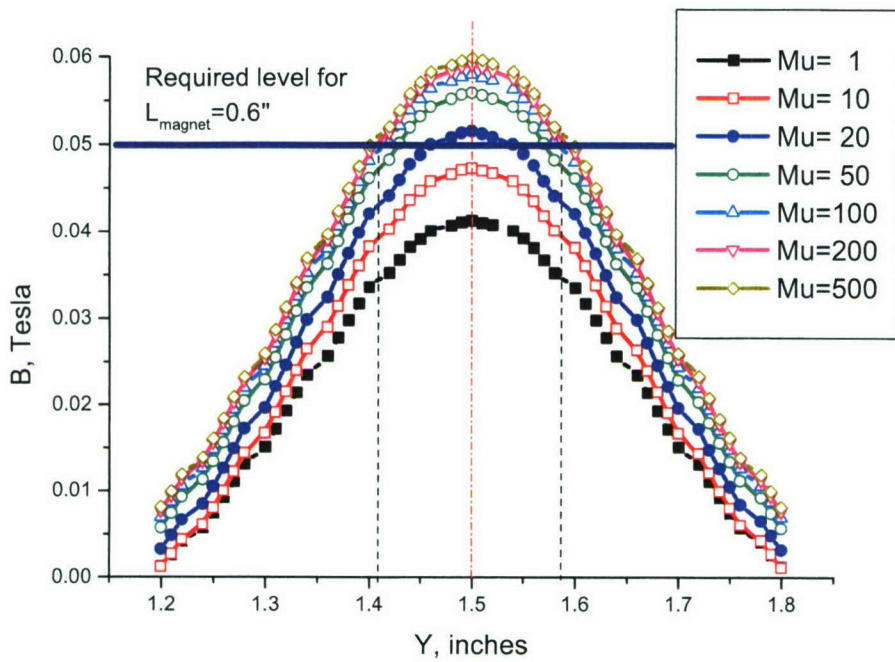


Figure ZZZ.10. Variation of the magnetic field profile with the magnetic permittivity of the magnet holder

Figure ZZZ.11 shows the influence of the magnet thickness on the field profile. One can see that the variation of the thickness from 0.118 to 0.238 does not result in a considerable change in the field strength.

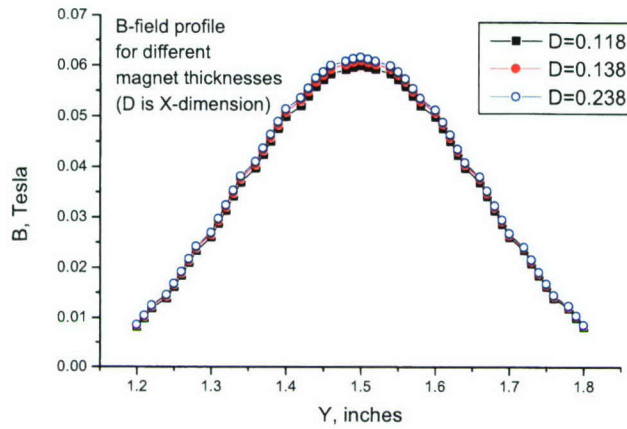


Figure ZZZ.11. The magnetic field profile for various magnet thicknesses.

ZZZ.7. Four magnets design for the anode with an increased collecting angle

The two magnet design does not provide the required field profile and field strength for the reflection of the electron beam. Thus we analyzed a four magnet system as shown in **Figure ZZZ.12**.

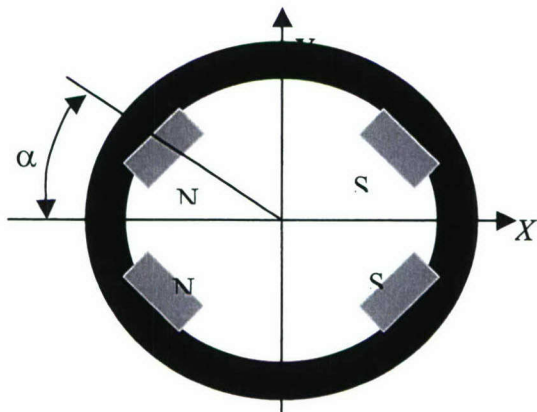


Figure ZZZ.12 Four-magnet design

The magnet dimensions were 0.1x0.2 inches (in plane) with a length of 0.3 inches. The magnets depth in the steel holder was chosen as 0.05 inches. The separation angle α was varied for the optimization of the field profile. The simulation results are shown in Figure ZZZ.13.

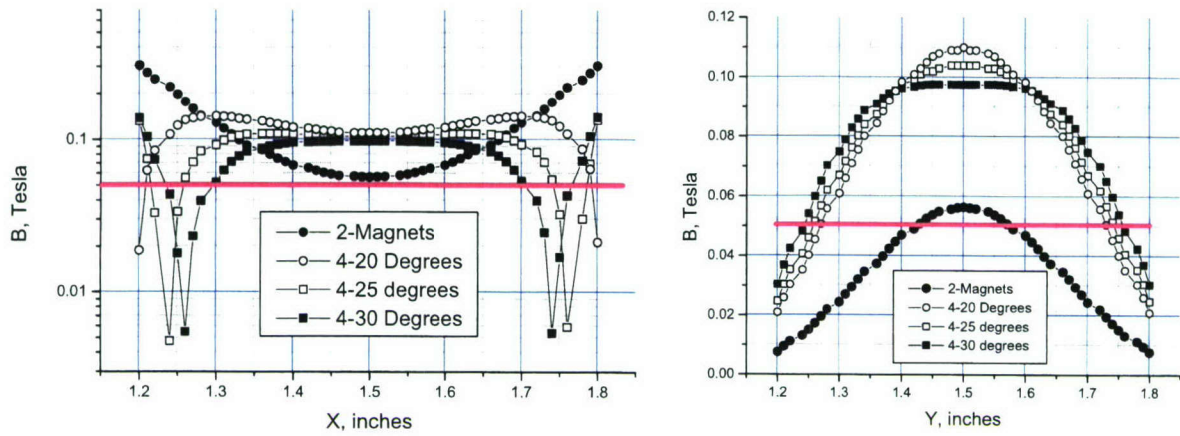


Figure ZZZ.13. Field profiles for a four magnets system

One can see that the goal of 1000 G can be reached in the four magnets design. The field uniformity for a separation angle of 20 degrees is optimal for the current design. To obtain a better reflection, two four-magnets system should be used. The systems should be separated by 0.2-0.3 inches from each other along the anode axis and should have a crossing fields orientation of 90°. This geometry should help to reflect also those electrons which would penetrate through the regions with reduced field.

8.0: Vacuum System

The vacuum system on the deliverable machine is similar to that on the laboratory prototype, but with several upgrades. The most prominent of these upgrades is that of complete computer controlled operation. No valves, switches etc. must be operated, and no pressures need be monitored in order bring the system from atmospheric pressure to full operational status, or to low pressure standby. In addition, various automatic protections were installed to isolate pumps and to rapidly shut down the system should any air or water leak develop.

The vacuum system was designed to meet an number of constraints. The chamber needed to be cooled so as to handle a large heat load. The shape of the chamber had to be such as to provide for proper recirculation of the working gas at high repetitive pulse rates. The chamber had to allow rapid, “no tools needed”, access to the electrodes so that replacement could be effected with a minimum in down time. The pumping system had to allow for the high, through the anode, gas feeds which obviate any need for a chopper. The system needed to be equipped with instruments and controls so that all functions and states of readiness could be under computer control, while all self protective features were hard wired.

The vacuum chamber is a stainless steel cylinder which sits on top of the cathode base. Vacuum seal to the top of the cathode base is effected with a concentric pair of O-rings. A differential pumping channel is provided between this O-ring pair. This feature allows good vacuum to be reached and it greatly simplifies leak detection. A set of four pneumatic toggling clamps press the chamber base against the cylindrical cathode base. A second set of pneumatic clamps press the cathode base against the transmission line insulation, where a second pair of O-rings also effect a vacuum seal. The toggling feature of the clamps insure that lockdown is maintained even if pneumatic pressure should be lost. This clamping system allows for almost instant removal or installation of the chamber, and if desired, the cathode. This system replaces the arrangement of more than 40 bolts on the spark gap driven source. These bolts had to be carefully torqued down in a sequence of small increments in order to effect a vacuum seal and current connection using copper gaskets.

The vacuum system is equipped with a small turbo pump that allows pressures in the mid 10^{-5} torr range to be reached. Such low pressures are not necessary for any phase of DPF operation. Nonetheless, this capability serves two useful functions. Firstly, it acts like a leak detector. If low pressure is not reached with the neon flow turned off, it means that there is either an air or water leak which can contaminate the working gas. Secondly, the vacuum chamber may be kept at low pressure when the source is not in use, thereby insuring the cleanliness of the walls of the chamber and a fast start up of X-ray output when operations are begun.

The vacuum system is designed to handle neon gas flows, up to 4.8 standard liters per minute (slm). This flow is achieved using a small, 21 cfm (600 slm) fore pump in series with a 108 cfm (3,000 slm) roots blower. With the chamber at a working pressure of 1.2 torr, a neon flow rate of 2 slm has been sufficient to keep vapor deposits on X-ray window to a level that shows no noticeable degradation in transmission over several hundred thousand pulses.

The fraction of discharge energy which reaches the chamber wall has been measured at approximately 40%. The distribution of energy on the chamber walls is not known in detail. Previous measurements have shown that most of the gas accelerated in the rundown phase

continues along the axis until it hits and the wall. This gas, with kinetic energy of order 200 eV per particle, shocks against the end wall. The dominant mechanism for heat loss by this shocked gas is through radiation. The end wall can be expected to intercept up to 50% of this radiation. The pinch likewise radiates strongly. From straightforward geometric considerations, a certain fraction of this radiation is intercepted by the electrodes, and the remainder transferred to the walls.

The chamber is not cooled directly. Rather, it has a water cooled liner. The liner is made to be readily removable so that it may serviced, and so that diagnostic ports in the chamber wall may have direct view of the plasma during low repetition rate experiments. At the end of the chamber opposite from the DPF electrodes, a cooled molybdenum beam stop is provided for the plasma which is axially accelerated to approximately 200 eV during the pre-pinch phase of the discharge. This beam stop is conical in shape, with the apex pointing back towards the pinch. Consequently, the shocked, stagnated plasma will experience a radially outward component of velocity, as well as a reversed axial component, as it begins to expand. A water cooled copper dome extends from the edge of the conical beam stop to the water cooled cylindrical wall liner. A photograph of this arrangement is presented in Fig. 15. These two elements, along with the beam stop, must dissipate much of the radiative energy given off by the axially directed plasma shocking against the beam stop, and by the radially directed pinch plasma. The beam stop, the dome, and the side wall liner all have separated water feeds.

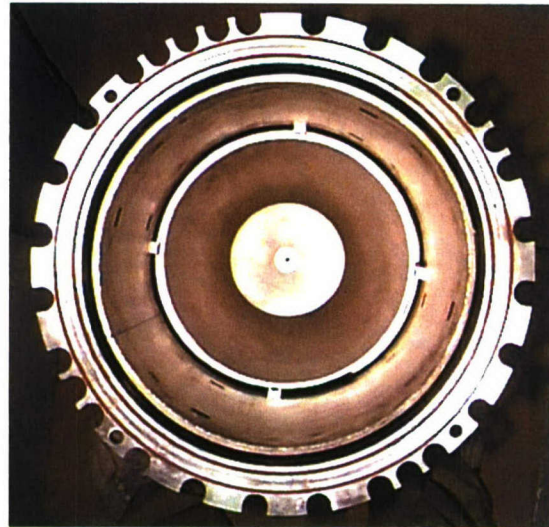


Fig. 15. View of interior of vacuum chamber, as seen from the pinch, showing cooled cylindrical liner, dome, and conical beamstop

The shapes of the beam stop, the adjacent domes and the wall liner are such as to encourage a toroidal flow of gas within the chamber during repetitive operation. That is, the gas that is accelerated along the axis hits the beam stop and reverses its flow so as to return along the cylindrical walls.

Upon nearing the plane of the cathode base, the flow turns radially inward, passes between the cathode bars, and fills the vacuum left by the snowplow phase of the previous pulse. Before passing through the cathode bars, the gas must pass between a set of cooled, radially orientated fins which are attached to the cathode base. Their primary function is to conductively cool the gas. However, when a second set of uncooled fins is interdigitated with the cooled fins, the combination forms a thermophoretic nanoparticle precipitator. Nano particles are driven to and adhere in the form of a film on the cooled fins.

9.0: Cooling System

The Cooling System for the DPF source provides the necessary temperature control of the various components. The cooling system is comprised of three primary closed flow circuits. The DI Cooling Subsystem provides deionized water flow to the components at high voltage potential – the anode, solid state modules, glass insulator, and anode plate. The Standard (STD) Cooling Subsystem provides water flow to the cathode, vacuum chamber components and ground plate cooling strips. The Chiller Subsystem removes the heat added to the DI Cooling and Standard Cooling subsystems and interfaces with these subsystems via the plate heat exchangers. Cooling requirements for each of the cooling circuits is given in Table 3 below. Schematics of the Cooling System and its subsystems are shown in Fig. 16 through Fig. 18.

Table 3. Heat Removal Rate and Flow Requirements of Cooling System

Cooling Circuit	Heat Removal Rate (kW)	Flow Rate (GPM)
<i>DI Cooling Subsystem:</i>		
Anode Cooling Circuit		16.0
Anode Plate Cooling Circuit		0.4
Insulator Cooling Circuit		2.0
Modules Cooling Circuit		24.0
<i>STD Cooling Subsystem:</i>		
Cathode Cooling Circuit		14.4
Chamber Cooling Circuit		10.2
Ground Plate Cooling Strips Circuit		13.0
<i>Chiller Subsystem:</i>		
DI Cooling Circuit	30	16.0
STD Cooling Circuit	70	16.0

9.1: DI Cooling Subsystem

The DI Cooling Subsystem, illustrated in Fig. 16 is comprised of the anode flow circuit and the module flow circuit. The anode flow is driven by a constant volume pump directly coupled to a 5 hp motor. A variable frequency drive is used to control the motor speed and therefore the pump speed. Volumetric flow is nearly linear with pump speed. Also, if pressure increases due to localized film boiling or other flow constriction, the constant volume pump will

maintain constant volumetric flow even though coolant pressure has increased. The anode pump speed is nominally set to 67% of full speed to meet the required flow rate given in Table 3.

The module flow circuit is comprised of flow through the solid state modules, flow to the insulator, and flow to the anode plate. Coolant is pumped from near the bottom of the storage tank by a constant speed pump after which the flow to the anode plate and insulator is split. There are separate feed and return lines for the anode plate and insulator flow as shown in The anode plate and insulator return flow is manifolded with the anode return flow and directed to the hot side of the DI Subsystem plate heat exchanger. The return flow from the solid state modules does not flow through the heat exchanger to minimize the back pressure in some of the module components.

The DI Cooling Subsystem also includes a DI filter and recirculating pump. The DI filter pump circulates water, at a rate of approximately 1 GPM, from near the bottom of the storage tank, through the DI filter bank and returns the flow to the top of the tank as shown in Fig. 16. The DI filter is a combination filter which outputs water deionized to 18 MΩ-cm and removes oxygen. The coolant in the DI storage tank is constantly recirculated through the DI filter to maintain the DI coolant deionized.

9.2: STD Cooling Subsystem

The STD Cooling Subsystem is comprised of the cathode flow circuit and the (vacuum) chamber flow circuit. This is illustrated in Fig. 17. The cathode flow, like the anode flow, is driven by the same model constant volume pump directly coupled to a 5 hp motor. This type of pump has been selected for the cathode for the same reasoning as it was chosen for the anode. If pressure increases due to localized film boiling or other flow constriction, the constant volume pump will maintain constant volumetric flow even though coolant pressure has increased. The cathode pump speed is nominally set to 65% of full speed to meet the required flow rate given in Table 3.

The chamber flow circuit is comprised of flow through the vacuum chamber cooled components, and flow to the cooling strips on the ground plates of the triplate current feed. The flow rate criteria for the cooling strips is set by the maximum allowable temperature rise of the triplate due, primarily, to skin effect heating. This maximum allowable temperature rise is in turn set by the differential expansion between the insulation sheets and the conductor plates in the triplate. (Gaps in the overlapped insulation joints allow for a controlled amount of differential expansion.) Coolant is pumped from near the bottom of the storage tank by a constant speed pump after which the flow to the cooling strips is split. There are separate feed and return lines for the chamber and cooling strip flow. The chamber and cooling strip return flow is manifolded with the cathode return flow and directed to the hot side of the STD Subsystem plate heat exchanger.

9.3: Chiller Subsystem

The chilled water provided by the on-site facilities is split into the DI cooling circuit and the STD cooling circuit as shown in Fig. 18. DI cooling flow and STD cooling flow is directed to the cold sides of the DI and STD plate heat exchangers. These plate style heat exchangers are compact and consist of a series of plates that are stacked together. Heat removal capability of the

heat exchangers can be easily increase by the installation of additional plates. The DI cooling flow removes the heat added to the anode, anode plate, insulator and solid state modules cooling circuits. The STD cooling flow removes the heat added to the cathode, chamber and cooling strip circuits. Flow and cooling requirements for the Chiller Subsystem is given in Error! Reference source not found. below.

9.4: Miscellaneous Coolant System Features

Flow rate diagnostics and instrumentation for each of the cooling circuits are installed on the return line. This location allows for not only loss of flow due to valve or pump failure but also for loss of flow due to a leak. Pressure diagnostics and instrumentation are include on the feed side of the cathode and anode cooling circuits to ensure that operating pressure at full flow does not change appreciably over time. Other diagnostics include feed and return temperatures, resistivity of the DI system, and valve positioning.

During normal operations the rotation speed of the cathode and anode pumps is changed gradually under computer control. Emergency turnoff of the constant volume anode and cathode pumps and of the module pump from full speed resulted in a water hammer. This caused overflow from the water thermal expansion chambers. The problem was fixed by installing a bypass circuit around the pumps. This circuit contains a check valve to prevent back flow from the high pressure side of the pump.

An automated water tank fill system was designed and fabricated. The system accommodates thermal expansion without the use of a pressurized accumulator. The top most point of the storage tank is at atmospheric pressure, thereby lessening stress on the insulator between the anode and cathode. Using logic programmed into the PLC, the system is able to detect a small water leak anywhere in the system by tracking the change in water level in the tanks. If a leak is detected, all valves are closed, the system is shut down, and a warning is displayed.

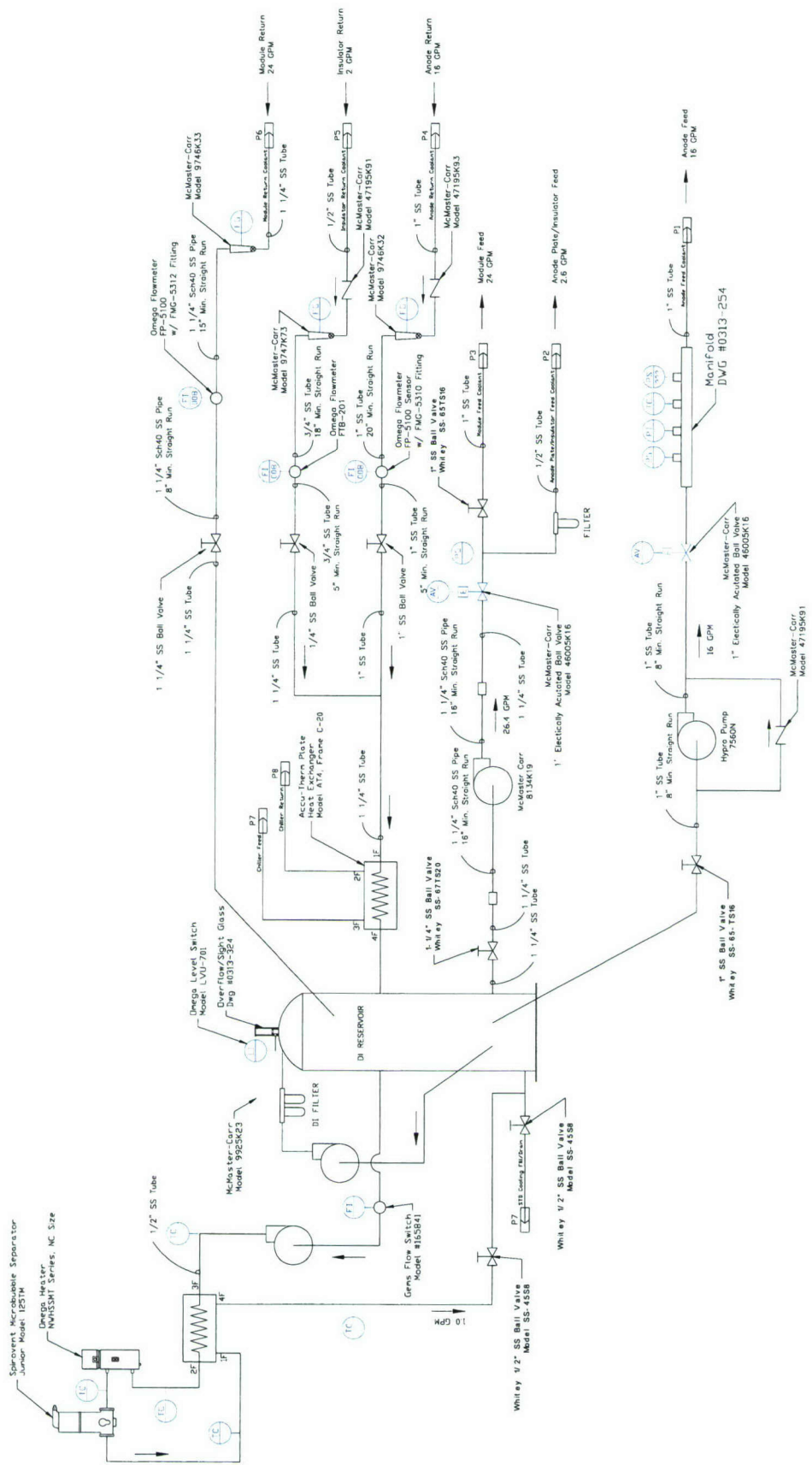


Fig. 16. DI Cooling Subsystem Schematic

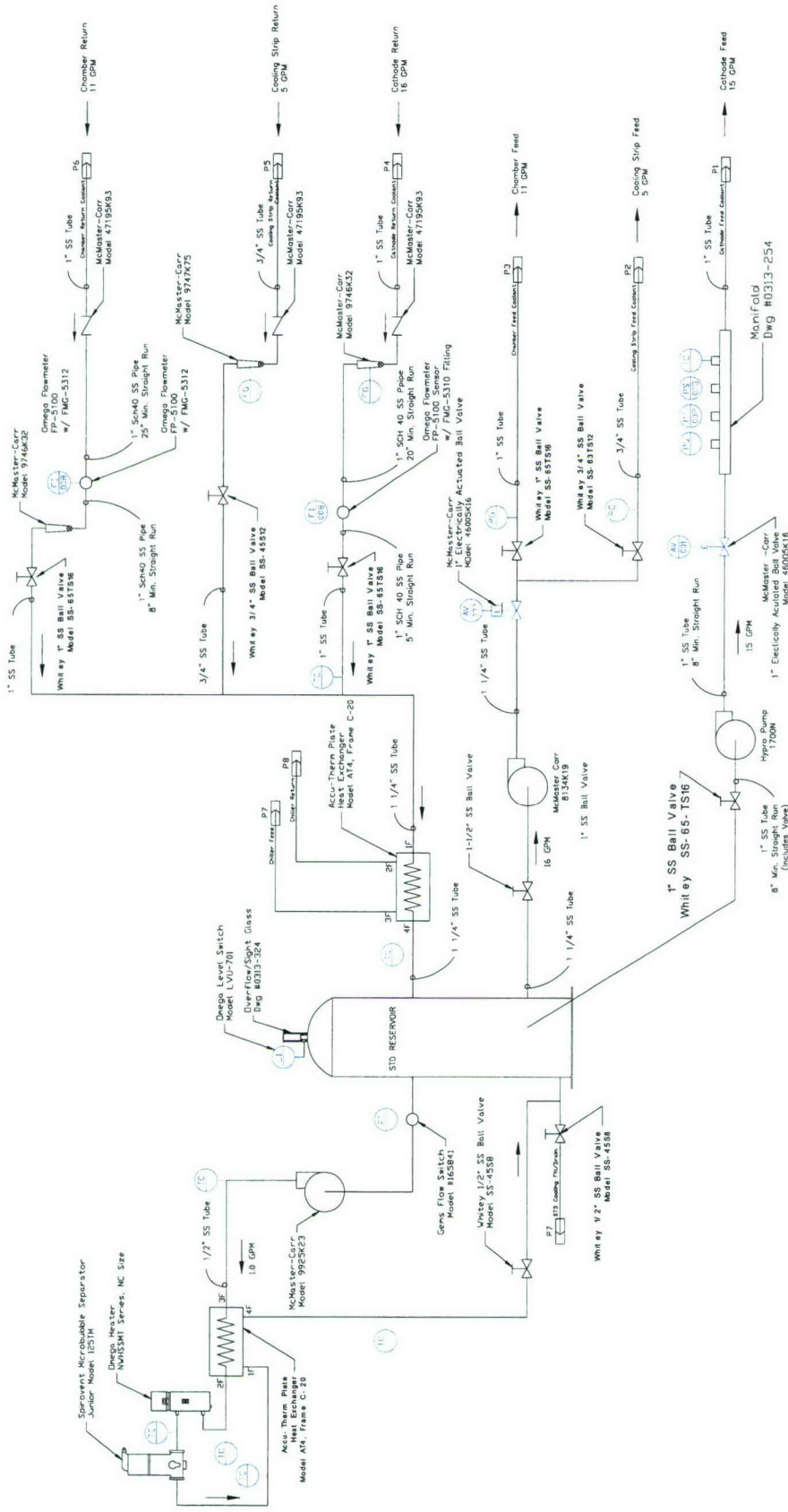


Fig. 17. Standard Cooling Subsystem Schematic

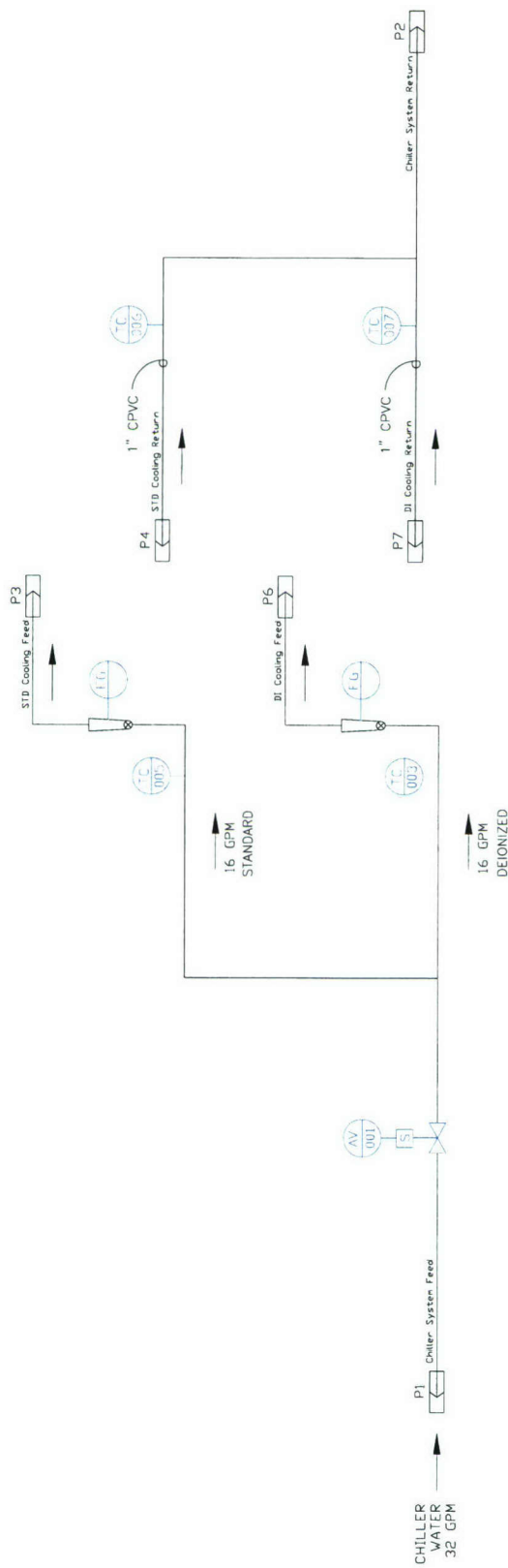


Fig. 18. Chiller Subsystem Schematic

9.5: Degassing System

Both the normal and deionized coolant water must be degassed. This prevents an accumulation of gas bubbles that could interfere with heat transfer in critical areas. A new coolant degassing system was implemented to replace partial vacuum towers used in the laboratory prototype machine. Those 16 ft tall towers maintained the top of the water column at 4/5 of an atmosphere. The dissolved gas concentration at this pressure is approximately 4/5 the air concentration (18.7 scc of air per liter of water) at atmospheric conditions. Experimentally, this difference in concentrations enough to insure that there is a fairly rapid dissolution of gas contained in bubbles entrapped at or above atmospheric pressure. Large bubbles disappeared from under the glass insulator in a matter of minutes.

The new system has the advantages that it is much more compact, and the dissolved air concentration in the water is reduced to a significantly greater degree. A stream of water, approximately 1/4 gal/min is diverted from the reservoir and is passed through a counter current heat exchanger that raises its temperature to approximately 80 deg C. The stream temperature is then boosted to approximately 100 deg C by passing it by a small, < 1 kW, electric heater element. From there the stream passes by a standard water/gas separator such as is used commonly in water heaters and boilers, both commercial and domestic. The separator incorporates a relief valve which lets off the devolved gas and the accompanying steam into the atmosphere. At a temperature near 100 deg C and a few psi gauge pressure, most of the gas is expelled. The stream then passes in the opposite direction through the heat exchanger, giving roughly 80% of its heat to the incoming stream.

The e-fold time for processing a reservoir of 50 gal of water is over 3 hours. When a new electrode is placed in the system, bubbles are invariably introduced into the water stream. Any significant wait of more than a few minutes to clear the bubbles would be unacceptable. However, even if several hundred cc of air were introduce (and this appears to be a pessimistic over estimate), and all of that gas were immediately dissolved rather than captured in the gas trap, the resulting amount of dissolved gas would be small compared to the approximately 3500 cc of gas at NPT that would be in an undegassed system.

10.0: Controls

The DPF control system is built on a hierarchical basis. Within the DPF control system there is an array of different communication, control, and sense systems. A top level view of the architecture is provided in Fig. 19. This diversity is required to meet the simultaneous requirements of flexibility and reliability, the integration of a wide variety of controls and sensors, and the demands of dealing with a breadth of time scales from micro seconds to minutes.

Top level control is in the hands of a dual Pentium II processor, 400 MHz PC running SRL's DPF X-Ray Control software under Windows NT operating system. The DPF X-Ray Control software is programmed in National Instrument's LabView software. The DPF X-Ray Control software accepts commands via TCP/IP from the stepper client, or, in the service mode, from the hardwired DPF operator console located in the clean room near to the DPF. Responses

to these commands are modified according to inputs from a variety of sources. These sources include 1) an Allen Bradley programmable logic controller (PLC), 2) a National Instrument Field Point (FP) system, 3) SRL's Charge/Trigger Logic Board, and 4) SRL's X-Ray Digitizer system. The DPF X-Ray Control software effects control, with the exception of charging and the triggering the driver modules, only through the PLC via 64 logic output lines. The computer is equipped with several boards so as to allow communications with the above enumerated sensor/control systems. These boards include a National Instruments PCI-6602 timer board, a National Instruments PCI-DIO-32HS digital I/O board, and an Ethernet card.

The Allen Bradley model SLC05 PLC is the system "watchdog" and principle effector. For the watchdog function, a PLC was chosen over relay logic on the basis of reliability, flexibility, compactness, and cost. Approximately 80 digital sense lines, including system power, coolant temperature, flow, pressure, and vacuum limits, open/closed status of valves, and safety interlocks are continuously scanned. A complete scan of the approximately 100 ladder logic rungs takes about 4 ms. This time is shorter than the minimum interpulse time, 7 ms, which occurs when the system is operating at its maximum repetition rate of 130 Hz. If a fault is detected, the next scheduled discharge is disallowed. The PLC is programmed to then take the system directly to the service mode.

The computer communicates with the PLC via 10 baseT Ethernet. Along with LabView based DPF X-Ray Control software, the computer runs Allen Bradley's RS Links OEM software to handle the communications protocol with the PLC. There are also three hardwired lines between the computer and the PLC via the TIO board. One line informs the DPF X-Ray Control software that the PLC has found a fault, the other line informs the PLC that the DPF X-Ray Control software has found a fault, and the third line transmits a "heartbeat" from the DPF X-Ray Control software to the PLC. If the PLC detects an interruption in a stream of software generated pulses from the computer, it will assume that the software has "hung", and it will direct system to the service mode.

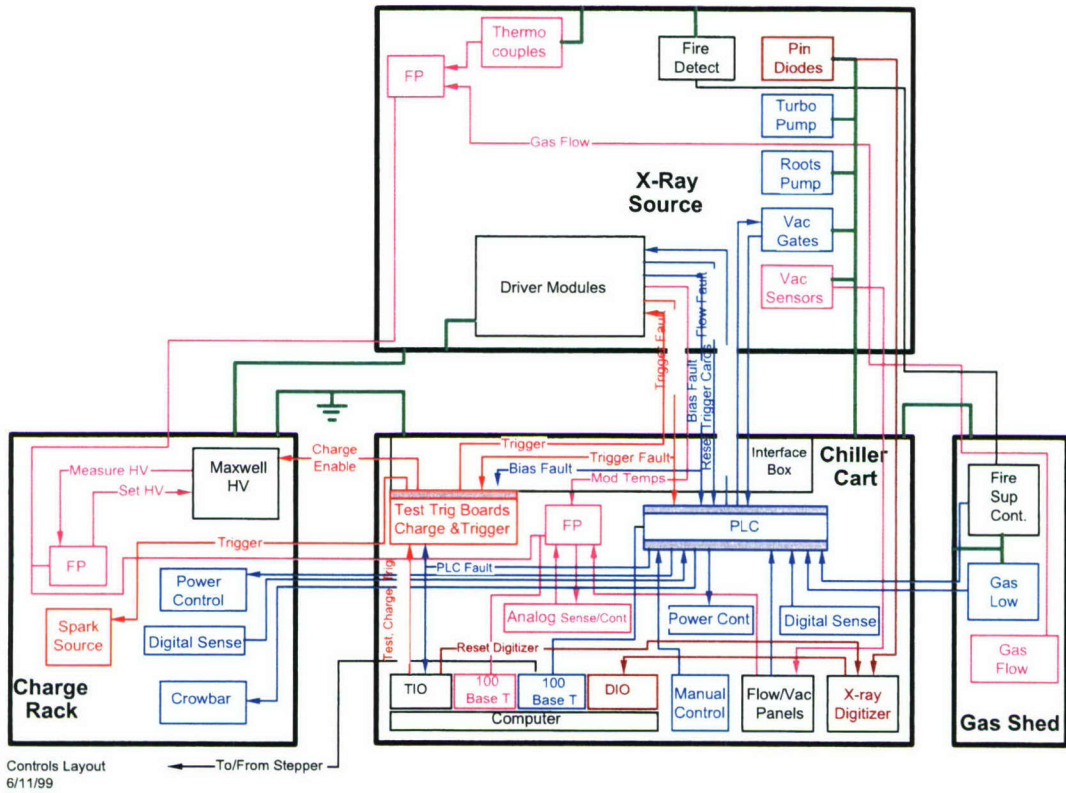


Fig. 19. Top level schematic of control system architecture

10.1: Trigger Controls

One issue with both LabView and the PLC is that these software packages respond relatively slowly (on the order of milliseconds) to changes in the state of the machine. The DPF discharge and associated power electronics deliver power pulses on the microsecond level, which is too fast for LabView or the PLC to detect. Consequently, in order to monitor trigger faults associated with the solid-state drive, it is necessary to integrate hard-wired control circuitry to monitor for faults and shut the system down if a fault is detected.

Fig. 20 shows a top-level block diagram of the solid-state module fault monitor circuitry. The trigger driver electronics from the LabView controller are located on the card, along with trigger fault latch circuitry that shuts down the triggers to both the capacitor charging module and the solid-state modules if a module trigger fault is detected. The response of the fault detection electronics is less than 1 μ sec, which disables any triggering in that time. A module fault flag is then sent to the LabView program which then shuts down the DPF system. The module fault latch is reset with a reset signal from the LabView controller, which allows the DPF system to again be operated at high power once the fault has been cleared.

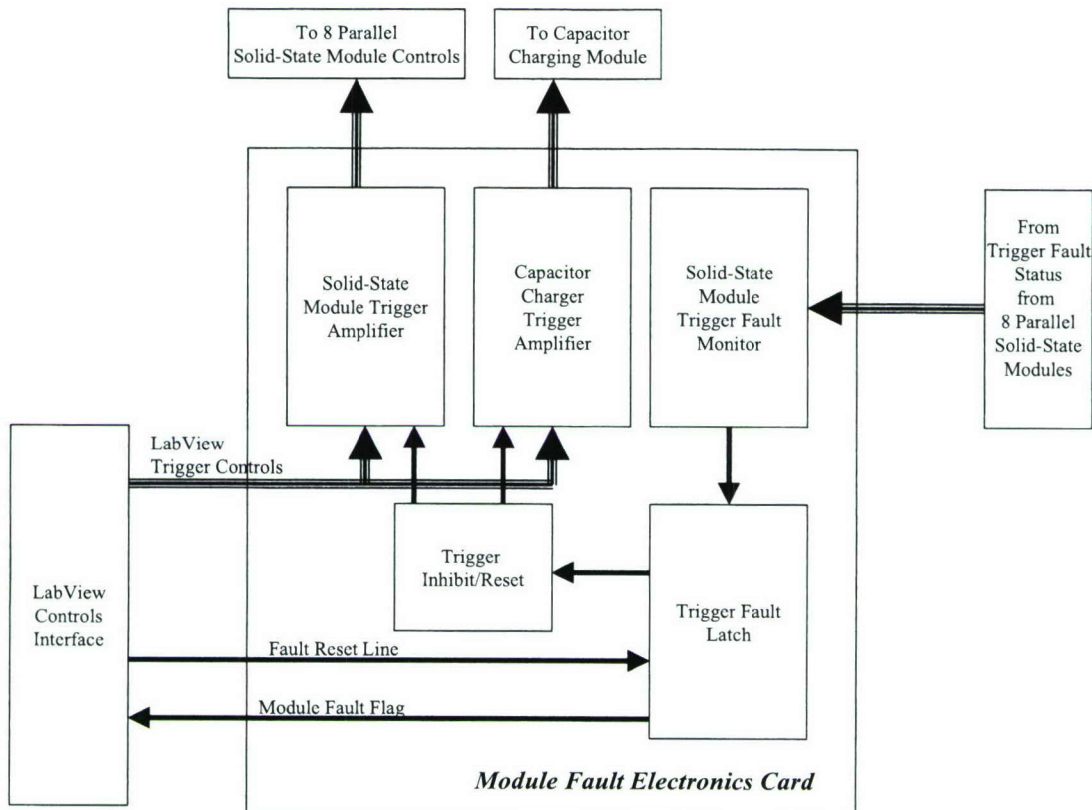


Fig. 20. Block diagram of the solid-state module fault detection card.

10.2: Dose Monitoring

The control system includes a method for digitizing the output from the pin diodes that measure the X-ray output. This device integrates the current pulse from two pin diodes using a RC circuits. A fast sample and hold circuits captures the integrated signals. This voltage is digitized, and the result is transmitted to the computer. The device allows the X-ray output to be monitored on every pulse, thereby enabling accurate total dose control. The output of the system was compared with the results of signals captured simultaneously by a fast digitizing oscilloscope. The scope is able to capture 49 pin diode current traces from shots fired in a burst. Following the burst, the scope traces were integrated using the oscilloscope's internal integration capability. The results of the two methods were in agreement.

10.3: State Machine Architecture

The LabView DPF X-Ray Control software design follows a state machine architecture. The X-ray source status has been broken down into six principle “Macro States”. These states correspond to various degrees of readiness of the machine to perform its function of producing X-rays. The stepper can command the system to transition to any of these readiness states. During the transition between “Macro States”, the machine is commanded by LabView DPF X-

Ray Control software to pass through a succession of micro states. Control over these individual "Micro States" is not available to the stepper.

Macro States

"Macro States" are denoted as integers that are integer multiples of ten. In particular these states are numbered 0, 10, 20, 30, 40, and 50. In between integers, such as 22, are reserved for "Micro States". These are discussed in a following section. Normal operational readiness increases with state number, starting from State 10, "System Available", in which the control computer is capable of accepting commands, through to State 50, "Expose Ready". The sixth state is state 0, the "Service Mode". The source may be commanded (with exceptions to be detailed below), either remotely from the stepper or locally from the DPF control screen, to transition between these states.

The normal "resting" state of the X-ray point source is State 20, "Vacuum Standby", with the source chamber under vacuum of less than 10^{-5} torr. This vacuum level is maintained by a turbo molecular pump.

Before X-rays can be produced neon gas must be introduced into the chamber at about a torr pressure. Roughly a liter per min flow of neon gas is maintained near the X-ray window to keep it clean. This gas flows, counter to the X-ray propagation, out through the anode into the vacuum chamber. A Roots blower vacuum pump is employed to evacuate this throughput of gas. (The turbo molecular pump of State 20 is isolated from the vacuum chamber and is turned off.) and This condition is realized in State 30, "Chamber Ready".

Line power connections to the drivers and cooling flows to the electrodes and other subsystems are established when the system is in State 40, Power & Coolant Ready". State 50, "Expose Ready", is the same as State 40, with the exception that the X-ray shutter, which otherwise blocks X-rays from passing from source to mask, is open. Rotating red beacon lights are activated when the system is in either State 40 or in State 50.

With one exception the Stepper can command the transition from any state to any other state, without specifying the intermediate states. The X-ray Source will automatically carry out the necessary intermediate transitions. For safety reasons, the Stepper cannot command a transition out of State 0, the "Service Mode". This must be done manually by an operator on X-ray source computer.

Micro States

During the transition between "Macro States", the machine is commanded by LabView DPF X-Ray Control software to pass through a succession of micro states. This progression can be viewed in the "Machine State" subpanel of the DPF2 Controller screen. However, control over these individual "Micro States" is not available. Nonetheless the individual commands that make up the transitions between "Micro States" can be issued by a "Factory" authorized personnel.

The tables below are presented so that the operator can acquire a sense of what is going on while the machine is transitioning between states. The Upstate Table covers the sequence for transitions from a lower numbered readiness state to a high numbered readiness state. The Downstate Table covers the sequence going from a higher numbered readiness state to a lower

one. “Micro States” are designated by integers which fall between the integer multiples of ten that number the bracketing “Macro States”. They are further designated by a prefix of U or D according to whether the system reached a given “Micro State” from, respectively, a lower numbered or a higher numbered “Macro State”.

Table 4. Upstate Table

State	Explanation
U0 Service Mode	Stepper control disabled.
U7	
U8	PLC fault lines are reset by toggling the PLC_FAULT_RESET register from false to true to false. The register remains true for 100 ms
U9	The commands to turn on the AC Master Relay (which supplies power to the Forepump), to turn on the DI Filter Pump and to enable DeGassing Operations are given
U10 System Available	Stepper control enabled. All systems off.
U16	The commands to open the turbo pump gate and foreline valves and turn on the forepump are given.
U17	System waits sufficient period for chamber pressure to be below 0.3 torr. If within this time period pressure is below 0.30 torr then turn proceed to next step otherwise go to Service Mode.
U18	The command to turn on the turbo pump controller is given.
U19	System waits sufficient period for chamber pressure to be below 1×10^{-4} torr. If within this time period, pressure is below 9×10^{-5} torr then system in Vacuum Standby otherwise go to Service Mode.
U20 Vacuum Standby	Vacuum chamber $< 9 \times 10^{-5}$ torr.
U23	The vacuum system is switched over to roots pump. The commands to close the turbo pump gate, foreline valves and turn off the turbo pump controller and to open the roots pump gate valve and turn on the roots pump are given.
U24	System waits for sufficient period for the vacuum system to stabilize.

U25	The commands to close the roots pump gate valve and open the bypass gate valve are given.
-----	---

Table 4. Upstate Table (cont'd)

State	Explanation
U26	The commands to open the anode, cathode, chamber, module, and chiller feed valves are given.
U27	System waits sufficient period for the above valves to open.
U28	The anode pump speed control is set to 67% and the cathode pump speed control is set to 65%. The commands to start anode pump and the cathode pump, and to turn on the chamber and module pumps are given.
U29	System waits sufficient period for the coolant flows to be established.
<i>U30 Chamber & Coolant Ready</i>	<i>Roots Pump On + Coolant Flows On.</i>
U34	The command to open neon flow valve is given.
U35	Commands to turn on the UPS's for module bank A and B are given.
U36	System waits sufficient period for the modules to be on and reset of fault lines.
U37	Voltage level is read and set. Commands to turn on Bank A and B power supplies are given.
U38	System waits sufficient period for the 480 VAC to be on and reset of fault lines.
U39	Command to open Crowbar is given.
<i>U40 HV Power Ready</i>	<i>Chamber & Coolant Ready + High voltage systems on and ready.</i>
U49	Command to open shutter valve.
<i>U50 Expose Read</i>	<i>Chamber & Coolant Ready + HV Power Ready + Shutter Valve Open.</i>

Table 5. Downstate Table

State	Explanation
D50 Expose Ready	Chamber & Coolant Ready + HV Power Ready + Shutter Valve Open..
D41	Command to close shutter valve.
D40 HV Power Ready	Chamber & Coolant Ready + High voltage systems on and ready.
D31	Commands are given to 1) close the crowbar switch, 2)close the neon valve, 3)set voltage level to 0, 4)turn off bank A and B power supplies, and 5)turn off bank A and B modules.
D30 Chamber & Coolant Ready	Roots Pump On + Coolant Flows On.
D29	Commands are given to turn off the chamber and module pumps.
D28	System waits sufficient period for the chamber and module flow to turn off..
D27	Commands are given to override anode & cathode flow faults, and to set anode and cathode pump speed controls to 0%.
D26	System waits sufficient period for the anode and cathode flow to turn off..
D25	Commands are given to stop the anode and cathode pumps and to close the anode, cathode, chamber, module and chiller supply feed valves and to remove the anode & cathode flow faults override..

Table 5. Downstate Table (cont'd)

State	Explanation
D24	Get ready to switch over to turbo pump. The commands to close the roots bypass gate valve, turn off the roots pump and to open the turbo pump gate valve and foreline valve are given.
D23	System waits sufficient period for chamber pressure to be below 0.3 torr. If within this time period pressure is below 0.30 torr then turn proceed to next step otherwise go to <i>Service Mode</i> .
D22	Command to turn on turbo pump controller is given.
D21	System waits sufficient period for chamber pressure to be below 9×10^{-5} torr. If after this time period pressure is below 9×10^{-5} torr then place system in <i>Vacuum Standby</i> otherwise go to <i>Service Mode</i> .
D20 Vacuum Standby	Vacuum chamber $< 1 \times 10^{-4}$ torr.
D11	Shutdown vacuum system. The commands to 1)turn off the turbo pump controller, 2)close the turbo pump gate and foreline valves, and 3)turn off the forepump are given.
D10 System Available	Stepper control enabled. All systems off.
D1	All boolean output and analog output registers are set to zero. All systems to their off state.
D0 Service Mode	Stepper control disabled.

11.0: Operation

There are two possible control sources for the DPF's functions. When the machine "Control Source", is set to "Remote", it is under control of the SAL Stepper. While operating with the "Control Source" set to "Remote", details of the DPF system performance may be viewed on the DPF X-ray Source control console. The console display presents a selection of nine windows that can be viewed. When the machine "Control Source", is set to "Local" various functions may be controlled (and viewed) from the DPF X-ray Source control console using the

mouse to manipulate buttons, etc. on the display windows. The “Control Source” can be changed from the “Utility” window. In order to control the machine in a given mode, an operator or service personnel must have proper “Authorization” for that mode. The software checks for proper authorization during the login procedure on the “Users” window.

11.1: Control Through Stepper Software

Under normal operating conditions, the stepper is the client, and the DPF is the server. Communications between the two is via Ethernet using TCP/IP. The “syntax” of the messages passed conform to a protocol developed by SAL. The “contents” of the messages consist of commands for the DPF to adjust settings, such as desired exposure level, to go to different readiness states, such as “vacuum standby”, to expose a field, to report on the results of the exposure, and to report on various internal conditions. The DPF system may also be placed in a service mode, either remotely by the stepper, or locally, either by an operator, or as an automatic response as a result of a fault. Once in the service mode, all functions are available to an authorized operator/service person. The system may not be removed from the service mode remotely by the client.

12.0: Safety & Fire Suppression Systems

The safety of personnel using the DPF and fire protection for the clean room environment were paramount considerations during the design of the delivered DPF. Self protection of the machine also received full consideration. All high voltage areas are completely enclosed and interlocks are in place on all doors which provide access to high voltage areas. Whenever the system is capable of being charged, rotating warning lights are activated. The system cannot be put in a charged state if a pulse is not requested. Before each and every requested pulse, even at the maximum repetition rate, the system is not be allowed to charge if the PLC survey of all digital sensors does not show that all systems are functioning normally.

Wherever practical, inflammable materials were utilized in the machine construction. This included stainless steel construction in the cooling cart, and fire resistant hoses where flexible connections were required. The transformers for the DC power supply are oil free. Unfortunately, the energy storage capacitors in the modules contain oil, and their casings are fabricated from ordinary PVC. Several steps were taken to insure the safety of the X-ray source against the threat of fire. Firstly, the modules were equipped with “drip pans” so that oil from a capacitor that burst would be collected in an enclosure that has limited access to air. Secondly, fire protection systems were installed that would 1) give early warning of a component which was starting to over heat, 2) shut down the system before ignition was likely, and 3) issue a general alarm and release fire suppressant within the X-ray source should there be a fire. This protection system is detailed below.

Two independent protection systems within the DPF source insure system protection against fire. The first protection system, the Analaser laser based smoke detection system, can detect particulates from an overheated component such as a resistor or transformer, even if there is no visible smoke. Through a system of tubes, this system samples air from the interior of all of the eight modules powering the DPF. If the lowest of the three (user set) levels of alarm is tripped, the DPF system is allowed to continue firing, and sampling of each module in turn is initiated by sequentially turning on and off solenoid valves in line with each sampling tube. The valves are controlled by the same programmable logic controller, PLC, that monitors and

actuates most of the other DPF systems. An analogue signal from the Analaser is simultaneously displayed on the control monitor, thereby allowing a defective module or modules to be readily identified. Sensitivity tests were conducted by overheating a small resistor at a level below that which produces smoke visible to the naked eye. The detector and the sequential sampling system worked as expected. If the second level of alarm is reached (the third level is not utilized), the PLC removes all power to the DPF source by turning off the internal solid state relays. It is expected that this action will be taken before any ignition is likely.

The second protection system uses a heat detector and a conventional smoke detector. If either one of these detectors is tripped, a warning light and horn located near the operator station alerts the operator. A signal is sent to the PLC to shut down the DPF system and, redundantly, contacts providing prime power to the DPF system are opened. If both the heat detector and the conventional smoke detectors are tripped, then, in addition to the aforementioned alarms and power shutdowns, the building fire alarm is set off and fire suppressant floods the interior of the X-ray source. The DPF source was sealed so that, upon release, the fire suppressant would be retained within the enclosure for the prescribed time. FMC conducted tests of the release and retention of the suppressant into the DPF source. All requirements were met.

13.0: Maintenance

The serviceability of the Phase II deliverable machine has been has been a prime consideration in all phases of the design. Most of the innovations in this area were developed for the Phase I laboratory prototype, and at most minor refinements were necessary on the deliverable machine. Although routine service was given a lot of attention, the following question was asked regarding virtually all parts of this device. "If, for whatever reason, this part should fail, will it be readily accessible for replacement?" If the answer was no, there was a redesign. Unfortunately, the environmental chamber around the stepper was a late addition to the overall integrated system design, and this change has significantly compromised access to the triplate for service.

14.0: Routine Service

The primary routine maintenance tasks consists of replacing the anode, the cathode and the insulator. First the chamber must be removed. Removal of the chamber involves turning a valve that releases the pneumatic clamps that maintain pressure on the chamber's O-ring seal, and pulling back the cart on which the chamber is mounted. Fig. 21 illustrates the vacuum cart in its retracted position. Note that the Roots blower mounted (and vibrationally isolated) on the lower cart shelf the moves back at the same time, so mid and high vacuum connections do not have to be broken. The forevac connection simply slides out as the cart is withdrawn. Note also the various hoses and cables on the carrier at the side of the cart. These provide cooling, power, control lines, and diagnostic lines to the vacuum cart. They do not have to be disconnected to allow withdrawal of the cart.

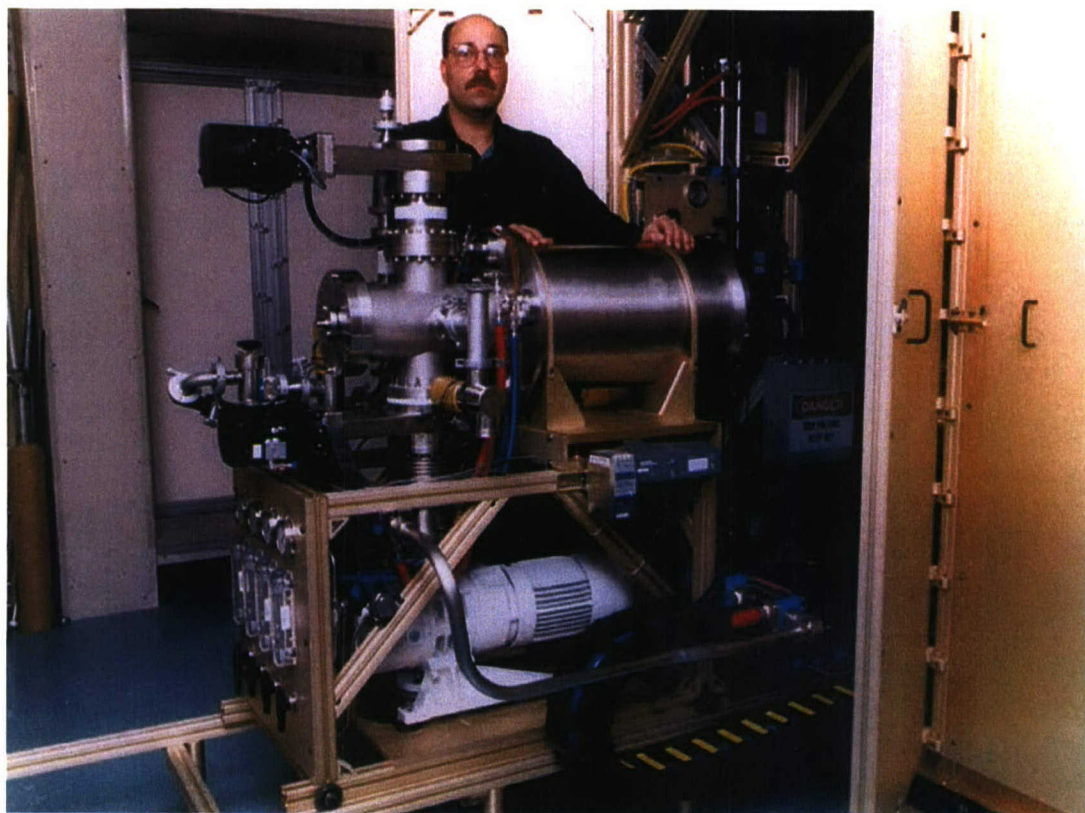


Fig. 21. View of vacuum chamber retracted to allow service of the DPF head

Fig. 22 shows the operators view of the head with the chamber withdrawn. If the anode is to be replaced, the operator simply throws a valve to release pressure on the anode piston, reaches in, twists the anode by 1/8 turn, and pulls it out along with the current connection gasket. A new or refurbished anode is put in place by reversing these operations. In order to remove the cathode, the quick disconnect fittings at the cathode cooling plenums are pulled off, and a valve is turned to release the cathode clamps that are shown in Fig. 22. The cathode simply pulls out. (The vacuum chamber and cart are used as jigs to assist the operator with the substantial weight of the cathode). If the insulator is to be removed, both the cathode and anode must be removed. Bringing the system back on line involves a reversal of the processes outlined above.

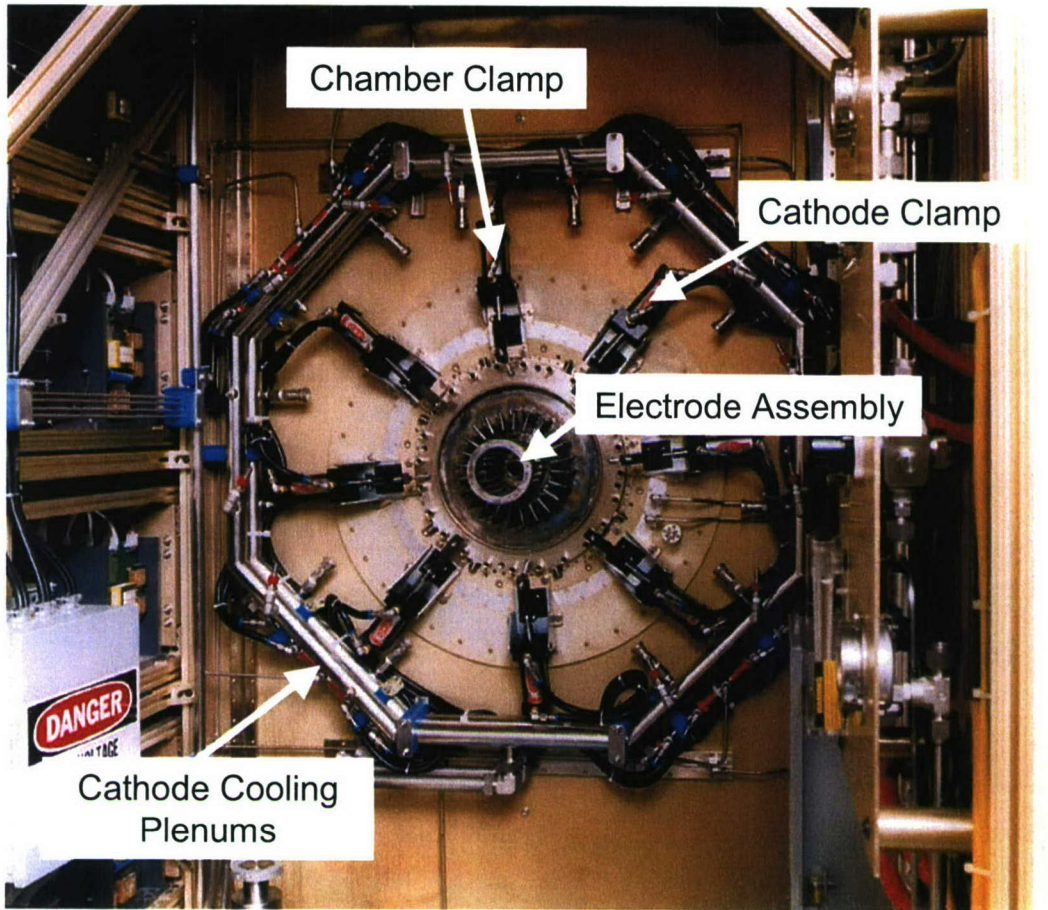


Fig. 22. View of the DPF head with the vacuum chamber removed.

15.0: Trouble Shooting

The designers of this machine were well aware that the time allowed for shakedown tests would not suffice to reveal all potential weak points. Consequently preparation for inevitable faults was built into the device. This included the safety and self protection features discussed above. In addition numerous steps were taken to ease the process of identifying the source of problems.

Data Logging

The data logging system monitors for, and records, any change in the roughly two hundred measured system parameters and control settings. The name of any item that has changed, the time of the change, the magnitude of the change, and a pointer to a comment file are stored for all changes exceeding an item specific threshold. The measured parameters have been shown to have a low noise content. Any time following an exposure, the user may easily select which of these parameters and settings he wishes to view, and they are graphically displayed. They may be reviewed on any time scale, down to a shot by shot basis. This capability has already proven to be a valuable trouble shooting tool.

Discharge Diagnostics

Because of speed limitations, the computer system is not used to analyze the discharge voltage or current traces. For the same reasons, these traces are not stored from shot to shot. Nonetheless, viewing of these waveforms can provide useful information to a trained service person. Consequently the basic diagnostic sensors for these measurements are built into the machine.

A new high voltage readout system was incorporated. The traditional bulky Tektronix HV probe would not fit in the confined space on the X-ray output side. Because of its non coaxial ground, such a probe would be a potential EMI source. The new system is compact and completely shielded. Voltage is measured by monitoring the current through a resistor between the anode base and ground mounted in a low inductance configuration. A Rowgowski loop is built into the ground circular plate to allow monitoring of the discharge current. Coaxial cables from each of these sensors are strung over to the control station where the computer monitor and keyboard reside. Any oscilloscope with a frequency capability of 100 MHz or greater may be employed to view these signals.

Operation and Service Manual

A comprehensive Operations and Service Manual was delivered with the system. This manual provides an overview of the system architecture, a description of the normal mode of operation, the "State Control Mode", along with the command structure employed for communications with the stepper. Detailed instructions are provided for operation in the "Manual Control Mode" which is available only under local (vs. remote) control. The Manual Control Mode allows low level control of subsystems. This is of use in tracking down system problems. Nine different control windows with an aggregate of hundreds of controls and indicators are available in this mode. The function of each of these controls and indicators is tabulated. All routine service operations are also presented in this manual, with step by step instructions.

16.0: System Tests

Methodology for Output Energy Measurement

There are a number of methods for measuring the x-ray output of the DPF. SRL has concentrated on the use of PIN diodes because, unlike the various photochemical methods, the results are not process dependent. A PIN diode operates in a manner similar to an ionization chamber. Within the intrinsic region, soft X-rays produce electron ion pairs with an energy cost of 3.62 eV per pair absorbed. This figure is independent of the X-ray photon energy. The intrinsic layer of the PIN diodes that are employed is substantially thicker than the absorption length of the highest energy photon, ≈ 18 eV, of interest.

A long vacuum beamline was used to determine if there were saturation losses in the pin diode detectors. The long beamline provided attenuation without altering the detected spectrum. The spectrum would change if foil attenuators were employed. Contrary to the claims of the pin diode manufacturer, saturation did lead to marked charge loss. This is probably due to recombination in the intrinsic layer. A second pin diode detector was employed on the chamber side of the pinch. This detector used a thicker Be foil, 12.5 micron vs 7.5 micron on the

beamline, in order to provide attenuation that would compensate for the shorter distance to the source. Good agreement between the two detectors was obtained.

Signals received from the PIN diodes are converted into energy at the source by taking into account the spectral absorption of all matter between the pinch and the active intrinsic region of the diode. To accomplish this, a bare source spectrum must be assumed. All interpretations of the output use the “hot” spectrum measured in Alameda. If the “cold” spectrum measured by C. Dozier on the solid state laboratory prototype DPF is substituted in the analysis, the inferred outputs are 14 % larger. This is because the “cold” spectrum suffers higher attenuation by the foil window and the gas.

17.0: Performance

In its present state, the source outputs up to 400 W of X-rays into a solid angle of 4π steradians. Fig. 23 presents the shot-by-shot output of a sequence of 3000 pulses taken at a rate of 60 Hz. It will be noted that in this run, there were no “drop outs”. A drop out is defined as a shot with an energy less than a value that is somewhat above the detection system noise level. Typically, the fraction of drop outs will be less than 1% over a run.

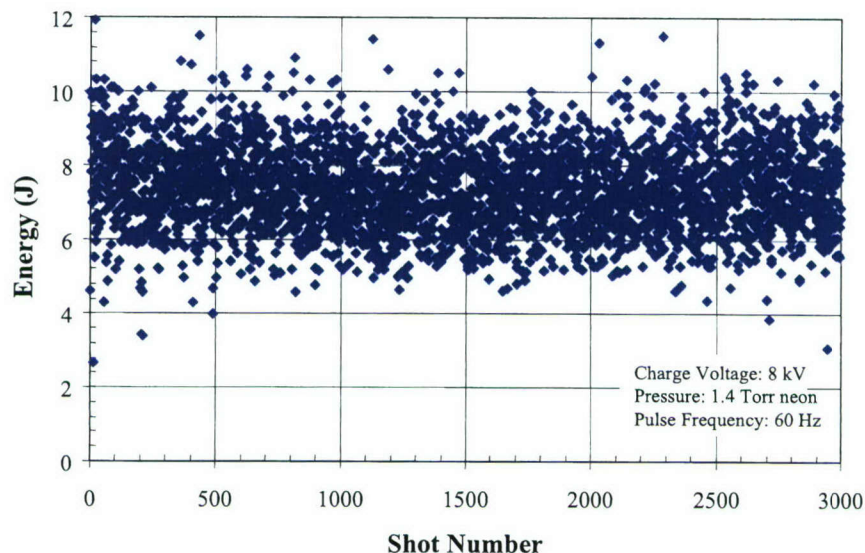


Fig. 23. X-ray pulse energy for a sequence of 3000 pulses fired at a rate of 60 Hz.

It was observed that the average pulse energy decreased markedly as the repetition rate was increased above 40 Hz. The gas flow was increased from 1.2 standard liters per min (slm) to 2.0 slm, but this had no effect on the decrease. It was also noted that at high repetition rates the first pulses had the same energy as at low repetition rate, but, after about a hundred pulses, the average energy had dropped to a lower level. This indicated a thermal issue. Either the gas or some portion of the electrodes was heating up. An increased gas temperature does not affect the feed rate of the gas, but it does increase the flow velocity at the pumping port. Consequently the

average gas density in the chamber is decreased. A partial solution to this problem was to monotonically increase the chamber pressure (prior to firing) with increase in input power. Chamber pressure is increased by throttling down the pumping port. The input power is proportional to the charge voltage squared times the repetition rate.

For each input power there is a pressure that maximizes the average pulse energy output. With the pressure so optimized, the pulse energy is initially low, because the gas density is too high. However, after roughly a hundred pulses, the density drops to the optimum level and the pulse energy increases to a value near that obtained at low input power. A gas control system could be implemented to yield optimum pulse output during the 100 pulse equilibrium time. However, given that an exposure runs to thousands of pulses, the gain in pulse output averaged over the exposure would be negligible.

Fig. 24 presents the average pulse energies achieved as a function of fill pressure (the chamber pressure before the system starts firing) for four different pulse repetition rates and three different charge voltage levels.

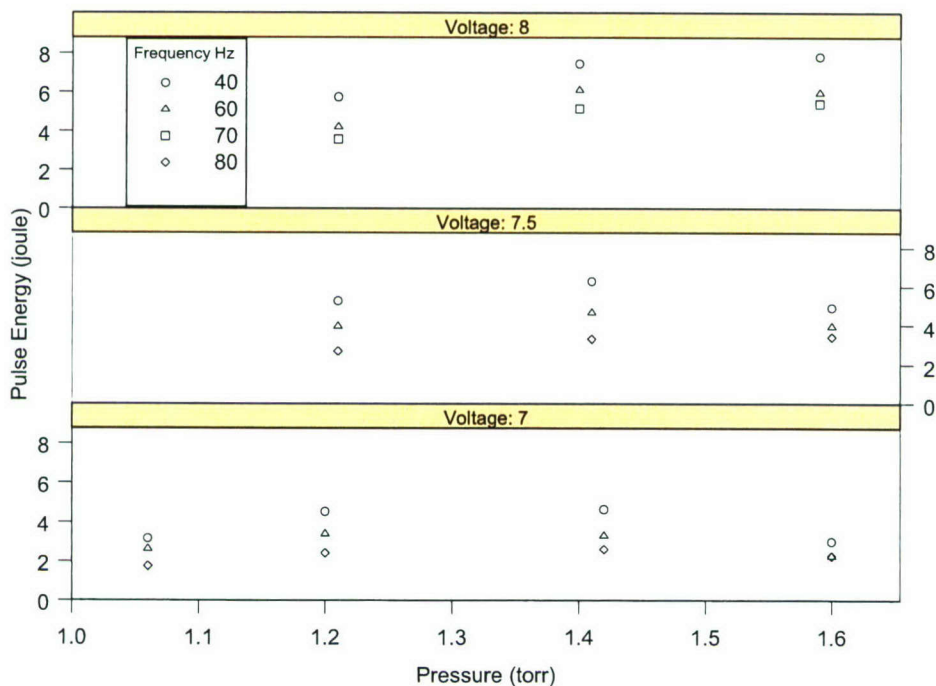


Fig. 24. Pulse energy as a function of pressure, taken at four different pulse repetition rates, and 3 different charge voltages.

Fig. 25 presents the average output power as a function of pressure taken at four different pulse repetition rates and three different charge voltages.

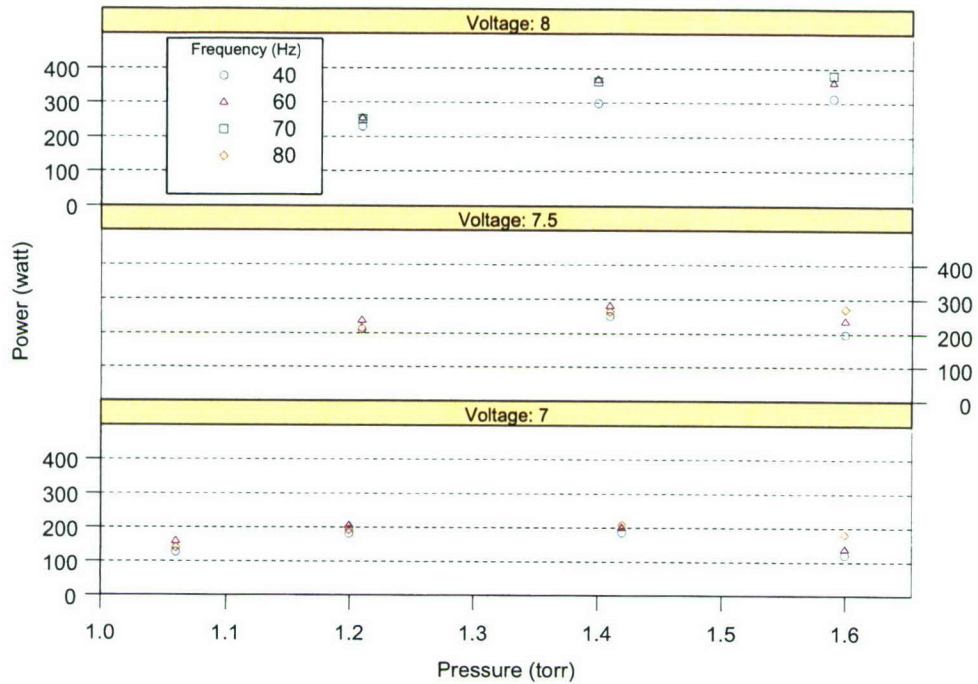


Fig. 25. Average output power as a function of chamber pressure taken at four different pulse repetition rates.

References

[1] C. Masonnier, F. Cipolla, C. Gourlan, M. Haegi, J.G. Linhart, A. Robouch, and M. Samuel *Plasma Phys. Contr. Nucl. Fusion Res. Proc. Conf., 3rd Novosibirsk, USSR, 1968* **2**. IAEA, Vienna, 1969.

Appendix B

**Point Source X-Ray Lithography Technology
IAW BAA 00-04**

**SAL Subcontract RP3067
In Accordance with
U.S. Government Contract N00019-01-C-0088**

Final Technical Progress Report

Prepared for
**BAE Systems
Nashua, New Hampshire**

Monday, 10 February 2003

SOW Task 3.1.3 Stepper Improvements (AWIS, Beamline & Composite Stage)

Task 1 AWIS (Adaptive Wavelength Illumination System):

The AWIS (Adaptive Wavelength Illumination System) is a very successful improvement and has exceeded our stated goals to improve contrast and fine align time by 3X and 4X respectively. Installation was completed during December 2001.

To date we have achieved almost 5X improvement in contrast and 10X improvement in fine align time due to the AWIS. One final avenue for improvement from the AWIS involves implementing the AWIS and associated ALX algorithms on 4 independently operating PC-104 computers. This allows alignment and AWIS operations to take place in parallel as opposed to the serial manner in which the BAE system is implemented. Recent work at JSAL with a PC-104 based AWIS system has shown that even better results can be obtained than those already recorded at BAE. On average, the PC-104 based AWIS enables another 3X reduction in alignment system operation times, with fine alignment accomplished in 4 seconds.

This task was completed in Dec 2002. There are further enhancements than can be made, but are beyond the scope of this task.

Task 2 Beamline Improvements:

This task included several activities to improve reliability and X-ray transmission in the stepper, as well as providing protection for the mask in the event of Beryllium window failures.

- For mask protection, the helium chamber has been redesigned to accommodate a large port, which holds a pressure relief membrane. In the event of a beryllium window failure, the low pressure pulse created deflects the pressure relief membrane against an adjustable blade which then punctures the membrane. Static tests of the pressure relief membrane have proven that the breaking pressure of the membranes is repeatable and controllable. The burst windows are cheap, easy to install, and currently have prevented the loss of masks for every Beryllium window failure since the burst window was installed, (~10 masks saved).
- A complete rework of the He seals design has resulted in significant improvement of their performance. We redesigned the seal to a double seal arrangement and results have been excellent. The new seals have been shown to maintain a He purity of at least 99.995% in a 500mm beamline with a transmission efficiency of 64%. Further the reliability of the new seals is from 6 to 10 times greater, reducing the required maintenance and replacement by a like amount. This is a significant improvement over the earlier designs.

During October 2002, JSAL completed all upgrades of the beamline systems, and implemented all proposed and planned improvements successfully.

Task 3 Composite Stage:

The granite butterfly is being replaced by an AlBemet 162 stage which is 30% lighter in weight, has a 2X improved static deflection ratio and a natural frequency resonance of 2X the granite stage.

The composite stage was contaminated with Beryllium dust upon arrival to JMAR/SAL. Wipe tests showed surface values of 21 μ grams per ft^2 , and it was decided that the stage would be cleaned and coated with Alodine to encapsulate the Beryllium away from any possible contact with assemblers or machine operators. The stage returned to JSAL, 5 November, 2002 with the Alodine coating. A subsequent wipe test was taken on 5 December as a formality, after which, test results indicated that there was still 7.4 μ gram per ft^2 of Beryllium on the surface of the stage.

It should be noted that the DOE recommends and exposure of no greater than 1.48 μ gram per ft^2 for the general public. It was concluded that the Alodine would not provide us with adequate protection, and that an alternative coating must be found. Electroless Nickel was identified as the best of the remaining coating candidates, and after testing to verify that coating process would not damage the Al_2O_3 ceramic bearing pads, the stage was sent out for plating. The plating for the stage was completed on January 13th and wipe tests were sent to Brush Wellman. On January 27th, Brush Wellman reported to us that the Beryllium levels on the stage were 10 times higher than initial test results and made agreed to ship the stage back to the Elmore Ohio facility for further tests and cleaning. At this point, the most likely scenario was that the plating facility had a dirty rinse bath and did not properly clean the stage.

Brush Wellman is making every effort to determine the cause and send the stage back to us. A new work slot was scheduled for mid-March. We then plan to fit and test the stage on the CNTech model 5C stepper in the JSAL cleanroom. The contamination problem must be solved before the stage is accepted and mounted on the 5C.

Task 4 Collimator Support:

Pending final installation and testing of the Xmetrics collimator, there is no further effort planned for this task. JSAL will support the testing of the collimator as required. No additional hardware changes have been requested or planned. This task is complete.

SOW Task 3.1.5 X-ray Mask Manufacturing Review and Assessment:

In June 2001 an X-ray Mask sizing study was commissioned through BAES by JSAL to determine the cost and extent of available x-ray mask making capability worldwide.

The events of 11 Sep 01 delayed a planned trip on 12 Sept to meet with potential mask suppliers and customers in Europe.

During Dec 2001, a trip was made to Europe and contacts with Asian masks shops concluded the following:

- While no clearly defined x-ray mask source exists in Europe, there exists reasonable mask capability in Japan.
- We should continue to explore and understand the capability that exists in Japan
- The final mask report, dated 30 Jan2002 was submitted during Feb 2002 as an attachment to the Monthly report. Additional copies are available, if needed.
- Given these findings, we will proceed with the IBM Mask Shop Plan to engage and fund them as a continuation of the current MCoC, DARPA funded effort. See comments below.

SOW Task 3.1.1 Mask Magnification Correction (UVM)

Year 1 – Develop mask stretching technology – Initially this will involve designing the micromechanical mask alteration system, which includes actuator geometry, placement and stiffening struts. Prototype systems will be built and demonstrated with in-house tooling. Different materials from the UVM Thin Films Laboratory will be tested and ranked and ranked according to their merit. Prior work from CNTech will be explored for applicability. Year one was awarded to UVM during March 2002.

Year 2 – Develop and select suitable metrology systems – This will involve a careful analysis of the capability of existing metrology systems and selecting and designing a system that is capable of providing real-time feedback about the position of precision points on both the wafer and mask. The system will utilize a multi-axis interferometer. The IBBI test bed developed by MIT will be considered as a possible candidate for at least one measurement axis.

Year 3 – Build and test a prototype system – A prototype system that includes the mask alteration mechanics, feedback metrology, and an adaptive control system will be built and tested on an available SAL stepper.

The activities at UVM during the month of January – February 2003 dealt with:

1. Understanding the aeroelastic mechanics of stepping a membrane mask at gap.
2. Designing and beginning the fabrication of a testbed for studying the mechanics of stepping at gap.
3. Refining and extending the computer simulations of mask stretching mechanics

1. Aeroelastic mechanics of stepping a membrane mask at gap.

The mechanics of membrane masks while stepping at gaps of 20 to 50 microns has not been studied extensively. A literature review and a preliminary analysis of the mechanics of stepping at gap were undertaken. The issues are whether aeroelastic effects can cause damage or excessive deflections and vibrations in the membrane mask. Aeroelastic effects occur when a structure is subjected to aerodynamic loads. The aerodynamic loads cause elastic deflections which deform the structure and alter the aerodynamic loads. This coupling or feedback of aerodynamic and elastic forces can cause instabilities, such as flutter or excessively large deflections. While there has not yet been much attention paid to aeroelastic effects of membrane masks other similar structures have been studied extensively. These include: thin prestressed plates that serve as the skins of airplanes and missiles and the deformations of elastic bearing elements in thin film lubrication. Studying the aeroelastic mechanics of membrane masks requires coupling models of the elastic deformations of the membrane masks with the fluid mechanics of the air (or helium) in the gap between the membrane mask and the wafer. The elastic mechanics of membrane masks can be calculated in a fairly straightforward manner, if the material properties and prestresses

in the mask are known. The fluid forces are a little less certain. If the fluid behaves as a viscous fluid, then the aerodynamic forces can be modeled using techniques from lubrication theory, including Reynolds' equation. However, if the gap is small enough, then the molecular nature of the fluid affects the fluid flow. A key parameter is the Knudsen number, which is a dimensionless parameter that relates the mean free path of the molecules to the critical dimension of the flow. Based on published values, it appears that if air is used in the gap, standard fluid mechanics applies. However, if helium is used, the no-slip boundary conditions break down. The result of this study is that a simple mathematical model of the membrane mask aeroelastic system has been setup for further calculations.

Another issue that has been raised in regard to stepping at gap is whether or not static electricity effects can cause the mask to suck into the wafer and make an unwanted contact. The combination of static electricity with the elastic deformation of the membrane is a similar situation to that of aeroelasticity in that the charges due to static buildup can cause the membrane to deform. As the membrane deforms, the electrical forces change. Since the forces vary as the inverse of the distance between the membrane and mask, if the membrane is attracted to the mask, an instability can occur where the membrane sucks into the wafer. It is not clear whether or not the forces due to the buildup of static charges are strong enough to cause collapse instability. Electrostatic actuators are common in MEMS devices. However, the gaps in MEMS actuators are usually on the order of a few microns, which is considerably smaller than the gaps between a mask and wafer.

2. Test rig for stepping at gap

An aeroelastic testbed has been designed and partially fabricated. This testbed will enable the measurement of aeroelastic effects while stepping at gap and serve as a testbed for various proposed aeroelastic countermeasure devices.

The basic concept is shown in [Figure 1](#) and [Figure 2](#).

The testbed replaces the wafer with a 640x400x70 mm³, 54 kg piece of granite with a precision flat surface. The granite floats on air bearings.

A photo of the testbed in an early stage of fabrication appears in [Figure 3](#).

At least three options are under consideration for the metrology system:

1. Use a laser to reflect off of the membrane mask. As the membrane deforms, the laser beam deflects. This is a simple system, but may not provide the detailed information that initially is needed.
2. Use a Michelson interferometer to measure the out of plane deflection of the mask. This is a well-established technique, and has been used previously at UVM for testing the deflection of membrane windows in bulge tester.
3. Use a Shearing interferometer. This technique has the potential for being simpler than a Michelson interferometer, but requires more investigation.

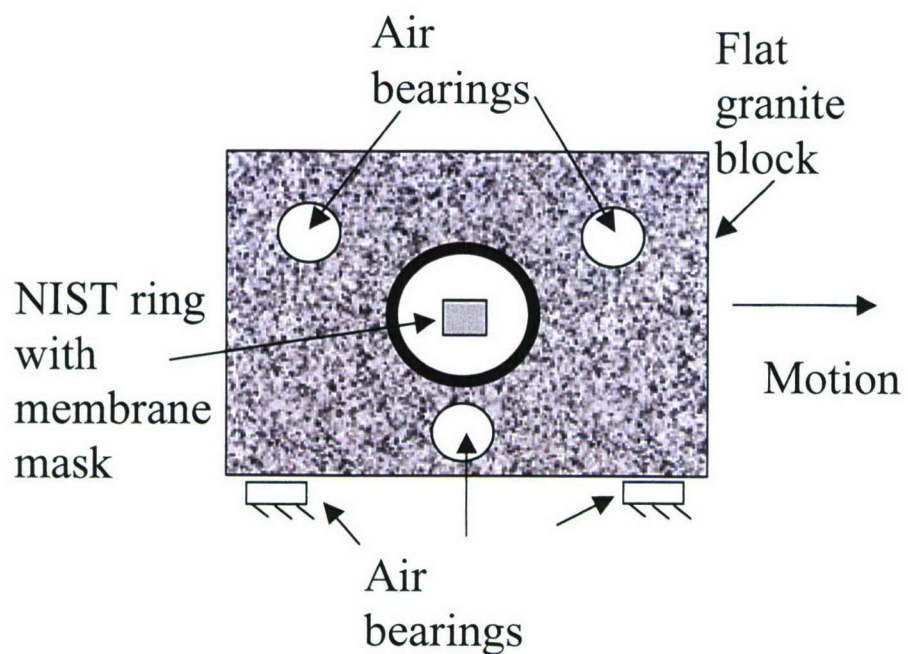


Figure 1 Side view schematic of aeroelastic stepping testbed

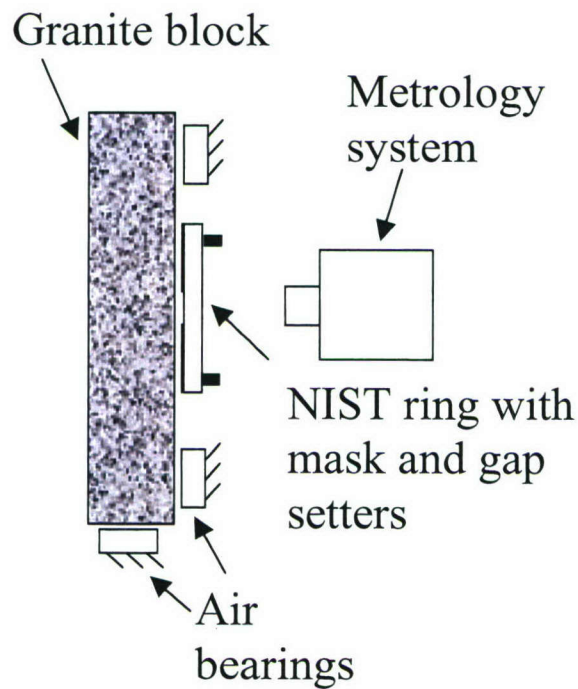


Figure 2 End view schematic of aeroelastic stepping testbed

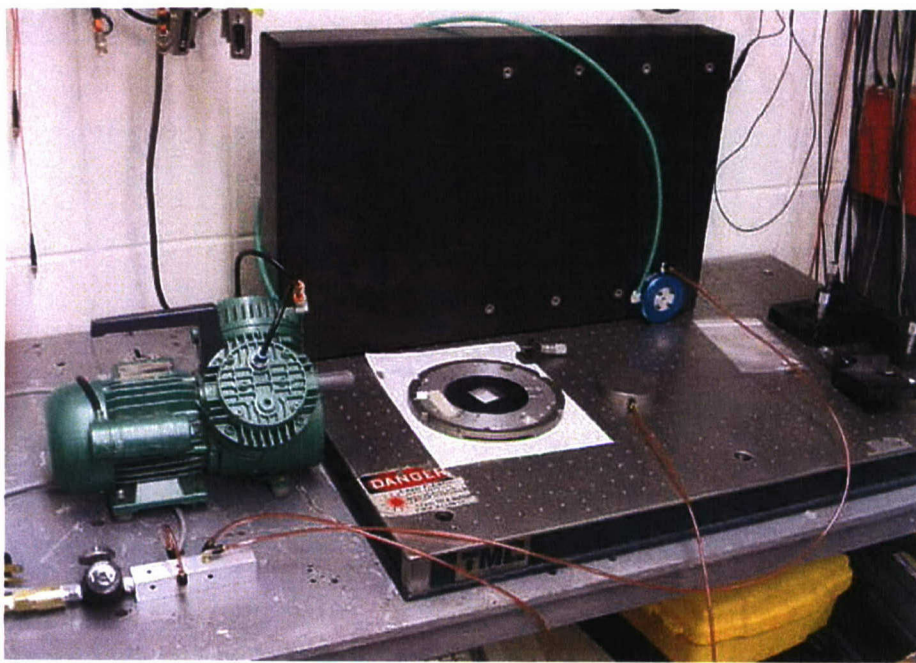


Figure 3 Aeroelastic testbed in early stage of fabrication

3. Refining and extending computer simulations of mask stretching mechanics

The various mask stretching computer simulations were extended and verified. Two software programs were used in this effort. SDRC Ideas was used to model the thermal mask stretching process. The Ideas software enables the modeling of the convective and conductive heat transfer from the fluid surrounding the mask as it is being heated. The previous simulations did not include this effect. Also included in these simulations was the use of gradient type heat fluxes, such as may be produced by a PowerPoint projector. Various cases have been considered, these include having the mask and wafer horizontal with a 10 micron gap in air (as may be used in the ALX testbed); the mask and wafer vertical with a 10 micron gap in air (as may be used in the Model 5); and the mask and wafer vertical with a 10 micron gap in helium. The results indicate that the system is sensitive to convection and conduction thermal effects. In addition to the Ideas computer simulations, Femlab simulations were also developed. Femlab is a relatively new finite element package that resides in the Matlab environment. Femlab has the most flexibility of the available finite element packages. It may prove to be useful in simulating nonlinear in-plane stiffening, feedback and aeroelastic effects.

Appendix C

Final Report, BAE/Shipley Subcontract
DARPA/BAE Systems Contract N00019-01-C-0088
Pramod Kandanarachchi, Scott Reeves, & Robert Brainard
June 16, 2003

Table of Contents

I.	Introduction.....	1
II.	ROBOMASC design and fabrication.....	2
III.	Materials screening.....	4
IV.	Resist characterization.....	13
	(A) Thermal flow.....	13
	(B) Wafer-to-mask gap & Resolution capability.....	21
	(C) PEB sensitivity.....	26
	(D) PED stability.....	28
	(E) Shelf life.....	30
V.	MMIC T-gate applications.....	32
VI.	Performance vs. Objectives.....	32
VII.	Conclusions.....	34
VIII.	References.....	35

I. Introduction

X-ray lithography has several apparent advantages over current optical lithographic technologies. The x-ray wavelength of about 1 nm may lead to resolution capability beyond that of optical lithographic methods. Also XRL has a much larger depth of focus (DOF > 5 μ m) than conventional optical lithography (DOF = 0.2-0.4 μ m).

Nonetheless, there are several challenges in x-ray development. These materials need improved sensitivity since most resists used in XRL are originally designed for deep ultraviolet (DUV) lithography and have a typical sensitivity range of 100-400 mJ/cm². Also XRL requires fabrication of 1X masks because it is a 1:1 technology. Therefore, image control, CD control, defect control, and stress control all pose significant challenges to the x-ray mask fabrication technology.

The goals for this program required advances in several areas, including: improved sensitivity, resolution and environmental stability as well as full MMIC T-gate process capability. Our chemical strategy was to pursue both high E_a (ESCAP) and low E_a polymer platforms in combination with a number of PAGs, bases, and solvents. Also a new binary mask was fabricated for cross-sectional SEM analysis to determine the image profiles of the resists. Modeling of aerial images was performed to determine the best mask-to-wafer gap and mask CD to reach the highest resolution, using the CNTech Toolset and tested using two photoresists.

Over the course of this two-year DARPA program, we developed chemically amplified resists for use in x-ray lithography (XRL). These resists were evaluated at both CNTech (U. Wisconsin) utilizing exposures from the synchrotron radiation source and BAE systems using point source x-ray lithography tool. Approximately 70-85 resist formulations were tested during fifteen experimental rounds. Several rounds of DUV (9) and e-beam (2) exposures were also done to support this study.

The resist development for this project was focused on six major areas:

- (1) Screening of resist components to identify top performing resists
- (2) Evaluation of the effects of mask-to-wafer gap for improved resolution
- (3) Post exposure bake temperature sensitivity (PEB)
- (4) Post exposure delay time sensitivity (PED)
- (5) Thermal flow study for MMIC T-gate process capability
- (6) Shelf life of top performing formulations

In this final report, we describe the screening of a large number of formulations to identify the top performing resists and the determination of resist performance parameters. Dr. Scott Reeves was primarily responsible for formulations, exposure and data analysis. Dr. Pramod Kandananarachchi took over Scott's responsibilities after he left Shipley in October 2003. Dr. Robert Brainard provided technical and managerial leadership.

II. ROBOMASC Design and Fabrication

In contrast to mask-to-wafer reduction ratio of 4:1 or 5:1 in optical lithography, XRL uses 1:1 proximity imaging. As a result, the fabrication of 1X masks with 50-70 nm resolution is a critical issue in XRL. We spent several months designing and fabricating a new binary mask called the ROBOMASC. This mask has a 2 μ m thick SiC membrane, 500 μ m thick TaSi₂ absorber, and 25 nm Cr etch stop. This mask was fabricated by IBM mask-fabrication workshop. The 5 mm long feature stack enabled us to do cross-sectional SEM analysis of imaged wafers. This pattern is also matched with an I-line mask so T-gates can be prepared. Figure 1 shows the layout of this mask.

Since it took several months to design and fabricate the ROBOMASC, most of our preliminary exposures were done through KONG02 mask (Rounds 2-6). The KONG02 mask had 2 μ m Si₃N₄ membrane and 350 nm Au absorber. The semi-dense trench features were only 1 mm long so cross-section SEMs were not possible. In addition, CNTech's phase shift and Res-5 masks were also used for imaging experiments.

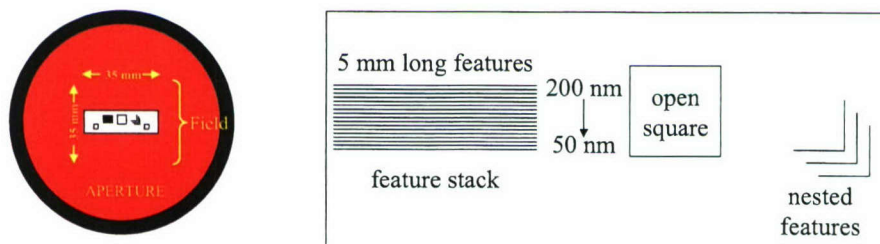


Figure 1a. ROBOMASC layout.

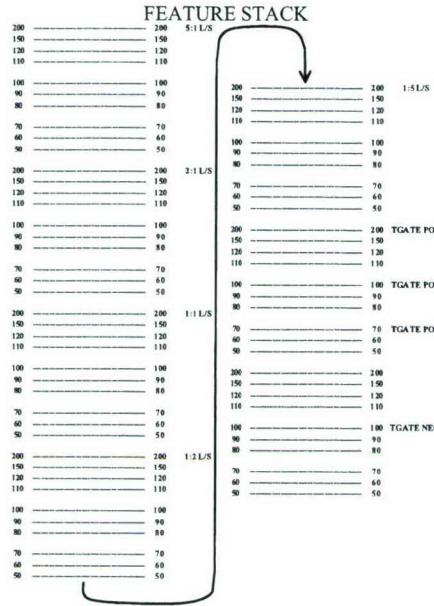


Figure 1b. Feature stack for cross-section.

Four copies of ROBOMASC (Copy A through D) were used during XRL rounds 10-14. The mask contrast together with absorbance and % transmittance data for the components of both ROBOMASC and KONG02 masks are listed in Table I. The contrasts of these x-ray masks are very low (3-4) with the ROBOMASC having the lowest contrast. The low contrast of these masks probably limits the resolution of x-ray lithography more than any other feature. The actual dimensions of the features were also determined and Figure 2 compares labeled and actual measurements of spaces. The plot for ROBOMASC is for isolated POS T-gate features and the plot for KONG02 mask is for semi-dense (2:1 L/S) features.

Table I. The absorbance/transmittance and contrast data for ROBOMASC & KONG02 masks.

Wave length(λ)nm	% T	A	% T	A	% T	A	Contrast
ROBOMSC							
	SiC		Cr		TaSi2		
0.8	0.712	0.147	0.957	0.019	0.425	0.371	3.2
0.9	0.625	0.204	0.942	0.026	0.330	0.481	3.1
1.1	0.443	0.354	0.907	0.043	0.183	0.738	2.9
KONG02							
	Si3N4		Au				
0.8	0.625	0.204			0.258	0.588	3.9
0.9	0.521	0.283			0.166	0.781	3.8
1.1	0.324	0.490			0.060	1.222	3.5

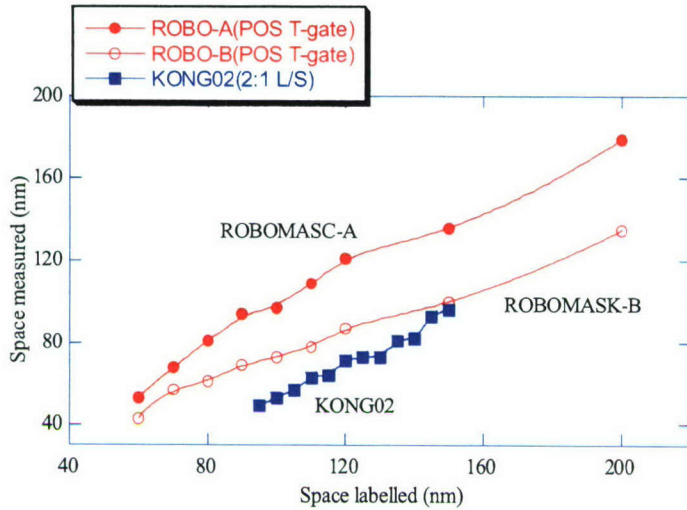


Figure 2. The comparison of labeled and measured space widths for POS T-gate features for ROBOMASK copies A & B and semi-dense (2:1 L/S) features for KONG02 mask.

III. Materials screening

Over the course of this 24-month study we have tested 70-85 formulations using x-ray, DUV and e-beam exposures at CNTech, BAE and Shipley. The following is an overview of the objectives and resist design as well as the outcome of different experimental rounds. The final benchmark resists were chosen based on these experiments for further characterization.

BAE Rounds 1 & 4. Four resists were selected to establish base-line performance of BAE's SAL stepper. Resists were UVIII, UVIIHS, UV6, and XP9947W. These resists were coated to 120 nm films over P210 thin films on GaAs wafers. Our original plan was to determine E_o with 50 kV e-beam exposures and use the e-beam E_o 's to make an estimate of x-ray E_{size} . The e-beam E_o 's would have allowed us to efficiently estimate what exposure energies to target the x-ray imaging of many new samples. Unfortunately, neither the e-beam nor x-ray imaging experiments could be completed because of various equipment issues.

CNTech Rounds 2 & 3. A set of 16 resist-formulations was designed for Round 2 experiments. Resists included the four resists from BAE Round 1 (UVIIHS, UVIII, UV6, and XP9947) as well as a DOE with an additional 12 resists that explored base loading, PAG loading, and PAG identity using the UVIII polymer. The DOE of fourteen resists that had the same polymer as in UVII is given in Table II. In this DOE the resist 2C is UVIIHS and the resist 2D is UVIII. The XP9947-W and UV6 are not included in this table because they had different polymers. The UV6 contained PAG 1 and XP9947-W had PAG 2. KONG02 mask in MOD-2 stepper was used in this run.

Table II. The DOE for BAE Rounds 2 and 3.

Base 1	PAG 1			PAG 2		
	Low	Medium	High	Low	Medium	High
V. Low	2A					
Low	2B					
Medium	2C	2E	2G	2I	2K	2M
High	2D	2F	2H	2J	2L	2N

Based on the performance of reference formulations using KONG02 mask in MOD-2 stepper, the XP9947-W formulation that had the best contrast ($\gamma = 12$) was identified as a potential benchmark (Table III). Also a preliminary post exposure delay stability (PED) and post exposure bake sensitivity (PEB) study of XP9947-W gave 8 nm/h and 5 nm/ $^{\circ}$ C sensitivities respectively. The determination of these properties will be discussed in detail in another section.

Table III. The performance of baseline resists.

Resist type	CNTech (XRL) E_0^* (mJ/cm ²)	% of UVIII	γ
XP9947-W	475	62	12
UV6	880	114	2.0
UVIIHS	580	75	2.0
UVIII	770	100	3.0

*Exposure to mask

We also learned from the formulation variations that:

- Decreasing base improves sensitivity, but decreases image quality
- Increasing PAG improves sensitivity, but decreases image quality
- Switching from the UVIII PAG to the XP9947 PAG improves both sensitivity and image quality

Five different terpolymers were also tested at Round 3 with the same PAG and base as in XP9947. We identified three polymers that were faster than the polymer used in XP9947-W formulation.

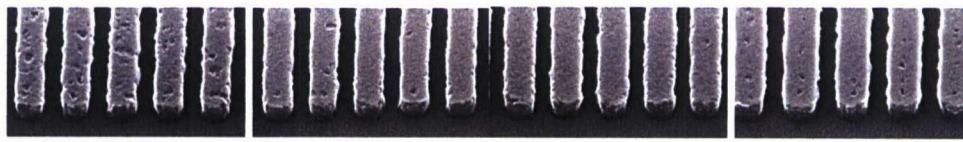
CNTech Round 5. This round consisted of 12 resist formulations lithographically evaluated on the MOD-2 stepper using KONG02 mask. Resists fit into three designs:

- UVIII Control
- Five resists in a 2x3 DOE that explored base loading and PAG loading in the XP9947-W polymer. XP9947-A, S and W were tested along with two other resists with higher PAG loading (XP1449-A, XP1449-B)
- Eight resists in a 2x4 DOE (two repeat formulations) that explored the use of four acrylate polymers with high PAG loading and against two different base loadings.

Table IV shows the results of 2x3 DOE in which 16-35% improvement in resist sensitivity over UVIII is achieved. Decreasing base caused an increase in “pitting” in the resist lines, possibly as a result of decreasing resist contrast. The increased level of PAG also appears to inhibit “pitting” without affecting resolution (Figure 3).

Table IV. PAG & base study at CNTech Round 5.

Resist	XP#	PAG	Base	E_0 to wafer (mJ/cm ²)	$E_{150/200}$ (mJ/cm ²)	$E_{150/200}/E_0$
5A	UVIII	-	-	175	ca. (280)	
5B	XP9947-A	Med	Low	36	65	1.8
5C	XP9947-S	Med	Med	58	100	1.7
5D	XP9947-W	Med	High	113	114	1.0
5E	XP1449-A	High	Low	29	44	1.5
5F	XP1449-B	High	Med	43	66	1.5



(B) XP9947-A (C) XP9947-S (D) XP9947-W (E) XP1449-A
 109 nm 110 nm 97 nm 112 nm
 69 mJ/cm² 106 mJ/cm² 131 mJ/cm² 51 mJ/cm²

Figure 3. SEMs for features from 120 nm mask space.

Acrylate terpolymers with different compositions were used with varying base loading to study the resist speed. This resulted in sensitivities that are 16-27% of UVIII, but did not establish any correlation between the polymer composition and speed. However the polymer containing the highest level of polystyrene (Highest Ohnishi number, 2.52) had the best sensitivity.

CNTech Round 6. This round compared E_0 values of sixteen resists along with XP9947-W as a control. The formulations fitted into three designs.

- XP9947-W as a control
- Ten resists in a 2x5 DOE that explored four new resist additives in two different resist formulations (EUV-2D as resist 6A and EUV-12Aas resist 6F in Table V)
- Eight resists in a 2x4 DOE (two repeat formulations) explored the use of new PAGs in a mixed PAG formulation (Table VI)

The formulation DOEs as well as clearing doses are given in Tables V and VI. Eleven resists in this round surpassed the target sensitivity (40% of UVIII) by a factor of 2-5 times. These results clearly showed that we have discovered Polymers, PAGs, PAG combinations, sensitizers, and bases that can lead to the formulation of highly sensitive x-ray resists. Our focus at this stage was changed to meet resolution and other lithographic properties.¹

Table V. DOE of Round 6 exploring additives and PAGs (The E_o values for corresponding formulations are given in the right hand side of the table).

Additive	PAG		E_o (mJ/cm ²)	
	1	1+3		
None	6A	6F	160	55
1	6B	6G	160	55
2	6C	6H	190	70
3	6D	6I	>400	160
4	6E	6J	85	<30

Table VI. DOE of Round 6 exploring PAG combinations (The E_o values for corresponding formulations are given in the right hand side of the table).

PAG	PAG		E_o (mJ/cm ²)	
	1	2		
None	6A	6K	160	100
3	6F	6L	55	70
4	6M	6O	55	70
5	6N	6P	30	50

CNTech Rounds 7 & 8. We designed fifteen resists along with XP9947-W in two DOEs to test at CNTech Rounds 7 and 8. The first DOE explored the use of four polymers synthesized with a range of molecular weights (M_w = 5K, 10K, 17K & 30K). A commercially available 10K M_w polymer was also included. The second DOE consisted of a PAG-Base study testing various amounts of PAG and base with 10K commercial polymer. These resists were intended to study the effect of M_w and PAG concentration on sensitivity and resolution. Since KONG02 mask was no longer available, CNTec's phase-shift mask was used, but the exposure process for this mask needed some improvements. This phase-shift mask did not meet our needs for resist screening. Attempts were made unsuccessfully to use a new device mask (DMA-144) on MOD-4 stepper.

BAE Round 9. ROBOMASK-A was used in MOD-5 stepper successfully to image our benchmark resist, XP9947-W, and first cross-section SEMs obtained.

CNTech Rounds 10 & 11. ROBOMASC-B was used in MOD-4 stepper. The objectives of this run were:

- Evaluate XP9947-W (Resist 10A) and XP1449-L (Resist 10B) with the binary mask, ROBOMASC
- Screen ten resists in 3 DOEs for base (ionic vs. non-ionic), a new additive and polymer variations (Table VII)
- Explore depth of focus at x-ray by imaging resists formulated at 150, 500 and 750 nm film thickness
- Explore mask-to-wafer gap on resolution
- Evaluate PED sensitivity of selected resists

Table VII. The resist design (DOE) for CNTec Rounds 10 & 11.

Base	PAG		Additive			Plymer	
	1	2	Low	Medium	High	2	3
High Ionic	10B						
Low non- ionic	10C	10F					
Med. Non- ionic	10D	10G	10H	10I	10J	10K	10L
High non- ionic	10E						

Resists 10B-10J had the same polymer as in XP1449-L

Resists 10H-10J had PAG 2 and 10K-10L had PAG 1

On the Mod-4 stepper, the E_{size} doses for 135 nm isolated trenches (Pos. T-Gate) for our two leading resists, XP9947-W and XP1449-L, were compared. Figure 4 shows the exposure latitudes of 135 nm and 100 nm isolated trenches for XP9947-W and XP1449-L. These cross-section images are the first detailed images that show the resist profiles. In general, XP9947-W demonstrated square profiles while XP1449-L exhibited reentrant profiles where single wafer exposures typically take between 30 and 60 minutes to complete. This suggests that the resists may have delay stability problems in the x-ray clean room environment. For XP9947-W the E_{size} was calculated to be 190 mJ/cm² (to the wafer) while for XP1449-L, the E_{size} was 150 mJ/cm². This suggests that XP1449-L has a sensitivity that is approximately 80% of XP9947-W. The resolution capabilities of these resists will be discussed in section IVB.

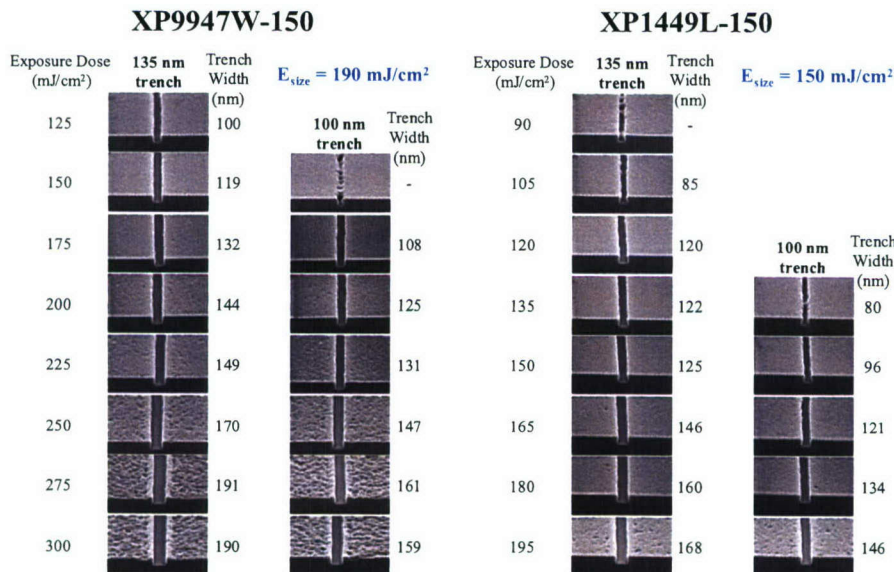


Figure 4. Exposure latitude for XP9947-W-150 isolated trenches (Pos. T-Gate) and exposure latitude for XP1449-L-150 isolated trenches (Pos. T-Gate).

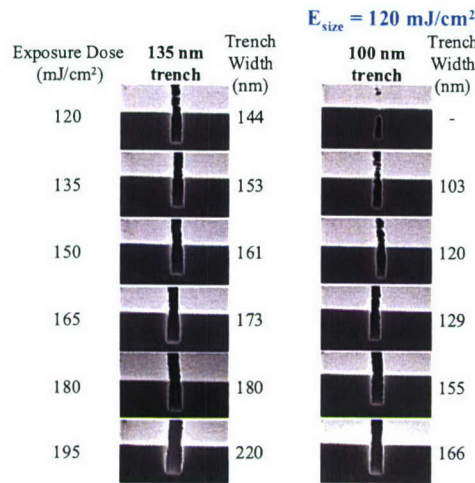


Figure 5. Exposure latitude for XP1449-L-500 isolated trenches (Pos. T-Gate).

The exposure latitude of 135 nm and 100 nm isolated trenches for XP1449-L-500, a 500 nm thick version of XP1449-L, was also examined (Figure 5). This thicker version of XP1449-L was tested to explore the large depth of focus (DOF) in proximity x-ray lithography. The E_{size} of 120 mJ/cm² for XP1449-L-500, which is 20% lower than the 150 nm thick version, suggests that film thickness may play a unique role in sensitivity. Previous screening experiments in DUV indicated that thicker films require higher exposure doses to reach sizing.

Stepper Sensitivity Differences. XP9947-W was imaged on the Mod 4 stepper. XP9947-W had an E_o to the mask of 250 mJ/cm² on the Mod 4 stepper (25 μ m gap). On the Mod 2 stepper, an E_o through a similar SiC mask membrane was 230 mJ/cm². This suggests a sensitivity difference of 9% greater on the Mod 4 stepper compared to Mod 2 stepper. Dan Malueg also had run an E_o sensitivity study that showed a 15% slower sensitivity for XP9947-W on the Mod 4 stepper versus the Mod 2 stepper. Comparing these values to a value of 60 mJ/cm² on the Mod 5 stepper indicates significantly higher sensitivity at longer wavelengths. The stepper wavelengths are \sim 9 \AA on the Mod 2, between 7 and 8 \AA on the Mod 4, and \sim 11 \AA on the Mod 5. The sensitivity for XP9947-W on the Mod 5 stepper is 26% of the exposure dose on the Mod 2 stepper or 24% of the dose on the Mod 4 stepper, which is approximately 4 times faster than either stepper at CNTech.

The clearing doses (E_o), sizing energies for 135 nm isolated trenches (POS T-gate), and exposure latitudes (% EL) for Rounds 10 & 11 formulations are given in Table VIII (dose to wafer). It should be noted that the sensitivities of resists change from run-to-run as well as from stepper-to-stepper, so the speed comparisons with UVIII are only approximations. However the relative sensitivities of different formulations were mostly unchanged.

The mask-to-wafer gap and PED sensitivity were also studied in Round 12. The results of those experiments will be given in separate sections (IVB and IVD).

Table VIII. Sensitivity and Exposure Latitude (%EL) data for Rounds 10 & 11 resists.

Resist	XP#	E_o (mJ/cm ²)	E_{size} (136nm,iso) (mJ/cm ²)	Esize % of UVIII*	% EL
10A	XP9947-W	125	190	57	27
10B	XP1449-L	105	153	46	20
10C	XP0608-A	50	56	17	36
10D	XP0608-B	50	66	20	29
10E	XP0608-C	65	80	24	32
10F	XP1271-A	<65	61	18	21
10G	XP1271-O	50	53	16	31
10H	XP-0609-A	63	69	21	30
10I	XP-0609-B	63	67	20	30
10J	XP-0609-C	42	63	19	
10K	XP0607-A	>200			
10L	XP0610-A	88	94	28	38

* The Esize of UVIII was taken as 333 mJ/cm²

CNTech Round 12. Numerous equipment problems prevented us from getting our desired exposures this round.

CNTech Round 13. Two polymer platforms in combination with three levels of base loadings in a 3x2 array were studied. A Low E_a /High E_a polymer blend was used in order to achieve improved sensitivity, PEB and PED stability. The XP9947-W formulation also was run as a reference in addition to high PAG formulation (XP1751-D). Unfortunately our third copy of ROBOMASK was also broken during this run. Nonetheless, Res-5 mask with its 100 nm top-down features was available to complete PEB, PED behavior of four of the resists at a gap of 25 μ m. Those experiments will be discussed in separate sections, IVC and IVD. Table IX gives data obtained for ROBOMASK-C. These data show that all of the resists are quite a bit faster than the XP9947-W control.

Figures 6A and 6B show the Trench CD (138 nm iso) vs. dose plots that were used to calculate % EL values. Both polymer platforms had excellent exposure latitudes.

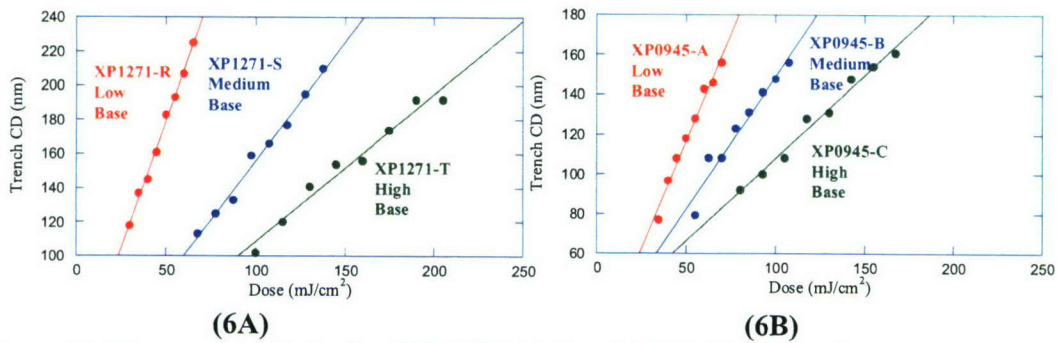


Figure 6. The exposure latitude of XP1271 (6A) and XP0945 (6B) series.

Table IX. XRL-13 polymer-base loading study.

Resist	XP #	Polymer Type	Base	E_o (mJ/cm ²)	$E_{size}(138nm)$ Pos T-gate	$E_{size}(138nm)^*$ % of UVIII	%EL
13A	XP9947-W	High E _a	high	125	178	53	28
13B	XP1751-D	High E _a	low	50			
13C	XP1271-R	High E _a	low	45	37	11	25
13D	XP1271-S	High E _a	medium	65	87	26	22
13E	XP1271-T	High E _a	high	100	134	40	23
13F	XP0945-A	High E _a /Low E _a Blends	low	35	60	18	21
13G	XP0945-B	High E _a /Low E _a Blends	medium	<55	92	28	23
13H	XP0945-C	High E _a /Low E _a Blends	high	80	136	41	24

* The Esize of UVIII was taken as 333 mJ/cm²

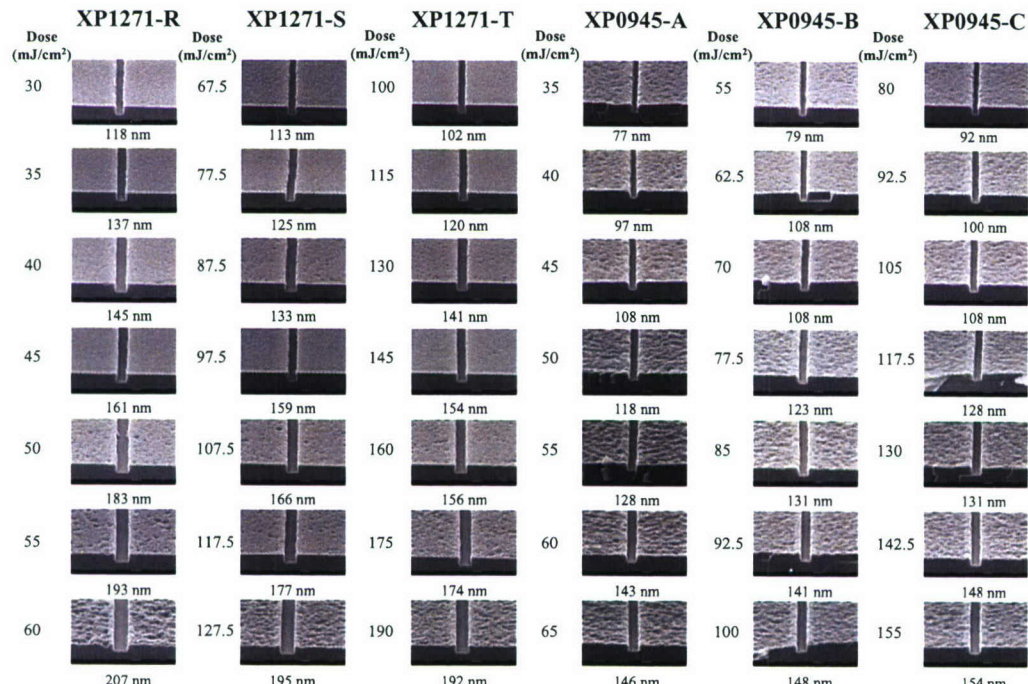


Figure 7. Image profiles of XRL-13 resists.

The XP0945 series had pitted surface even at lower doses (Figure 7). The pitted surface is thought to have arisen from absorption through the opaque region due to low contrast of the mask. This effect may not be obvious with high E_a polymer formulations since small amounts of acid generated in the dark region would be neutralized by environmental amines before PEB step. However the low E_a polymers can de-block at

room temperature in the stepper chamber thereby enhancing this effect. A two-month room temperature shelf-life study was also done for Round 13 resists (Section IVE).

BAE Round 15. This round was planned to measure PED stability of our benchmark resist, XP9947-W in BAE MOD-5 stepper chamber. Since PED stability is very much dependant on the environment, the program goal was set for more than two hours stability where mean amine concentration is less than 5 ppb. This experiment could not be completed so we have to rely on extrapolations from data obtained at CNTech that is not an amine-filtered environment.

CNTech Round 14. Four benchmark resists were chosen for final resist performance parameter determination (XP9947-W, XP1449-L, XP1271-S, and XP0945-B). They were selected based on the results obtained from previous CNTech and BAE experiments as well as DUV studies. The PEB, PED stability, thermal flow properties, mask-to-wafer gap & resolution, and 4.5-month refrigerated shelf life were evaluated for these formulations.

In addition to these x-ray rounds, DUV screening work, especially thermal flow study, polymer synthesis, and dissolution rate studies also contributed immensely to the development of resists in this program. A bulk of DUV study dealt with pre-screening of resists before x-ray exposure that allowed us to develop correlations between them. The results of DUV thermal flow experiments will be presented in Section IVA.

Polymer synthesis. Terpolymers with different average molecular weights were obtained by varying the amount of AIBN in free radical polymerization. The effects of polymer molecular weight on the unexposed film thickness loss (UFTL) of resists were studied. Since the UFTL is a measure of an inhibition of a resist, it is an important property that must be modified for each resist application. This study showed that the UFTL (Å) of resists could be controlled by increasing either PAG loading or terpolymer molecular weight.

We also made three homopolymers using living free radical polymerization (LFR) chemistry. Polymerizations were carried out without solvent at ~123 °C for ~22 hours yielding homopolymers with molecular weights and poly-dispersities of: 13.8 K, 1.3; 8.2 K, 1.5; and 14.4 K; 2.3. The low poly-dispersity of the first two polymers indicated good LFR control. The high dispersity of the third polymer is characteristic of a conventional free radical reaction. We were not too concerned about the high dispersity as the terpolymer results listed below are pretty promising.

We also carried out LFR polymerizations to make terpolymers. The reaction was carried out without solvent at ~123 °C for 18 hours and followed as a function of time. Table X shows the molecular weight, and poly-dispersity over time. Clearly, we are obtaining low dispersity terpolymers by this method.

Table X. LER polymerization of a terpolymer as a function of time.

Reaction time (h)	Mw	PD (Mw/Mn)
2	3856	1.2
4	5798	1.23
8	9829	1.32
16	13605	1.43

Dissolution rate (DR) study. Small molecule (non-polymeric) additives were studied to determine their effect in x-ray resists with the expectation that they will affect resist performance such as profile, LER, sensitivity, contrast, and thermal flow. The effects of the blocking level, PAG, a new additive, and *tert*-butyl phenol on DR (Å/sec) of polyhydroxy phenol (PHS) copolymers were tested. Dissolution inhibiting effect for increasing blocking level, PAG and HEPS-BCOA additive loading was observed. As expected the addition of *tert*-butyl phenol increased the DR of PHS co-polymers.

IV. Resist Characterization

The benchmark resists were further characterized for resist performance parameters. Four top-performing resists (XP9947-W, XP1449-L, XP1271-S, XP0945-B) were selected for this purpose. These resists consisted of two polymer platforms (High E_a & High E_a/Low E_a blend), two PAG systems, two bases, and two solvents (Ethyl Lactate (EL) and Propylene Glycol Monomethyl Ether Acetate (PMA)). Their formulation DOE is given in Table XI.

Table XI. The formulation DOE for top performing resists.

Polymer platform	PAG A Base A EL	PAG B Base A EL	PAG B Base B PMA
High E _a	XP9947-W	XP1449-L	XP1271-S
High E _a /Low E _a Blend			XP0945-B

IVA. Thermal flow experiments

The controlled thermal flow (TF) was employed to image positive T-gate trenches for MMIC applications. The target image profiles are shown in Figure 8. Since 6" wafers require a longer throwing distance for CVD than 3" wafers, a greater sloped sidewall is required for 6" wafers. We performed the bulk of thermal flow experiments by DUV exposure because a suitable x-ray mask was not available for a considerable period of time (for cross-sectionable features). In a typical experiment, resists were made to XP1449 type formulations, coated, imaged and processed using standard conditions: SB at 130°C/60sec, PEB at 130°C/90sec, develop in MF-26A/45sec. Then the wafers were hard-baked (HB) at a given temperature and time. The hard bake temperatures were chosen based on the T_g values of polymers measured by DSC and TGA. The x-ray experiments were performed for a number of different formulations using the process conditions determined by DUV study.

The DUV experiments tested several hard-bake/thermal flow parameters;

- (1) Molecular weight (M_w)
- (2) Feature size and film thickness
- (3) Hard-bake time and feature type (isolated vs. dense)

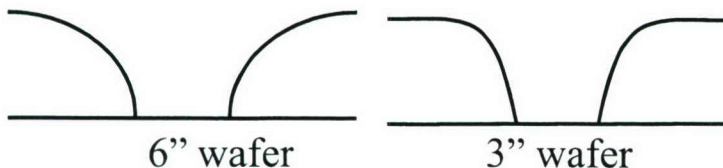


Figure 8. Ideal trench profiles for MMIC T-gate applications.

Molecular weight (M_w) of terpolymers. Four terpolymers with average molecular weights of 5K, 10K, 17K, and 30K were synthesized by varying the amount of AIBN initiator used in the polymerization reaction (Table XII). A commercially available 10K polymer was also included in this study. The molecular weight of a polymer is expected to have a direct effect on the thermal flow properties of the resists because of the changes in T_g . Since the UFTL of the resists were depended on not only M_w but the PAG loading also, a uniform UFTL could be achieved by varying the PAG amount. Standard processing conditions were used followed by 60-second hard-bake to induce thermal flow.

According to the Table XII, the thermal flow ($\text{nm}^{\circ}\text{C}$) decreased when the molecular weight of the polymer is increased provided the T_g is remained constant. Figures 9 and 10 show the sidewall angles and image profiles for the various resists at increasing hard bake temperatures. In this experiment, thermal flow reduced trench widths by as much as 100 nm. The sidewall incident angles are inversely proportional to hard bake temperature and are also dependent on the terpolymer molecular weight (Figure 9). Additionally, the profile shoulders become rounded when the hard bakes produce sidewall angles at or below 50°. The target profile in our original statement of work is rounded shoulders with sidewall angles of <85°. Presumably other processing conditions such as soft bake and PEB will also influence the thermal flow characteristics.

Table XII. Polymers with varying molecular weights for thermal flow experiments.

Resist	XP #	M_w	T_g (°C)	Temp. Range (°C) ²	Thermal Flow (nm [°] C)
A ¹	XP1449-L	10K	179	160-172°C	7.2
B	XP1449-M	5K	164	144-152°C	2.2
C	XP1449-N	10K	180	160-172°C	6
D	XP1449-O	17K	180	160-172°C	3.1
E	XP1449-P	30K	181	160-172°C	1.9

1. A commercial polymer

2. Temp. increased in 4°C increments

Feature size and Film thickness. For the 200 nm nominal trench features, the profiles start to close up after the hard baking process (Figure 11). Perhaps changes in thermal flow (TF) conditions may result in target profiles for higher resolution features.

Film thickness and processing conditions were also altered to determine their effect on resist TF. Hard bake (HB) processing was conducted at 160 and 168 °C for 60 sec. The sidewall incident angles and trench widths of isolated trenches were measured for 100, 150 and 300 nm thick films of the resist XP1449-L (Tables XIII). SEM images for 200 nm features are shown in Figure 12. The sidewall incident angle and thermal

flow rate (nm/ $^{\circ}$ C) were proportional to film thickness. The PEB temperature does not seem to affect sidewall angle or thermal flow.

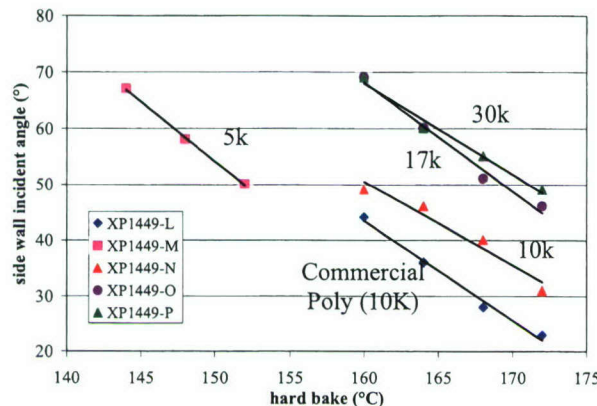


Figure 9. Incident sidewall angles vs. hard-bake temperature for five polymers.

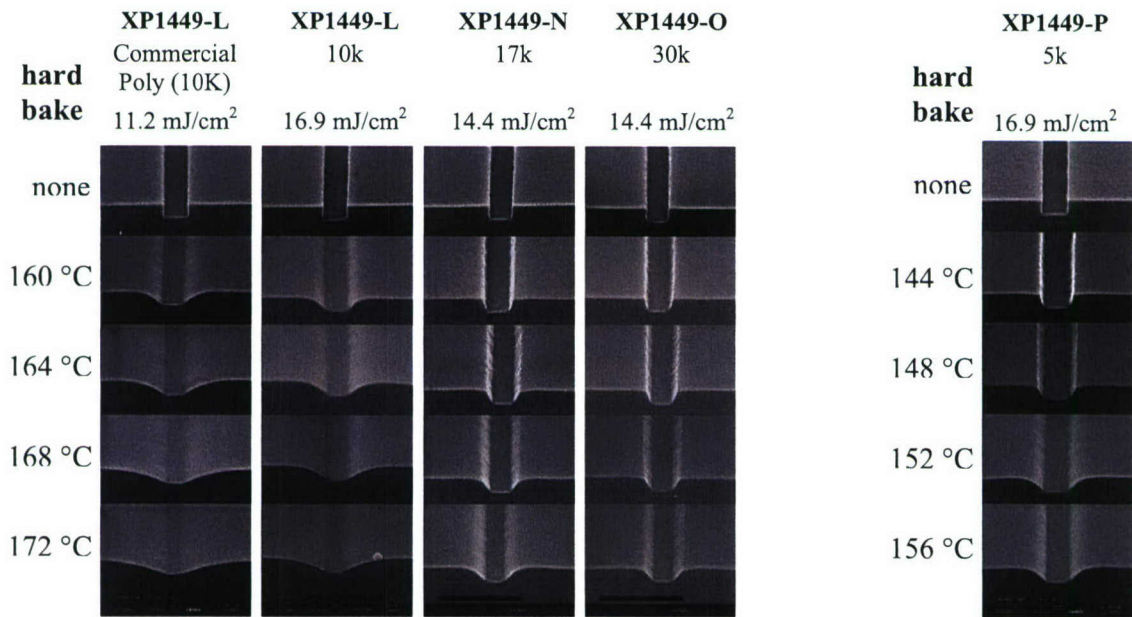


Figure 10. Thermal flow properties for 250 nm trenches for resists containing terpolymers with a range of molecular weights.

Table XIII. The effects of film thickness and PEB temperature for XP1449-L.

Film Thickness (nm)	PEB ($^{\circ}$ C)	Sidewall angle			Thermal Flow (nm/ $^{\circ}$ C)
		none	160 $^{\circ}$ C	168 $^{\circ}$ C	
100	130 $^{\circ}$ C/90s	90 $^{\circ}$	42 $^{\circ}$	24 $^{\circ}$	5.8
150	130 $^{\circ}$ C/90s	90 $^{\circ}$	45 $^{\circ}$	28 $^{\circ}$	7.2
150	140 $^{\circ}$ C/90s	90 $^{\circ}$	46 $^{\circ}$	29 $^{\circ}$	7.4
300	130 $^{\circ}$ C/90s	90 $^{\circ}$	53 $^{\circ}$	32 $^{\circ}$	10.6

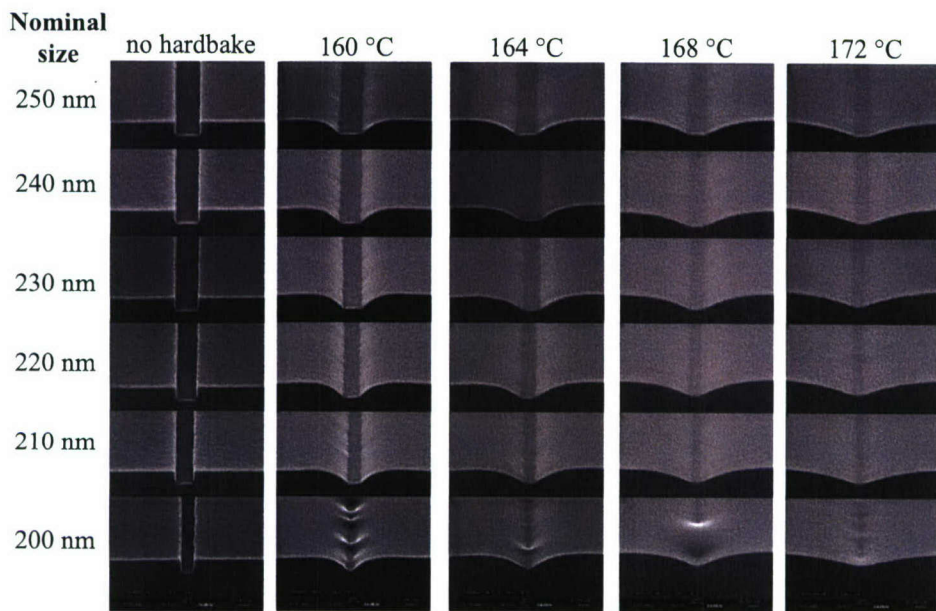


Figure 11. Thermal flow profiles as a function of trench size for XP1449-L.

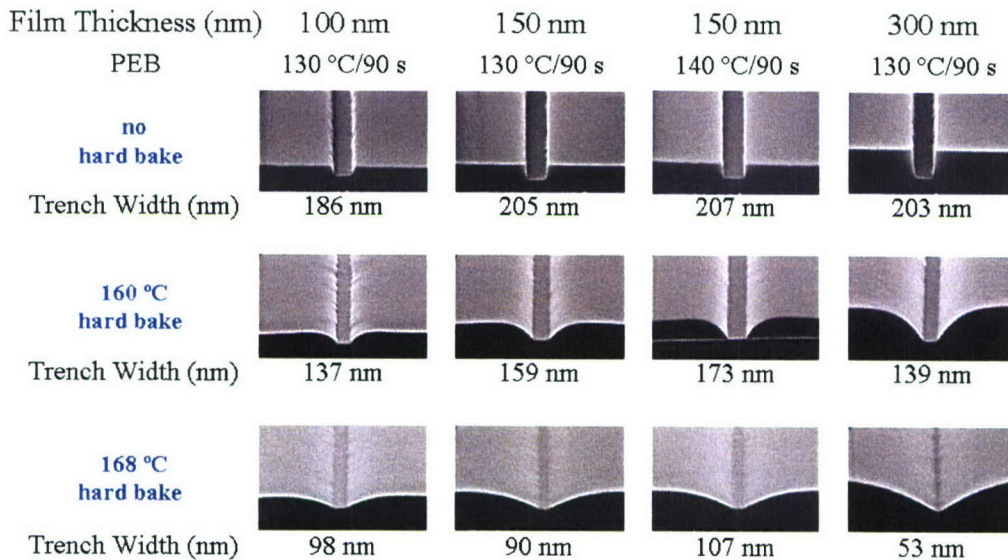


Figure 12. SEM profiles for 100, 150, and 300 nm thick films of XP1449-L.

Hard-bake time and feature type (isolated vs. dense). The effect of the HB time on TF of dense and isolated trenches was studied using XP1449-L resist. Figures 13A, and 13B illustrate both isolated and dense 200 nm trench features for the wafers exposed at DUV and subsequently hard baked. Narrow trench of 31 nm width was

formed by hard baking a 200 nm trench for 120 sec at 168 °C while a dense trench of 33 nm was obtained by hard baking a 170 nm trench for 30 sec at 168 °C.

A number of trends in this experiment became readily apparent. For any given HB, sidewall angles were lower for isolated trench features than for dense trench features. Both sidewall angle (°/sec) and thermal flow rate (nm/sec) were shown to be non-linear with respect to time (Figures 14 and 15). Dense trenches were also shown to close up before isolated trenches. For example, as seen in Figure 13B, 200 nm dense trenches that were hard baked for longer than 30 sec at 168°C became closed. Furthermore, the line heights of dense trenches decreased steadily as HB was increased (Figure 16). Note that for dense trenches the line is eroded from both sides by thermal flow while for isolated trenches the resist material can be conceived as infinite.

Based on the DUV results a HB temperature range of 160-168°C was decided for x-ray experiments. Four resists (XP1449-L, XP9947-W, XP1271-S and XP0945-B) were chosen and formulated for 150 nm film thickness for x-ray thermal flow studies. A typical process conditions (SB at 130°C/60sec, PEB at 130°C/90sec, Develop in MF-26A/45sec) were used followed by HB at 160°C for 30, 60, and 90 seconds.

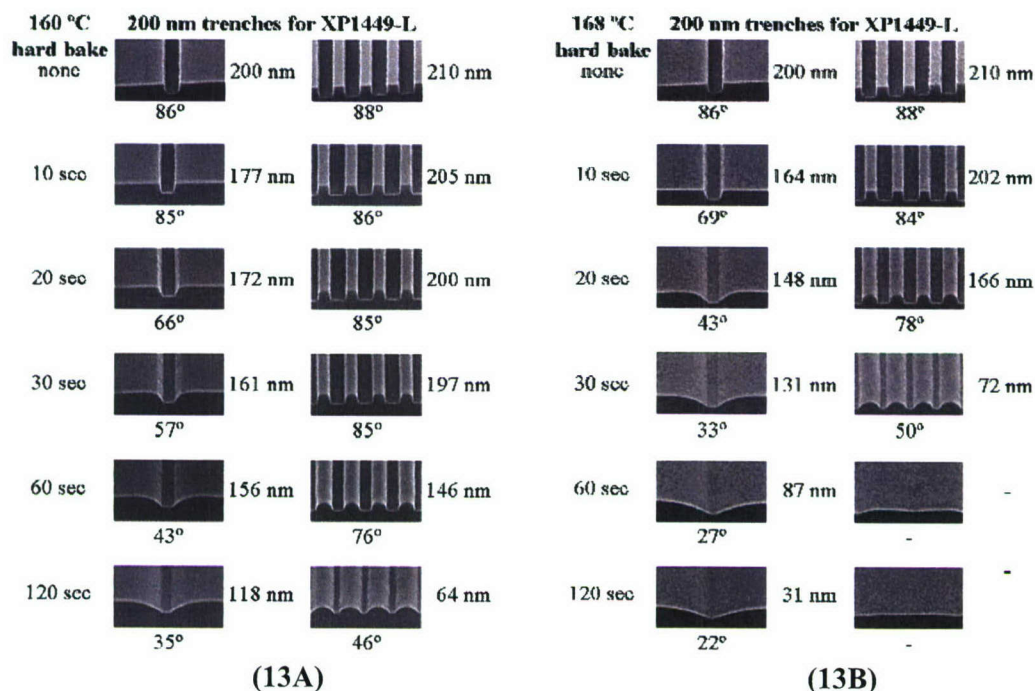


Figure 13. Effects of hard-bake time at 160°C and 168°C for XP1449-L.

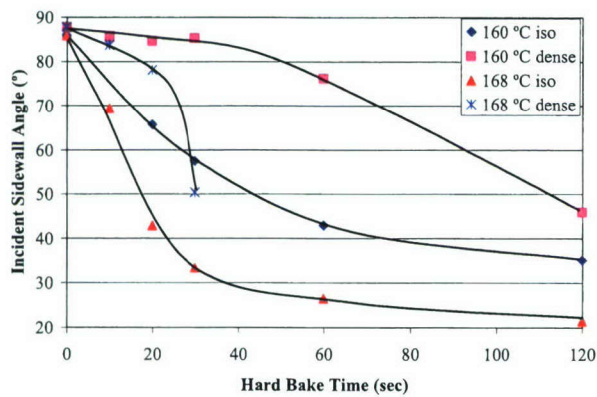


Figure 14. Incident sidewall angle as a function of hard-bake time.

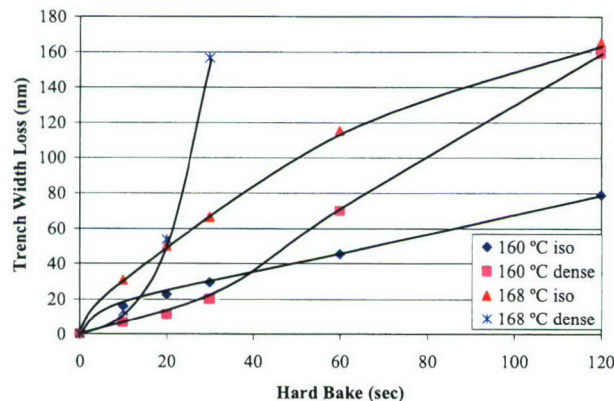


Figure 15. Thermal flow as a function of sidewall angle.

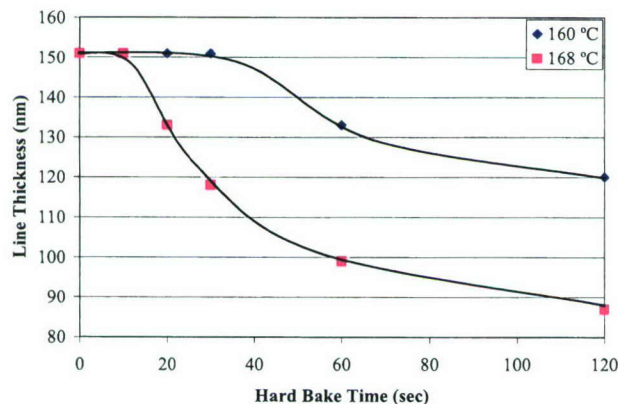


Figure 16. Effect of line height as a function of hard-bake time.

X-ray thermal flow study

Figure 17 shows the image profiles for 150 nm-isolated trenches of XP1449-L with and without TF. The incident sidewall angles reduced from 98-102° to 49-56° under

these conditions (A sidewall angle of 57° was obtained for 200 nm isolated trenches at 160°C/30sec for DUV exposure). It appears that the HB conditions used at DUV experiments for XP1449-L results in similar performance for x-ray exposure. Three more formulations (XP9947-W, XP1271-S, and XP0945-B) were subjected to 160°C HB.

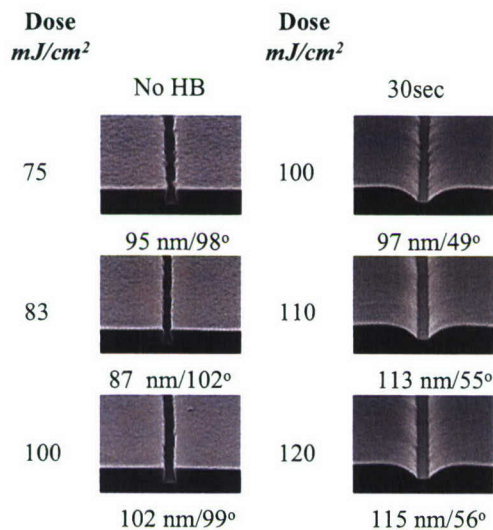


Figure 17. The thermal flow of XP1449-L at 160°C/30sec hard-bake.

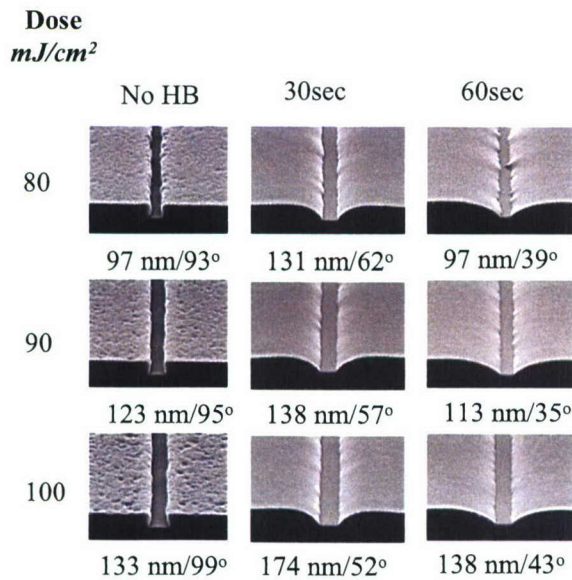


Figure 18. The thermal flow of XP1271-S at 160°C: the effects of hard bake time.

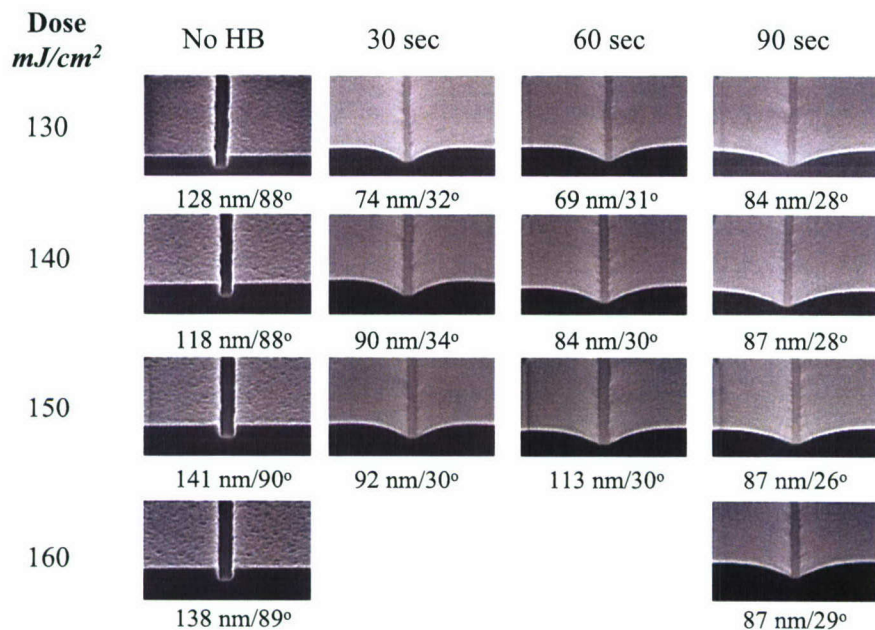


Figure 19. The thermal flow of XP9947-W at 160°C: the effects of hard bake time.

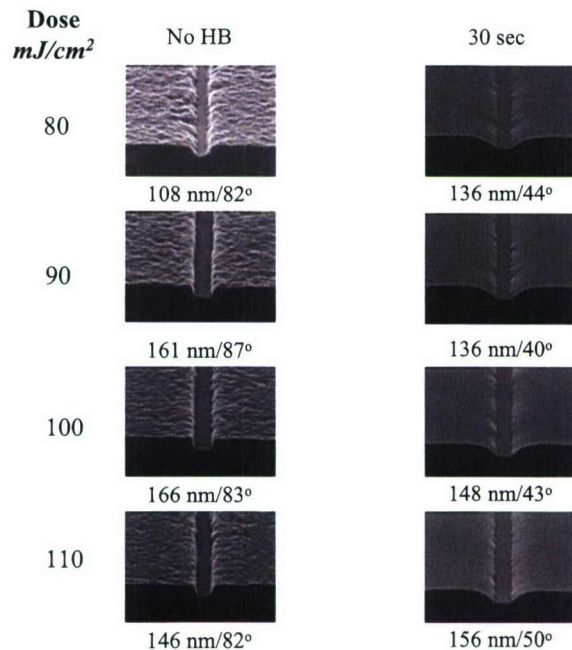


Figure 20. The thermal flow of XP0945-B at 160°C.

The XP1271-S formulation that had an identical polymer and a higher PAG loading compared to XP1449-L had TF properties similar to XP1449-L (Figure 18). The trench-widths as well as sidewall angles got smaller at higher HB times. However much lower sidewall angles were obtained for XP9947-W that had a slightly different polymer and a lower amount of the same PAG compared to XP1449-L (Figure 19). The HB time had only a marginal effect in this case. A formulation that had identical PAG loading to XP1271-S but containing a polymer blend (XP0945-B) showed a thermal flow behavior similar to XP9947-W (Figure 20). The higher sidewall angles obtained for XP1449-L and XP1271-S may be at least partly due to their re-entrant trench profiles in contrast to square profiles for XP9947-W and XP0945-B. While the thermal flow is a function of many parameters, the identity of the polymer appears to play a significant role.

The extensively pitted surface obtained with XP0945-B became smooth after hard-bake indicating an additional advantage of thermal flow. The pitted surface originates from the low contrast of the mask. This is more prominent with low E_a resists since the de-blocking can occur before PEB is done with these polymers.

IVB. Mask-to-wafer gap & Resolution capability

One of the advantages of x-ray is its very large depth of focus (DOF). In state of the art optical lithography, DOF is approximately 0.2-0.4 μm . Therefore, wafer must be placed accurately within this small DOF. Any placement error or topography difference on the wafer may result in out of focus. In XRL, the DOF is over 5 μm , and hence the placement accuracy is apparently not as critical. However, the opposite is true in practice.

As the critical dimension gets smaller, the gap between the wafer and mask becomes a critical factor. The maximum gap at which a feature can be printed decreases quadratically with shrinking feature size and is determined by the Fresnel Number. An aggressively optimized process can use a gap that corresponds to Fresnel number of 0.55.² A mask-to-wafer gap of 15 μm or less is needed to print 100 nm CD, but it is not feasible to work at gaps less than 10 μm because of the risk of damaging the delicate mask membrane.

The radiation used in synchrotron based x-ray source is fairly broad, which allows slightly higher gap setting than would be possible when using a monochromatic source of the same energy. Modeling of aerial images was utilized to determine the best mask-to-wafer gap and mask CD to reach the highest resolution using the CNTech Toolset.³

Two experimental photoresists, XP1449-L and XP9947-W, were used at 150 nm film thicknesses. Typical process conditions were used (SB at 130°C/60sec, PEB at 130°C/90sec, develop in MF-26A/45sec). Two mask-to-wafer gap settings (15 & 25 μm) were chosen to explore the effect of gap on resolution.

Figures 21 & 22 show the resolution capabilities of XP9947-W and XP1449-L at 150 nm film thicknesses. The highest resolutions were obtained using doses that are slightly above the required sizing energies. The XP9947-W resist had slightly better resolution (69 nm and 75 nm at 15 and 25 μm gap settings respectively through 61 nm mask space) than XP1449-L (75 nm and 83 nm at 15 and 25 μm gap settings respectively through 78 nm mask space). Also the XP9947-W had square profiles at both gap settings while XP1449-L profiles were slightly reentrant. However, the XP1449-L formulation was up to 20% more sensitive than XP9947-W.

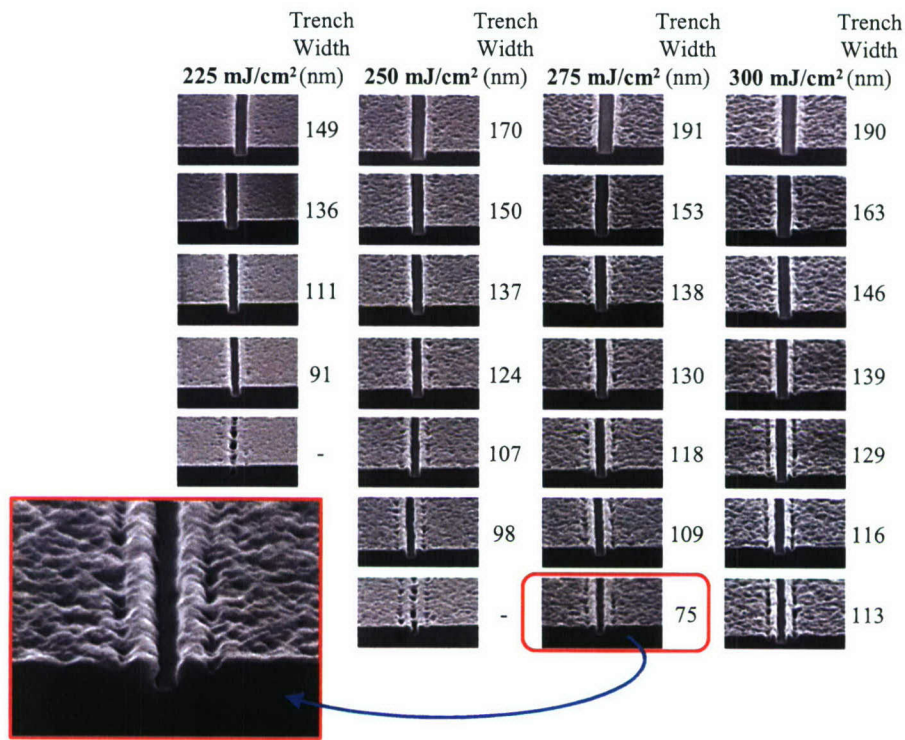


Figure 21A. The resolution of XP9947-W at 25 μm mask-to-wafer gap.

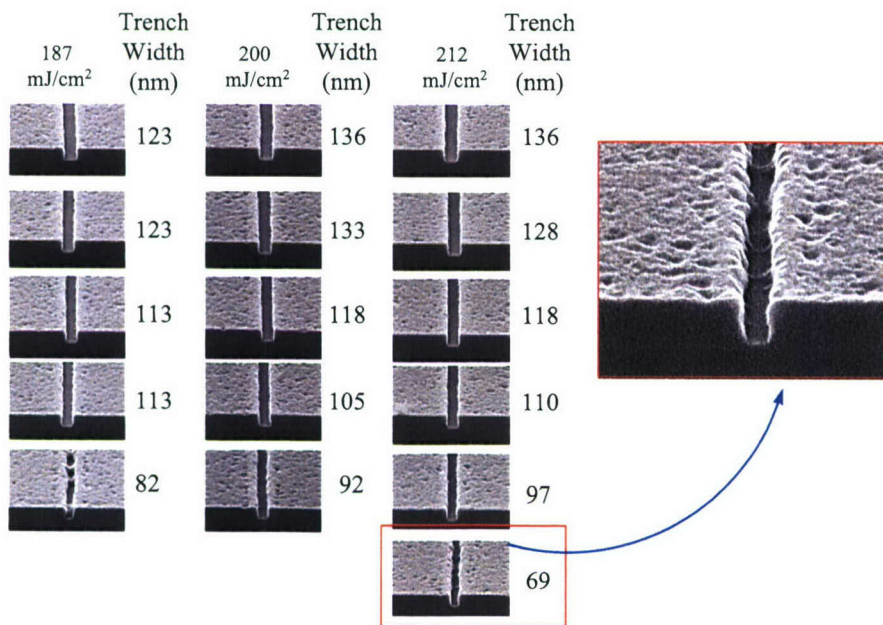


Figure 21B. The resolution of XP9947-W at 15 μm mask-to-wafer gap.

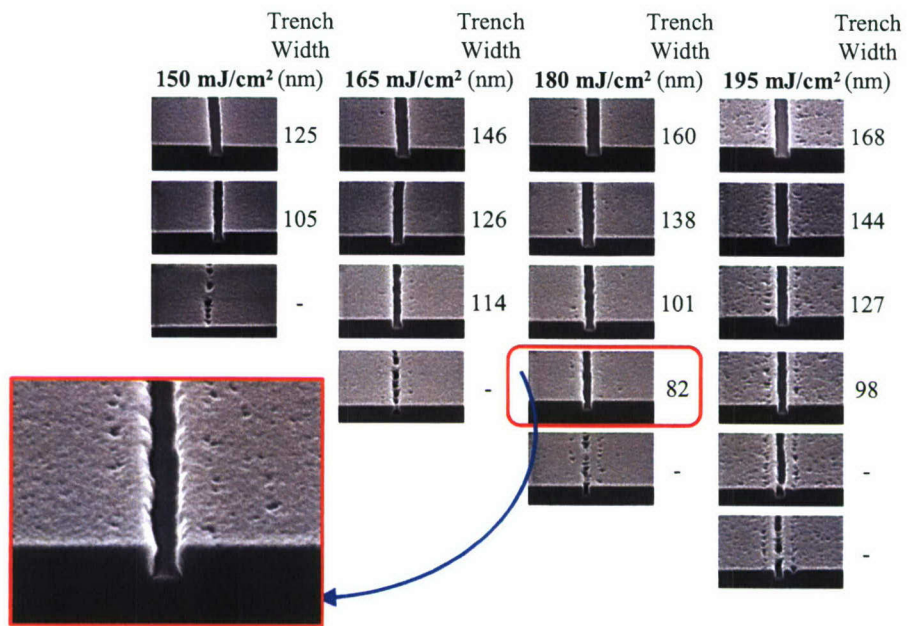


Figure 22A. The resolution of XP1449-L at 25 μ m mask-to-wafer gap.

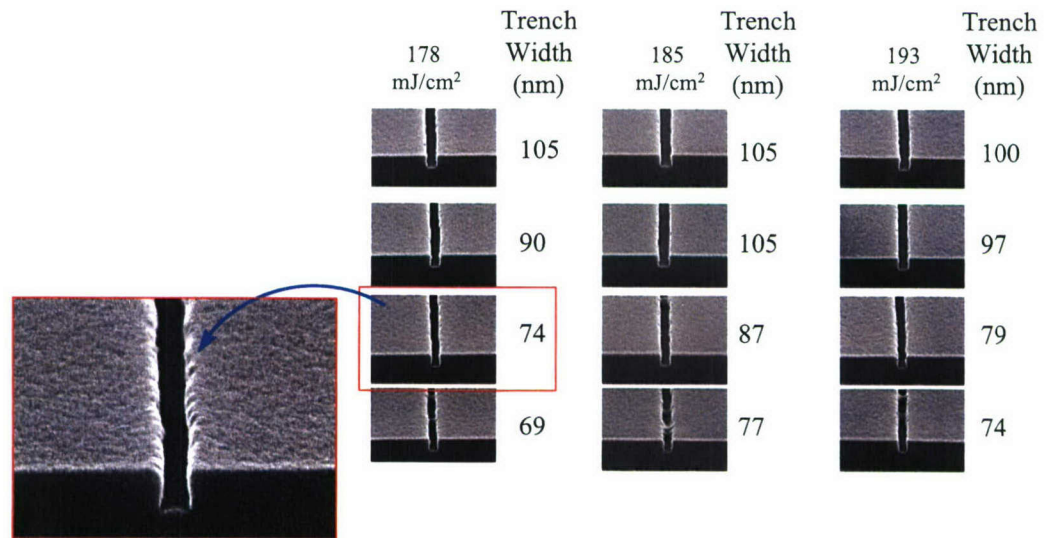


Figure 22B. The resolution of XP1449-L at 15 μ m mask-to-wafer gap.

One of the problems of ROBOMASK (a binary mask) is its low contrast. This causes the absorber regions to have a certain amount of exposure. However, in certain situations, this contrast issue can be utilized to print small features by taking advantage of phase-shift effects. A 65 nm resolution was obtained for XP9947-W at 25 μm gap by overexposing through a semi-dense mask space of 83 nm with a pitch of 330 nm (Figure 23). These smaller trenches are the result of diffraction effects at the edge of the mask absorber. This diffraction causes photoresist clearing, in effect, through the absorber region on the mask.

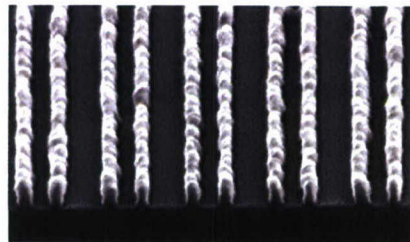


Figure 23. SEM image of XP9947-W displaying high resolution caused by x-ray diffraction effects through ROBOMASK (150 nm film thickness at 25 μm mask-to-wafer gap).

Figure 24 shows the masking linearity of another benchmark resist, XP1271-S. The best resolution was only 97 nm with 1.5 aspect ratio for the 150 nm thick film at 25 μm gap. The profiles were not as reentrant as XP1449-L and had a better sensitivity. XP0945-B containing a polymer blend had a resolution of 107 nm (Figure 25). This is not unexpected since the process conditions are not optimized for this new polymer. There is obviously a trade-in between the resist sensitivity and resolution. The Table XIV summarizes the resist sensitivity-resolution data obtained for a range of resists. Figure 26 clearly demonstrates the sensitivity-resolution trade-off.

The target resolution of 50 nm for this program was not achieved by any of the three benchmark resists, XP9947-W, XP1449-L or XP1271-S. It should be noted that XP1449-L is capable of 26 nm resolution using EUV lithography. Large improvements to resolution are possible by using a high contrast mask and an optimized x-ray tool for the existing resists.

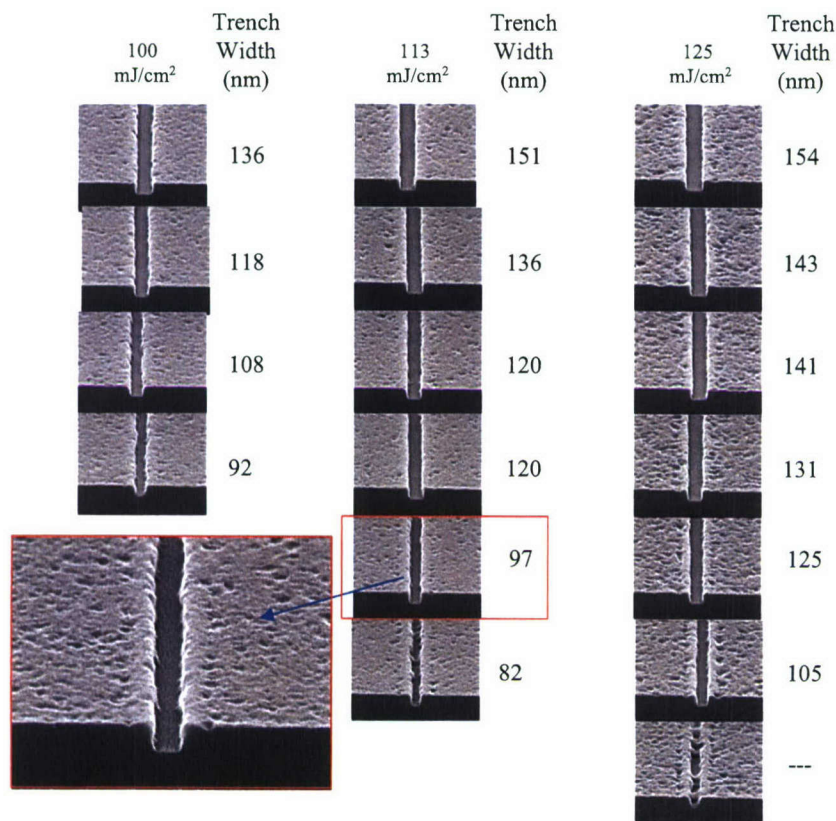


Figure 24. The resolution of XP1271-S resist for 150 nm thick film at 25 μm gap.

Table XIV. The resist sensitivity (dose to wafer) and resolution data for a range of resists at 150 nm thickness and 25 μm mask-to-wafer gap.

Resist	E_0 (mJ/cm ²)	E_{size} (mJ/cm ²) 136nm iso*	Resolution (nm)	Aspect ratio
XP9947-W	125	190	75	2.0
XP1449-L	105	153	83	1.8
XP1271-S	65	87	97	1.5
XP1271-O	50	53	97	1.5
XP0945-B	55	92	107	1.4
XP0608-C	63	80	97	1.5
XP0609-A	63	69	92	1.6
XP0609-B	63	67	95	1.6
XP0610-A	88	94	87	1.7

* ROBOMASK Pos T-gate (1:10)

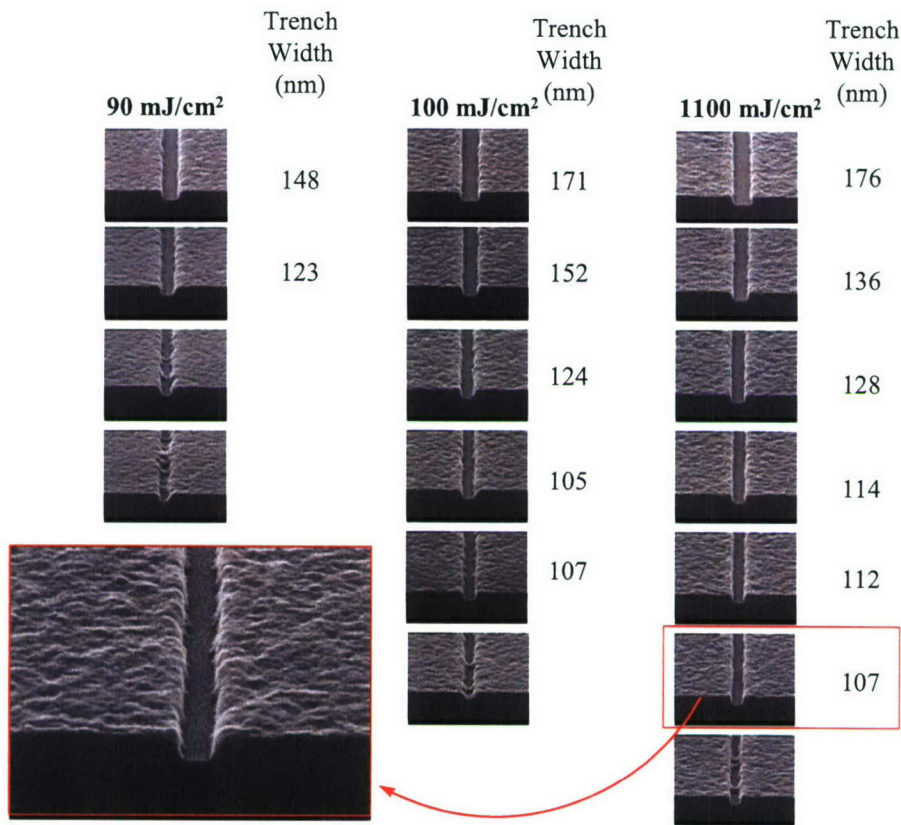


Figure 25. The resolution of XP0945-B resist for 150 nm thick film at 25 μm gap.

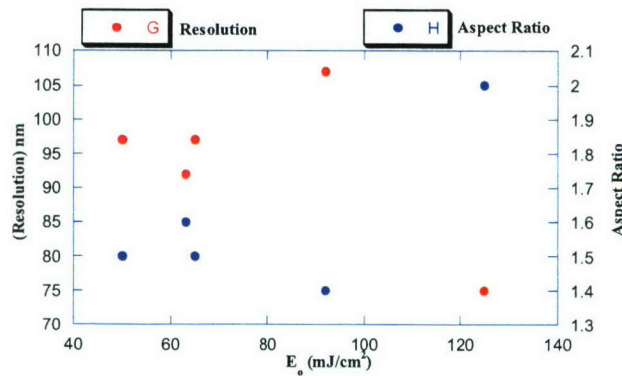


Figure 26. The trade-off between the resist sensitivity and resolution (aspect ratio).

IVC. Post exposure bake temperature sensitivity (PEB)

The post exposure bake temperature (PEB) sensitivity is defined as the CD change (nm) in response to the changes in post exposure bake temperatures and measured as nm/ $^{\circ}\text{C}$. Resists with higher PEB sensitivity are not desired because it can affect CD

uniformity and limit the PEB process window. The program goal was set for less than 5 nm/ $^{\circ}\text{C}$ PEB sensitivity.

Four resists were selected for PEB measurements. The Reso-5 mask with 100 nm top-down isolated trenches were used for XP9947-W, XP1271-S and XP0945-B. The ROBOMASK was used for XP1449-L with 150 nm-isolated trenches (Pos T-gate). All the process parameters (FT = 150 nm; SB = 130 $^{\circ}\text{C}/60\text{sec}$; develop MF-26A/45sec) were kept constant except PEB temperature. Two or three PEB temperatures at 115-140 $^{\circ}\text{C}$ range were used.

Figure 27 demonstrates how PEB was measured for XP9947-W. The Reso-5 mask was used to print 100 nm top-down isolated trenches (1:10) at two PEB temperatures. As can be seen from the SEMs the resist sensitivity (speed) is decreased at low PEB temperatures resulting in a drop of CD at the same dose. The PEB sensitivity could be determined by two methods.

- (1) Plotting the trench CD vs dose (EL) for each case and calculating the extrapolated CD loss at the sizing energy (E_{size} (100 nm)) for 130 $^{\circ}\text{C}/90\text{sec}$ PEB.
- (2) Comparing individual CD measurements and averaging the results.

Although the first method was more desirable in this type of calculations, it was not always used since a large extrapolation was needed. The comparison of individual CD measurements was used to estimate PEB in this case. The value (0.8 - 1.5 nm/ $^{\circ}\text{C}$) obtained was well below the program goal (< 5 nm/ $^{\circ}\text{C}$). The PEB sensitivity for XP1449-L was estimated to be in the range of 1.3 - 3.4 nm/ $^{\circ}\text{C}$. The PEB sensitivity for XP1271-S was 3 nm/ $^{\circ}\text{C}$. All three of the above resists had a high E_a polymer platform and certain PEB sensitivity was expected. The XP0945-B formulation that had a polymer blend containing a low E_a polymer had a remarkably low PEB sensitivity of 0.5 nm/ $^{\circ}\text{C}$. Figure 28 clearly shows the PEB sensitivity difference between these two polymer platforms.

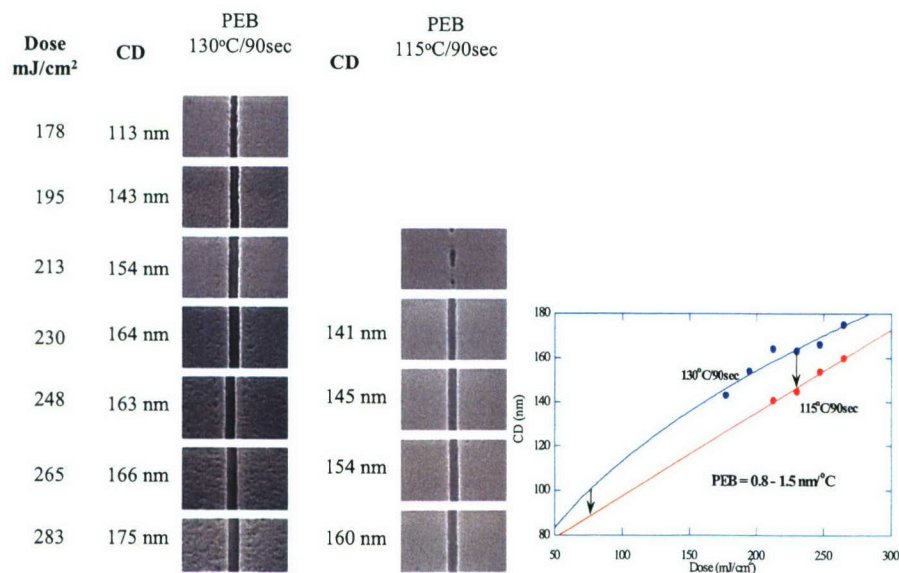


Figure 27. The exposure latitudes of XP9947-W at 130 $^{\circ}\text{C}/90\text{sec}$ and 115 $^{\circ}\text{C}/90\text{sec}$ PEB.

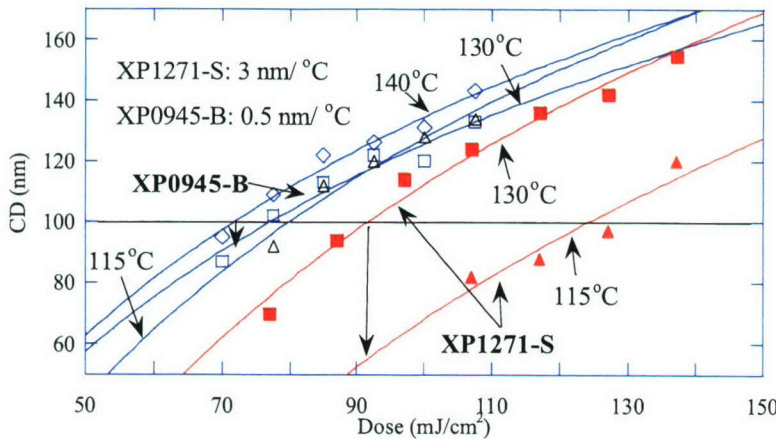


Figure 28. The exposure latitude plots of XP1271-S and XP0945-B at different PEB temperatures.

IVD. Post exposure delay stability (PED)

The post exposure delay stability is defined as the change in CD (nm) in response to the time delay between exposure and post exposure bake. This property is measured as nm/h and usually associated with a CD loss for most chemically amplified resists. There are some exceptions when low activation energy polymers are used, in which a CD gain is observed with time delay.

The PED CD loss is caused by the neutralization of photo-generated acid by environmental amines. If the photo-generated acid is partially neutralized, it can lower the resist speed. Also this effect is more prominent on the resist surface than inside the film and could lead to T-topping. Obviously this phenomenon is dependent on the degree of amine contamination in the environment. Hence the PED standards cannot be universal and will be clean room dependant.

Originally, the PED experiments were planned to be conducted at BAE, inside the stepper chamber, where the mean amine concentration level is estimated to be < 5 ppb. The program goal was set for more than 2 hours PED stability in this environment. However, the PED experiments could not be successfully carried out at BAE because of a number of tool issues. These measurements were instead made in non-amine filtered CNTech clean room.

We have extensively studied the PED behavior of similar resists employing DUV exposure at Shipley's FAB 3 and also using e-beam exposure at Lawrence Berkeley National Laboratory (LBNL) and MIT Lincoln Laboratory (MIT-LL). The CD loss has a huge variation between those environments, i.e. 86 nm/h at non-amine filtered LBNL, 2 nm/h at MIT-LL and 0 nm/h at Shipley FAB 3 for the same resist. Therefore it is difficult to set a universal scale to this property and one can only make rough estimates. Based on our e-beam/DUV results we expect at least 10 times better stability at BAE amine filtered environment than CNTech.

PED experiments were conducted in a similar way to PEB studies except only the delay time was varied keeping other parameters constant. Some measurements were

made by imaging two identical sets of four fields in a single wafer, cleaving them and doing the PEB at two different delay times. The PED in nm/h were determined by plotting trench CD vs. exposure dose at different delay times (0 – 2hrs) and calculating the CD loss. The ROBOMASC with 150 nm (136 nm actual space) isolated trenches (Pos T-gate) was primarily used for these measurements. Res-5 mask with top-down 100 nm-isolated trenches was used for XP0945-B resist.

A representative example is shown in Figure 29 where a single wafer was imaged with two identical sets of four fields. The wafer was cleaved after exposure and baked after 0 and 2-hour delays. There is a significant CD loss at 2-hour delay as seen in SEMs and EL plots. The CD loss at the sizing energy for XP9947-W (E_{size} (136 nm) = 174 mJ/cm²) and XP0609-A (E_{size} (136 nm) = 92 mJ/cm²) were calculated and a PED stability of 38 nm/h and 17 nm/h were obtained.⁴

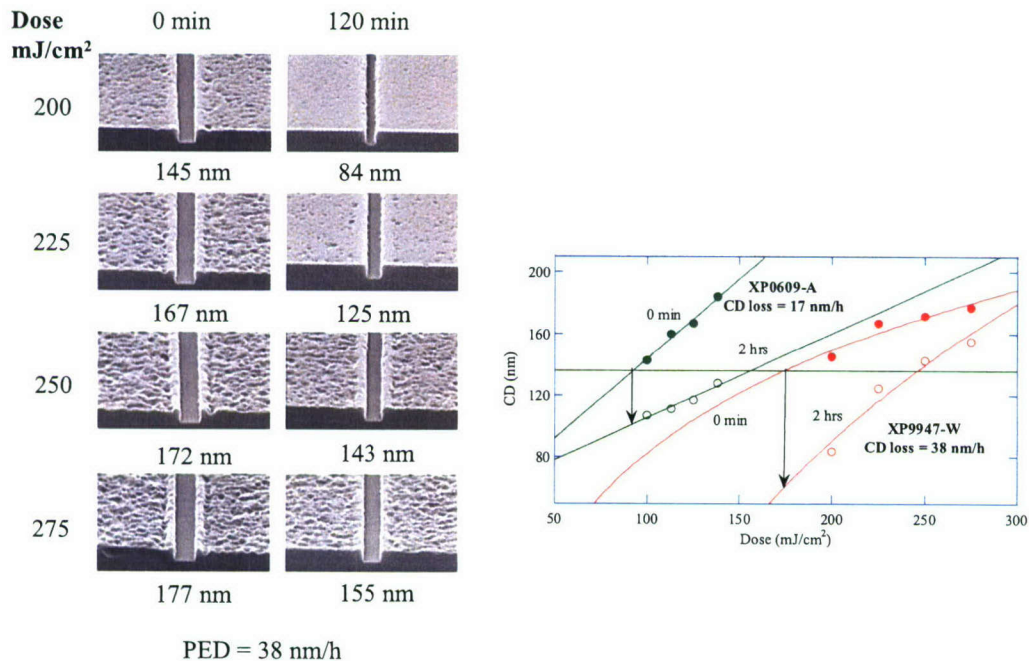


Figure 29. The PED stability of XP9947-W & XP0609-A.

The CD loss per hour and sizing energies for 136 nm isolated trenches for a number of formulations are listed in the Table XV. The sizing energies in the Table XV were determined using the wafers that had eight different exposure fields rather than PED wafers those had only four exposure fields. There seem to be no correlation between the resist speed and PED sensitivity with these x-ray exposures. The XP0945-B formulation that had a low E_a polymer gave negative PED (the trench CD increased with delay). The XP0608-C formulation had an exceptionally good PED (6 nm/h) coupled with excellent speed and exposure latitude. XP0609-A through C had an increasing amount of an additive that was expected to improve both speed and stability and it indeed did improve both.

Table XV. The resist speed (dose to wafer) and PED stability.

	$E_{size}(136\text{nm})$ (mJ/cm^2)	PED (nm/h)
XP9947-W	190	38
XP1449-L	153	22
XP1271-S	87	(29)*
XP0945-B	92	-8
XP0608-C	80	6
XP0609-A	69	17
XP0609-B	67	15
XP0609-C	63	10

* measured for XP1271-O

As discussed previously the above PED measurements were made in unfiltered CNTech environment, hence unrelated to amine-filtered BAE stepper chamber. However, we are confident that changing to an amine free environment would significantly improve PED performance of all these resists.

Since wafer exposure takes 30 to 60 minutes, an experiment was conducted to evaluate the effects of delay during exposure. XP1449-L was imaged at 160 mJ/cm^2 to the wafer for all 8 fields. All profiles looked similar with slight changes in trench CD. At short PED times, “pitting” are present in the resist surface presumably caused by minimal exposure through the absorber regions of the mask. As time goes by, the “pitting” disappears. The explanation for this is probably because of base contaminants in the clean room, which quenches acid formed in the low exposure regions.

IVE. Shelf life

The program goal for shelf life of resists is more than six months stability *in the refrigerator* (5°C). Initially, we evaluated six resists using an accelerated shelf-life method (room temperature, 2 months). Resists were stored at room temperature (20°C) and in the freezer (-5°C). The stabilities of these resists were evaluated by following changes in Unexposed Film Thickness Loss (UFTL) and DUV E_o (clearing dose). Comparisons were made between resists stored at room temperature and those stored in the freezer (control). The E_o values did not change for three of the resists after two months at room temperature, and small changes were observed for XP9947-W (6%) and XP1449-L (3%), with the largest change exhibited by XP1271-R (12%)(Table XVI). The UFTLs decreased slightly for some resists.

Four resists were selected for the final refrigerated aging study (XP9947-W, XP1449-L, XP1271-S, and XP0945-B). Three resists were formulated and kept at -5°C (freezer), room temperature, and in a refrigerator. The UFTL and DUV E_o values were

compared after 4.5 months (Table XVII). Unfortunately, it was not possible to start this shelf-life study earlier because of mask-related delays which did not allow final resist candidates to be selected 6 months prior to the end of the program. Nonetheless, the refrigerated shelf-life results are excellent. The small change in the clearing dose for XP9947-W (4%), and no change in XP1449-L (0%), and XP1271-S (0%) during this time indicate a good refrigerated shelf life. The changes of UFTL of those three resists were negligible. The fourth resist (XP0945-B), however, showed modest increases in E_o and UFTL (11%, 15%), and will not be among the recommended resists.

Table XVI. The room temperature (2-month) shelf life of six resists.

Resist	Polymer Type	Base	Freezer(-5°C)		RT-2 months		ΔE_o	$\Delta UFTL$ (A)
			E_o	UFTL(A)	E_o	UFTL(A)		
XP1271-R	High E_a	low	1.7	84	1.5	75	-0.2	-9.0
XP1271-T	High E_a	high	4.2	82	4.2	74	0.0	-8.0
XP0945-A	High E_a /Low E_a Blends	low	1.3	96	1.3	80	0.0	-16.0
XP0945-C	High E_a /Low E_a Blends	high	3.8	94	3.8	79	0.0	-15.0
XP1751-D	High E_a	low	1.3	68	1.3	59	0.0	-9.0
XP9947-W	High E_a	high	4.9	106	4.6	108	-0.3	2.0
XP1449-L	High E_a	high	3.5	73	3.6	73	0.1	0.0

Table XVII. The room temperature, and refrigerated (4.5-month) shelf life of benchmark resists.

Resist	Polymer Type	Freezer(-5°C)		Refrigerator		Room Temp.		Refrigerator		Room Temp.	
		E_o	UFTL(A)	E_o	UFTL(A)	E_o	UFTL(A)	ΔE_o	$\Delta UFTL$	ΔE_o	$\Delta UFTL$
XP9947-W	High E_a	5.2	107	5.4	107	4.6	110.0	0.2	0.0	-0.6	3.0
XP1449-L	High E_a	3.6	90	3.6	91	3.0	90.0	0.0	1.0	-0.6	0.0
XP1271-S	High E_a	2.6	87	2.6	89	2.6	89.0	0.0	2.0	0.0	2.0
XP0945-B	High E_a /Low E_a Blends	2.4	82	2.6	94	2.6	122.0	0.2	12.0	0.2	40.0

V. MMIC T-gate applications

The primary objective of this project was to develop x-ray resists having desired trench profiles (sidewall angles) for MMIC T-gate fabrication. MMIC fabrication involved t-gate lithography (i-line) on top of x-ray lithography. Figure 30 shows cross-sectioned T-gate showing recess etches that was formed after x-ray/t-gate lithography.

Maureen Roche (BAE) performed the MMIC T-gate device demonstration.

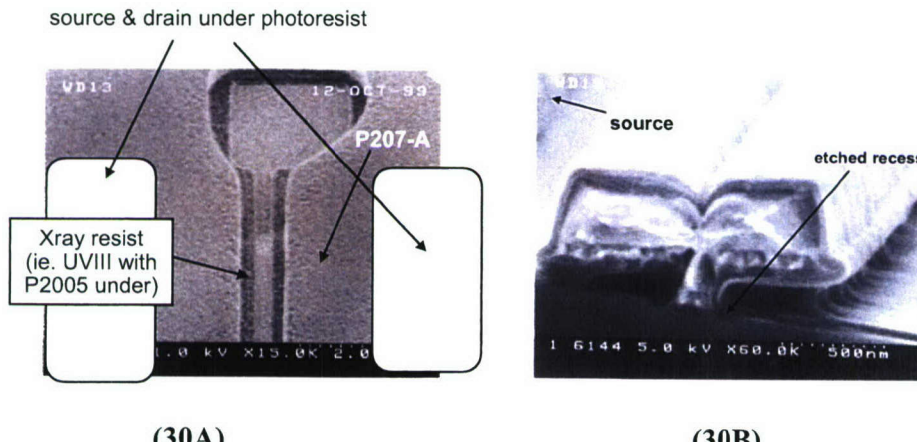


Figure 30. T-gate lithography on top of x-ray lithography (30A) and a cross-sectioned T-gate (30B).

VI. Performance vs. Objectives

As mentioned before, the goals of this two-year project required advances in several areas, the most important of which were improved sensitivity, resolution, environmental stability as well as full T-gate process capability. The successful implementation of this project needed a concerted effort by Shipley, BAE, and CNTech with the support from SAL. Many technical challenges were encountered and overcome during this period. Figure 31 shows the progress of the project during the 2-year period.

About 70-85 formulations were tested during these rounds and more than 240 wafers were imaged at CNTech alone (Figure 32). Three resist formulations were developed simultaneously and their performance parameters are compared to program goals in Table XVIII. The resist sensitivity, % EL, PEB sensitivity, aspect ratio and refrigerated shelf life targets were achieved. The PED stability could not be determined at BAE, but the results obtained at CNTech are promising. Both XP9947-W and XP1449-L had comparable intermixing with MA-P210 to that of UVIII as required. The thermal flow experiments demonstrated the ability for controlling sidewall angles. However, only one set of TF studies could be done using x-ray exposure. T-gate process capability was demonstrated by BAE for XP9947-W.

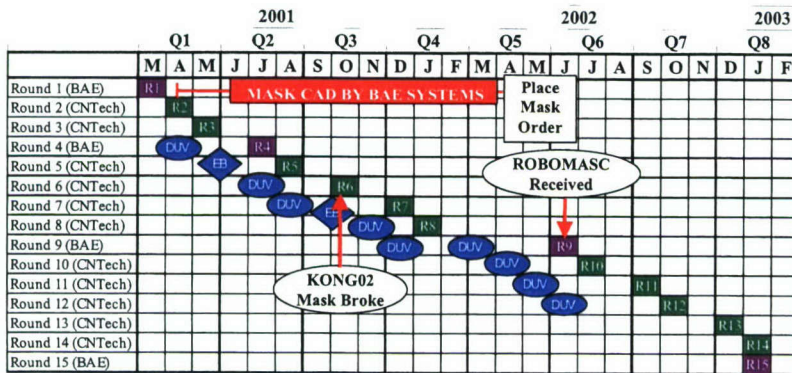


Figure 31. The progress of the program.

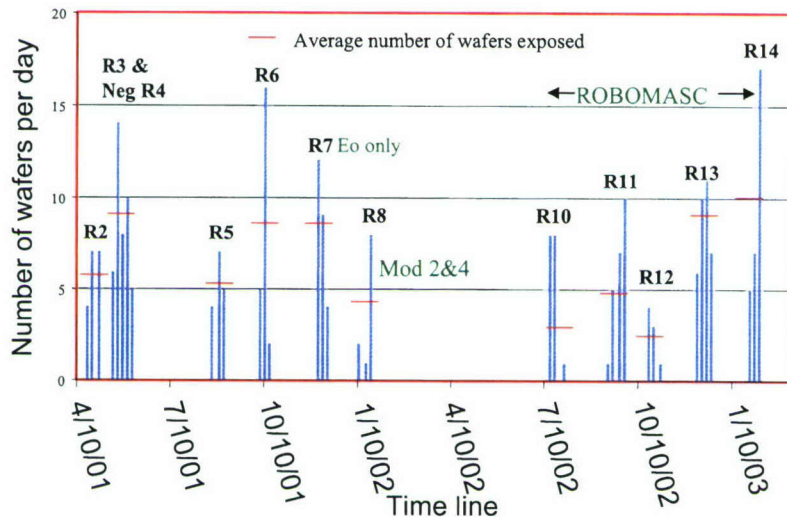


Figure 32. Wafer exposures at CNTec.

The Table XVIII summarizes all of the target goals and the performance of top three resists. The targets reached are depicted in dark green background. The PED and sidewall angle performance is depicted in light green because the capabilities of those parameters were not clearly demonstrated although we believe those can be achieved with these resists. The resolution targets (~ 50 nm) could not be reached. However, we believe that improvements in this regard are possible with a high contrast mask.

Table XVIII. The resist performance against objectives for final formulations.

Property	UVIII	Program Goal	XP9947W	XP1449-L	XP1271-S
Aspect Ratio (Thickness resolution)	≥ 1	≥ 1	2.0	1.8	1.5
E_{size} to the wafer (vs. UVIII)	100%	40% of UVIII	57% of UVIII	47% of UVIII	26% of UVIII
Resolution (nm) for isolated trenches	140	= 20 nm less than smallest mask feature, but ≥ 50 nm	75 nm (from a 61 nm mask space)	82 nm* (from 78 nm mask space)	97 nm
EL @ 200 nm CD (%)	38%	≥ 10	37%	32%	22%
PEB Sensitivity (nm/ $^{\circ}$ C)	TBD	< 5	0.8 - 1.5	1.3 - 3.4	3.0
PED stability in stepper chamber(hr) (mean concentration <5 ppb)	TBD	> 2	38 nm/h**	22 nm/h**	29 nm/h** (XP1271-O)
Additional Objectives					
Full T-gate process capability	TBD	Yes	Completed by BAE		
Extent of Intermixing with MA-P210	Intermixes with Bottom Layer Only	= UVIII	= UVIII	= UVIII	
Profile					
Sidewall angle	TBD	< 85	88-90	>90	>90
Rounded shoulders	TBD	Yes	w/thermal flow	w/thermal flow	w/thermal flow
Refrigerated Shelf-life (mo.)	≥ 6	≥ 6	>4.5months@ Refrigerator	>4.5months@ Refrigerator	>4.5months@ Refrigerator

* Resist capable of 28 nm resolution using EUV lithography

** measured in air in CNTec

VII. Conclusions

The objective of this project was to develop resist(s) that meet specified targets. We have identified three benchmark resists (XP9947-W, XP1449-L, and XP1271-S) and evaluated them for resist performance parameters stipulated in the statement of work. Shipley would make available any or all of these resists to BAE. We accomplished the following:

- The sensitivity, exposure latitude, PEB sensitivity, aspect ratio and shelf life goals were achieved
- The available data for PED stability indicates that this goal is also feasible
- Thermal flow experiments demonstrated that rounded shoulders and proper side wall angles are achievable although the TF process was not optimized
- The target resolution could not be achieved, but we expect that improvements to demonstrated resolutions are possible using a high contrast mask
- The extent of intermixing with MA-P210 was comparable to that of UVIII as required for two resists XP9947-W and XP1449-L
- Full T-gate process capability was demonstrated by BAE for XP9947-W

References

- (1) KONG02 mask was broken during this run and the completion of the ROBOMASC was delayed several months. DUV screening was used as the primary source of information gathering at this stage.
- (2) M. Khan, G. Han, G. Tsvid, J. Maldonado, F. Cerrina *J. Vac. Sci. Technol. B*, **2001**, *19*(6), 2423.
- (3) M. Khan, S. Bollepalli, F. Cerina, *UW-Madison Technical Report*, 1997
- (4) Sizing energy calculated from only four exposure fields may not be accurate, but this wouldn't have significant bearing on the PED value. The sizing energies in table XV were measured using eight fields

Appendix D

TASKS SUPPORTING BAE DARPA CONTRACT N00019-01-C-0088

**UNDER SUBCONTRACT WITH BAE SYSTEMS AND
COLLABORATING WITH SHIPLEY (UW # 144KN75)**

*Final Scientific and Technical Report Covering the
Period:*

March 01, 2001 to February 28, 2003

Date of this Report: March 24, 2003

Submitted by:

Franco Cerrina, Don Thielman, Quinn Leonard,
Dan Malueg, and James W. Taylor

University of Wisconsin-Madison

Center for NanoTechnology

**FINAL REPORT ON THE CNTech TASKS SUPPORTING BAE DARPA
CONTRACT N00019-01-C-0088 OVER THE CUMULATIVE PERIOD
MARCH 01, 2001 AND EXTENDED TO FEBRUARY 28, 2003 UNDER UW
144KN75. DATE OF THIS FINAL REPORT IS MARCH 24, 2003.**

I. Description of CNTech Tasks.

CNTech is working with the Shipley Company to provide exposures on the steppers at the Aladdin storage ring for the positive-tone chemically amplified resists that Shipley is formulating to the specifications determined by BAE Systems and DARPA. CNTech prepares for each Shipley visit, which is nominally on an every other month basis but was delayed at times because of mask breakage and stepper issues. CNTech pre-characterizes the equipment before Shipley arrives by hot plate characterization and running test samples through the equipment. CNTech provides facility support by providing an X-ray mask with resolution features, by working with Shipley personnel to provide the necessary exposures, and by providing support for some of the SEM measurements. Shipley uses those SEM measurements to determine the appropriate exposure conditions for the resists. Shipley takes the final exposed wafers back to their facility and performs detailed SEM measurements to correlate the formulation variations with the observed experimental results to determine the best formulation to meet the resist specifications.

II. Results from Exposures during the periods of December, 2002 and January, 2003.

In these periods, we have seen significant support from both JSAL and BAE while the exposures were obtained. This support has significantly improved both the quantity and quality of the data that could be obtained on the various resist formulations. Mask breakage by the stepper was addressed by JSAL, because two ROBOMASCs were lost in the December - Shipley Round #13; one was caused by the stepper and one was due to human error at CNTech. JSAL, however, supplied two replacement ROBOMASCs in time for the January exposure period – Shipley Round # 14.

The results from the December, 2002 exposures are shown in Table I, and the exposures done in January, 2003 are shown in Table II. Shipley has reported on the December exposures and reported on most of the January exposures at the BAE review on March 6, 2003.

In addition to the exposure support, CNTech continued the study of optimization conditions for some of the more promising resist candidates. The last quarterly report described a preliminary process latitude study of KRS-XE for clearing dose and contrast. Optimization of Shipley XP-9947W was done previously and was reported.

III. Final Conclusions for the Resist Studies.

CNTech has provided exposures for the studies of resist formulations that Shipley provided. At the conclusion of the effort, there have been 249 wafers exposed at CNTech and 3452 fields. As noted in Table II, the one-day record of exposures was 17 wafers with 8 fields each for a total of 136 fields. In addition, a number of resists have been optimized by CNTech through design of experiments statistical approaches. These data have been provided to BAE through the quarterly reports and will not be summarized here.

Table I. Shipley/BAE Round 13 Photoresist Characterization Exposures
12/09/02 - 12/13/02 Total Wafers 362 Total Fields 280

Table II. Shipley/BAE Round 14 Photoresist Characterization Exposures**01/28/03 - 01/30/03 Total Wafers 29 Total Fields 232****Shipley/BAE Photoresist Characterization Exposures**

DHM	Total Wafers	29
	Total Fields	232
Round 14	Total Dose	56432 (mJ/cm ²)

1/28/03 - 1/30/03

<u>Date</u>	<u>Wafer ID</u>	<u># Fields</u>	<u>Mask</u>	<u>Gap</u>	<u>Tool</u>	<u>Dose</u>	<u>Step</u>	<u>Comment</u>
1/28/2003	A1	8	ROBOMASC	25	Mod4	100	25	
1/28/2003	E1	8	ROBOMASC	25	Mod4	200	25	
1/28/2003	D2	8	ROBOMASC	25	Mod4	150	20	
1/28/2003	E3	8	ROBOMASC	25	Mod4	260	10	X2 (two fields)
1/28/2003	E4	8	ROBOMASC	25	Mod4	260	10	X2 (two fields)
1/29/2003	A2	8	ROBOMASC	25	Mod4	140	10	X2 (two fields)
1/29/2003	A3	8	ROBOMASC	25	Mod4	140	10	X2 (two fields)
1/29/2003	B1	8	ROBOMASC	25	Mod4	160	10	X2 (two fields)
1/29/2003	D3	8	ROBOMASC	25	Mod4	180	10	X2 (two fields)
1/29/2003	D4	8	ROBOMASC	25	Mod4	180	10	X2 (two fields)
1/29/2003	B3	8	ROBOMASC	25	Mod4	160	10	X2 (two fields)
1/29/2003	A4	8	ROBOMASC	25	Mod4	149	10	X2 (two fields)
1/30/2003	C1	8	ROBOMASC	25	Mod4	260	15	X2 (two fields)
1/30/2003	C2	8	ROBOMASC	25	Mod4	260	15	X2 (two fields)
1/30/2003	D5	8	ROBOMASC	25	Mod4	160	20	
1/30/2003	D6	8	ROBOMASC	25	Mod4	160	20	
1/30/2003	E5	8	ROBOMASC	25	Mod4	260	10	X2 (two fields)
1/30/2003	E6	8	ROBOMASC	30	Mod4	200	25	
1/30/2003	D7	8	ROBOMASC	30	Mod4	150	25	
1/30/2003	E7	8	ROBOMASC	20	Mod4	200	25	
1/30/2003	D8	8	ROBOMASC	20	Mod4	150	25	
1/30/2003	E8	8	ROBOMASC	25	Mod4	200	25	
1/30/2003	D9	8	ROBOMASC	25	Mod4	150	25	
1/30/2003	B4	8	ROBOMASC	25	Mod4	125	25	
1/30/2003	B5	8	ROBOMASC	25	Mod4	125	25	
1/30/2003	E9	8	ROBOMASC	25	Mod4	260	10	X2 (two fields)
1/30/2003	D10	8	ROBOMASC	25	Mod4	180	10	X2 (two fields)
1/30/2003	E10	8	ROBOMASC	25	Mod4	200	25	
1/30/2003	D11	8	ROBOMASC	25	Mod4	150	25	

Issues Identified:

1. Stepper ran well. A new throughput record of 17 wafers (8 fields each) was established one day.

Appendix E

**Final Report
To
BAE Systems
High Gain Collimator Project**

November 11, 2004

The High Gain Collimator (HGC) was designed to make optimal use of off-axis x-rays emerging from the pinch source. By redirecting these rays that would otherwise be lost to the side, the collimator reduces exposure time.

Completion of Project

The project reached completion when the collimator and windows were delivered to BAE systems on November 10, 2004. Given the difficulties with the windows, BAE will not need maintenance support for the collimator and this report is the final activity under the contract. It represents full compliance by Xmetrics.

Windows

Because of the difficulties with the 10μ thick beryllium windows encountered with the predecessor collimator, all three test windows procured under the contract were 15μ thick. While this reduces the intensity of the beam it allowed us the greatest chance of success in the initial testing.

We built and delivered three large area windows that would keep the full atmosphere of helium from entering the source. The first was a simple grid structure with 100μ wide ribs that supported the foil. The second was a similar window except that the central square of the grid was never cut out. The idea was to protect the center of the foil against the worst ravages of the pinch. The third window featured a grid as in the first one, but also a thin mesh that would distribute the load more finely.

All three windows were fabricated with no difficulty. They held vacuum and transmitted x-rays as designed. Window number one is shown in Figure 1 after its failure on the pinch source.

Collimator

The collimator was developed over a 20 month performance period. This collimator utilized thin, nested mirrors for the first time. Xmetrics expected that this would represent a technical challenge and indeed it did.

The first version of the collimator featured 125μ stainless mirror substrates. These mirrors were polished and coated by a variety of techniques, none of which proved to be adequate in both figure and polish to meet the specifications. A picture of the collimator is presented in Figure 2

To solve the problem we went to polished silicon substrates of 600μ thickness. These proved to meet specification. However, because of the greater substrate thickness, fewer mirrors could be nested and the resultant gain dropped.

Xmetrics is investigating techniques to move back to thinner substrates, thereby raising gain.

Performance at Xmetrics

To ensure performance prior to delivery at BAE Xmetrics built a testbed facility. This featured a soft x-ray Manson source with an adapter to use the foil windows at the same distance from the source as in the pinch. The x-rays emerged into a helium chamber. At the correct distance from the source was a proportional counter mounted on a three axis positioner which was used to measure gain and uniformity. Alternatively, film could be placed at the focal plane to search for non-uniformity.

Initially we had hoped to achieve a net gain of 3.8 from the high gain collimator. The thick windows, by shifting the spectral output to higher energy reduced the expected gain to about 3.2. The thicker mirrors further reduced the expected gain to about 2.4. When the gain of the collimator was measured, we found a gain of about 2.3, in agreement with what was expected. When an adequate thin mirror technique allows for denser packing of mirrors, the gain will undoubtedly rise to above 3.

The uniformity of the flux at the focal plane was initially poor. Several factors caused this. First, the collimator was out of alignment. A simple shimming on one side solved this problem. Second, several of the mirrors were poorly aligned within the stack. Individual analysis and correction of the setting solved this problem. Third, toward the edge of the field of view, the gain rose due to poor curvature control of the silicon near its ends. This was solved by spreading the focus further, at which point, the collimator met specification in the Xmetrics testbed.

We believe that the collimator would likely have had a similar set of problems when first placed on the pinch source. Each source is slightly different and the optic needs to be tuned to maximize performance in any given setup. We believe the techniques developed

for correction of uniformity problems would rapidly allow for correction of any problems on other sources.

Delivery to BAE

Webster Cash of Xmetrics hand carried the (rather fragile) collimator to BAE for delivery and testing on November 10, 2004.

The window and collimator were mounted on the source without difficulty. Figure 4 shows the collimator in position.

When the source was turned on, the first windows popped within 100 pulses of the source. The other two windows fared no better. Because of the extreme speed with which the windows popped, no useful data were obtained.

Next

We have shown that high gain collimators of great uniformity are possible, but they need further development. Were the project to continue past this point the next steps would be clear.

1. The key problem is the windows. When the pinch source is opened up for a greater solid angle of x-rays to escape, the intensity of the pressure pulses increases as does the flux of small particles. Together these blow out the thin windows. Techniques for suppressing these effects will be needed before a high gain collimator can be employed.
2. Further investigate thin mirrors so that the gain may be increased to the level predicted theoretically.

Appendix F

SRL-F-10-2006

**IMPROVE X-RAY OUTPUT FROM BAE DPF
BY A FACTOR OF FIVE**

Prepared by

Science Research Laboratory, Inc.
15 Ward Street
Somerville MA 02143

DRAFT FINAL TECHNICAL REPORT

06/07/05 TO 10/20/06

Subcontract No. 200428

Prepared for

**BAE Systems
Information and Electronic Warfare Systems
Nashua, NH 03060**

10/20/06

Improve X-Ray Output From BAE DPF By a Factor of Five

Table of Figures

Figure 1 Schematic of anode, foil window and shock wave interaction.....	1
Figure 2 Anode design with shock attenuators.....	1
Figure 3 Photograph of the four uncooled anodes tested under this effort.	2
Figure 4 Block-diagram of diagnostics system for shock wave measurements.....	3
Figure 5 Pressure transducer (sensing area is covered with black vinyl film) installed into a mechanical adapter. An in-line amplifier is connected to the pressure transducer.	4
Figure 6 Block-diagram of system for Fiber Optics Transmission of the Analog Signal (FOTAS)	4
Figure 7 Photo of the FOTAS System.....	5
Figure 8 Transmission of rectangular pulse via FOTAS system.	5
Figure 9 Oscillograph traces of Rigowski coil current and transducer pressure.	7
Figure 10 Slotted anode design.	8
Figure 11 X-ray dosage versus shock overpressure at the foil window location.....	9
Figure 12 Shock overpressure versus time of transit from pinch to foil window.....	9
Figure 13 X-ray dosage versus shock overpressure at the foil window location.....	10
Figure 14 Shock overpressure versus time of transit from pinch to foil window.	10
Figure 15 X-ray dosage versus shock overpressure at the foil window location.....	11
Figure 16 Shock overpressure versus time of transit from pinch to foil window.	11
Figure 17 X-ray dosage versus shock overpressure at the foil window location.....	12
Figure 18 Shock overpressure versus time of transit from pinch to foil window.	12
Figure 19 x-ray dose Vs shock overpressure at foil window location	13
Figure 20 Shock overpressure versus time of transit from pinch to foil window.	13
Figure 21 Test of data correlation in the form for an intense explosion.	14
Figure 22 Unnormalized shock pressure for comparison with Figure 10.....	15
Figure 23 Details of the cooled anode design. The red portion is the tungsten tip.....	16

Table of Contents

1. Introduction	1
2. Diagnostics system for shock wave measurements	2
3. Experimental Results.....	7
4. Tests Results of Solid anode with Enlarged Aperture	12
5. Theory of Intense Explosions	13
6. Detailed Engineering Design of Cooled Anode	15
7. Summary and Conclusions:	16

1. Introduction

A Dense Plasma Focus (DPF) device is used to produce a point x-ray source for micro-lithography. This source is produced by an electromagnetic pinch that is concentrated on the centerline near the tip of the discharge anode. That is shown in schematic in [Figure 1](#).

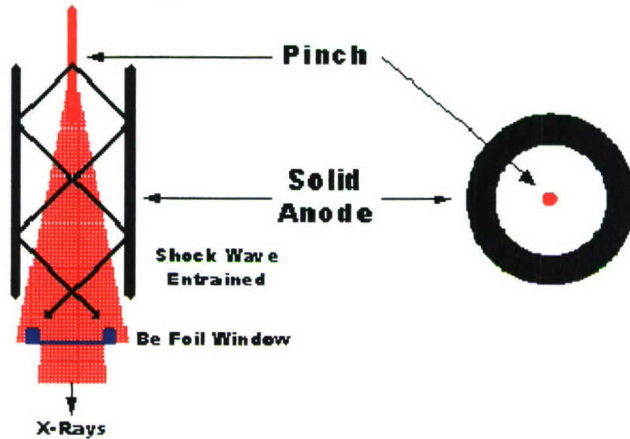


Figure 1 Schematic of anode, foil window and shock wave interaction.

A portion of these x-rays passes through a beryllium foil window at the base of a hollow anode. This foil separates the neon DPF environment from the stepper air environment. Strong shock waves are produced by the focus and they impinge on the beryllium foil window after some attenuation in transit. Repeated shock overpressure is one cause for rupture of this foil so steps have been taken to attenuate shock strength. The anode shown in section in [Figure 2](#) has attenuating baffles for this purpose.

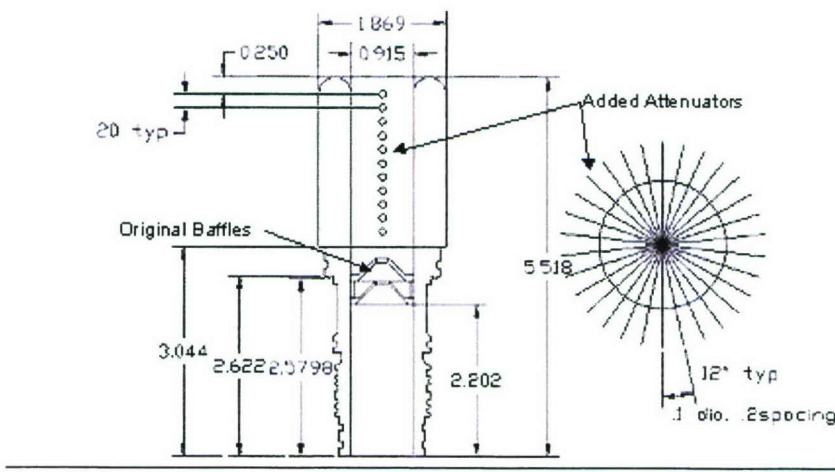


Figure 2 Anode design with shock attenuators.

The original baffles were as close as is practical to the pinch while avoiding excessive erosion due to the pinch environment. The solid angle of the center hole in the baffles as viewed from the pinch region defines the acceptance fraction of x-rays and thereby the efficiency of the device.

There are additional holes around the periphery of the two baffles that are out of registration, that is, there is no clear view from the pinch through both baffles. These were thought to act as a choke to provide dissipation of the shock wave in transmission.

This study is an effort to further reduce foil overpressure without added reduction in x-ray yield. This added margin in foil loading may then be used to optimize the trade between increased x-ray utilization and foil survival. Three uncooled anodes were fabricated and one of these had slots machined into its annulus. This anode was retested after it was subsequently plugged. Figure 3 is a photograph of the four anodes that were tested.



Figure 3 Photograph of the four uncooled anodes tested under this effort.

In the next Section, the diagnostics developed to measure the shock waves will be presented followed by the test results of the four uncooled anodes

2. Diagnostics system for shock wave measurements

A strong shock wave is characterized by fast rising pressure pulse that can be measured by a pressure transducer. Parameters of the fastest commercially available pressure transducers (from PCB Piezotronics, Depew, NY) are listed in Table 1.

Table 1

Pressure transducer specifications

Model	134A24
-------	--------

Sensing bar material	Tourmaline
Dynamic range	1000 psi (68 atm)
Sensitivity	5 mV/psi (0.1 mV/torr)
Resolution	0.02 psi (1 torr)
Resonant Frequency	≥ 1.5 MHz
Rise Time (reflected)	≤ 0.2 μ s
Low Frequency Response (-5%)	0.25 Hz
Length	1.6"
Diameter	1/2-20 UNF thread

The pressure transducer was sealed in a specially designed mechanical adapter and was installed in the anode at the Be foil interface. Shock wave measurements are complicated by the presence of a high voltage pulse that is transiently imposed on the anode. A fiber optic system for transmitting the analog pulse signal was built for this purpose. Block-diagram of the diagnostics system is shown in [Figure 4](#).

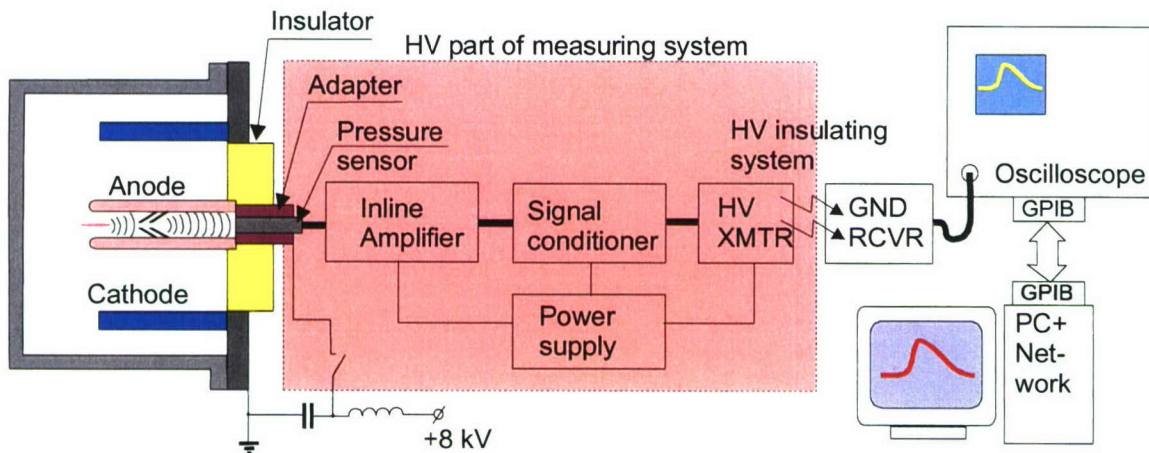


Figure 4 Block-diagram of diagnostics system for shock wave measurements.

This pressure pulse diagnostic system includes: a pressure pulse transducer with a signal conditioner, power supply, amplifier, fiber optics transmitter (modulator), fiber optics receiver (demodulator), digital oscilloscope and GPIB interface for computer data acquisition. The signal is transmitted via fiber optics for high voltage (up to 50 kV) isolation from the recording equipment. The pressure transducer that was installed into mechanical adapter is shown in [Figure 5](#).

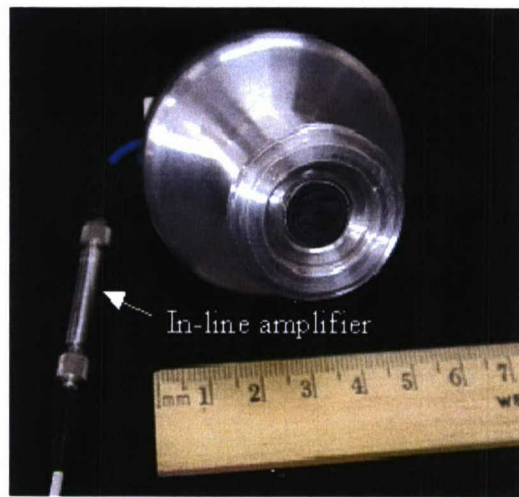


Figure 5 Pressure transducer (sensing area is covered with black vinyl film) installed into a mechanical adapter. An in-line amplifier is connected to the pressure transducer.

A block-diagram system for the Fiber Optics Transmission of Analog Signal (FOTAS) is shown in [Figure 6](#).

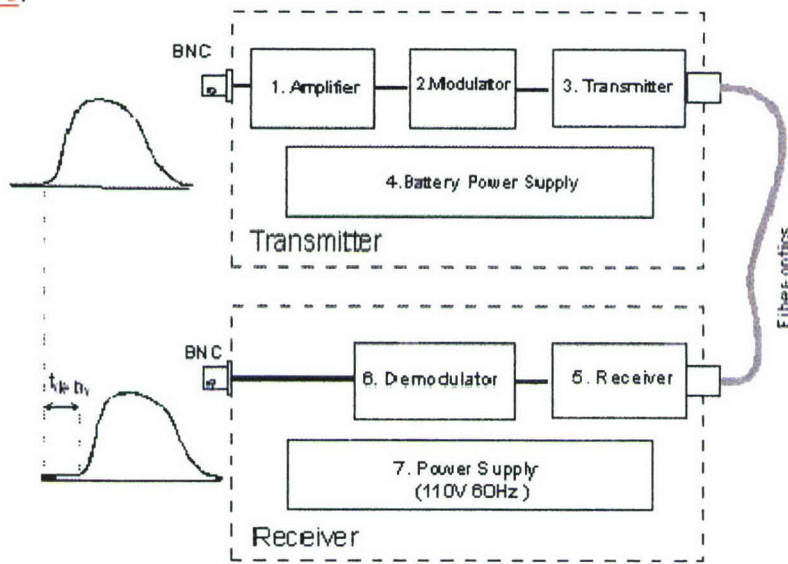


Figure 6 Block-diagram of system for Fiber Optics Transmission of the Analog Signal (FOTAS)

A photo of the FOTAS system is shown in [Figure 7](#).

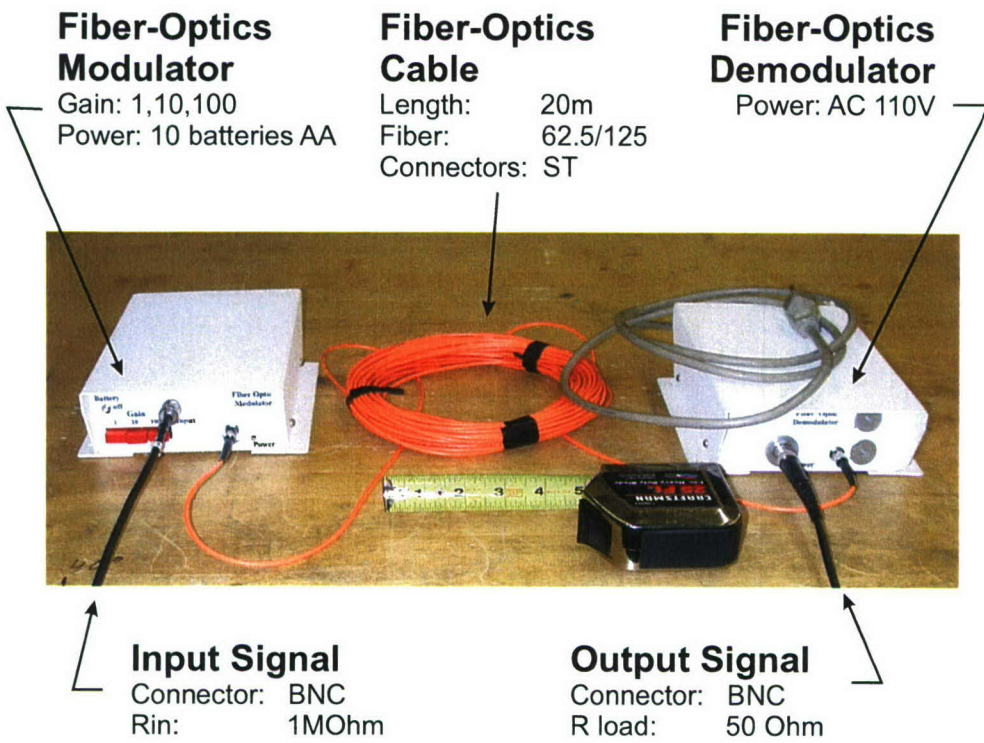


Figure 7 Photo of the FOTAS System

A calibration waveform was a rectangular pulse transmitted via FOTAS system as shown in [Figure 8](#).

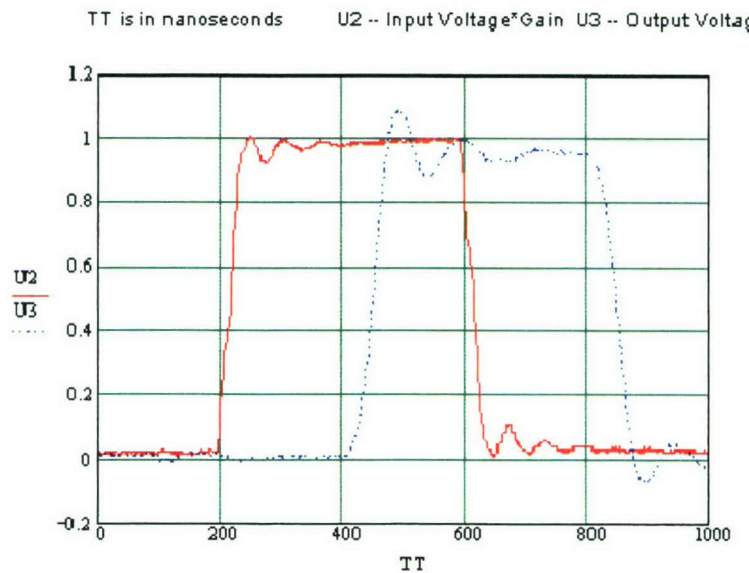


Figure 8 Transmission of rectangular pulse via FOTAS system.

Here the transmitted signal is recorded 230 ns later than the input signal. This time delay is fixed.

The transmitter of the FOTAS system contains an amplifier with a fixed gain coefficient (1X, 10X and 100X). The noise level of the FOTAS system is 20mV for all gain coefficients. For the gain of 10X, which was typically used for these tests, this corresponds to a pressure of 20 torr. The FOTAS system is linear for output signals up to 2.0 V bandwidth of the system is 9 MHz.

The combination of the pressure transducer with the FOTAS system enables one to measure pressure pulses with the following parameters:

Pressure Pulse Rise Time:	$\leq 0.2 \mu\text{s}$
Pressure Pulse Duration time:	1 ms
Maximum Pressure Peak:	15 atm
Sensitivity for the gain of 10X:	1 torr/mV
Equivalent noise level for the gain of 10X:	20 torr

Shock strength and arrival time at the foil window location were measured in a configuration where the foil was replaced by a piezoelectric transducer. A detector positioned in the discharge chamber wall provided an uncalibrated measure of x-ray dosage. These are the three key measurements that are reported here.

In summary, this system includes: a pressure pulse transducer with a signal conditioner, power supply, amplifier, fiber optics transmitter (modulator), fiber optics receiver (demodulator), digital oscilloscope and GPIB interface for computer data acquisition. The signal is transmitted via fiber optics for high voltage (up to 50 kV) isolation from the recording equipment. A strong shock wave is characterized by fast rising pressure pulse that can be measured by the pressure transducer (from PCB Piezotronics, Depew, NY) with a demonstrated rise time less than 200 nsec. The transmitter contains an amplifier with fixed gain coefficients (1X, 10X and 100X). The noise level of the FOTAS system is 20mV for all gain coefficients. For the gain of 10X, which was used for all reported tests, there is a one to one conversion between signal in mV and pressure in Torr. The FOTAS system is linear for output signals up to 2.0 V and the bandwidth of the system is 9 MHz. A representative oscillograph trace from tests is shown in [Figure 9](#). The discharge current waveform shows spikes at the time of discharge initiation and at the time of pinch (pick up). This provides the time origin for measurement of the delay for shock arrival at the pressure transducer. In this case the pulse overpressure is approximately 270 Torr after a delay of 34 microseconds.

TT is in microseconds U1 -- Voltage, U2 -- Rogowski coil, U3 -- Pressure

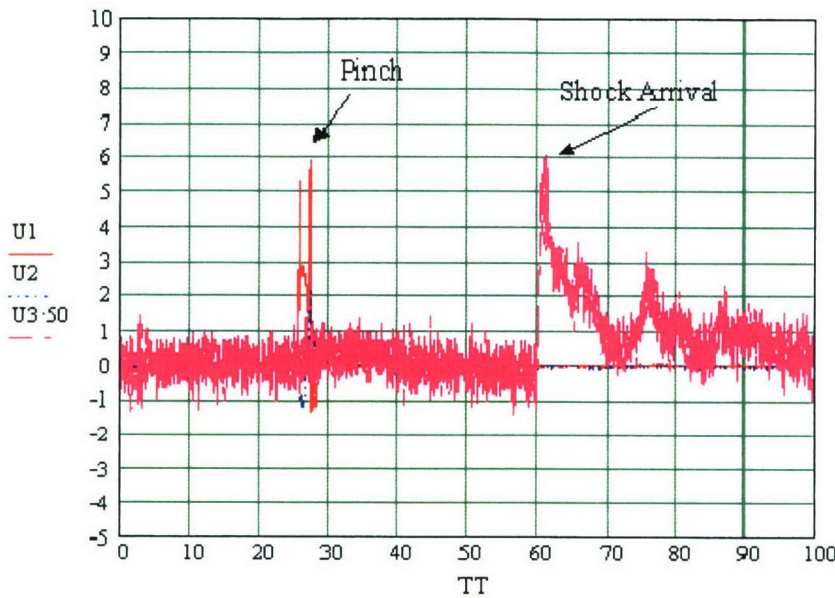


Figure 9 Oscillograph traces of Rigowski coil current and transducer pressure.

3. Experimental Results

As stated earlier, measurements were performed on four different anode geometries. The first, called the original the anode annulus (See photograph in [Figure 3](#)). The original anode had the baffle pair as shown and these had a series of peripheral holes out of registration as described previously. The second anode, called the perforated anode, had the additional holes as shown in [Figure 2](#). These were intended to provide pressure relief for the shock in transit from pinch to foil window. Test results compare the trade between added shock attenuation and possible reduction in x-ray yield. The third anode design, called the slotted anode, is shown in [Figure 6](#). It has slots in the annulus instead of perforations. These slots are much more limited in extent than the perforations. It has two additional features intended to increase shock attenuation. The baffles with peripheral holes were replaced by ones with only the center collimating holes. The view taken was the “choke” holes in balance likely added to transmitted shock strength. This anode also had undercut rings around the inner wall, as indicated, to act as scramblers and to break-up the plasma as it propagates down the barrel of the anode. The fourth anode is characterized by the simple aperture baffle as distinguished from the choke baffle. It has the baffle and undercut grooves in [Figure 10](#) but the slots were plugged to form again a solid annulus anode. This development of design revisions was guided by test results from each preceding configuration. Test results below show some striking differences in performance between configurations and the progression to significant performance improvement with minimal anode design changes.

Measurements were done at several levels of neon background pressure as listed in results.

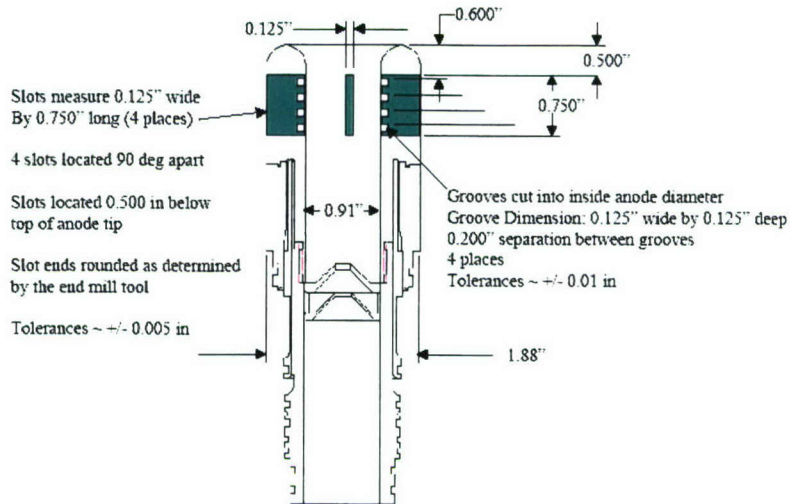


Figure 10 Slotted anode design.

All anodes were uncooled to simplify fabrication and testing. Burn in of approximately 1,000 pulsed was conducted after anode installation for each test series. All reported tests were done at a charge voltage of 7.8 kV in bursts of five or ten seconds at a pulse rate of 10 Hz. Data was recorded for the last pulse in five pulse bursts at 10 Hz. Data was selectively recorded by ignoring drop outs when drop outs were frequent. Drop out means no signal on x-ray dosage diagnostics. Key measurements of x-ray dosage, transducer pressure rise and pressure pulse time of flight are presented here. Time of flight is the time delay from discharge initiation to pressure pulse arrival at the transducer.

Original solid anode: Tests results for the original solid anode are presented in Figures 11 and 12 at five levels of neon background pressure. The dose data in Figure 11 is in a broad range of about 0-15 Joules, with a mean of 5.59 J. Shock strength data ranges from roughly 200-700 Torr with a mean of 404 Torr. Broad scatter is likely indicative of an unseasoned anode, since extensive burn-in was not practical without cooling. Nonetheless, data in this format will show clear trends in performance between different anode configurations.

Pressure is plotted against shock transit time in Figure 12. Data in this format shows a correlation despite the wide scatter. These data will be discussed further in the context of the theory of intense explosions. For the present this format provides a test for consistency in performance.

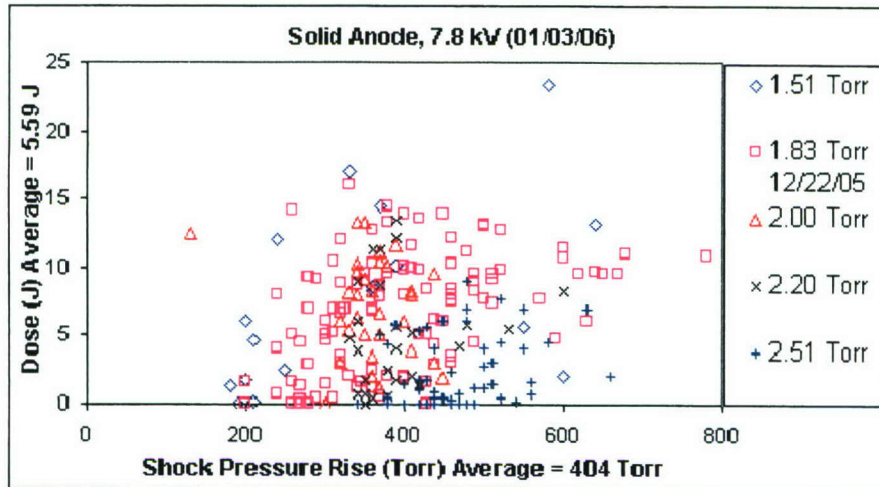


Figure 11 X-ray dosage versus shock overpressure at the foil window location.

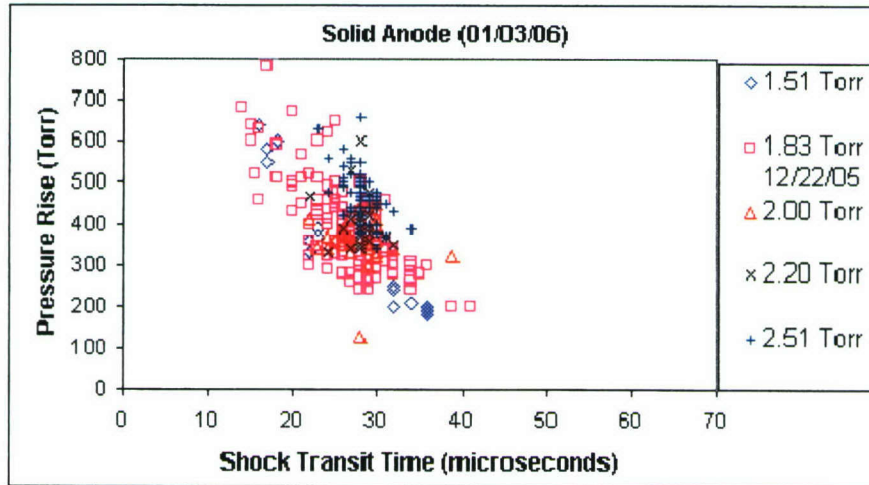


Figure 12 Shock overpressure versus time of transit from pinch to foil window.

Perforated anode: Results in the same formats are shown for the perforated anode in Figures 13 and 14. Axis scales are the same in all cases to allow a simple visual comparison of results. The dose data in Figure 13 is in a range of about 0-5 Joules, with a mean of 2.22 J. Shock strength data ranges from roughly 50-250 Torr with a mean of 136 Torr. Pressure is plotted against shock transit time in Figure 14. Results for the original solid anode solid and for perforated anode appear as separate regions of what may be the same functional correlation.

The clear conclusion from comparison of results for these two anodes is: the perforated anode does provide better shock attenuation but at a roughly proportional decrease in x-ray yield. The number of drop-outs (no measured dosage) was also higher for the perforated anode although this is not shown in the selected data.

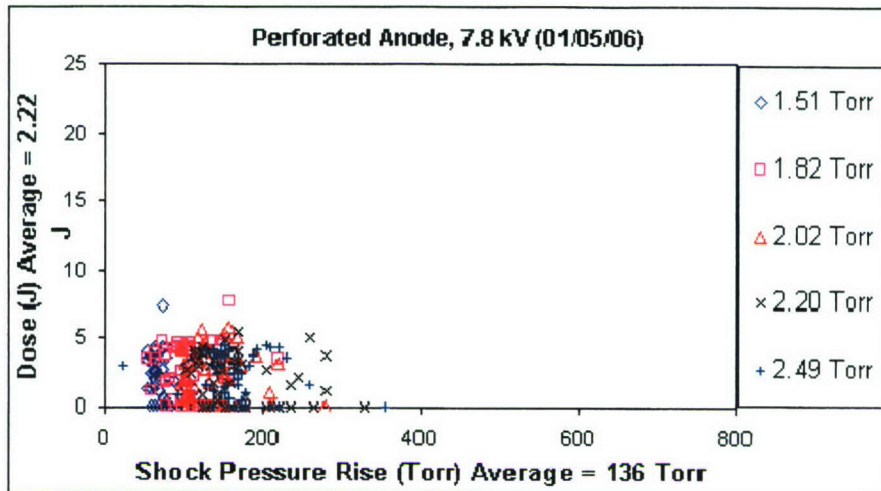


Figure 13 X-ray dosage versus shock overpressure at the foil window location.

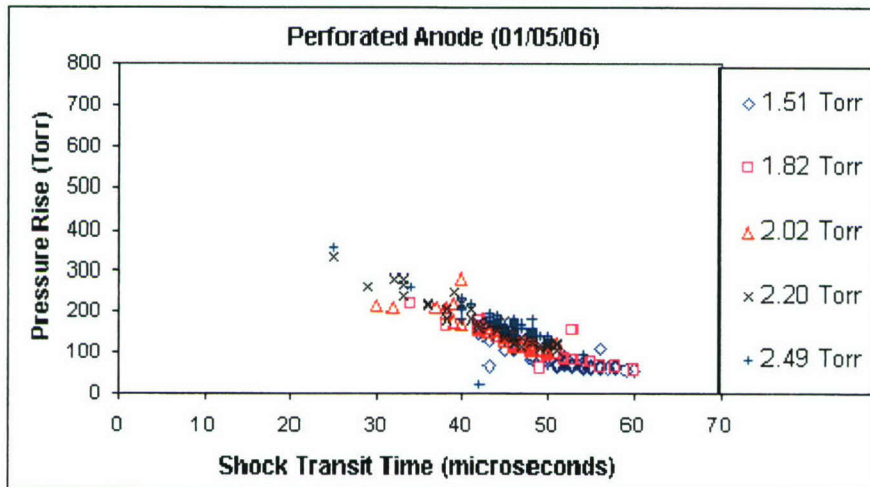


Figure 14 Shock overpressure versus time of transit from pinch to foil window.

Slotted anode, single aperture baffle: Results for the slotted anode with only a center hole in the baffle are shown in Figures 15 and 16. Dose data in Figure 15 is in a range of about 0-20 Joules, with a mean of 6.67 J. Shock strength data ranges from roughly 50-250 Torr with a mean of 106 Torr. Pressure is plotted against shock transit time in Figure 16. The correlation observed in previous results appears to apply here also

Direct comparison of Figure 9(a) with previous data is slightly misleading. Data at one additional Neon pressure level was included here, 1.27 Torr. With that excluded the average dose is reduced from 6.67 J to 5.88 J. Still the clear conclusion from comparison of results for these three anodes is: the slotted anode does provide as good shock attenuation as the perforated anode but at an x-ray yields as good or better than the original solid anode.

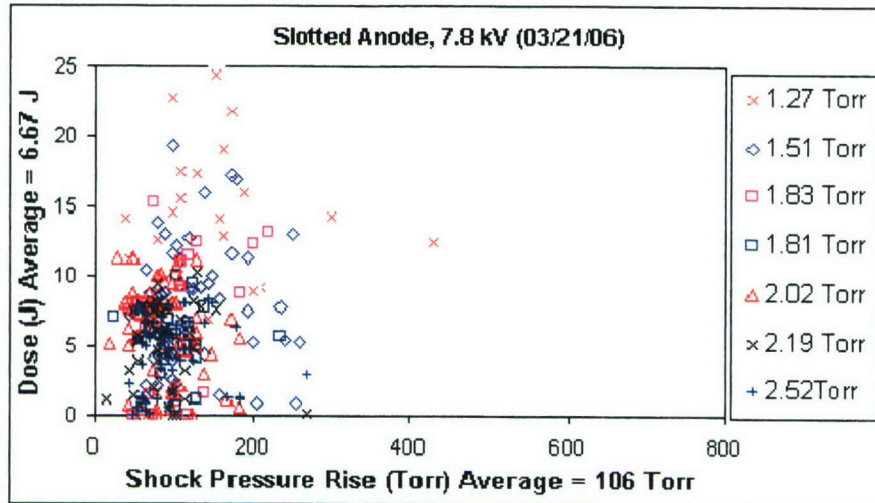


Figure 15 X-ray dosage versus shock overpressure at the foil window location.

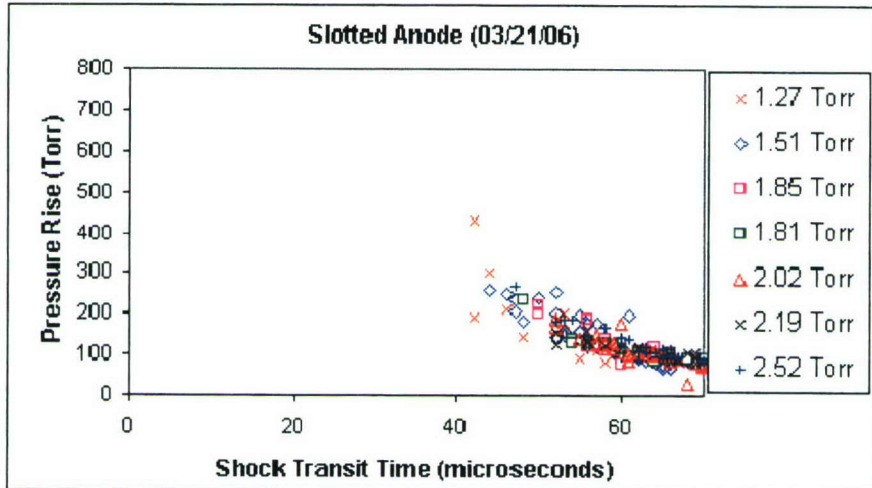


Figure 16 Shock overpressure versus time of transit from pinch to foil window.

Solid anode, single aperture baffle: The slotted anode departs from the original solid anode in three respects: the slots through anode walls, the undercut rings on the inner wall and the elimination of peripheral holes in the baffles. The first of these presents a significant challenge in anode cooling. Also, the removal of peripheral holes in the baffles was thought to have provided the major gain in performance. Consequently, the anode was reworked by plugging the slots in order to provide a manageable configuration for future cooling design.

Results for the anode with single aperture baffles are shown in [Figure 17](#) and [Figure 18](#). Dose data in [Figure 17](#) are in a range of about 0-25 Joules, with a mean of 9.32 J. Shock strength data ranges from roughly 50-350 Torr with a mean of 166 Torr. Pressure is plotted against shock transit time in Figure 10(b). The previously observed correlation again applies.

Comparison of [Figure 17](#) with best previous results, [Figure 15](#), shows essentially equal performance. Mean x-ray yield is increased by 40 % while mean shock overpressure is increased

by 57 %. So this last configuration is superior in terms of both performance and fabricability for cooled operation.

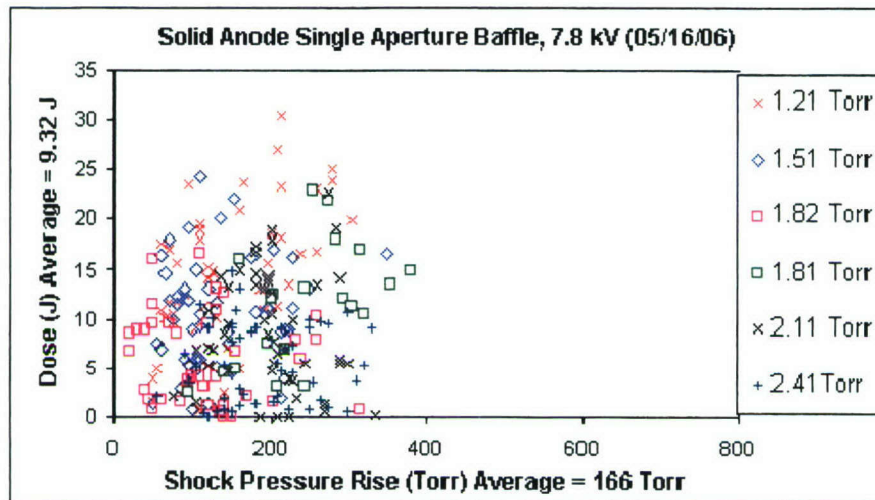


Figure 17 X-ray dosage versus shock overpressure at the foil window location.

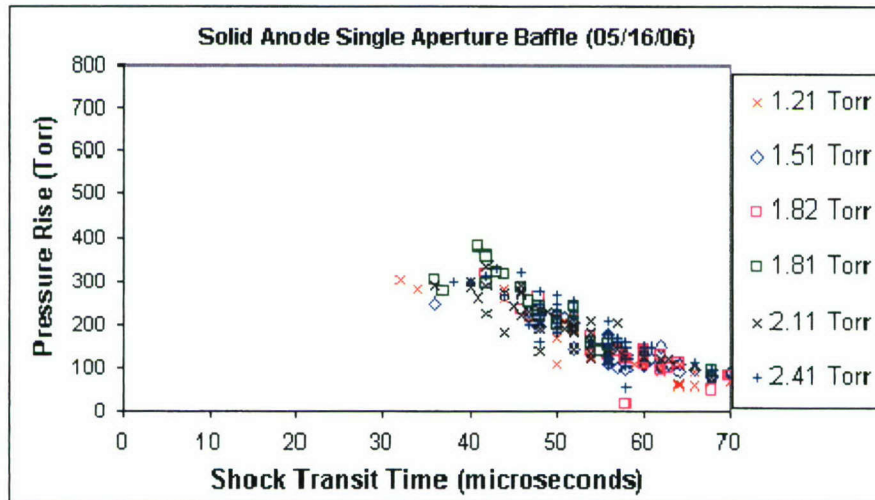


Figure 18 Shock overpressure versus time of transit from pinch to foil window.

4. Tests Results of Solid anode with Enlarged Aperture

A final set of data was taken with the solid anode with the baffle having a single orifice. The diameter of the orifice was enlarged by a factor of two to learn if the shock waves from this new configuration would be adequately decreased so as not to blow-out the Be foil windows.

The results are presented in [Figure 19](#) and [Figure 20](#).

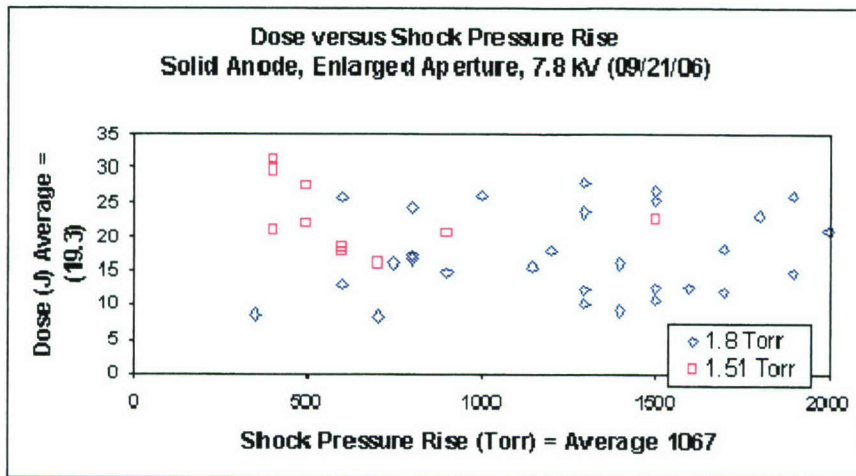


Figure 19 x-ray dose Vs shock overpressure at foil window location

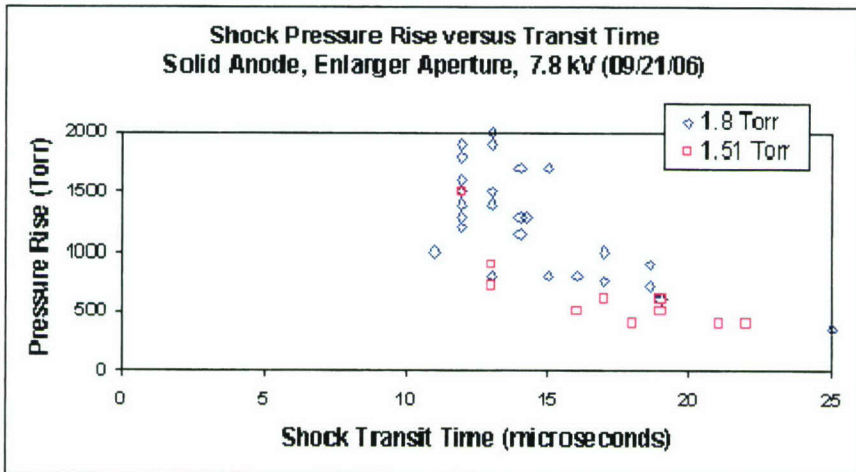


Figure 20 Shock overpressure versus time of transit from pinch to foil window.

From the data in [Figure 19](#) and [Figure 20](#), it appears that operating the solid anode with the orifice aperture increased by a factor of four, the foil window will survive provided one operates the DPF at 1.5 torr. Since the energy per pulse at these pressures was an acceptable 19 joules, which is considerably higher than for the results for the anodes, the DPF at BAE will provide an increased x-ray yield of 4-5, which was the goal of this effort.

5. Theory of Intense Explosions

Intense explosions have been analyzed extensively within the USA, UK and the previous USSR. The presentation by L. I. Sedov (Similarity and Dimensional Methods in Mechanics, Academic Press, New York, 1959) is used here for comparisons with measurements. Intense explosions refer to the flow fields from point source, line and planar energy releases where the shock strength is so large that the static pressure of the ambient gas may be ignored. The case of planar energy release is used to attempt to correlate data in Figure 8. These data were chosen

simply because they show good performance with the least systematic variation over the course of test day. The complex phenomenon as depicted in Figure 1 with inclusion of the attenuating baffles is not likely to be well characterized by a planar explosion. Still, it may be instructive to apply that analysis.

Two important relationships for released (deposited) energy, shock overpressure and shock transit time are derived from this theory. In the strong shock limit the pressure rise after reflection at the transducer is three times the incident value, for a monatomic gas. With this adjustment the analysis of Sedov yields the following two equations,

$$(\Delta p / \rho)^{1/2} = L/t \quad (1)$$

$$E_0 = 0.606 \cdot \Delta p \cdot L \cdot A \quad (2)$$

where Δp is reflected shock overpressure, ρ is ambient gas density, L is distance from pinch to transducer, t is transit time from pinch to transducer, E_0 is the deposited energy and A is the cross-sectional area of the anode opening. These deceptively simple equations apply for one-dimensional (planar energy release) explosions in a monatomic gas. The deposited energy would not be that actually associated with the pinch since the anode geometry is designed to attenuate shock strength. If this analysis has meaning the derived E_0 might be compared with the actual deposited energy to serve as an indicator of attenuation efficiency.

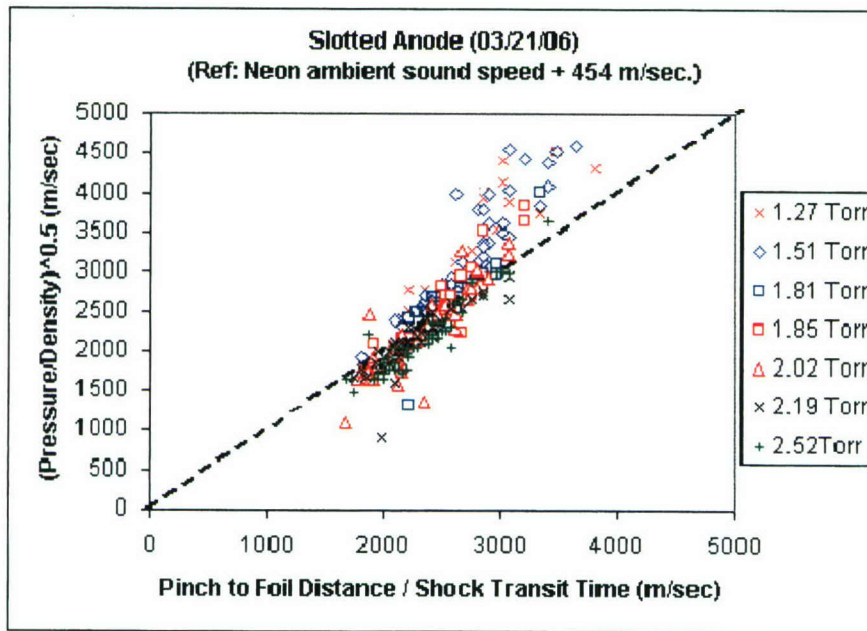


Figure 21 Test of data correlation in the form for an intense explosion.

To test the relevance of explosion theory the results in Figure 9 are recast in the form of Equation (1). These are plotted in Figure 15. The theory is represented as a straight line of slope unity. The data on the whole correlate quite well considering no fitting parameter was used. The scatter is perhaps too large to determine if the density normalization of pressure provides correlation. To test, this unnormalized pressure data is presented in Table 11 in the format of Table 10. Display of square root of pressure was chosen to allow direct visual comparison.

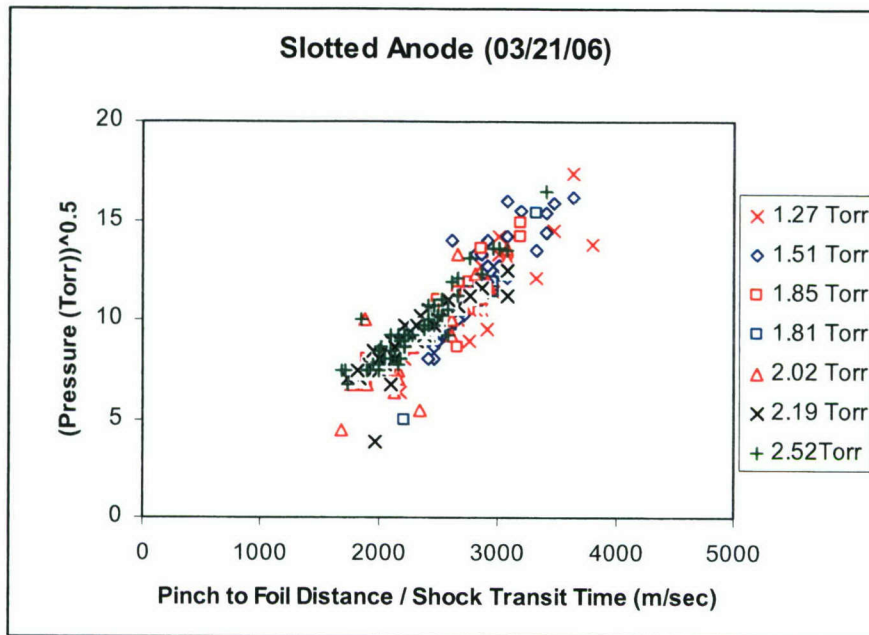


Figure 22 Unnormalized shock pressure for comparison with Figure 10.

Density scaling in Figure 11 may provide somewhat better correlation (compression of data) than Figure 16. More accurate measurements may be needed to verify this. A cooled anode will provide such measurements since that will allow the repeatability that is associated with a well-seasoned cathode.

If in fact this correlation applies we might ask: What practical insight will it provide? Equation (2) provides the negative prediction that, for a fixed geometry, there is a direct relationship between x-ray yield and shock overpressure. This means there is no dependence on background density (pressure). Background pressure may then be chosen strictly on the basis of discharge optimization.

6. Detailed Engineering Design of Cooled Anode

SRL completed a detailed engineering design of a cooled anode based on the data, presented above, obtained from testing the uncooled anodes. Figure 23 shows two perspectives of the design. The anode has been designed with slots in the annulus, and a baffle with only one orifice. Fortunately, the slots may not be necessary and they are easily removed. The inner surface of the anode has grooves to break-up the plasma after the pinch to rapidly cool the plasma as it propagates down the inside of the anode. This feature will increase the lifetime of the baffle and anode and simultaneously decrease the debris.

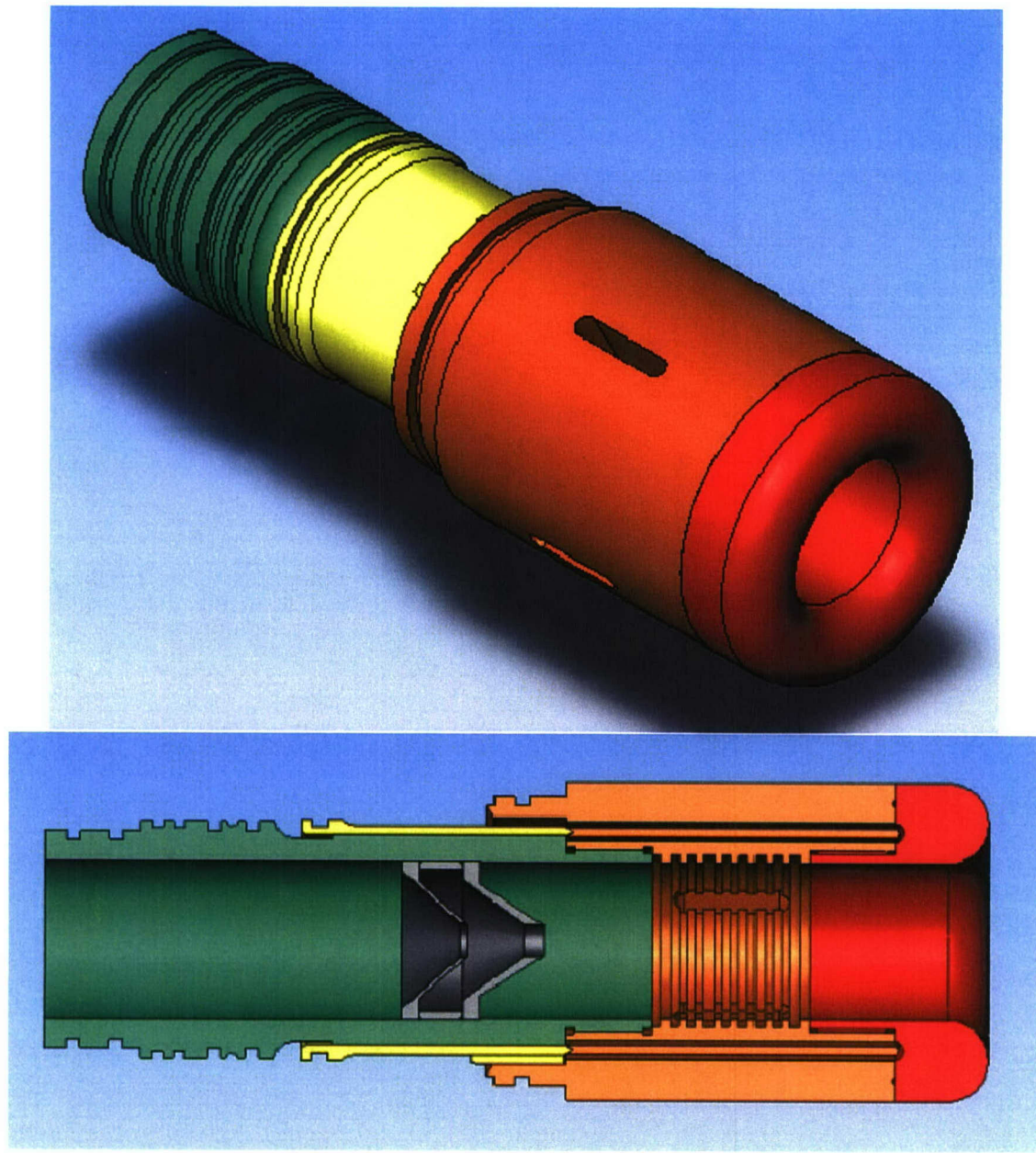


Figure 23 Details of the cooled anode design. The red portion is the tungsten tip.

7. Summary and Conclusions:

Four anode configurations were tested. In these comparative tests they were not actively cooled. A simple figure of merit for anode performance might be the ratio of x-ray yield to shock overpressure. This could be a basis for trade of dosage against risk of foil window rupture. Data are presented in a format to facilitate that comparison. Fabricability for the implementation of anode cooling is also a consideration. On these bases, the fourth anode variation, the solid anode with a single aperture baffle, is clearly superior. Global results for each anode configuration are listed in Table 2 for comparisons.

A more detailed study of the effects of neon background pressure on performance may be useful after active anode cooling is implemented.

TABLE 2: Comparison of performance for four anode configurations.

The last anode in the Table above was retested after the diameter of the orifice in the baffle was increased by a factor of two. This provides the possibility of increasing the x-ray collection by a factor of four. From the data presented in Figure 16, this anode will work provided the DPF is operated at 1.5 torr and below. The x-ray yield at this pressure was a very respectable 19 joules per pulse, which is twice that of the other anodes. It is not clear why the x-ray yield was that much more except to speculate that the anode had been used previously and perhaps was better “burned-in.” In summary, this effort has achieved its goal of increasing the x-ray yield from the DPF by the factors of 4-5.

Appendix G

Performance summary on a high power dense plasma focus x-ray lithography point source producing 70 nm line features in AlGaAs microcircuits

Rodney Petr,^{a)} Alexander Bykanov, Jay Freshman, Dennis Reilly, and Joseph Mangano
Science Research Laboratory, 15 Ward Street, Somerville, Massachusetts 02143

Maureen Roche, Jason Dickenson, Mitchell Burte, and John Heaton
BAE Systems, Microelectronics Center, 65 Spit Brook Road, Nashua, New Hampshire 03061

(Received 13 February 2004; accepted 27 April 2004; published 26 July 2004)

A high average power dense plasma focus (DPF), x-ray point source has been used to produce ~ 70 nm line features in AlGaAs-based monolithic millimeter-wave integrated circuits (MMICs). The DPF source has produced up to 12 J per pulse of x-ray energy into 4π steradians at ~ 1 keV effective wavelength in ~ 2 Torr neon at pulse repetition rates up to 60 Hz, with an effective x-ray yield efficiency of $\sim 0.8\%$. Plasma temperature and electron concentration are estimated from the x-ray spectrum to be ~ 170 eV and $\sim 5 \cdot 10^{19}$ cm $^{-3}$, respectively. The x-ray point source utilizes solid-state pulse power technology to extend the operating lifetime of electrodes and insulators in the DPF discharge. By eliminating current reversals in the DPF head, an anode electrode has demonstrated a lifetime of more than 5 million shots. The x-ray point source has also been operated continuously for 8 h run times at 27 Hz average pulse recurrent frequency. Measurements of shock waves produced by the plasma discharge indicate that overpressure pulses must be attenuated before a collimator can be integrated with the DPF point source. © 2004 American Institute of Physics. [DOI: 10.1063/1.1771502]

I. INTRODUCTION

The dense plasma focus is a candidate high-brightness soft x-ray source for next generation lithography (NGL) applications requiring sub-70-nm device structures. The plasma discharge characteristics of the DPF in neon result in its high-brightness capability in the soft x-ray region nominally centered around 1.1 keV photons that are useful for lithography purposes. Referring to Fig. 1, the DPF reported here utilizes a Mather-type geometry, in which a coaxial discharge arrangement uses a fast-rising current pulse. In our application the inner electrode is the anode and the outer electrode is the cathode. The plasma discharge is initially ignited along a dielectric insulator at one end of the electrode structure, and generates $\mathbf{J} \times \mathbf{B}$ forces that drive a plasma sheath down the electrode bore.¹ Once the plasma sheath has traversed the length of the anode, magnetic forces rapidly accelerate the plasma radially inward across the top of the electrode. The high pressure induced by these magnetic pinch forces rapidly compresses and heats a small volume of gas to high temperature. Plasma temperatures in a neon pinch can approach 200 eV for tens of nanoseconds while the plasma radiates x-ray energy.² The plasma pinch is ellipsoidal in shape, with its long dimension aligned along the anode axis, so that the DPF resembles a point source when x-ray energy is extracted along the electrode axis. Microcircuit lithography is performed with a precision stepper located near the x-ray source, which is used to position a semiconductor wafer and lithography print mask in the x-ray beamline.³

II. SOLID-STATE PULSE POWER

The dense plasma focus presents several technical challenges that must be overcome in order to extend the operating life of the x-ray source to levels suitable for commercial applications.⁴ One issue is minimizing pulser circuit inductance, which limits the peak drive current, and consequently DPF x-ray energy and conversion efficiency. The DPF is a low impedance load (on the order of milliohms) and it is difficult to achieve the desired driver inductance of 1–10 nH that is typically needed to match the driver impedance (given approximately as $\sqrt{L/C}$) with the plasma resistance. Another issue is electrode lifetime. The usual approach of driving a DPF with a simple sparkgap-switched capacitor bank leads to significant electrode damage because these pulsers generate ringing current discharges after termination of the pinch. Electrode damage occurs when current reverses polarity, because it drives ions into the anode, which in turn causes localized heating and electrode sputtering. Electrode vapor also coats out on the ignition insulator, leading to erratic plasma initiation and x-ray energy.

We have already developed a solid-state driver that eliminates current reversal in the DPF in order to improve DPF x-ray source lifetime.⁵ Eight parallel solid-state modules are used to generate drive currents for the DPF load. A schematic of an individual module is shown in Fig. 2, and consists of a storage capacitor that is connected to the x-ray head through a set of fast-switching thyristors and a saturable magnetic isolator stage. The magnetic isolator is used to delay turn-on current in the thyristors until their gate-cathode regions are fully ionized, and the isolator acts as a magnetic

^{a)}Electronic mail: rpetr@srl.com

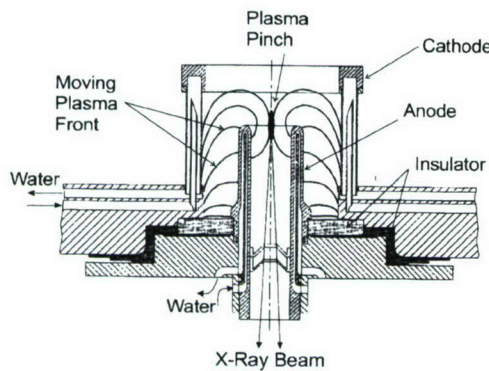


FIG. 1. Schematic of the DPF electrode structure. The plasma is initiated along the insulator surface and is driven up the coaxial electrode bore by $J \times B$ forces. The plasma pinches at the top of the anode and x rays are extracted back through the clear aperture in the anode.

diode that impedes current reversal through the DPF electrodes. This allows the snubber diodes placed across the storage capacitor to dissipate reflected energy due to the impedance mismatch with the DPF load and eliminate current ringing. Figure 3 shows a photograph of a solid-state drive module. We have upgraded each module to contain a $6 \mu F$ capacitor, and the full-scale driver has an effective storage capacitance of $48 \mu F$ with an output inductance of 12 nH . The capacitor charging supply is rated at 100 kJ/s , and the solid-state DPF driver is designed to operate up to 65 Hz pulse rate at 8 kV charge voltage. Figure 4 shows a photograph of the DPF x-ray housing assembly seen from the wafer stepper position. Table I summarizes the operating parameters of the solid-state DPF power system.

III. DPF THERMAL MANAGEMENT

A key issue with developing a high average power soft x-ray source is providing adequate thermal management to critical components. Table II summarizes the parameters of the DPF thermal management system. The DPF point source is water-cooled, and water calorimetry measurements indicate the percentage of input electrical power dissipated in the point-source subassemblies as follows: pulse power and snubber electronics: $\sim 20\%$; anode electrode: $\sim 30\%$, cathode electrode: $\sim 30\%$; and the combination of gas, insulator, and vacuum chamber: $\sim 20\%$. Consequently the anode and cathode electrodes can each dissipate up to 30 kW at the maximum design point of 100 kW input electrical power.

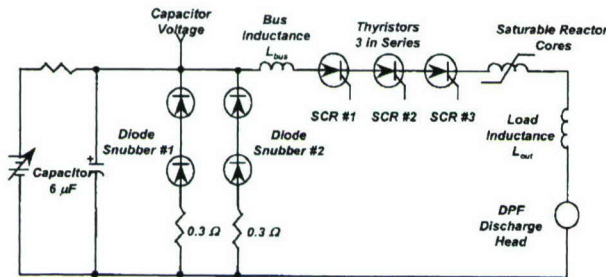


FIG. 2. Schematic diagram of a single-pulse power module used in the DPF point source. Eight parallel modules power the DPF discharge.

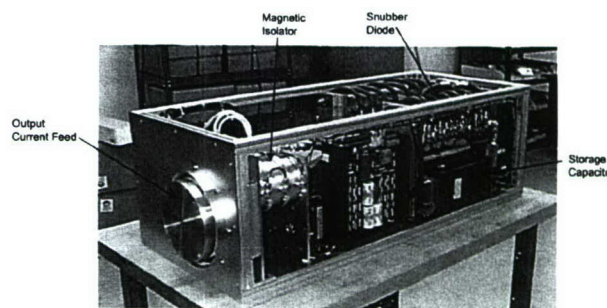


FIG. 3. Photograph of a DPF solid-state drive module. The module measures approximately 46 cm wide by 36 cm high by 107 cm long.

Assuming uniform heat distribution, the worst-case surface heat flux to the cathode is 300 W/cm^2 , which is manageable with water cooling. The maximum heat flux into the anode electrode is three times higher at 1 kW/cm^2 , however, which approaches the limit where water transitions from nucleated to film boiling at the cooling surface.⁶ If film boiling occurs, the local heat transfer coefficient will drop dramatically, and the local anode temperature will rapidly increase, which can result in electrode damage. We operate the electrode cooling loop at high pressure (approximately 19 atm at the anode tip, where heat flux is highest), which allows the ΔT across the electrode-coolant boundary to exceed 100°C for enhanced heat transfer, and still avoid tripping into film boiling. The DPF anode is operating at the limits of water-cooling capability at a heat flux density of around 1 kW/cm^2 , and increasing average input power further will require changing the cooling design in the anode. One approach is to operate the anode tip at higher temperature and utilize liquid-metal heat-pipe technology, which can operate at thermal flux densities approximately 10 times higher than water.⁷

IV. DPF X-RAY ENERGY SCALING

The plasma physics involved with high-energy DPF discharges is complicated, and does not lend itself to accurate predictive modeling. Various simulation codes like the SNOWPLOW model and its derivatives, and MHD codes have

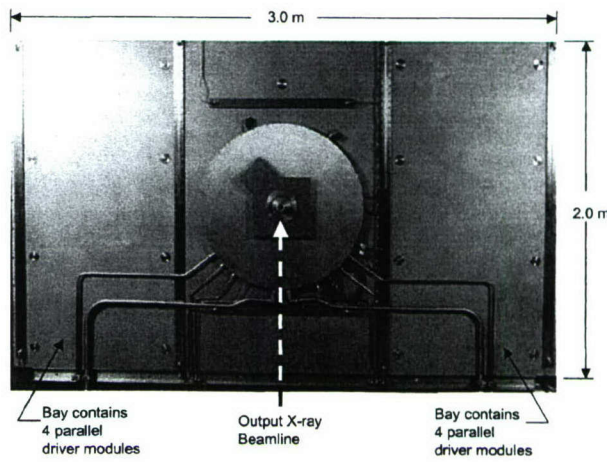


FIG. 4. Photograph of the DPF x-ray point source assembly. The structure measures 3.0 m wide by 2.0 m high by 1.5 m deep.

TABLE I. DPF solid-state driver performance.

Nominal parameters (8 module configuration)	Measured performance
Charge voltage	8 kV
Output current	260 kA into DPF with no current reversal
Current duration (half sine)	2.5 μ s FWHM
Current rise time (10%–90%)	800 ns
Load energy (per pulse @ 8 kV)	1.53 kJ
Charging power supply rating	100 kJ/s @ 8 kV charge voltage
Maximum pulse recurrent frequency	65 Hz @ 8 kV charge voltage
Solid-state driver inductance	12 nH
Feed-plate inductance	2 nH
Total system inductance	14 nH

been developed and used with varying degrees of success to calculate the dynamics of imploding plasmas.^{8,9} Design trade-offs for optimizing x-ray output involve adjusting the plasma rundown time to coincide with peak discharge current, in order to produce the highest magnetic pinch pressure and plasma temperature. Plasma velocity v_p scales with discharge current I_o , magnetic field B_o , gas density ρ_g , anode outer radius r_o , as

$$v_p = \sqrt{\frac{B_o^2}{2\mu_o\rho_g}}, \quad (1)$$

where μ_o is vacuum magnetic permeability, and the drive magnetic field B_o is

$$B_o = \frac{\mu_o I_o}{2\pi r_o}. \quad (2)$$

Anode diameter, length, and gas pressure are adjusted according to the pulse power current rise time to achieve optimal x-ray energy and yield. Figure 5 shows an open-shutter photograph of the DPF plasma ignition in neon gas. The view is along the electrode axis, where the illuminated inner ring is the anode, and the dark outer ring is a cathode flow plenum. Twenty-four individual cathode rods surround the anode structure. The brightly illuminated cylinder between anode and cathode is a sapphire insulator, which is covered with numerous surface discharge streamers that are generated by introducing a fast-rise time, high voltage pulse across

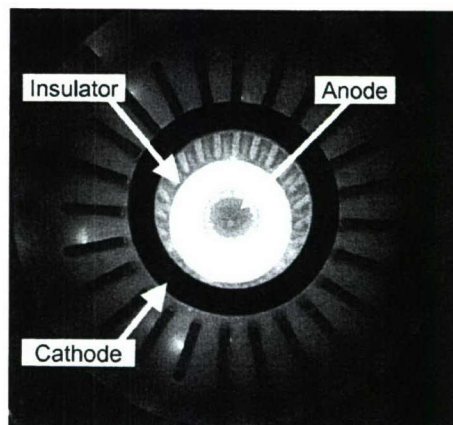


FIG. 5. Top view of the DPF discharge looking down the electrode axis. The inner cylinder is the anode, and the dark outer ring is the cathode plenum. Cathode rods extend down the discharge bore. The illuminated ring is the sapphire insulator.

the insulator.¹⁰ Igniting a spatially uniform plasma is critical to the overall performance of the DPF, because ignition non-uniformities can result in an unbalanced plasma front traveling down the electrode, which leads to poor x-ray emission. We typically ignite the surface discharge streamers along the insulator with rising voltage fronts exceeding 30 kV/ μ s.

Plasma temperature and x-ray energy measurements have shown that x-ray energy scales roughly between I_{peak}^2 to I_{peak}^4 for various Z-pinch machines.¹¹ For noble gases that produce primarily K-edge radiation, the literature reports that x-ray yield is higher, and scales approximately as $E \sim I_{\text{peak}}^4$. This scaling relation has been reported in DPFs for drive currents ranging from 500 kA to 3 MA.¹²

We have measured the same x-ray energy trend in our DPF system, but at lower currents varying from 200 to 330 kA. Figure 6 shows the average x-ray energy output for a sparkgap-switched DPF source operated at various energy

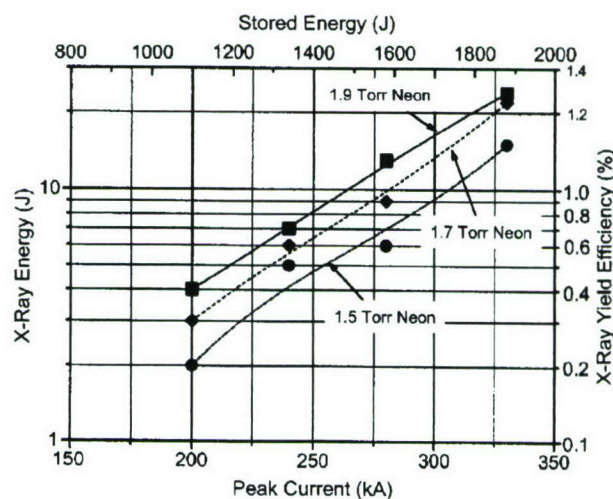
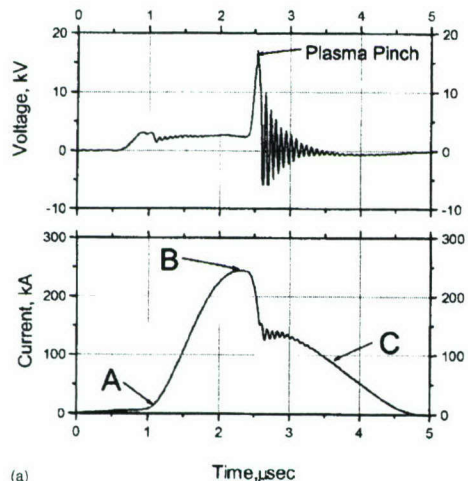


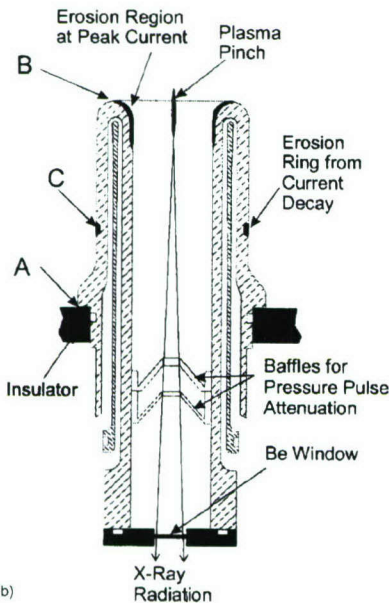
FIG. 6. Plot of measured average x-ray energy into 4π steradians versus peak discharge current for a sparkgap-switched DPF in neon gas. The effective x-ray energy conversion efficiency versus drive current and stored energy is also displayed. X-ray energy scales approximately with peak current raised to the 3.9 power.

TABLE II. Summary of DPF thermal management system.

Parameter	DPF source subassembly				
	Anode	Cathode	Insulator	Vacuum chamber	Power electronics
Heat dissipation @ 100 kW	30	30	5	15	20
input power (kW)					
Surface area (cm ²)	30	100	100	$8 \cdot 10^5$	N/A
Heat flux (W/cm ²)	1000	300	50	0.02	N/A
Water flow rate (1pm)	44	60	2	8	60
Inlet water pressure (atm)	19	10	0.4	0.4	1



(a)



(b)

FIG. 7. (a) Oscillogram showing DPF voltage and current waveforms, and (b) anode cross-sectional drawing showing approximately where in time the plasma resides on the anode during the current discharge.

levels and with varying gas pressure.³ Each of these data points represents the average of several hundred discharge measurements. The x-ray energy data reported here are referenced to a point source radiating into 4π steradians. X-ray energy was measured with an x-ray PIN diode detector¹³ that was calibrated to the spectral characteristics of the neon discharge.¹⁴ The general trend for output x-ray energy scales approximately with peak current to the 3.9 power. Figure 6 also shows that gas pressure plays an important role in optimizing output x-ray energy. This generally involves adjusting the anode electrode length to coincide with peak drive current and the plasma front arriving at the end of the electrode.

V. ELECTRODE EROSION MEASUREMENTS

We have operated the DPF x-ray point source continuously for many hours, and have collected accurate data on

TABLE III. Summary of anode erosion measurements.

Parameter	Specification
Anode type	Molybdenum body and tungsten tip
DPF storage capacitance (μ F)	48
Coulomb transfer per shot (C)	0.57
Number of shots ($\times 10^6$)	5.1
Initial anode mass (g)	1480
Mass loss (g)	176
Erosion rate ($\mu\text{g}/\text{C}$)	60
Projected anode lifetime (shots $\times 10^6$)	10

Parameter	Measured	Projected
Cathode lifetime (shots $\times 10^6$)	5 (Titanium cathode rods)	10 (Molybdenum rods)
Sapphire insulator lifetime (shots $\times 10^6$)	5	10

electrode erosion rates with the solid-state pulser. Figure 7(a) shows a typical DPF voltage-current waveform. The electrode current rises to peak value of 260 kA in approximately 1 μ s when the plasma pinches, after which snubber electronics dissipates the remaining energy in the circuit so that current does not reverse through the electrodes. Figure 7(b) shows a cross-sectional drawing of the anode, and calls out approximately where in time the plasma resides on the anode during the discharge pulse. Erosion measurements show that most of the electrode damage occurs at the anode tip, where peak current is highest, but there is also significant erosion lower down on the anode sidewall, which is from the current decay after the plasma pinch. This sidewall electrode erosion manifests itself as a thin ring around the entire anode structure, as indicated in the Fig. 7(b) drawing.

We have operated an anode that combines a molybdenum sidewall with a tungsten tip for 5.1 million shots. The measured anode electrode erosion, defined here as the ratio of electrode mass loss to electric charge transfer, is summarized in Table III. The tungsten/molybdenum anode showed an erosion rate at 60 $\mu\text{g}/\text{Coulomb}$ over its operating lifetime. Assuming uniform electrode wear, we project the tungsten tip can support 10-million shot operation before replacement. The higher 10-million shot rating corresponds to roughly 80 h of continuous operation in a fabrication facility.

Cathode and insulator erosion is also an issue with DPF x-ray energy and lifetime performance. The sapphire insulator has been tested with the tungsten anode to 5 million shots, and we project the insulator can last up to 10 million shots before replacement is necessary. The cathode consists of water-cooled titanium hollow rods that have lasted up to 5 million total shots, and we project that changing the cathode material to molybdenum can provide greater than 10 million shot life on the cathode.

VI. DPF X-RAY PERFORMANCE MEASUREMENTS

For lithography applications, the user is primarily interested in maximum in-band x-ray energy, plasma pinch spa-

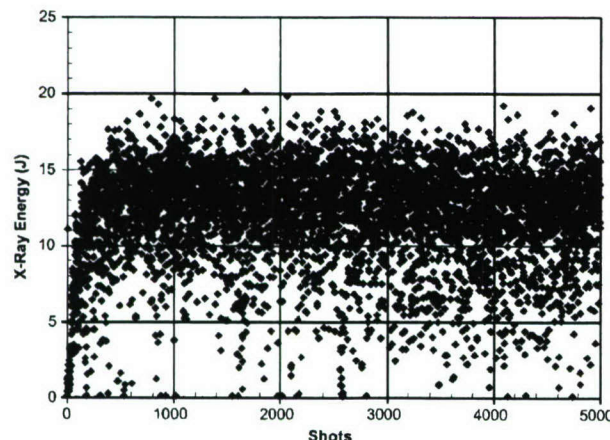


FIG. 8. Measured x-ray output energy at 8 kV charge voltage and 92 kW average input electrical power. Average x-ray energy is 12 J at 60 Hz pulse recurrent frequency and 2.4 Torr neon pressure.

tial stability, and long-duration source operation. We have operated the DPF at a maximum input power that produced 12 J of average x-ray energy into 4π steradians at 60 Hz pulse recurrent frequency for an effective x-ray power output of 720 W. The x-ray yield efficiency was $\sim 0.8\%$ at 260 kA peak current and 1.9 Torr neon, which is consistent with the measured output performance of a sparkgap-driven DPF presented earlier in Fig. 6. The character of the x-ray output as a function of shot count is shown in Fig. 8, and Table IV summarizes DPF performance specifications of this high power test. Maximum x-ray energy was 20 J, and the fractional standard deviation around the 12 J average was nominally 40%. The percentage of dropouts, defined as plasma discharges that produce less than 10% of the average x-ray energy, was less than 1%. For lithography exposures every x-ray pulse is recorded and integrated to track the total x-ray fluence delivered to the semiconductor wafer. The control of x-ray dose-on-target can be maintained to an accuracy of less than 0.1%, which provides for repeatable wafer exposures.

One issue with achieving long DPF electrode lifetime and reliable x-ray production is to ensure the plasma ignites uniformly around the coaxial structure. Electrodes can wear unevenly if the plasma sheet is unbalanced and preferentially resides on one side of the discharge structure. The tungsten/molybdenum anode that operated for 5 million shots showed

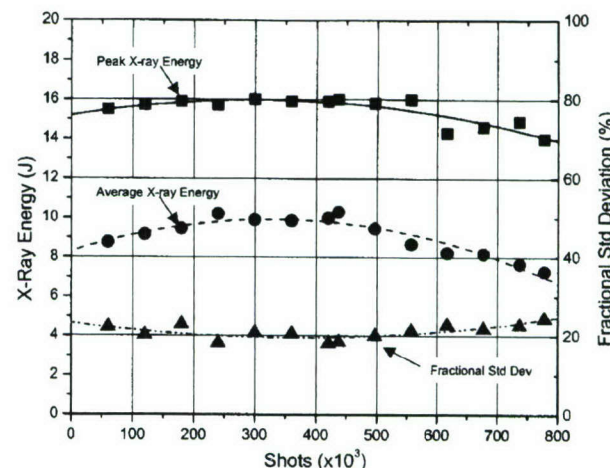


FIG. 9. Measured x-ray output energy with a tungsten anode for continuous 8 h demonstration test #3 listed in Error! Reference source not found. Each data point represents an average of nominally 50 K shots. Charge voltage is 7.8 kV and the effective pulse recurrent frequency is 27 Hz.

some nonuniform wear in a segment of its sidewall and tip that was approximately 30 deg along the outer anode circumference. Plasma ignition nonuniformity that fluctuates over long operating times can explain this uneven wear behavior. The character of x-ray data for continuous operation tests supports this premise. Figure 9 shows typical x-ray output characteristics for the DPF operating continuously for 8 h data points presented represent an average of nominally 50 000 shots. A detailed summary of performance statistics for three continuous-operation tests is presented in Tables V. We have at the present time operated an electrode set for 40 h before replacing electrodes. The average x-ray energy produced over the 40-h period varied between 7.2 and 9.1 J per shot, as indicated in Table V. More work is needed in the area of plasma ignition, especially at high average power operation, in order to fully understand the variability of the discharge as a function of the repetition rate and average power.

VII. DPF X-RAY BEAMLINE, SPECTRA, AND LITHOGRAPHY RESULTS

The x-ray beamline that supports photon propagation from the DPF source to the target wafer has important effects

TABLE V. Summary of DPF x-ray performance for continuous-operation demonstration tests.

Parameter	Test #1	Test #2	Test #3
Anode type	Tungsten	Tungsten	Tungsten
Charge voltage (kV)	7.8	7.8	7.8
Pulse recurrent frequency (Hz)	27	27	27
Neon pressure (Torr)	1.7	1.7	1.7
Peak x-ray energy (J)	15.2	14.7	15.4
Average x-ray energy (J)	7.2	7.2	9.1
Fractional standard deviation (%)	45	40	21
Dropouts (%)	0.26	0.51	0.02
Continuous operating time (h)	7	8	8

TABLE IV. Summary of DPF performance for highest output x-ray power operation.

Parameter	Measurement
Charge voltage (kV)	8.0
Stored electrical energy (kJ)	1.53
Pulse recurrent frequency (Hz)	60
Average input electrical power (kW)	92
Neon pressure (Torr)	2.4
Average x-ray energy into 4π steradians (J)	12
Peak x-ray energy (J)	20
Fractional standard deviation (%)	40
X-ray yield efficiency (%)	0.78
Average x-ray power @ 60 Hz (W into 4π steradians)	720

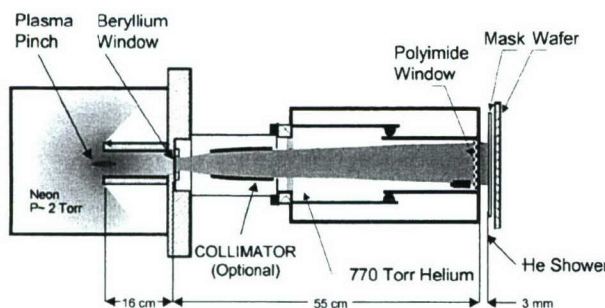


FIG. 10. Schematic of the x-ray beamline. X-ray beam travels from left to right to the wafer plane. Included in the schematic is a collimator optic that can be inserted directly into the beamline.

on both feature-size resolution and wafer-throughput capability. A schematic of the DPF x-ray beamline is shown in Fig. 10, and consists of 16 cm of low-pressure neon gas, a 14 μm thick beryllium window, and 55 cm of atmospheric helium that extends into the stepper wafer positioner. There is also a 25 μm thick polyimide window that supports a 3 mm helium flow shower near the wafer, and an x-ray mask that is modeled as 2 μm of tantalum silicide. The beamline optical components are summarized in Table VI.

Figure 11 shows the measured DPF x-ray spectra referenced to the plasma pinch position taken with a bent-crystal spectrometer.¹⁵ The neon spectrum contains strong line radiation between 0.9 and 1.1 keV. Radiation in the continuum beyond 1300 eV is determined by the recombination of free electrons with fully ionized neon atoms. According to Boltzmann kinetics, the intensity of recombination radiation for a given energy E is proportional to $\exp(-E/k_b T)$, where k_b is Boltzmann's constant and T is plasma temperature. The slope of this high-energy tail indicates the effective plasma temperature in the pinch is approximately 170 eV. The electron concentration in the plasma pinch can also be estimated using the observed x-ray spectrum. According to the Inglis-Teller formulation, the electron density in the plasma must be below the limit^{16,17}

$$n_e \approx \left(\frac{Z^3}{a_o^3} \right) \cdot \left(\frac{1}{2} \right)^{15/2} \cdot k^{-15/2}, \quad (3)$$

where Z is the nuclear charge, a_o is the Bohr radius, and k is the maximum observed energy quantum number for hydrogen-like ions (Lyman radiation) in the spectrum. The various radiation lines for neon in the DPF x-ray spectrum are called out in Fig 11(a). The highest observed energy level in the Lyman series is $k=6$, from which we estimate the electron concentration to be $n_e \sim 5 \cdot 10^{19} \text{ cm}^{-3}$.

TABLE VI. Summary of x-ray beamline components.

Parameter	Specification
Neon gas @ 2 Torr	16 cm
Beryllium window	14 μm
Helium beamline at @ 770 Torr	55 cm
Polyimide window	25 μm
He shower @ 770 Torr	3 mm
TaSi x-ray mask	2 μm

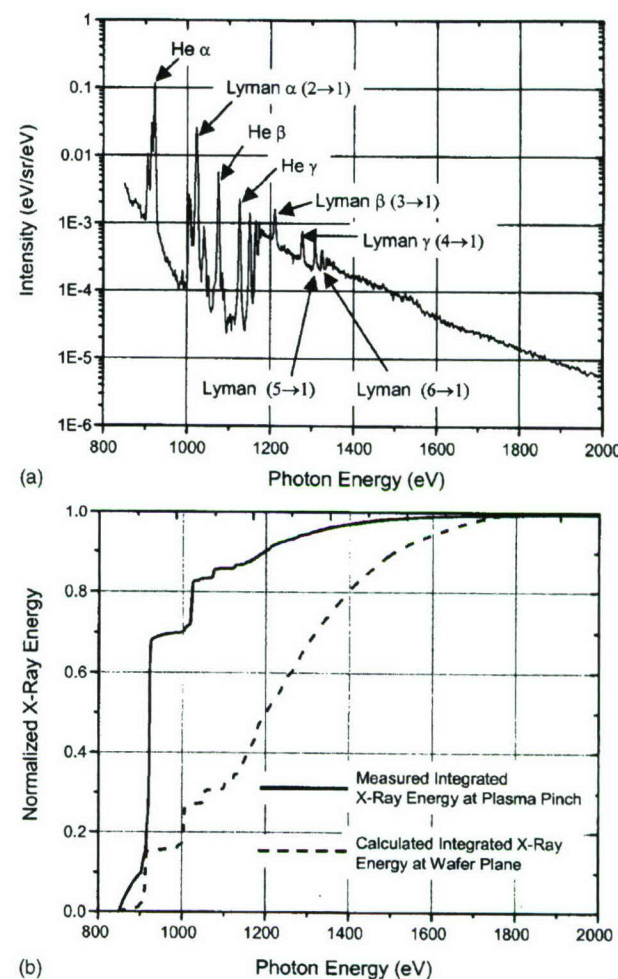


FIG. 11. (a) Measured integrated DPF x-ray spectra referenced to the plasma pinch (from Ref. 15), and (b) calculated integrated energy versus photon energy for the spectra at the plasma pinch and at the wafer plane.

Figure 11(b) presents a calculation of normalized integrated x-ray energy versus photon energy at the pinch position and at the wafer plane. The effective wavelength for the spectra is defined here at the half-amplitude point, and is approximately 920 eV at the plasma pinch. Beamline components harden the spectra as x rays propagate along the structure, and the calculated effective wavelength is approximately 1200 eV at the wafer plane.

The amplitude and spectral content of the DPF x-ray energy are key parameters in fine-line resolution and wafer-throughput capability. Proximity x-ray lithography at ~ 1 keV photon energy is limited to direct one-to-one printing, because at present there are no practical reflective or refractive optics that can operate at these wavelengths. Consequently, the smallest feature on the x-ray print mask will determine the minimum feature size on the semiconductor wafer. The resolution of the printed feature size is given as^{18,19}

$$R = \sqrt{\frac{\lambda \cdot g}{\alpha}}, \quad (4)$$

where g is the gap separation between mask surface and the wafer, λ is the effective wavelength, and α is a scaling factor

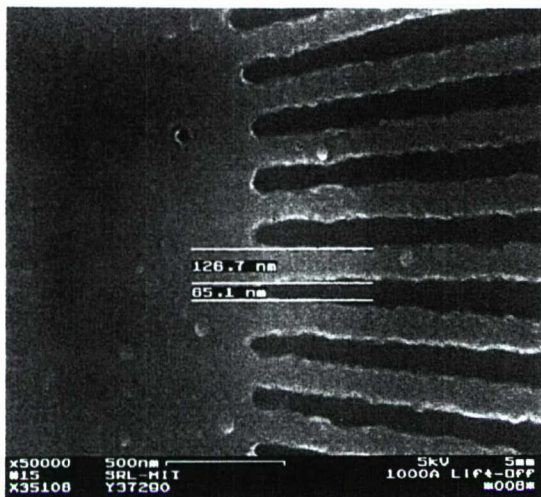


FIG. 12. Photograph showing 65 nm feature sizes produced by the DPF point source in PMMA. The x-ray mask-to-wafer separation was 3 μm . These data were obtained by the Nanolithography Laboratory, MIT, Cambridge, MA.

nominally related to the effective Fresnel number. The factor α is ~ 1 for photoresist materials like polymethylmethacrylate (PMMA) that activate linearly with dose level, and can be significantly higher for chemically amplified resists that have a sharp hysteresis in the dose contrast required to activate the resist.²⁰ Advanced x-ray mask designs that employ phase-shift techniques on the mask optical edges can also improve line resolution.²¹ However, for the nonphase shift masks used here, a high value for the α factor is important in order to achieve sub-100-nm line features because a practical limit for gap separation is nominally 10–15 μm due to parallelism issues between mask and commercial-grade GaAs wafer surfaces. Silicon wafers generally have better parallelism specifications, and gap separation settings of less than 5 μm are possible using high-precision x-ray steppers.

Lithography demonstration tests with PMMA photoresist have confirmed the effective x-ray wavelength calculation at the wafer plane. Figure 12 shows fine-line printing results that were obtained on the DPF point source by staff from the Nanolithography Laboratory.²² This measurement was obtained with a test fixture that spaced the x-ray mask gap 3 μm off the wafer surface. The measured linewidth of 65 nm is in reasonable agreement with the calculated 1200 eV effective x-ray wavelength at the wafer plane.

Figure 13 shows lithography test results obtained by BAE Systems using an experimental Shipley-XP1449L chemically amplified photoresist with the DPF source and wafer-position stepper.²³ This scanning electron microscope photograph shows a trench width of 71.6 nm that was produced for AlGaAs-based monolithic millimeter integrated circuits. This feature size was produced with a mask-to-wafer separation of 15 μm , and an activation x-ray fluence of 65 mJ/cm^2 on the wafer surface. The DPF point source can support a throughput of 8–10 field exposures per hour at this activation energy fluence, not including the time overhead for stepper alignment. The effective x-ray fluence im-

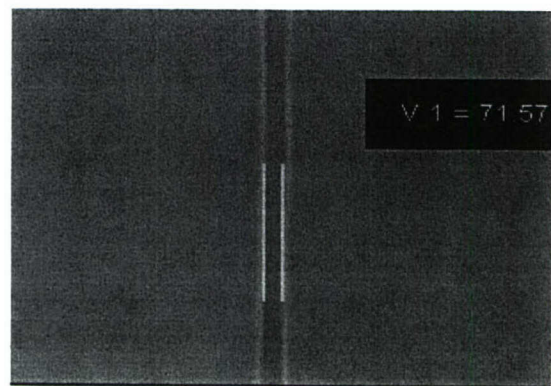


FIG. 13. Photograph showing a 71.6 nm trench feature produced using chemically amplified photoresist with the DPF point source and wafer-position stepper. The x-ray mask-to-wafer spacing was 15 μm , and the x-ray fluence on wafer was 65 mJ/cm^2 .

pinging on the wafer surface, after attenuation from beamline and mask components, is approximately 3 $\mu\text{J}/\text{cm}^2$ per shot.

The spatial stability of the emitting plasma is good, which allows small features to be printed accurately on GaAs wafers. Trench walls printed on GaAs wafers typically have a line-edge roughness and variability of less than 7 nm (3 σ) over an exposure length of tens of microns. Working back to the source, we estimate the effective emitting plasma diameter is less than 400 μm , and the shot-to-shot spatial variability of plasma centroid is less than 200 μm .

VIII. DPF COLLIMATOR DEVELOPMENT AND SHOCK WAVE ISSUES

An x-ray collimator is an important component for improving wafer-throughput capability because it can increase x-ray dose on target. A collimator optic that utilizes grazing incidence surfaces to collect and collimate the x-ray flux is presently under development, and is designed to increase the x-ray fluence by a factor of 2. This is achieved by increasing the effective collection solid angle by a factor of 3 from the simple line-of-sight optical approach.²⁴ This collimator optic can be inserted directly in the existing beamline structure, as illustrated in Fig. 10.

One issue involved with implementing a collimator optic with a large collection solid angle is the increased size of the vacuum window separating the low-pressure neon discharge and the high-pressure helium beamline. As discussed below, rapid plasma-pinch formation and adiabatic gas heating during x-ray generation generates an acoustic shock front that resembles an expanding spherical wave, which the hollow anode bore channels toward the x-ray window. Measurements of acoustic pressure pulses produced by the DPF discharge have shown that acoustic overpressure pulses must be carefully attenuated in order to avoid excessive mechanical stress on the vacuum window.

Measurements of pressure pulses generated by the DPF plasma pinch were measured using a fast-response piezo-transducer (type 134A24 from PCB Piezotronics, Depew, NY) that was placed 16 cm from the plasma pinch in the hollow anode assembly. This is the position where a beryllium window normally resides in the x-ray beamline (see

TABLE VII. Summary of acoustic pressure measurement diagnostics.

Parameter	Specification
Transducer	Type 134A24, PCB Piezotronics, Depew, NY
Transducer signal rise time	>200 ns
Transducer sensitivity	1.31 atm/V
Equivalent noise level	0.01 atm
Pressure range	0–15 atm
Distance between transducer and plasma pinch	16 cm

Fig. 10). The parameters of the pressure measurement system are listed in Table VII. The pressure diagnostic apparatus is able to measure pressure pulses up to 15 atm with a signal rise time of less than 200 ns, and is suitable for measuring the pressure pulses developed by the DPF discharge.

Figure 14 shows oscilloscope waveforms of a typical pressure pulse that was measured on a DPF, together with the associated anode voltage waveform. Peak acoustic pressure was determined according to the transducer's calibrated voltage signal specifications, and shock wave propagation velocity U_o was estimated from the delay time between the plasma pinch and the leading edge of the detected pressure signal.

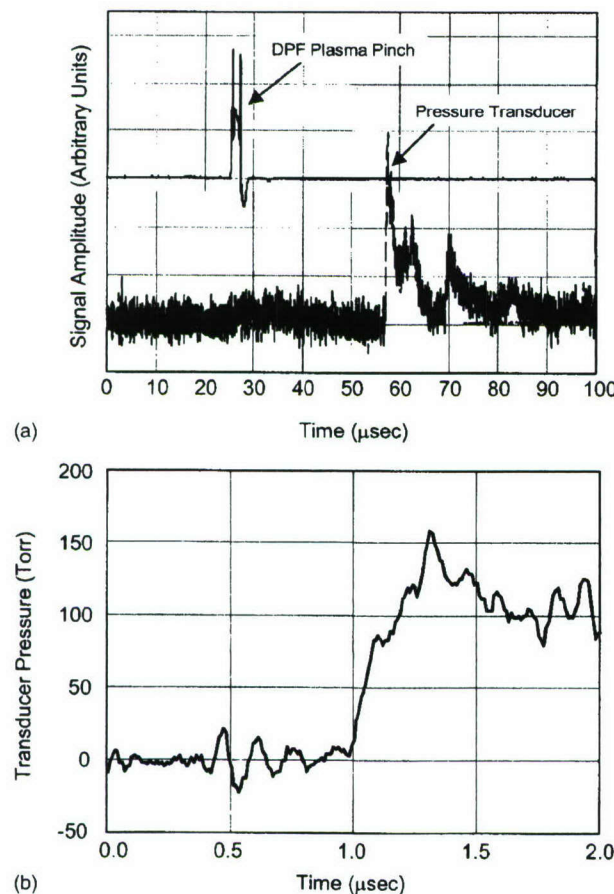


FIG. 14. (a) Oscillogram showing the time delay between plasma pinch and pressure transducer signals with the DPF operating at ~1 Torr neon. Plasma pinch to pressure transducer distance is 16 cm. (b) Pressure transducer waveform showing shock front amplitude and rise time.

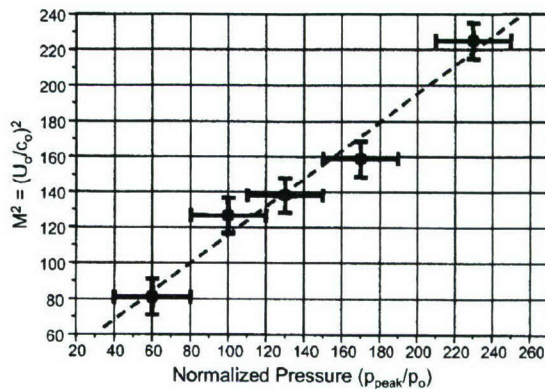


FIG. 15. Plot showing the square of acoustic shock Mach number (M^2) versus normalized acoustic shock overpressure for a DPF operating at ~1 Torr neon. The slope of the velocity-pressure curve is ~0.8.

We have also assumed a sound speed c_o of 390 m/s in undisturbed neon gas to calculate an effective Mach number $M = U_o/c_o$ for the pressure pulse.

Figure 15 plots the square of the measured Mach number M^2 versus normalized pressure, where the measured peak transducer pressure P was normalized to the undisturbed gas pressure P_o , which was typically 1 Torr in our experiment. The observed linear dependence of M^2 with normalized pressure is well described by shock wave theory.^{25,26} According to the Hugoniot equation

$$\left(\frac{U_o}{c_o}\right)^2 = M^2 \cong \frac{1}{2} \left(1 + \frac{1}{\gamma}\right) \cdot \frac{P}{P_o}, \quad \text{for } P \gg P_o, \quad (5)$$

where $\gamma = c_p/c_v$, c_p is specific heat at constant pressure, and c_v is specific heat at constant volume. The slope of the curve presented in Fig. 15 is ~0.8, and corresponds to the parameters $1/2(1+1/\gamma) \sim 0.8$ in Eq. (5). This implies $\gamma \sim 1.67$, which is the value for a monotonic gas like neon, and confirms that pressure pulses generated by the plasma pinch are accurately described by shock wave theory. These data also demonstrate that pressure pulses of 240 times and greater over the background gas pressure can be directed to the x-ray window.

Acoustic shock wave issues must be carefully addressed in the anode, x-ray window, and collimator designs in order to avoid mechanical failure with the x-ray window. We have employed special baffles in the anode for shock wave attenuation, as shown in Fig. 7. New types of baffle designs will be needed to support DPF operation with large solid-angle collection optics and x-ray windows.

ACKNOWLEDGMENTS

This work was performed for the DARPA Advanced Lithography Program, Dr. David Patterson, Program Manager. The authors acknowledge technical support provided by Dr. Henry Smith and staff at the Nanostructures Laboratory, MIT, Cambridge, MA.

¹ J. W. Mather, Phys. Fluids **8**, 366 (1965).

² N. Qi, S. Fulghum, R. Prasad, and M. Krishnan, IEEE Trans. Plasma Sci. **26**, 1119 (1998).

³ K. Simon, R. Macklin, R. Selzer, Q. Leonard, and F. Cerrina, Proc. SPIE

³ 3048, 168 (1997).
⁴ Yasuo Kato, Jpn. J. Appl. Phys., Part 1 **33**, 4742 (1994).
⁵ R. Petr, D. Reilly, J. Freshman, N. Orozco, D. Pham, L. Ngo, and J. Mangano, Jpn. J. Appl. Phys., Part 1 **39**, 607 (2000).
⁶ F. Incropera and D. DeWitt, *Fundamentals of Heat and Mass Transfer* (Wiley, New York, 1990).
⁷ R. Reid, M. Merigan, and J. Sena, "Review of Liquid Metal Heat Pipe Work at Los Alamos," *Proceedings of the IX International Heat Pipe Conference, Albuquerque NM* (1995).
⁸ D. E. Potter, Phys. Fluids **14**, 1911 (1971).
⁹ T. Butler, I. Henins, F. Jahoba, J. Marshall, and R. Morse, Phys. Fluids **12**, 1904 (1969).
¹⁰ V. Borisov, A. Davidovskii, and O. Khristoforov, Sov. J. Quantum Electron. **12**, 1403 (1982).
¹¹ M. Liberman, J. DeGroot, A. Toor, and R. Spielman, *Physics of High-Density Z-Pinch Plasmas* (Springer, New York, 1999).
¹² N. R. Pereira and J. Davis, J. Appl. Phys. **64**, R1 (1988).
¹³ Emerge Semiconductors, Inc., Freemont, CA.
¹⁴ P. Burkhalter, G. Mehlman, D. Newman, M. Krishnan, and R. Prasad, Rev. Sci. Instrum. **63**, 5052 (1992).
¹⁵ R. Whitlock, C. Dozier, D. Newman, R. Petr, J. Freshman, D. Hoey, and J. Heaton, Proc. SPIE **4781**, 54 (2002).
¹⁶ H. Griem, *Spectral Line Broadening in Plasmas* (Academic, New York, 1974).
¹⁷ D. Inglis and E. Teller, J. Astrophys. Astron. **90**, 499 (1939).
¹⁸ S. Hector, M. Schattenburg, F. Anderson, W. Chu, V. Wong, and H. Smith, J. Vac. Sci. Technol. B **10**, 3164 (1992).
¹⁹ W. Chu, H. Smith, and M. Schattenburg, Appl. Phys. Lett. **59**, 1641 (1991).
²⁰ F. Houle, W. Hinsberg, and M. Sanchez, Proc. SPIE **5039**, 334 (2003).
²¹ L. Yang, M. Khan, J. Taylor, Y. Vladimirsky, and N. Dandekar, Proc. SPIE **3997**, 530 (2000).
²² Nanolithography Laboratory, Professor H. I. Smith, Director, Massachusetts Institute of Technology, Cambridge, MA.
²³ Shipley Company LLC, Marlboro, MA.
²⁴ W. Cash, Proc. SPIE **4144**, 228 (2000).
²⁵ Y. Zeldovich and Y. Raizer, *Physics of Shock Waves and High-Temperature Hydrodynamic Phenomena* (Academic, New York, 1966).
²⁶ A. Shapiro, *The Dynamics and Thermodynamics of Compressible Fluid Flow* (Wiley, New York, 1953), Vol. 1.